Propagation of ultra-high-energy cosmic rays and their secondaries with CRPropa

Dissertation with the aim of achieving a doctoral degree

at the faculty of Mathematics, Informatics and Natural Sciences

Department of Physics

of Universität Hamburg

submitted by Arjen René van Vliet

2014 in Hamburg

Day of oral defense: December 3rd, 2014
Examiners of the oral doctorate defense:
Prof. Dr. Dieter Horns
Prof. Dr. Johannes Haller
Prof. Dr. Caren Hagner
The following evaluators recommend the admission of the dissertation:
Prof. Dr. Günter Sigl
Prof. Dr. Marcus Brüggen

Zusammenfassung

Mit Experimenten wie dem Pierre Auger Observatory (Auger) und dem Telescope Array (TA) ist es möglich, Daten mit einer hohen Statistik für das Energiespektrum, die Zusammensetzung und die Ankunftsrichtungen ultrahochenergetischer kosmischer Strahlung (ultra-high-energy cosmic rays – UHECR – kosmische Strahlung mit Energien über $\sim 10^{17}$ eV) zu erhalten. Um diese Daten in Bezug auf die tatsächlichen astrophysikalischen Parameter zu interpretieren oder um die astrophysikalischen Modelle in Hinblick auf die gesammelten Daten zu überprüfen, sind spezialisierte Simulationen der Ausbreitung von UHECR von ihrer Quelle zur Erde nötig. Zu diesem Zweck wurde die UHECR-Propagationssoftware CRPropa entwickelt. Sie berücksichtigt sowohl alle relevanten Wechselwirkungen mit der elektromagnetischen Hintergrundstrahlung (Paarproduktion, Photodisintegration und Photopionproduktion) als auch Kernzerfälle, Effekte der kosmologischen Entwicklung des Universums und Ablenkungen aufgrund von extragalaktischen und galaktischen Magnetfeldern. CRPropa, einschließlich ihrer neuesten Funktionen, wird in dieser Arbeit beschrieben.

Betrachtet man die Ausbreitung ultrahochenergetischer Kerne, so ist die dominierende Wechselwirkung für die meisten Isotope und Energien die Photodisintegration. Um die Photodisintegration in CRPropa für alle relevanten Isotope (bis hin zum Eisen) und Reaktionskanäle zu implementieren, wurden die Berechnungen unter Einbeziehung der entsprechenden Wirkungsquerschnitte, inklusive der Erweiterung hin zu geringen Massenzahlen, mithilfe der öffentlich zugänglichen TALYS-Software durchgeführt. Diese Umsetzung der Photodisintegration wurde ausgiebig mit dem Photodisintegrationsschema von Puget, Stecker und Bredekamp verglichen, was zu zahlreichen Verbesserungen der in CRPropa benutzten Wirkungsquerschnitte führte.

Die Wechselwirkungen der UHECR mit den elektromagnetischen Hintergrundfeldern können dazu führen, dass sekundäre Neutrinos und Photonen, die sogenannten kosmogenen Neutrinos und Photonen, entstehen, deren Produktion und Propagation CRPropa ebenfalls simulieren kann. Dem IceCube Neutrino Observatory (IceCube) ist es kürzlich gelungen, zum ersten Mal extraterrestrische Neutrinos mit Energien im PeV-Bereich zu beobachten. In der vorliegenden Arbeit wird unter Beachtung der durch den Fluss der kosmogenen Photonen gesetzten Grenzen untersucht, ob diese Neutrinos als Sekundärprodukte von UHECR-Wechselwirkungen entstehen könnten. Wir zeigen, dass die IceCube-Ereignisse höchstwahrscheinlich keine kosmogenen Neutrinos sind.

Eine weitere Methode, Einschränkungen an astrophysikalische Modelle zu bestimmen, besteht darin, die Ankunftsrichtungen von UHECR zu betrachten. Dazu wurden zahlreiche Untersuchungen bezüglich der Anisotropien am UHECR-Himmel durchgeführt. So hat beispielsweise Auger die Suche nach einem Äquatorialdipol in der Ankunftsrichtungen von UHECR unternommen. Die gemessenen Amplituden dieses Dipols werden in der vorliegenden Arbeit mit Simulationen realistischer Szenarien des UHECR-Universums verglichen. Auf diese Weise können diese Szenarien den tatsächlich gemessenen Daten gegenübergestellt werden. Ferner wird die Wirkung bestimmter Bestandteile des UHECR-Universums, wie z.B. der Ablenkung von UHECR in galaktischen und extragalaktischen Magnetfeldern und der Quellendichte der UHECR-Quellen, auf die Dipolamplitude untersucht. Hierbei zeigt sich, dass die Ablenkungen aufgrund der zuvor erwähnten Magnetfelder die erwartete Dipolamplitude in den untersuchten Fällen signifikant beeinflussen, gleichzeitig aber keine starke Abhängigkeit von der Quellendichte besteht.

Abstract

Due to experiments like the Pierre Auger Observatory (Auger) and the Telescope Array (TA), high-statistics data is becoming available on the energy spectrum, the composition and the arrival directions of ultra-high-energy cosmic rays (UHECRs, cosmic rays with energies above $\sim 10^{17}$ eV). To interpret this data in terms of actual astrophysical parameters, or to test astrophysical models against the measured data, dedicated simulations of the propagation of UHECRs from their sources to Earth are needed. To this end, the UHECR propagation code called CRPropa has been developed. It can take into account all relevant interactions with ambient photon backgrounds (pair production, photodisintegration and photopion production) as well as nuclear decay, cosmological evolution effects and deflections in extragalactic and galactic magnetic fields. CRPropa, including its newest features, is described in this thesis.

When considering the propagation of ultra-high-energy nuclei, the dominant interaction for most isotopes and energies is photodisintegration. Photodisintegration has been implemented in CRPropa for all relevant isotopes (up to iron) and all relevant photodisintegration channels using cross-section calculations with the publicly-available code called TALYS, including extensions for the low mass numbers. This photodisintegration setup is compared here extensively with the photodisintegration scheme developed by Puget, Stecker and Bredekamp, leading to several improvements on the cross sections implemented in CRPropa.

In the interactions of UHECRs with background photon fields, secondary neutrinos and photons, so-called cosmogenic neutrinos and photons, can be created. CRPropa can simulate the production and propagation of these secondary particles as well. The IceCube Neutrino Observatory (IceCube) has recently reported the first observation of extraterrestrial neutrinos in the PeV energy range. In this work is investigated whether these neutrinos could have originated as secondaries from UHECR interactions, taking into account limits on the cosmogenic photon flux. We show that the IceCube events are most likely not cosmogenic neutrinos.

An additional way to constrain astrophysical models is by looking at the arrival directions of UHECRs. Many different investigations into anisotropies in the UHECR sky have been reported. For instance, Auger has done a search for an equatorial dipole in the UHECR arrival directions. The measured amplitudes of this dipole are compared in this thesis with simulations of realistic scenarios of the UHECR universe. In this way these scenarios can be tested against the measured data. Furthermore, the effects of specific components of the UHECR universe on the dipole amplitude, as e.g. the deflections of UHECRs in galactic and extragalactic magnetic fields and the source density of UHECR sources, are investigated. Here it is shown that, for the investigated scenarios, the deflections in both aforementioned magnetic fields have a significant effect on the expected dipole amplitude, while no strong dependence on the source density has been found.

Contents

List of Figures

List of Tables

Introduction

Cosmic rays, energetic extraterrestrial particles mainly consisting of protons and atomic nuclei, have been a subject of intense research for over 100 years. There are, however, still many open questions concerning the interpretation of the measurements of cosmic rays. Cosmic rays with energies spanning many orders of magnitude, from below 10^9 eV to over 10^{20} eV, have been observed. In this thesis, done as part of the Pierre Auger Collaboration (Auger), the focus lies on the ultra-high-energy cosmic rays (UHECRs), cosmic rays with energies above $\sim 10^{17}$ eV. The two biggest experiments in operation at the moment measuring these UHECRs are Auger and Telescope Array (TA).

The slope of the observed energy spectrum of UHECRs shows a flattening at around 5×10^{18} eV, the so-called "ankle" (see e.g. Refs. [10–13]). The origin of this ankle is still unclear. Proposed reasons for it are, amongst others, a signature from interactions of ultra-high-energy (UHE) protons with the cosmic microwave background (CMB) (see e.g. Refs. [14–16]), a transition from galactic to extragalactic sources (see e.g. Refs. [17–20]), a transition from an extragalactic proton component to a different extragalactic heavy-nuclei component (see e.g. Refs. [21]), or a transition from lighter to heavier elements coming from the same sources (see e.g. Refs. [22, 23]).

Moreover, the UHECR spectrum shows a drop, or cut-off, at about 5×10^{19} eV (see e.g. Refs. [10–13]). This cut-off was predicted at around this energy by Greisen, Zatsepin and Kuzmin (GZK) due to energy losses of UHE protons in photopion-production interactions with the CMB. However, it is still unclear whether the measured cut-off is really due to this effect (see e.g. Refs. [14–16] for scenarios that produce this cut-off due to the GZK effect) or, for instance, due to a similar effect where UHE nuclei lose energy in photodisintegration interactions, or due to the UHECR sources reaching their maximum acceleration energy, or due to any combination of these effects (see e.g. Refs. [17–23]).

Furthermore, mass composition measurements by Auger suggest an increase in mass with energy above around 2×10^{18} eV [24–26]. This could be explained, for example, by a combination of a rigidity-dependent maximum acceleration energy at the sources and energy- and mass-dependent propagation effects (see e.g. Refs. [18–23]). In contrast, data from TA are compatible with a proton dominance in the same energy range (see e.g. Refs. [14–16] for pure-proton scenarios). Investigations are ongoing at the moment to explain the differences between the measurements of Auger and TA [12].

In addition, multiple ways of looking for anisotropies in the UHECR arrival directions have been performed on both TA and Auger data (see e.g. Refs. [13, 27–38]). Whereas many of these searches did not find any significant deviation from isotropy, some hints for anisotropies were still discovered. For example, recent results from TA indicate a significant clustering of events, a hot spot, in the sky [38]. Concerning large-scale anisotropy, recent results of Auger might give a hint for a dipole component in the equatorial plane [34–36].

When UHECRs propagate through the intergalactic medium, they can interact with background photons fields. In these interactions secondary neutrinos and photons, so-called cosmogenic neutrinos and cosmogenic photons, can be created. The IceCube Neutrino Observatory (IceCube) has recently detected extraterrestrial neutrinos in the 10^{13} eV to 2×10^{15} eV energy range [39–41]. The origin of these neutrinos is not clear at the moment. One possibility might be that they are cosmogenic neutrinos, which will be investigated in Chapter 4.

In order to interpret these measurements in terms of the different possible astrophysical scenarios, and thus to investigate what the sources of UHECRs and their characteristics are, dedicated simulations of the propagation of UHECRs from their sources to Earth are needed. CRPropa is a publicly available software package which is designed to simulate this propagation of UHE protons and nuclei as well as the production and propagation of their secondary photons and neutrinos [1, 4, 42–44]. From simulations with CRPropa realistic energy spectra, mass compositions and arrival directions can be obtained.

In Chapter 1 an overview is given over the field of cosmic rays and their secondary photons and neutrinos. It includes a historical overview as well as the current status of UHECR, cosmic neutrino and diffuse photon measurements. Furthermore, the propagation of UHECRs through the intergalactic medium is discussed. In this light, several possible interpretations of the UHECR data are presented. The effects that different realizations of the cosmic magnetic fields and UHECR source distributions can have on the UHECR observables are indicated as well. The predictions for the cosmogenic neutrino and photon flux depend strongly on the specific astrophysical scenarios and are therefore discussed as well.

In Chapter 2 version 2.0 of CRPropa [1, 43] is presented. Here an overview is given of all the included interactions and of the ways the UHECR sources and observers can be simulated. Several example applications are shown as well.

When considering the propagation of UHE nuclei the dominant interaction for most isotopes and energies is photodisintegration. In Chapter 3 the photodisintegration setup of CRPropa is compared extensively with the widely-used photodisintegration scheme developed by Puget, Stecker and Bredekamp [8, 9].

In Chapter 4 it is investigated whether the extraterrestrial neutrinos observed by IceCube could be cosmogenic neutrinos [45, 46]. This is done for several scenarios, including pure-proton composition scenarios (taking into account the cosmogenic photon flux as well), pure-iron injection scenarios and mixed-composition source scenarios.

In Chapter 5 version 3.0 of CRPropa [4, 44], which is currently under development, is presented. CRPropa 3.0 incorporates a complete redesign of the code structure to facilitate high performance computing and includes new physical features such as an interface for galactic propagation using lensing techniques, and the possibility to do four-dimensional simulations, which makes it possible to include cosmological effects as well as deflections in magnetic fields in a single simulation.

Finally, in Chapter 6 the measured dipole amplitudes by Auger [36] are compared with the dipole amplitudes for simulations of realistic scenarios of the UHECR universe. In this way these scenarios can be tested against the measured data. Furthermore, the effects of specific parts of the UHECRs universe on the dipole amplitude, such as the deflections of UHECRs in galactic and extragalactic magnetic fields and the source density of UHECR sources, are investigated.

Unless stated otherwise, we use natural units $\hbar = c = 1$ throughout this thesis.

Chapter 1

Cosmic rays and their secondaries

Cosmic-ray physics has a long and rich history, with the first discovery occurring more than 100 years ago. In this chapter a short overview is given of some selected important events concerning cosmic-ray physics. Furthermore, the current status of cosmic-ray physics at ultra-high energies (UHEs, energies above 10^{17} eV or 0.1 EeV) is presented. During the propagation of cosmic rays through the intergalactic medium (IGM) secondary neutrinos and photons can be produced in interaction with background photon fields. Therefore, cosmic-neutrino physics at energies above 10^{14} eV (0.1 PeV) and the diffuse photon spectrum at energies above 10^{8} eV (0.1 GeV) are closely related to the physics of ultra-high-energy cosmic rays (UHECRs) and will be treated here as well. For a general review on UHECR physics, mostly focused on the experimental side, see e.g. Ref. [47]. Additionally, Ref. [48] gives a review of the extragalactic propagation of UHECRs specifically and is more focused on the theoretical side. For a very recent brief overview of UHECR physics, see e.g. Ref. [49].

1.1 Historical overview

As early as 1901 extraterrestrial radiation was mentioned for the first time [50]. At that time Charles Thomson Ress Wilson, who would become a Nobel Laureate in 1927 for his invention of the cloud chamber in 1911, found that ion production appears in closed and isolated detectors even in the absence of a source. He was wondering at that time already whether this penetrating radiation could be extraterrestrial, but concluded that it was unlikely that the ionization was due to radiation which has traversed our atmosphere. At the time it was thought that this radiation emanates from the Earth's crust.

In the following years, 1902-1904, Franz Linke would perform ionization measurements with an electrometer during twelve balloon flights [51]. He compared his ionization measurements with the ionization level on the ground. It was about the same between altitudes of 1000 meters to 3000 meters, but larger by a factor of four at 5500 meters. His published results have unfortunately never been broadly recognized.

A few years later, in 1908, the actual term "cosmic radiation" was born. Theodor Wulf and Albert Gockel used the term for the first time in their publication about their study of ionization rates on high mountains in the Alps. They did not observe strong deviations from measurements at sea level.

1.1.1 The first discovery

In 1912 the actual first discovery of cosmic rays took place. In that year Victor Hess undertook seven balloon flights, the highest one on the seventh of August reaching an altitude of 5350 meters. All detectors aboard the balloon during this highest-altitude flight measured a strong increase in ionization at altitudes above 4000 meters. Hess concluded that a radiation of high penetration power hits the atmosphere from above, which cannot be caused by radioactive emanations [52]. As one of the balloon flights was during an eclipse, he also concluded that this radiation did not originate from the sun.

The first theoretical investigation of possible sources of the cosmic radiation was presented by Egon Schweidler in 1915. Based on the existing knowledge of ionizing radiation, he excluded the upper atmosphere, the moon, the planets, the sun and other fixed stars as sources of cosmic rays. He concluded that "the less extreme requirements prefer the hypothesis of radioactive substances distributed in outer space".

The first cosmic-ray tracks in a cloud chamber were discover in 1927 by Dmitri Skobeltsyn. He investigated beta rays in a cloud chamber operating in a magnetic field. By chance, he observed straight tracks which he interpreted as being due to high-energy cosmic rays. This was the first visual proof for the existence of charged secondaries produced by primary cosmic rays.

Another noteworthy event for cosmic-ray physics was the prediction of the neutrino by Wolfgang Pauli in 1930 [53]. It was introduced by him as a neutral particle to preserve momentum conservation in beta decays, which had to be a three-body decay. He assumed that it would never be detectable.

1.1.2 New particles discovered

One year after Paul Dirac's prediction of the existence of the positron in 1931 [54] it was observed for the first time in cosmic-ray tracks by Carl Anderson [55, 56]. He found unexpected tracks in photographs of his cloud chamber that he correctly interpreted as having been created by a particle with the same mass as the electron but with opposite charge.

In 1934 Walter Baade and Fritz Zwicky identified supernovae as a new category of astronomical objects [57]. Based on the estimated energy release, they proposed that these supernovae could be possible sources of cosmic rays. This hypothesis is still valid, but not completely confirmed.

In the meantime another new particle, the pion, was predicted by Hideki Yukawa in 1935 [58]. He estimated that this particle's mass would be about 10^8 eV (100 MeV) and predicted that these particles could be produced in cosmic particle interactions. One year later the pion was assumed to be discover by Seth Neddermeyer and Carl Anderson [59, 60]. However, the new particle that they had discovered turned out to be the muon, not the pion. The pion was eventually found in 1947 by Perkins [61], Lattes, Occhialini and Powell [62, 63], also in cosmic-ray tracks. After this discovery, in 1949, Yukawa would become the first Japanese Nobel laureate.

1.1.3 Extensive air shower

Pierre Auger, together with his colleagues Ehrenfest, Maze, Daudin and Robley, was the first to detect extensive air showers originating from a single cosmic-ray event in 1939 [64]. They estimated that the energy of the primary cosmic particles had to be at least 1 PeV. This discovery led to the beginning of air-shower experiments after the second world war.

A model for the acceleration of charged cosmic particles still used today was developed in 1949 by Enrico Fermi [65]. The basic idea behind his model was that charged particles can get accelerated by collisions against moving magnetic fields in e.g. plasma clouds. One of the features of this theory is that it naturally yields an inverse power law for the slope of the energy spectrum of cosmic rays. However, it is not straightforward to explain acceleration up to ultra-high energies with this model.

Starting from the year 1954, a first generation of extensive air shower (EAS) arrays was developed. For instance, in Britain an EAS array was built covering an area of about 0.6 km^2 operating from 1954 to 1957. Other strong initiatives were taking place in the USA, Japan and the Soviet Union.

The era of space experiments started with the launch of Sputnik 2 in 1958. On board was a Geiger counter used to measure the intensity of cosmic rays. A strong increase in radiation was measured at a latitude of 60°, which would later be interpreted as the outer radiation belt [66].

In the same year the first prototype of a water Cherenkov detector was built [67]. It consisted of a steel tank filled with water and a photomultiplier looking from the top into the water. This model is still very similar to the design of the modern water Cherenkov detectors at e.g. IceTop and the Pierre Auger Observatory (Auger).

1.1.4 Features in the cosmic ray spectrum

One of the significant features in the energy spectrum of cosmic rays, the so-called "knee" at an energy of around 10 PeV, was discover also in 1958 by Kulikov and Khristiansen [68]. They demonstrated that there is a change in the slope of the spectrum of cosmic rays at this energy.

A setup for the detection of high-energy cosmic neutrinos was first proposed in 1960 by Markov [69]. He suggested to install arrays of photomultipliers in deep lakes or in the sea to search for rare neutrino interactions. This started the first generation of undersea neutrino-telescope projects.

In the meantime the Volcano Ranch EAS experiment had started operation in 1960 at an altitude of 1770 meters in New Mexico. The first cosmic ray with an energy larger than 100 EeV was detected by this experiment [70]. Moreover, it gave the earliest hint of a flattening of the energy spectrum above around 1 EeV, the so-called "ankle".

In 1965 Penzias and Wilson found, by chance, an excess temperature of 3.5 K, which was isotropic, unpolarized and independent of seasonal variations, in their background noise measurements of the Bell Labs horn-reflector antenna [71]. Dicke, Peebles, Roll and Wilkinson realized that this effect was the cosmic microwave background radiation (CMB) [72].

The first atmospheric neutrinos were detected by two different groups in the same year. This kind of neutrinos are decay products from pions or kaons produced in interactions of cosmic rays in the atmosphere. The Bombay-Osaka-Durham group operated a detector in the Kolar Gold Field in India [73, 74], while the Case-Witwatersrand-Irvine collaboration did their research in a gold mine in South Africa [75].

One year later the Greisen-Zatsepin-Kuzmin (GZK) cut-off in the cosmic ray spectrum was predicted [76, 77]. This cut-off is due to a theoretical upper limit of $E_{\mathrm{GZK}} \approx 5\times10^{19}$ eV on the energy that protons coming from distant sources can have. When UHE protons (p) propagate through the universe they can interact with the CMB photons

(γ) and produce pions ($\pi^{+,0}$) through the delta resonance (Δ^+):

$$\begin{aligned} p + \gamma \to \Delta^+ &\to p + \pi^0 \ , \qquad (1.1)\\ &\to n + \pi^+ \ , \qquad (1.2) \end{aligned}$$

where n is a neutron. The energy loss per interaction in this process is typically about $m_\pi/m_p \approx 15\%$, where m_p is the proton mass and m_π is the pion mass. The cross section for this reaction near the threshold is $\sigma = 2 \times 10^{-28}$ cm^2, and the total CMB photon number density is $\rho = 400$ cm^{-3}, giving a collision mean free path of $\lambda = 1/\rho\sigma = 4.1$ Mpc for all the CMB photons. For the 10% of photons with the highest energies the mean free path would be of the order of 50 Mpc. Therefore, one can expect that protons with $E > E_{\mathrm{GZK}}$ coming from beyond the local galactic supercluster would have their energies attenuated by collisions with the CMB.

1.1.5 Large arrays

In 1970 the Yakutsk EAS array, located in Siberia, started data-taking [78]. The array consisted of scintillation counters, air Cherenkov detectors as well as muon detectors. It was at the time, with a surface of 18 km^2, the largest, most complex array to measure the energy spectrum, the incoming direction and the mass composition of cosmic rays in the energy range of 0.1 EeV to 100 EeV.

The Fly's Eye Detector [79] began observations in 1981 and was the first fluorescence detector array. It was operated until 1993 and was located in the desert of Utah at an altitude of about 1370 meters. This array was able to register fluorescence light over an area of about 1000 km^2 on moonless nights. The cosmic ray with the highest energy ever measured ($(3.2 \pm 0.9) \times 10^{20}$ eV) was detected by this array in 1991 [80].

On February 23th 1987 a supernova explosion (SN1987A) in the Small Magellanic Cloud, approximately 51.4 kpc from Earth, was discovered by optical telescopes and was even visible to the naked eye. Approximately two to three hours before the visible light of SN1987A reached Earth, data of three different underground detectors looking for proton decays in large volumes of water and in liquid scintillators observed an excess of neutrino events. The Japanese Kamiokande II detected 11 events within 13 seconds, the US IMB 8 events within 6 seconds and the Soviet Union Baksan 5 events within 9 seconds [81]. These were the first detections of low-energy cosmic neutrinos and marked the beginning of neutrino astronomy.

From 1990 until 2004 the Akeno Giant Air Shower Array (AGASA) in Japan was in operation. It consisted of 111 scintillator detectors and 27 muon detectors distributed over an area of 100 km^2. They measured in total 11 events with an energy greater than 100 EeV [82], which did not show the decrease expected for the GZK effect.

The Antarctic Muon And Neutrino Detector Array (AMANDA) was a neutrino telescope array located beneath the Amundsen-Scott South-Pole Station. The first string of photomultiplier modules was installed in the ice in 1993. In its latest development stage AMANDA was made up of an array of 677 optical modules mounted on 19 separate strings that were spread out in a rough circle with a diameter of 200 meters. In 2005 AMANDA officially became part of its successor project, the IceCube Neutrino Observatory (IceCube). No significant neutrino signals from sources outside of our solar system were found by AMANDA [83, 84].

1.1.6 Modern experiments

The experiments discussed here are a selection of the most modern detectors in cosmic-ray and cosmic-neutrino physics. They will be discussed in slightly more detail than the previous experiments.

1.1.6.1 KASCADE and KASCADE-Grande

A new generation of modern EAS arrays came into operation with the start of the Karlsruhe Shower Core and Array Detector (KASCADE) [85] in 1996. It measured simultaneously the electromagnetic, muonic and hadronic components of extensive air showers initiated by cosmic rays [86]. In 2003 KASCADE was extended with 37 scintillation counter stations to become KASCADE-Grande [87]. This allowed the study of the composition of cosmic rays from 1 PeV to 1 EeV. On March 30th 2009 KASCADE-Grande was officially shut down.

One of the main results obtained by these two experiments is showing that the composition becomes increasingly heavier above the knee, caused by a break in the spectrum of the light components [88, 89]. Conventional acceleration models predict this change of the composition towards heavier components. The discovery of the knee in the heavy components (the so-called "second knee"), would be a convincing verification of these theories. From the observed rigidity-dependent breaks of the spectra of different lighter primaries observed between 0.1 and 10 PeV, the iron knee is expected at around 100 PeV. The KASCADE-Grande Collaboration reported a first evidence of the observation of a steepening in the cosmic-ray energy spectrum of heavy primary particles at about 80 PeV in 2011 [90].

A further contribution from the Karlsruhe group is the CORSIKA (Cosmic Ray Simulations for KASCADE) simulation program for cosmic-ray air showers [91], which is still used worldwide today for far more applications than just for KASCADE data.

1.1.6.2 High-Resolution Fly's Eye

The High-Resolution Fly's Eye (HiRes) experiment [92], operational from May 1997 until April 2006, replaced the first-generation Fly's Eye detectors in Utah. HiRes consisted of two fluorescence observatories, HiRes-I and HiRes-II, separated by 12.6 km.

HiRes measured the energy spectrum of UHECRs and detected, at energies greater than 50 EeV, a decrease in the measured particle flux in agreement with the expectations from the GZK effect [10, 93, 94]. They also investigated the composition of UHECRs, which turned out to be compatible with a proton-dominated distribution above 1.6 EeV [95]. Analyses of anisotropies in HiRes data did not find any significant deviations from an isotropic flux [96, 97].

1.1.6.3 The IceCube Neutrino Observatory

After seven years of work, starting in 2004, IceCube [98] was completed on December 18th 2010. Its thousands of sensors are distributed over a cubic kilometer of volume under the Antarctic ice. IceCube consists of spherical optical sensors called Digital Optical Modules (DOMs), each with a photomultiplier tube (PMT) and a single board data-acquisition computer which sends digital data to the counting house on the surface above the array. The DOMs are deployed on 86 strings of 60 modules each at depths ranging from 1450 to 2450 meters.

To extend the observable energies of IceCube to below 100 GeV, a more dense region of strings is employed at the Deep Core low-energy extension [99]. The Deep Core strings are deployed at the center of the larger array, deep in the clearest ice at the bottom of the array (between 1760 and 2450 meters deep).

On top of IceCube, an array called IceTop of 81 pairs of Cherenkov detector tanks is installed on the surface to investigate cosmic-ray air showers in the "knee" energy region [100]. Besides being used for cosmic ray composition studies, it looks for coincident detections as a way to veto IceCube events coming from cosmic-ray air showers.

In 2013 IceCube reported the first observation of two neutrinos in the PeV range, named "Ernie" and "Bert" [39]. After improving their sensitivity and extending their energy coverage down to around 3×10^{13} eV (30 TeV), 26 additional events were observed [40]. With one year more of data the total number of events increased to 37, including one event, called "Big Bird", with an energy of ~ 2 PeV, the highest-energy neutrino interaction ever observed [41]. Whereas IceCube has not been able to find any extraterrestrial point sources yet, it has set an upper limit on the neutrino flux associated with gamma-ray bursts (GRBs, possible candidate sources of UHECRs) that is at least a factor of 3.7 below the predictions [101].

1.1.6.4 The Pierre Auger Observatory

The largest extensive air shower array ever built, and still in operation today, is the Pierre Auger Observatory (Auger) [102] located on the Argentinian Pampa Amarilla. Its development was first proposed in 1992 by Jim Cronin and Alan Watson. Its construction began in 2000, the first data collecting started in 2004 and its full construction was officially completed in 2008. It is the first true hybrid cosmic ray observatory, employing two independent methods to detect UHECRs. Its main detector array consists of 1600 water Cherenkov detectors (or SD, surface detector) distributed on a grid of 1.5 km spacing over an area of 3000 km^2 [103] and 24 air fluorescence telescopes (or FD, fluorescence detector) located at four stations on the periphery of the observatory [104].

Besides the main detector array several additional types of detectors are being operated, developed or tested at Auger. As an enhancement to the main detector array, in order to lower the energy threshold to around 0.1 EeV, extensions on both the SD and the FD arrays have been implemented. The extension to the SD array includes a subarray, the Infill, with 71 water Cherenkov detectors on a denser grid of 750 m spacing covering nearly 30 km^2 [105]. This subarray is part of AMIGA (Auger Muons and Infill for the Ground Array) which will have underground scintillator muon counters at each of the 71 water Cherenkov detectors as well [34]. The extension to the FD array is called HEAT (High Elevation Auger Telescopes) and includes three additional fluorescence telescopes, located at one of the fluorescence stations, that are tilted upwards to extend the elevation range [105]. This allows the station to see the shower development including shower maximum for lower energy events. These extensions of Auger allow the study of the energy range where the transition from a galactic to an extragalactic origin of cosmic rays could occur.

Furthermore, a prototype radio-telescope array (AERA, Auger Engineering Radio Array) for detecting radio emission from the cosmic-ray showers in the 10-100 MHz frequency range, consisting of 124 radio sensors covering 6 km^2, is under development [105]. An additional subarray of 61 radio sensors (EASIER, Extensive Air Shower Identification with Electron Radiometer), covering 100 km^2, is operating in the GHz range [34]. Besides, two prototypes of GHz imaging parabolic dish radio telescopes, AMBER (Air shower Microwave Bremsstrahlung Experimental Radiometer) [105] and MIDAS (MIcrowave Detection of Air Showers) [106], have been added to Auger.

Moreover, several upgrades of the main detector array are being tested at the moment. This includes upgrades to the SD electronics to improve the timing resolution and the dynamic range. In addition, several ways of including muon detectors to the SD array are being tested. With these muon detectors the information on the mass of the cosmic rays in an event-by-event basis can be improved.

Important results of Auger include the exploration of the UHECR spectrum at and above the cut-off around 40 EeV. The first detection of this suppression of the flux by Auger was reported in Ref. [107], for a more recent determination of the UHECR spectrum see Refs. [12, 13]. Furthermore, they investigated the particle composition of UHECRs, see Refs. [24–26]. Additionally, a first hint of the extragalactic origin of the highest-energy cosmic particles has been observed by them, see Refs. [13, 27, 28, 108].

1.1.6.5 Telescope Array

The Telescope Array (TA) project [109] in Utah is the successor regarding air fluorescence shower detection of Fly's Eye and HiRes. It operates three fluorescence stations with 12-14 telescopes each [110], and combines it with a ground array of 507 scintillator counters with 1.2 km spacing distributed over an area of 762 km^2 [111]. It started data-taking in 2007.

TA is complemented by a low-energy extension called TALE (Telescope Array Low Energy) [112]. With TALE cosmic rays with energies between 30 PeV and 10 EeV can be observed. TALE adds 10 new telescopes, tilted upwards to extend the elevation range, to one of the fluorescence stations, making it 24 telescopes in total at that station. As in the case with HEAT, this allows the station to see the shower development including shower maximum for lower energy events. Furthermore, the TALE project also includes a graded infill array of scintillator stations spaced 400 m and 600 m apart, extending the detection capabilities of the ground array down to 30 PeV.

A project in development at TA is the Telescope Array RADAR (TARA) [113]. The goal of TARA is to develop a bistatic radar detection system that is able to maintain a 24 hour duty cycle at a fraction of the cost of conventional detection systems. This system will be built alongside the existing Telescope Array and will use analog television transmitters and digital receivers to observe cosmic rays. Once completed, this new facility will be known as the W.M. Keck Radar Observatory.

Being located on the northern hemisphere, while Auger is located on the southern hemisphere, makes the two experiments complimentary when looking at arrival directions. TA found a significant clustering of events, a hot spot, in the northern hemisphere [38]. Further important results include the confirmation of the presence of the ankle and the cut-off in the UHECR spectrum [11, 113–115]. In addition, TA also looks at the composition of UHECRs [113]. Auger and TA have started collaborating to measure the large-scale anisotropy in the arrival directions of UHECRs of their combined data set [37], to do a cross-calibration of the fluorescence telescopes of both experiments and to better understand the differences in the separate analyses of the mass composition between the two experiments [12].

1.1.6.6 PAMELA

PAMELA (Payload for Antimatter Matter Exploration and Light-nuclei Astrophysics) [116] is an operational cosmic-ray detection module attached to the upward-facing side of the Earth-orbiting Russian Resurs-DK1 satellite. It was launched by a Soyuz rocket from Baikonur Cosmodrome on 15 June 2006 and is dedicated to the exploration of the antimatter component of cosmic rays.

PAMELA measured an unexpected increase in the positron fraction at energies between 10 GeV and 100 GeV [117, 118], a possible sign of dark-matter annihilation. However, no excess of antiprotons was found [119, 120]. This is inconsistent with predictions from most models of dark matter sources, in which the positron and antiproton excesses are correlated. Another explanation for the increase in positron fraction would be the production of electron-positron pairs on pulsars with subsequent acceleration in the vicinity of the pulsar.

1.1.6.7 Fermi Large Area Telescope

The Fermi Gamma-ray Space Telescope (FGST) [121], formerly called the Gamma-ray Large Area Space Telescope (GLAST), carries two experiments, the Large Area Telescope (LAT) [122] to perform an all-sky survey measuring high-energy photon in the energy range from 30 MeV to 300 GeV and the Gamma-ray Burst Monitor (GBM) [123], formerly GLAST Burst Monitor, for the detection of GRBs in the energy range from 8×10^3 eV (8 keV) to 30 MeV. FGST was launched on 11 June 2008 aboard a Delta II 7920-H rocket.

The high sensitivity of both instruments allowed the detection of many new galactic and extragalactic gamma-ray sources (with LAT) and GRBs (with GBM) (see e.g. Refs. [124–127]). Furthermore, with the LAT electromagnetic calorimeter the electron flux was measured in the energy range from 7 GeV to 1 TeV [128, 129]. The number of positrons in the energy range from 20 GeV to 200 GeV was investigated as well and an increase in the positron fraction was observed [130]. Additionally, Fermi-LAT determined that supernova remnants act as accelerators for cosmic rays [131]. Moreover, Fermi LAT measured the extragalactic diffuse gamma-ray emission [132], important when considering photons originating as secondaries from cosmic rays interacting with extragalactic background light.

1.1.6.8 Antimatter-Matter Spectrometer

The Antimatter-Matter Spectrometer [133] (AMS-02) is a cosmic particle spectrometer installed on the International Space Station (ISS). The principal investigator of AMS-02 is Nobel laureate Samuel Ting. AMS-02 was launched on the space shuttle Endeavour flight STS-134 on May 16th, 2011. It was designed to detect cosmic particles and antiparticles in the energy range from 0.5 GeV to 1 TeV. In this way the claims of a rising positron fraction from PAMELA and Fermi LAT can be investigated and a possibility to do an indirect search for dark matter exists.

The first results of AMS-02 are published in Refs. [134–136]. There, precision measurements of the positron fraction in primary cosmic rays in the energy range from 0.5 to 500 GeV by AMS-02 are presented. The data show that the positron fraction is steadily increasing from 10 to $\sim$200 GeV, but, from 20 to 200 GeV, the slope decreases by an order of magnitude. Above $\sim$200 GeV the positron fraction no longer exhibits an increase with energy. The positron-fraction spectrum shows no fine structure, and the positron to electron ratio shows no observable anisotropy. These results are consistent with the positrons originating from the annihilation of dark matter, but not yet sufficiently conclusive to rule out e.g. the production of electron-positron pairs by pulsars with subsequent acceleration in the vicinity of the pulsar.

1.1.6.9 EUSO

The Extreme Universe Space Observatory (EUSO) [137] is the first space-mission concept designed to investigate UHECRs, aiming especially at the highest energies, $E > 50$ EeV. It is designed to detect UHECRs by looking at the fluorescence light produced by particle showers in the Earth's atmosphere. The area that can be monitored by EUSO will be $> 1.3 \times 10^5$ km^2, the exact value depending on its operation mode. Due to the orbit of the ISS it will have a full sky coverage as well as a nearly uniform exposure over the whole sky. The annual exposure of EUSO will be about 9 times that of the SD detectors of Auger.

Initially EUSO was a mission of the European Space Agency (ESA), designed to be hosted on the ISS as an external payload of the module Columbus. However, in 2004 ESA decided not to proceed with the mission because of programmatic and financial constraints. Thereafter, EUSO was redesigned as a payload to be hosted on board of the Japanese Experiment Module (JEM) of the ISS [138]. The mission was then renamed JEM-EUSO. The complete funding and the launch date for JEM-EUSO are still unclear. Before JEM-EUSO is launched, however, a Russian-Japanese initiative called KLYPVE or K-EUSO is planned to go up to the Russian segment of the ISS [139]. K-EUSO can be considered as a plain experiment for some specific, although not exhaustive, science items, but also as a pathfinder for the bulk of the physics of JEM-EUSO and for demonstrating the space-based concept for UHECR studies.

1.2 Current status

Here the current measurements of the different observables of UHECRs, cosmic neutrinos and cosmic photons that will be of the most importance for the following chapters are discussed. The two biggest experiments concerning the measurement of UHECRs are Auger and TA. An overview will be given of the spectrum, composition and anisotropy results of these two experiments in the next sections. As secondary neutrinos and photons can be produced when UHECRs interact with ambient photon backgrounds, the current status of the cosmic neutrino spectrum and the diffuse photon spectrum will be discussed as well.

1.2.1 UHECR spectrum

The cosmic ray energy spectrum is a smooth power-law spectrum over many orders of magnitude in energy and flux. It contains three clear general features, the cosmic-ray knee above 1 PeV, the cosmic-ray ankle at about 5 EeV and the cut-off above 40 EeV. The cosmic-ray spectrum below the knee is a power law $\mathrm{d}N/\mathrm{d}E \propto E^{-\alpha}$ with spectral index $\alpha = 2.7$. Above the knee the spectral index increases to about $\alpha = 3.1$. Above the ankle the spectral index becomes similar again to the one before the knee. Both Auger and TA measure at which energy the ankle and the cut-off occur and what the spectral indices in the regions before and after the ankle are.

Auger measures the ankle at $\log_{10}(E_a/\mathrm{eV}) = 18.72 \pm 0.02$, where the spectral index changes from 3.23 ± 0.07 to 2.63 ± 0.04 [12, 13]. The cut-off starts at about 20 EeV, where the spectrum starts to deviate from a simple power law and a flux suppression is observed. When fitted with a power law with smooth suppression above the ankle, at an energy of $\log_{10}(E_{50\%}/\mathrm{eV}) = 19.63 \pm 0.01$ the observed spectrum is half of what is expected from the extrapolation of a power law without suppression. When compared to a simple continuation of the power law starting just above the ankle, the significance of the cut-off is more than 20 standard deviations (sigma). The overall systematic uncertainty on the absolute energy scale of Auger is 14%.

Both the ankle and the cutoff are clearly visible in the spectrum measured by TA [11] as well. In this case a fit to a broken power law with three different regions finds the ankle at an energy of $E_a = 4.6 \pm 0.3$ EeV and the start of the cut-off at $E_c = 54 \pm 6$ EeV. The spectral indices for the regions below the ankle, between the ankle and the cut-off and above the cut-off are, respectively, -3.34 ± 0.04, -2.67 ± 0.03 and -4.6 ± 0.6, furthermore $\log_{10}(E_{50\%}/\mathrm{eV}) = 19.72 \pm 0.05$. When again compared to a simple continuation the power law starting just above the ankle, the significance of the cut-off is 5.5 sigma. The systematic uncertainty on the flux of TA is 37%.

Within systematic uncertainties the flux measurements of Auger and TA are in good agreement, with one exception, the cut-off energy E_c seems to be at a lower energy in the Auger case than in the TA case [11]. Even with a 20% energy scale correction, the difference between the Auger and TA measurements of E_c is three sigma. The origins of both the ankle and the cut-off are, however, yet to be determined.

A likely scenario is that cosmic rays with energy up to the knee are accelerated at galactic astrophysical objects. The principal candidates for galactic cosmic-ray acceleration are supernova remnants, although powerful binary systems could also play a role. The knee itself is probably a result of reaching the maximum energy of such accelerators. Cosmic rays above the ankle are believed to come from extragalactic sources. Possible extragalactic accelerators are active galactic nuclei (AGNs), radio galaxies, GRBs or other energetic astrophysical systems. Where the particles between the knee and the ankle are accelerated is not clear, possibly at different, very efficient, galactic accelerators.

1.2.2 UHECR composition

The composition of UHECRs is measured by Auger and TA by looking at the depth of maximum, X_{max} (measured in g/cm^2), of the longitudinal development of air showers induced by UHECRs. There are, however, large intrinsic fluctuations of X_{max} from shower to shower due to the random nature of the interaction process. Nevertheless, due to the difference in the cosmic-ray cross section with air, the average value of X_{max} can be used as an energy-dependent measure of the composition of the primary cosmic rays. This is done by comparing the measured values of $\langle X_{\mathrm{max}} \rangle$ with air shower simulations to determine the composition of the primary cosmic rays. Air shower simulations, however, are subject to uncertainties mostly because hadronic interaction models need to be employed at energy ranges far beyond those accessible to man-made particle accelerators. This combination makes composition studies of UHECRs particularly difficult. Besides $\langle X_{\mathrm{max}} \rangle$, another statistical observable which distinguishes composition, and is less model dependent, is given by the width of the X_{max} distribution ($\sigma(X_{\mathrm{max}})$).

Both the $\langle X_{\mathrm{max}} \rangle$ and $\sigma(X_{\mathrm{max}})$ data measured by Auger suggest an increasingly heavier mass composition above 4 EeV [25]. The TA measurements, however, are compatible with a proton-dominated composition at all energies [113], but have much larger statistical uncertainties due to the smaller size and shorter runtime compared with Auger. Due to complications and differences in the data analysis, both collaborations have started to jointly investigate the origin of these differences in mass composition measurements. The result of that preliminary study shows that the proton- and Auger-like composition cannot be discriminated from one another within the presently available TA statistics [12].

1.2.3 UHECR anisotropy

Another important observable of UHECRs is the distribution of their arrival directions over the sky. Unlike the energy or the primary mass, the arrival direction is practically free from systematic errors. The measured arrival directions by the ground arrays of Auger and TA have an angular resolution of about ∼1° [11, 140]. When events are detected by the fluorescence detectors in the stereo or hybrid modes, the angular resolution can even be up to an order of magnitude better [104]. With Auger in the southern hemisphere and TA in the northern hemisphere, together, they cover the whole sky.

The UHECR anisotropy is mainly determined by the distribution of sources over the sky and the deflections in both extragalactic magnetic fields (EGMFs) and galactic magnetic fields (GMFs). The distribution of the sources is completely unknown, although could be assumed to follow the large-scale structure (LSS) baryon density. There is not that much known about the EGMFs either. They are usually assumed to have a magnitude below $\lesssim 10^{-9}$ G and a correlation length up to ∼1 Mpc due to measurements on Faraday rotations of extragalactic sources [141]. Several LSS simulations provide predictions for the EGMF (see e.g. Refs. [3, 142–148]), but they vary strongly amongst each other.

The GMF is known much better than the EGMF. Several models of the GMF have been constructed based on measurements of the Faraday rotations of extragalactic sources, see e.g. Refs. [149–151].

At the highest energies the propagation distances of UHECRs are expected to be relatively small (a few tens of Mpc) due to the GZK-effect for protons and photodisintegration interactions of heavier nuclei. Due to these small propagation distances the sources are expected to be distributed anisotropically following the LSS of the universe.

If the primary cosmic rays are predominantly protons, one might expect possible bright spots of the size of a few degrees corresponding to individual bright sources. On the other hand, if the primary cosmic rays are heavier nuclei, they will undergo stronger deflections in the different magnetic fields, but the arrival directions of the cosmic rays are still expected to be anisotropic in a manner similar to the source distribution at the scale of a few tens of degrees.

1.2.3.1 Localized excesses of UHECRs

One way to search for local excesses in the UHECR sky is by using the two-point angular correlation function [152]. This method is particularly useful when there are no obvious bright spots but rather many excesses with a small amplitude and similar angular size. In that case an excess in correlations at the corresponding angular scale is expected. Both Auger and TA data have been examined by using this method, but so far without any positive results [30, 31].

Another way to identify local excesses, best suited to find individual bright spots, is by looking for excesses in a moving window of given angular size and estimating the background either from Monte Carlo (MC) simulations or directly from the data. The overall significance is then corrected for the effective number of trials, typically calculated by MC simulations. Auger applied this method to its data for $E > 1$ EeV with window sizes of 5° and 15° [34], again without finding any significant deviations from isotropy. TA performed analogous searches in several energy bands around 1 EeV with a search window of 20° and a position-dependent window of several degrees [33]. They did not find any significant excesses either.

However, when looking solely at the highest energies, the situation changes. Auger has reported an excess of events with $E > 55$ EeV around the direction of Centaurus A, an AGN at a distance of about 3.5 Mpc [29]. Recent results of TA indicate, for $E > 57$ EeV, a significant clustering of events, a hot spot, in a different position in the sky [38]. The hot spot was found with a search window of 20°. It has a significance of 5.1σ and is located about 19° off of the supergalactic plane. The probability of a cluster of events of 5.1σ significance appearing by chance in an isotropic sky is estimated to be 3.4σ.

1.2.3.2 Point sources

If the composition of UHECRs is light, and the extragalactic and galactic magnetic fields are not unexpectedly strong, one might expect that at the highest energies arrival directions point back to their sources. The number of potential sources within the GZK horizon is limited, and directional correlation between the position of candidate sources and the cosmic-ray arrival direction could occur.

This was investigated by Auger in Ref. [27], where the observation of a correlation between the arrival directions of cosmic rays with $E > 55$ EeV and the positions of nearby AGNs from the 12^{th} edition of the catalog of quasars and active nuclei by Véron-Cetty and Véron [153] (VCV catalog) was reported. The parameters of the correlation ($E > 55$ EeV, maximum source distance in the catalog of 75 Mpc, maximum opening angle of 3.1°) were fixed from the exploratory scans in the independent data set. In Ref. [27] it was found that the hypothesis of an isotropic distribution of cosmic rays above 6×10^{19} eV could be rejected with at least a 99% confidence level.

However, in a more recent update on this correlation, with an increased number of events from 27 to 69 [28], the correlating fraction went down from $(69^{+11}_{-13})\%$ to $(38^{+7}_{-6})\%$ with 21% expected for isotropic cosmic rays. The latest update on this correlations with the VCV catalog shows a similar result with the correlation signal at 2σ above the expected fraction for an isotropic sky [13, 32]. When showing the number of correlating events in an energy ordered plot, the onset of the correlation signal is visible at about 55 EeV.

The same correlation, with the parameters fixed at the values set by the Auger analysis, has been investigated by TA [31]. TA found a slight excess of correlating events over an isotropic distribution, compatible both with isotropy and with the latest results of Auger. The combined probability to observe such a correlation from an isotropic distribution is around 10^{-3}, which is too large to draw any firm conclusions.

1.2.3.3 Spherical harmonic moments

Harmonic analysis is a standard tool in searches for medium- and large-scale anisotropies. The application of this method is limited, however, in the case of UHECRs due to the incomplete sky coverage of the current experiments. Auger covers only the southern hemisphere and TA covers only the northern hemisphere. Therefore, not all components of the low multipoles can be obtained unambiguously from the data of a single observatory. For example, only the (x, y)-components of the dipole, in equatorial coordinates, can be obtained in a straightforward way by a single experiment.

Auger has reported a search for the equatorial dipole [34–36]. The measured amplitude of the dipole is consistent with expectations from the isotropic background. The dipole amplitude is, however, not the most sensitive observable because of the energy binning and the related loss in statistics. The phase of the dipole may show a regular behavior with energy, which would be an indication of a non-zero dipole. When looking at the measured phase, one sees that the values of the phase are correlated in adjacent energy bins and the phase behavior is consistent with a continuous curve. This may indicate the presence of a non-zero dipole in the Auger data, with an amplitude just below the detection threshold.

The problem of the incomplete sky coverage can be resolved by combining the data of Auger and TA. However, this is not straightforward due to the uncertainty in the relative flux calibration resulting probably from possible differences in the energy scales of the two experiments. Despite these difficulties Auger and TA did a joined analysis of spherical harmonic moments with full-sky coverage for energies above $E > 10$ EeV [37]. No significant deviations from isotropic expectations were found in this analysis. Upper limits on the amplitudes of the dipole and quadrupole moments were obtained as a function of the direction in the sky, varying between 7% and 13% for the dipole and between 7% and 10% for a symmetric quadrupole.

The measured amplitudes of the dipole are compared with simulations of realistic scenarios of the UHECR universe in Chapter 6. In this way these scenarios can be tested against the measured data. Furthermore, the effects of specific components of the UHECR universe on the dipole amplitude, as e.g. the deflections in GMFs and EGMFs and the source density, can be investigated.

1.2.3.4 Correlation with the large-scale structure

A correlation with the local LSS is expected if the deflections of UHECRs do not exceed 10-20°, as would be the case for a predominantly light composition and relatively small EGMFs. The strongest correlations are expected at the highest energies, as there the propagation distances as well as the deflections in magnetic fields are limited. By checking such a correlation, if there is no positive detection, one can put a lower limit on the UHECR deflections, which are related to the magnetic fields strengths and the composition of UHECRs.

Following this method, an expected arrival-direction map can be obtained for e.g. a generic model where sources trace the distribution of matter in the nearby universe [154, 155]. With some assumptions for the UHECR composition, energy and magnitudes of deflections the expected map can be compared with the measured UHECR distribution by making use of an appropriate statistical test. The results of this analysis using the latest TA data set show that for $E > 10$ EeV the data is compatible with isotropy and incompatible with the LSS model for all but the largest smearing angles. For $E > 57$ EeV, however, the data is compatible with the LSS model and not compatible with isotropy.

A similar analysis has been done using publicly released Auger data for $E > 55$ EeV [156]. Here it was found that the correlation of the Auger events with the LSS model is larger than for 94%-98% of the realizations that would be expected for complete isotropy. However, it is smaller than that expected from $\gtrsim 85\%$ of realizations predicted in the model where the UHECR sources follow the local LSS matter distribution.

1.2.3.5 Additional anisotropy searches

If multiple cosmic rays from the same source reach Earth, they are expected to be deflected by magnetic fields, where the cosmic rays with lower energies will be deflected more than the cosmic rays with higher energies. Auger has studied anisotropies is the search for groups of this kind of directionally-aligned events (or multiplets) which exhibit a correlation between arrival direction and the inverse of the energy [157]. The observation of several events from the same source in this way would allow for the reconstruction of the position of the source as well as the determination of the integral of the component of the magnetic field orthogonal to the trajectory of the cosmic ray. No statistically significant evidence for the presence of these kind of multiplets in the present data was found.

Another way anisotropies can be looked at is by investigating additional energy-dependent patterns in the arrival directions of cosmic rays. If the highest-energy cosmic rays ($E > 60$ EeV) roughly point back to their sources some of the lower-energy cosmic rays in a region around them may be of the same origin. The distribution of their arrival directions may show energy-dependent patterns from deflections in cosmic magnetic fields. Auger investigated the local regions around cosmic rays with $E > 60$ EeV by analyzing cosmic rays with energies $E > 5$ EeV (just above the ankle) arriving within an angular separation of $\sim 15°$ [158].

Two different methods were used to characterize the energy distributions inside the local regions. One method is by looking for energy-energy correlations between pairs of cosmic rays depending on their angular separation from the center of the region. In the other method the directional energy distribution is decomposed along its principal axes. Thereafter, the strength of collimation of energy is measured along these principal axes. No significant patterns are found with this analysis.

1.2.4 Cosmic neutrino spectrum

The only experiment able to measure the cosmic neutrino spectrum for energies above $\sim$10 TeV is IceCube. Their most recent results, with three years of data collected from the complete IceCube detector, give a total of 37 events in the energy range between 10 TeV and 2 PeV [41]. These observations reject a purely atmospheric origin for all events at the 5.7σ level. The extraterrestrial neutrino flux ($\nu + \overline{\nu}$) as a function of energy is provided in Ref. [41]. The best-fit power law to this flux with a per-flavor normalization $(1:1:1)$ is $E^2\phi(E) = 1.5 \times 10^{-8}(E/100\text{TeV})^{-0.3}$ GeV cm^{-2}s^{-1}sr^{-1}.

In addition to the neutrino spectrum IceCube also measures the arrival directions. To identify any bright neutrino sources a maximum-likelihood clustering search was employed, as well as a directional correlation search with TeV gamma-ray sources. None of these investigations yielded statistically significant evidence of clustering or correlations. The strongest clustering, although statistically not significant, is near the galactic center. A test statistic greater than or equal to the observed value was found in 28% of scrambled datasets.

With or without a possible galactic contribution, the high galactic latitudes of many of the highest-energy events suggest at least a partially extragalactic component. Local large diffuse sources, e.g. the Fermi bubbles [159] or the galactic halo [160, 161], could also contribute to the events with a high galactic latitude, but these models can typically only explain at most a fraction of the data. Previous point-source studies would have been sensitive to a northern-sky point source producing more than 1-10% of the best-fit flux, depending on declination and energy spectrum [162]. Due to the lack of any evidence for such sources as well as the wide distribution of the IceCube events it is expected that the neutrinos originate from many individual dim sources. Contributions from a few relatively bright sources cannot be ruled out, however, especially in the southern hemisphere where the sensitivity of IceCube to point sources is reduced by the large muon background and small target mass above the detector.

Whereas IceCube has not been able to find any extraterrestrial point sources yet, it has set an upper limit on the neutrino flux associated with GRBs [101]. GRBs have been proposed as possible candidate sources for UHECRs [163–165]. Cosmic-ray acceleration should be accompanied by energetic neutrinos produced in the decay of charged pions created in interactions between the high-ernergy protons and gamma-rays [166]. IceCube has reported a limit on the flux of high-energy neutrinos associated with GRBs that is at least a factor of 3.7 below the predictions of Refs. [166–169]. This implies that GRBs are not the sources, or at least not the only sources, of UHECRs or that the neutrino-production efficiency in GRBs is much lower than what has been predicted.

Another possible source of neutrinos in the PeV range is as secondaries from UHECRs that interact with ambient photon backgrounds, the so-called cosmogenic neutrinos. This possibility is discussed in Chapter 4, based on Refs. [45, 46].

1.2.5 Diffuse photon spectrum

When UHECRs interact with ambient photon backgrounds, they will not only produce neutrinos but photons as well. These photons can cascade down to energies in the 0.1-100 GeV range. Therefore not only the cosmic neutrino spectrum, but also the extragalactic diffuse gamma-ray spectrum, commonly designated as "extragalactic gamma-ray background" (EGB), is important. The EGB by definition has an isotropic distribution on the sky and is generally considered to be the superposition of many different contributions. These contributions range from unresolved extragalactic sources including AGNs [170], GRBs [171], star-forming galaxies [172–174], starburst galaxies [175] and blazars [176, 177] to truly-diffuse photon-emission processes. These diffuse processes include e.g. the possible signatures of LSS formation [178, 179], the annihilation or decay of dark matter [180, 181], the interactions of UHECRs with ambient photon backgrounds [182, 183] and many more (see e.g. Ref. [184] and references therein). It is not completely clear, however, that the measured EGB is actually extragalactic. For instance, the diffuse gamma-ray emission from inverse Compton scattering by an extended galactic halo of cosmic-ray electrons could also be attributed to the EGB if the size of the halo is large enough [185]. In addition, gamma-ray emission from cosmic rays interacting in populations of small solar-system bodies [186] as well as the all-sky contribution of inverse Compton scattering of solar photons with local cosmic rays can provide contributions [187, 188].

The EGB was first detected by the *SAS-2* satellite [189] and later confirmed by analysis of the EGRET data [190]. The most recent measurements on the EGB, however, are from Fermi LAT [132]. The EGB measured by Fermi LAT is consistent with a power law with differential spectral index $\alpha = 2.41 \pm 0.05$ and intensity $I(E > 0.1 \text{ GeV}) = (1.03 \pm 0.17) \times 10^{-5} \text{ cm}^{-2}\text{s}^{-1}\text{sr}^{-1}$.

The EGB can be considered as an upper limit for the photon flux produced in UHECR interactions with ambient photon backgrounds as many other sources could contribute to the EGB but the contribution from secondary photons from UHECR interactions should at least not exceed the total EGB. In Chapter 4 the secondary photon flux from UHECR interactions is compared with the EGB for several different scenarios.

1.3 The propagation of UHECRs

UHECRs do not propagate freely in the IGM. During their propagation they can lose energy in interactions with intergalactic background light, nucleons can be separated (for nuclei heavier than proton) due to these interactions or due to nuclear decay and they can be deflected in cosmic magnetic fields. In order to interpret the measurements on UHECRs in terms of characteristics of sources of UHECRs, it is essential to understand the effects of their propagation from source to Earth. This requires extensive simulations of the propagation of UHE nuclei and their secondaries within a given scenario.

The propagation starts with the injection of cosmic rays into the IGM at their sources. However, there is not much known yet about the sources of UHECRs. The source distribution, the injection spectrum of UHECRs at the sources, the maximum energy up to which the sources can accelerate particles and the mass composition of cosmic rays at their sources are all unknown. One of the goals of the measurements on UHECRs is to actually find out (some of) these open questions. Therefore, to simulate the propagation of UHECRs through the IGM, some assumptions have to be made about the sources. With the outcome of the simulations these assumptions can be tested against measured UHECR data.

During the propagation of UHECRs from their sources to Earth, they can undergo several different types of interactions. When they traverse the IGM they can interact with the CMB and with the cosmic UV/optical/IR background (IRB). As UHECRs carry charge they can suffer energy losses by e^+e^- pair production on these photon fields,

$$N + \gamma \to N + e^+ + e^- \ , \tag{1.3}$$

with N the UHECR nucleus, γ the background photon, e^+ the positron and e^- the electron. This can occur when photon energies boosted into the rest frame of the nucleus are of the order of $\epsilon \sim 1$ MeV. For UHE protons pair-production is the dominant energy-loss interactions for $E \lesssim 50$ EeV. Furthermore, pair production is the most important reaction for the creation of secondary photons in the TeV range.

For photon energies in the rest frame of the nucleus at or above the nuclear binding energy $\epsilon' \gtrsim$ 8-9 MeV, nucleons and light nuclei can be stripped off the nucleus (photodisintegration),

$$N + \gamma \to N^* + X \ , \tag{1.4}$$

where N^* is the remainder of the photodisintegrated nucleus N and X can contain any combination of nucleons and light nuclei. Photodisintegration does not affect free protons or neutrons, but is essential in the propagation of nuclei. There are many competing photodisintegration processes which could occur when nuclei propagate through the background photon fields. Depending on the nucleus, photodisintegration can be the dominant energy-loss interaction over the whole UHE energy range up to extremely high energies $\sim 10^{22}$ eV.

At photon energies in the rest frame of the nucleus exceeding $\epsilon' \sim$145 MeV the quark structure of free or bound nucleons can be excited to produce mesons. Here the production of pions (being the lightest mesons) is the most common (photopion production),

$$N + \gamma \to N^* + \pi^{0,+} \ , \tag{1.5}$$

with $\pi^{0,+}$ the created pion. This is the interaction, for UHE protons interacting with the CMB, behind the GZK cut-off. In the case of nuclei, pion production is only relevant for extremely energetic cosmic rays. However, it is important to be included to properly account for the production of secondary UHE photons and neutrinos, as well as for the propagation of secondary and primary protons and neutrons.

In these interactions the nucleus can be disrupted and unstable elements can be produced. Hence, nuclear decay plays a role in the propagation of UHECRs as well,

$$N \to N^* + X^* \ , \tag{1.6}$$

where X^* can contain neutrons, protons, alpha particles, electrons, positrons, neutrinos and photons.

Due to the possibly long extragalactic propagation times of UHECRs, the effects of cosmological evolution should also be taken into account. Not only can cosmological evolution affect the cosmic ray itself, it also alters the background photon fields with which the cosmic rays can interact. Furthermore, it can also affect the density of UHECR sources.

In addition, as UHECRs are charged particles, they can be deflected by magnetic fields both in the IGM as well as in our own galaxy. To take into account all these different types of interactions dedicated simulations tools for the propagation of UHECRs are needed.

There are different tools available that can do such simulations. CRPropa [1, 4, 42–44] (see also Chapters 2 and 5) is an example of a publicly available software package that is designed to simulate the propagation of UHECRs and their secondary gamma rays and neutrinos. From simulations with CRPropa, realistic energy spectra, mass compositions and arrival directions of UHECRs can be obtained.

Another Monte Carlo simulation code for the propagation of UHECRs is SimProp [191]. The developers of SimProp focused on a tool which can provide fast and reliable analysis of the predictions on the spectrum and chemical composition. It uses a simplified nuclear model and a one-dimensional (1D) treatment of the propagation. Currently a paper is in progress on comparisons between CRPropa and SimProp.

Another example of a UHECR propagation code is HERMES [192]. Other groups have reported simulations of the propagation of UHECRs as well, not using any of these publicly available codes (see e.g. Refs. [193–195]).

1.4 Interpretation of the UHECR data

Even though a wealth of different data is available, there are still many open questions concerning the interpretation of the measurements on cosmic rays and their possible secondaries. It is, for example, not clear yet where the ankle at around 5 EeV and the cut-off at about 40 EeV in the UHECR spectrum comes from or what the composition of UHECRs is.

A popular model is the extragalactic pure-proton model where both the ankle and the cut-off are explained by proton propagation signatures, see e.g. Refs. [14–16]. In this case the ankle originates from electron-positron pair production signatures on the CMB, while the cut-off is due to the GZK cut-off. The transition from galactic to extragalactic cosmic rays is assumed to happen at $E \lesssim 1$ EeV. A pure proton composition of UHECRs is consistent with TA data, but ruled out by Auger composition measurements. In Ref. [15] the spectrum of protons was calculated analytically by assuming a homogeneous distribution of sources in space and continuous energy losses. It was obtained for protons interacting with the CMB using the conservation of the number of protons. The spectrum calculated here is called the universal proton spectrum (see also Ref. [196]).

However, many other possible interpretations can be found in the literature as well. One such interpretation is, for example, presented in Ref. [22]. Here a model was developed to explain the Auger spectrum and, in particular, the fact that the mass composition data of Auger becomes steadily heavier with increasing energy for $E > 3$ EeV and is proton dominated below this energy. In this model the proton component, assumed to be of extragalactic origin, disappears at higher energies due to a low maximum energy of acceleration $E_p^{\max} \sim$ 4-10 EeV. Under the assumption of a rigidity acceleration mechanism, the maximum acceleration energy for a nucleus with charge number Z is $ZE_p^{\max}$. Therefore, the highest energy in the spectrum, reached by iron, does not exceed 100-300 EeV.

The assumption that heavy nuclei are accelerated to higher energies than protons or light nuclei is based on stronger deflections of the heavier nuclei in the electromagnetic fields of the cosmic ray sources. The acceleration of UHECRs due to magnetic fields leads to the well-known Hillas criterion [197]. When a particle escapes the region where it was being accelerated, it will not gain any more energy. This imposes a limit on the maximum energy of the accelerated particle,

$$E_{\max} = qBR \ , \tag{1.7}$$

where q is the charge of the accelerated particle, B is the magnetic field strength and R is the size of the accelerator. This equation is obtained by demanding that the Larmor radius of the particle, $R_L = E/(qB)$, does not exceed the size of the acceleration region. This is known as the Hillas criterion and is used for determining potential acceleration sites.

The observed increase in mass composition with energy is, in the case of Ref. [22], explained by this rigidity mechanism of acceleration. This model was named the "disappointing model" as it has disappointing consequences for future observations: very low cosmogenic photon and neutrino fluxes are expected, the GZK cut-off does not occur (the cut-off is explained by a combination of the sources reaching their maximum acceleration energy and energy losses due to photodisintegration) and the correlation with nearby sources is likely to be absent due to the stronger deflections in magnetic fields of the heavier nuclei present at the highest energies in this model. In this case the ankle is explained by a transition from protons to heavier nuclei. The UHECR spectrum was calculated in an analytic way as explained in Refs. [198, 199].

Another possibility could be that the ankle is due to a transition from galactic to extragalactic sources, as for instance in the model proposed in Ref. [19]. The cut-off is in this case due to a combination of the UHECR sources reaching their maximum acceleration energy and energy loss due to photodisintegration interactions of heavy nuclei (as in the previous cases). Here the propagation of UHECR nuclei was studied with the code described in Ref. [195]. This code uses the simplified photodisintegration chain described in Refs. [8, 9] (see also Chapter 3) where, instead of the Gaussian model of Ref. [9], they implemented a generalized Lorentzian model as parametrized in Ref. [200] for nuclei with a nuclear mass number $A > 10$. They took into account the deflections by EGMFs in their 1D simulations by approximating the path extension due to the EGMFs in the small-angle limit assuming many small deflections from different uniform magnetic fields. The results were fitted to the spectrum, the $\langle X_{\max} \rangle$ measurements and the $\sigma(X_{\max})$ measurements by Auger. They reported their best fit to the combined Auger data for the case that the sources accelerate primarily intermediate-mass nuclei such as nitrogen or silicon up to relatively low energies ($\sim 10^{21}$ eV).

In Ref. [18] comparisons are made between the pure-proton model (see the first model discussed in this section) and a mixed-composition model. In the case of the mixed-composition model the ankle is again due to a transition from galactic to extragalactic sources and the cut-off is again due to a combination of the UHECR sources reaching their maximum acceleration energy and energy losses due to photodisintegration interactions of heavy nuclei. The composition of UHECRs at their sources is assumed here to be similar to the composition of galactic cosmic rays at lower energies as given in Ref. [201]. Both models are compared against the UHECR spectrum and composition measurements. To simulate the propagation from the extragalactic sources to Earth, they used the code described in Refs. [193, 194]. The photodisintegration is in this case handled by a full two-dimensional set-up in (A, Z) space including all the possible paths with cross sections obtained, as described in Ref. [200], from the code named TALYS [202]. The effects of magnetic fields are assumed not to significantly influence the propagation of the UHECRs. They conclude that the mixed-composition model is favored over the pure proton model, mainly due to the composition measurements.

The assumption that EeV protons up to the ankle (as both Auger and TA measure a proton-dominated mass composition at EeV energies) could have a galactic origin contradicts the standard model for galactic cosmic rays (see e.g. Ref. [203, 204]), where the maximum galactic acceleration energy of $E_{\rm max}^{\rm gal} \approx 0.1$ EeV is attained by iron nuclei. However, one could assume an additional high-energy proton component of the galactic cosmic rays extending up to a few EeV. Normally, a galactic source of such high-energy protons is excluded by arrival-direction measurements. However, this can be bypassed when considering a case as suggested in Ref. [17]. Here it is suggested that a GRB could have occurred in our galaxy 10^6-10^7 years ago producing high-energy protons. These protons propagate in a non-stationary diffusion mode, so that by now most of them have already escaped the galaxy and only the tail of retarded particles with a reduced anisotropy is observed. In this way the transition from galactic to extragalactic cosmic rays occurs at the ankle.

A similar model even suggests a complete galactic origin of UHECRs [23] where past galactic GRBs are considered as sources. In this case the energy-dependent mass composition measured by Auger comes from the difference in diffusion time in the GMF for different species. The anisotropy in the direction of the galactic center is expected to be a few percent on average, while the locations of the most recent/closest bursts could be associated with observed clusters of UHECRs. In this scenario the ankle is explained by a transition from protons to heavier nuclei, while the cut-off is explained by the heaviest cosmic rays diffusing out of the galaxy.

Recently two different groups reported combined fits of the spectrum, $\langle X_{\rm max} \rangle$ and $\sigma(X_{\rm max})$ measurements of Auger, see Refs. [20, 21]. Both of these studies concluded that hard source spectra ($\alpha \sim$ 1-1.8) as well as relatively low maximum sources energies ($\sim 5Z$ EeV) are needed to fit the data.

In Ref. [20] the UHECR simulation code as first described in Ref. [195] was used. Three different mass groups, proton, nitrogen and iron, were injected at the sources, with their abundances being a parameter in the fit. The source spectral index in the range $1 < \alpha < 3$ was scanned over as well. The fits were done for two maximum source-energy cases, $E_{\rm max,Fe} = 10^{20}$ eV and $E_{\rm max,Fe} = 10^{20.5}$ eV with $\mathrm{d}N/\mathrm{d}E \propto E^{-\alpha} e^{-E/E_{\rm max,\mathit{Z}}}$ and $E_{\rm max,\mathit{Z}} = (Z/26) E_{\rm max,Fe}$. In the fit with the lower maximum source energy a very hard source spectral index of $\alpha = 1$ (on the edge of the parameter range) and a dominantly light composition with abundances at the $\sim 10\%$ level for intermediate nuclei and at the $\sim 1\%$ level for heavy nuclei was found as best fit. For the fit with the higher maximum source energy, a heavier composition (50% proton, 30% nitrogen and 20% iron) and a higher source spectral index of $\alpha = 1.8$ was found. Both maximum source energies are, however, relatively low, close to the GZK cut-off energy for the different species considered.

For Ref. [21] a kinetic-equation approach, assuming the continuous-energy-loss approximation, is used to calculated the propagation of UHECRs. In this case the combined fit requires again a hard injection spectrum at the sources, $\alpha \leq 1.5$-1.6, and a relatively low maximum source energy, $\sim 5Z$ EeV. In this case the spectrum below the ankle is shown to be composed of extragalactic light nuclei with an injection spectrum with a slope of $\alpha \sim 2.7$.

The hard injection spectra obtained here for energies above the ankle are far harder than that typically produced by non-relativistic first-order Fermi shock acceleration. This might point to alternative acceleration scenarios, such as drift acceleration at relativistic shocks [205], or such as those that take place in the magnetosphere of rapidly rotating neutron stars [206–209], which can naturally give rise to hard spectra.

1.5 Effects of magnetic fields and source distribution

Cosmic magnetic fields are expected to significantly deflect UHECRs during their propagation from their sources to Earth. Our understanding of the GMF has made some progress in the recent years, due to several models of the GMF constructed based on measurement of the Faraday rotations of extragalactic sources, see e.g. Refs. [149–151]. Studies on the propagation of UHECRs in the GMF and the expected consequences on their arrival directions can be found, for instance, in Refs. [210–217].

The EGMFs, however, remain rather poorly known, especially outside of structures like galaxy clusters. Nevertheless, detailed studies on their impact on the expected anisotropies in the UHECR sky, including discussions on composition-related effects and proposed interpretations of the available data, can be found, for instance, in Refs. [218–227]. The small-scale anisotropy case for negligible magnetic fields has been studied in Ref. [228].

Next to affecting the expected anisotropies in the UHECR sky, several effects on the energy spectrum can be expected as well in the case of non-negligible EGMFs due to the existence of magnetic horizons evolving with the rigidity of charged particles, see e.g. Ref. [229]. These effects do not only depend on the EGMFs themselves, but also on the particular source distribution model. The so-called propagation theorem [196] states that, in the case of a uniform distribution of sources (assumed to be identical) with a separation between them much smaller than all characteristic propagation lengths, the diffuse spectrum of UHE particles has a universal form, independent of the mode of propagation. A given extragalactic magnetic field model can therefore only affect the UHECR spectrum and composition if the source distribution does not fulfill the requirements of the propagation theorem at some energy or rigidity.

If, however, the observer is outside the confinement sphere around a source (the UHECRs from this source take longer than the age of the universe to reach Earth), which becomes smaller as the energy decreases or the particle charge increases, the flux observed from that sources decreases below a certain rigidity. Such a scenario has been invoked to lower the contribution of extragalactic protons around 10^{17} eV [230–233] and to explain the hard source-injection spectra found in fits to the combined Auger spectrum and composition data [234]. While these studies assumed homogeneous turbulent magnetic fields, Refs. [235, 236] considered more realistic inhomogeneous magnetic fields and found a weaker dependence of the cosmic ray spectrum on the spatial distribution of the field. See also Refs. [237, 238] for similar effects on the spectrum due to inhomogeneous EGMFs.

The EGMF enhancement in large scale structures has been studied using LSS formation simulations including mangetohydrodynamic (MHD) treatment for the evolution of the magnetic fields in, for instance, Refs. [3, 142–148]. Here the simulations in Refs. [145, 146] are constrained by the local observed large-scale density field to provide more realistic field configurations in the local universe. Different assumptions on the origin of the fields and the mechanisms involved in their growth are made in these different simulations. As a result, the outcomes of the different simulations differ strongly. In particular, the volume filling factors for fields $\gtrsim$1 nG can vary by several orders of magnitude from one simulation to the other, leading to opposite conclusions on the feasibility of UHECR astronomy.

1.6 Predictions for secondary neutrinos and photons

When UHECRs interact during their propagation through the universe, secondary neutrinos, e^+e^- pairs and photons can be produced. Neutrinos can be produced when during photopion production a π^+ is created (see Eq. 1.5). This π^+ will, after it is produced, decay into a muon (μ^+) and a neutrino (ν_μ), after which the muon will again decay into a positron (e^+) and two neutrinos (ν_e and $\overline{\nu}_\mu$):

$$\begin{aligned} \pi^+ &\rightarrow \mu^+ + \nu_\mu \ , && (1.8) \\ &\rightarrow e^+ + \nu_e + \overline{\nu}_\mu + \nu_\mu \ . && (1.9) \end{aligned}$$

This way of producing cosmogenic neutrinos was first pointed out in Ref. [239].

However, neutrinos can be produced not only through pion decay, but also through nuclear decay. When UHE nuclei interact with the photon backgrounds through photopion production or photodisintegration, unstable nuclei can be created, which can then decay and produce neutrinos (see Eq. 1.6). This can even occur in the case of protons, as when pion production occurs with a proton it can produce a neutron and a π^+ (see Eq. 1.1). This neutron will then decay into a proton, an electron and a neutrino ($\overline{\nu}_e$):

$$n \rightarrow p + e^- + \overline{\nu}_e \ . \tag{1.10}$$

The expected flux on Earth of these cosmogenic neutrinos has been investigated intensively for different astrophysical scenarios, see also Chapter 4, based on Refs. [45, 46], where it has been investigated whether the extraterrestrial neutrinos seen by IceCube could be cosmogenic neutrinos. Other studies on the possible origin of the IceCube neutrinos as secondaries in cosmic-ray interactions were done in Refs. [240, 241]. For additional investigations into neutrinos produced in this way, see for instance Refs. [14, 194, 242–262].

The expected cosmogenic neutrino flux depends mostly on several astrophysical parameters such as the cosmological evolution of the sources, the composition of the UHECRs, the maximum energy at the sources and the source spectral index. Strong cosmological evolutions provide large weights to distant sources for which interactions with more energetic and denser photon backgrounds take place, increasing the expected cosmogenic neutrino flux. On the other hand, to get such a strong cosmogenic neutrino flux, the maximum acceleration energy at the sources must be high enough for particles above the pion-production threshold to be present at all redshifts. At a given maximum energy per nucleon, the expected cosmogenic neutrino flux is in general lower for heavier primaries. The source spectral index required to fit the UHECR spectrum influences the expected cosmogenic neutrino flux as well, in general a harder spectral index will increase the expected neutrino flux at the highest energies (~EeV), but decrease it at lower energies (~PeV).

Besides neutrinos, e^+e^- pairs and photons can also be produced in the different interactions of UHECRs with the photon backgrounds. e^+e^- pairs will be produced during pair production (see Eq. 1.3). Photons can, for instance, be produced during pion production. When during pion production a π^0 is produced (see Eq. 1.5) it is most likely to decay into two photons:

$$\pi^0 \to \gamma\gamma \ . \tag{1.11}$$

Furthermore, photons, electrons and positrons can again be produced in the decay of unstable nuclei, as for example in the decay of the neutron (Eq. 1.10).

Whereas the propagation of neutrinos after their production is straightforward, the secondary electrons, positrons and photons will initiate electromagnetic cascades. In these electromagnetic cascades the initial particle will lose energy by creating more electrons, positrons and photons through pair production as well as up-scattering of low-energy background photons by inverse Compton scattering. As a result, the universe is opaque to photons from a few hundreds of GeV to a few EeV. Above ~10 EeV the universe becomes more and more transparent to photons and they can propagate a few tens of megaparsecs without losing a large amount of energy.

The level of the flux of the electromagnetic cascades, piling up below 100 GeV, is likely to be associated with the production of cosmogenic neutrinos, as they can both be produced in similar processes during the propagation of UHECRs. Therefore, measurements on the diffuse gamma-ray background could allow to put constraints on the cosmological evolution of the UHECR luminosity [263] and on the maximum allowable cosmogenic neutrino fluxes [264]. The cosmogenic photon flux has been investigated in Chapter 4 for several cosmological evolution models comparing with diffuse gamma-ray background data from Fermi LAT [132]. Similar studies can be found in Refs. [241, 256–261] and using older diffuse gamma-ray background data from EGRET [190, 265] in Refs. [182, 244, 245]. The Fermi LAT estimate of the diffuse gamma-ray background provides constraints on the most optimistic scenarios in terms of UHE neutrino fluxes for strongly evolving UHECR sources with redshift.

Chapter 2

CRPropa 2.0

Ultra-high-energy cosmic rays (UHECRs) do not propagate freely in the intergalactic medium (IGM). During their propagation they suffer from catastrophic energy losses in reactions with the intergalactic background light and are deflected by poorly known magnetic fields. Thus, the effects of propagation alter the cosmic ray spectrum and composition injected by sources in the IGM and form the features detected by UHECR observatories. In order to establish the origin of UHECRs, it is of prime interest to quantitatively understand the imprint of the propagation and to disentangle it from the properties of the cosmic rays at their sources. In this respect, it is essential to compare the measured UHECR spectrum, composition and anisotropy with model predictions. This requires extensive simulations of the propagation of ultra-high-energy (UHE) nuclei and their secondaries within a given scenario. In particular, the observation that UHECRs may consist of a significant fraction of heavy nuclei challenges UHECR model predictions and propagation simulations. Indeed, compared to the case of UHE nucleons, the propagation of nuclei leads to larger deflections in cosmic magnetic fields and additional particle interactions have to be taken into account, namely photodisintegration and nuclear decay.

To provide the community with a versatile simulation tool, CRPropa 2.0 [1, 43], a publicly available Monte Carlo code which allows one to simulate the propagation of UHE nuclei in realistic one- (1D) and three-dimensional (3D) scenarios taking into account all relevant particle interactions and magnetic deflections, has been developed. To this end, the former version 1.4 of CRPropa [42], which was restricted to nucleon primaries, has been extended to include the propagation of UHE nuclei. CRPropa 1.4 provided an excellent basis for this effort as many of its features could be carried over to the case of UHE nuclei propagation. CRPropa 2.0 covers the energy range $7 \times 10^{16} < E(\mathrm{eV}) < A \times 10^{22}$ where A is the nuclear mass number. In this chapter, based on Refs. [1, 42, 43], the underlying physical and numerical frameworks of CRPropa 2.0 are introduced. CRPropa 2.0 can be obtained from `https://crpropa.desy.de`.

2.1 Inherited features from CRPropa 1.4

The previous version 1.4 of CRPropa is a simulation tool aimed at studying the propagation of UHE neutrons and protons in the IGM. It provides a 1D and a 3D mode. In 3D mode, magnetic field- and source distributions can be defined on a 3D grid and deflections of protons in the implemented extragalactic magnetic field (EGMF) can be taken into account (see also Sec. 2.6). This allows one to perform simulations in realistic source scenarios with a highly structured magnetic field configuration as provided by, e.g., cosmological simulations.

In 1D mode, magnetic fields can be specified as a function of the distance to the observer, but their effects are restricted to energy losses of electron-positron (e^-e^+) pairs due to synchrotron radiation within electromagnetic cascades. Furthermore, it is possible to specify the cosmological and the source evolution as well as the redshift scaling of the background light intensity in 1D simulations (see also Sec. 2.5).

Both in 1D and 3D all important interactions for proton and neutron propagation with the cosmic UV/optical/IR background (IRB) and the cosmic microwave background (CMB) are included, namely, production of e^+e^- pairs (see also Sec. 2.4.1), photopion production (see also Sec. 2.4.3) and neutron decay. Additionally, CRPropa allows for the tracking and propagation of secondary $\gamma-$rays, e^+e^- pairs and neutrinos (see also Sec. 2.8). For this purpose a module [266] is included that solves the one-dimensional transport equations for electromagnetic cascades that are initiated by electrons, positrons or photons taking into account single, double and triple pair production as well as up-scattering of low-energy background photons by inverse Compton scattering. Moreover, with this module the simulation of synchrotron radiation along the line of sight is possible.

All these features are still available in version 2.0 of CRPropa, but with the additional possibility to include UHE nuclei.

2.2 Technical details

Technically, CRPropa is a stand alone object-oriented C++ software package which also includes some external modules. The C++ standard template library is used, as well as the high energy physics library CLHEP [267] for e.g. random numbers, vector transformations and the unit system. The interactions of nuclei with low-energy photon backgrounds are handled with the SOPHIA event generator [268], which is written in FORTRAN. The propagation of electromagnetic cascades is handled by a module called DINT [266], which is written in C. Additionally, several functions of ROOT [269] and FFTW [270] are used.

When running CRPropa it reads an input file which specifies technical parameters as well as details of the simulated "Universe" such as source positions and magnetic fields. This configuration file must be in XML format and is handled with the TinyXML library. The CRPropa simulations for a given scenario generate output files of either detected events or full UHECR trajectories. The output files can be written in ASCII, FITS or ROOT, therefore the CFITSIO [271] and ROOT libraries are required.

2.3 Distribution and properties of sources

At the moment little is known about what the sources of UHECRs are, what their distribution in space is, or what their properties are when they inject UHECRs in the IGM. Possible candidates are for example active galactic nuclei (AGNs) and gamma-ray bursts (GRBs). Both single sources as well as realizations of discrete, randomly drawn from a spacial density or specified by hand, or continuous, following a certain spacial density or flat, source distributions can be used in CRPropa. In the latter case the distributions can be selected, for example, to follow the baryon density from a large-scale-structure simulation box, and can be periodically repeated.

The UHECR particles are injected isotropically around the sources with a monochromatic or a power-law energy distribution between a minimal energy $E_{\min}$ and a maximal energy $E_{\rm max}$ or maximal rigidity $R_{\rm max} = E_{\rm max}/Z$ (with Z the charge number):

$$\frac{\mathrm{d}N}{\mathrm{d}E_0} \propto E_0^{-\alpha_0} \ , \tag{2.1}$$

$$E_{\rm min} \leq E_0 \leq E_{\rm max}, R_{\rm max} \ . \tag{2.2}$$

The composition at the sources can be any combination of nuclei up to mass number $A = 56$. The option to inject particles having energies up to a given maximum rigidity at the source is included. This is provided as basic arguments about astrophysical acceleration mechanisms in magnetic fields indicate that mixed compositions should be accelerated up to a given maximum rigidity instead of a maximum energy.

For each event registered at the observer the original identity at the source and the source position are stored as well. In this way a reweighting procedure can be applied on the detected events after the simulation is done in order to vary source properties such as the injection power law index α_0, the composition at the sources or the luminosity of individual sources. For example, it is most efficient in terms of CPU time to inject the UHECRs with a spectral index of $\alpha_0 = 1$ at the sources, meaning a uniform distribution in the logarithm of the energy. By reweighting each recorded event by a factor $w \propto E_0^{\alpha_0 - \alpha}$, the injection power law index would effectively be changed from α_0 to α.

2.4 Interactions in CRPropa 2.0

When propagating through the IGM, UHECRs can interact with ambient photon backgrounds such as the CMB and IRB (see also Sec. 1.3). Nuclei as well as free protons suffer from energy losses by e^+e^- pair production when photon energies (ϵ) boosted into the rest frame of the nucleus are of the order of $\epsilon' \sim 1$ MeV. For photon energies at or above the nuclear binding energy $\epsilon' \gtrsim$ 8-9 MeV, nucleons and light nuclei can be stripped off the nucleus (photodisintegration). Finally, at photon energies exceeding $\epsilon' \sim$145 MeV the quark structure of free or bound nucleons can be excited to produce mesons (photopion production). In these reactions the nucleus can be disrupted and unstable elements can be produced. Hence, nuclear decay has to be taken into account as well. As target photon fields the CMB and IRB, for which the "best-fit model" parametrization developed in Ref. [272] is adopted, are implemented.

In CRPropa 2.0 a nucleus with energy E and mass number A is considered a superposition of A nucleons with energy E/A. Thus, if one or several nucleons are stripped off, the initial energy E will be distributed among the outgoing nucleons and nuclei. The ultra-relativistic limit $\beta \to 1$ (with $\beta = v/c$ of the nucleus) is used in CRPropa such that all nuclear products are assigned the same velocity vector as the initial particle. This corresponds to a Lorentz factor $\Gamma \simeq 10^8 \cdot \left(E/10^{17} \text{ eV}\right) \cdot A^{-1}$ and a forward collimation within an angle $\simeq 1/\Gamma$.

2.4.1 Pair production

The first interaction discussed here, relevant for the propagation of UHE protons and nuclei, is the creation of electron-positron pairs on the CMB (also known as the Bethe-Heitler process [273]):

$$p + \gamma \to p + e^+e^- \ . \tag{2.3}$$

For UHE nuclei, pair-production is less important in terms of energy loss of the primary nuclei than photodisintegration (see Fig. 2.1 for an example). For UHE protons, however,

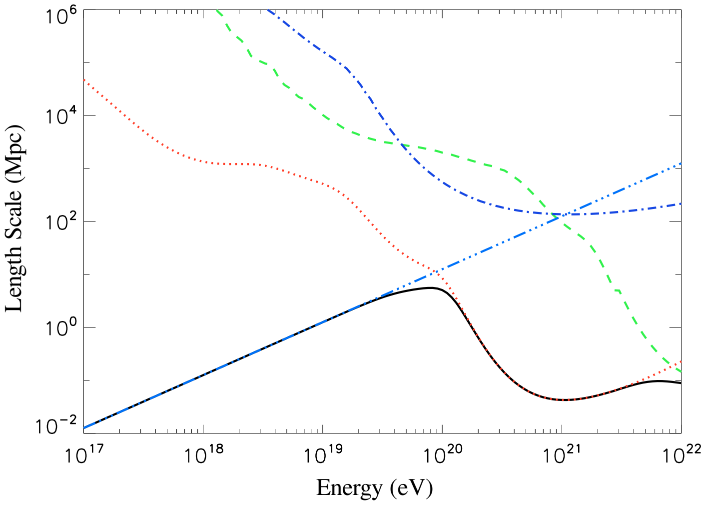

Figure 2.1: Length scales for all interactions of ^{47}Ca as used by CRPropa (obtained from Ref. [1]). In the plot the dark blue (dash-dotted) line denotes the energy loss length of pair production. The red (dotted) and green (dashed) lines are the photodisintegration and pion-production mean free paths, respectively, and the blue (dash-triple-dotted) line shows the decay length. The black (solid) line is the total mean free path of the catastrophic energy losses as used in the propagation algorithm. ^{47}Ca was chosen because the half life time of 4.5 days corresponds to a decay length comparable to the other interactions.

pair-production is the dominant energy-loss interactions for $E_p \lesssim 50$ EeV. Furthermore, pair production is the most important reaction for the creation of secondary photons in the TeV range.

The mean free path for pair production is relatively short, but the energy loss in each individual reaction is small (about $2m_e/m_p \approx 0.1\%$ per interaction, where m_e and m_p are the electron and proton rest masses, respectively). Thus, pair production is treated as a continuous energy loss. For interactions with the CMB it can be parametrized by [8]

$$-\frac{\mathrm{d}E_{A,Z}^{e^+e^-}}{\mathrm{d}t} = 3\alpha_{\mathrm{em}}\sigma_T h^{-3} Z^2 (m_e c^2 k_{\mathrm{B}} T)^2 f(\Gamma) \ . \tag{2.4}$$

Here, σ_T is the Thomson cross section, α_{em} is the fine structure constant, T is the temperature of the CMB, and $f(\Gamma)$ is a function which depends only on the Lorentz factor Γ and was parametrized in Ref. [274].

The energy loss length $l_{A,Z} = E(\mathrm{d}E_{A,Z}^{e^+e^-}/\mathrm{d}t)^{-1}$ for nuclei can therefore be expressed in terms of the energy loss length for protons $l_p = E(\mathrm{d}E_{1,1}^{e^+e^-}/\mathrm{d}t)^{-1}$ as

$$l_{A,Z}(\Gamma) = \frac{A}{Z^2} l_p(\Gamma) \ . \tag{2.5}$$

This scaling relation holds for arbitrary target photon backgrounds as it can be traced back to the scaling of the cross section and to the definition of the energy loss length. Eq. (2.5) is used in CRPropa 2.0 to generalize the pair production loss rates from protons to nuclei, which in practice is obtained by integration over the corresponding secondary spectra as parametrized in Ref. [275].

The energy loss for e^+e^- pair production is calculated after each time step Δt and is therefore taken into account at discrete positions and times. It is possible to propagate secondary electromagnetic cascades initiated by the e^+e^- pairs or by the γ-rays resulting from π^0-decay with CRPropa. For the injected secondary spectra we use the parametrization given in Ref. [275]. It should be noted that, in particular close to an observer, a large time step can degrade the accuracy of the propagated spectra due to the discrete injection of the electromagnetic cascade.

2.4.2 Photodisintegration

Photodisintegration does not affect free protons or neutrons, but is essential in the propagation of nuclei. There are many competing photodisintegration processes with different cross sections which need to be accounted for when the nucleus propagates through the background photon fields. Therefore the specific photodisintegration channels of each propagated nucleus are implemented, in an efficient way, in CRPropa.

The effects of the propagation of UHE nuclei have first been studied by Puget, Stecker and Bredekamp (PSB) [8] (see also Chapter 3). However, the approach to model the photodisintegration process chosen in CRPropa 2.0 is similar to what was more recently discussed in Ref. [200].

2.4.2.1 The photodisintegration cross sections

For CRPropa 2.0 the publicly-available TALYS framework, version 1.0 [202], is used to compute photodisintegration cross sections. TALYS was applied for these purposes to 287 isotopes with charge numbers up to iron. In principle there are no restrictions to extend this framework to nuclei heavier than iron. However, this is not done in CRPropa 2.0 as there is no significant contribution expected of elements with $Z > 26$.

The nuclear models in TALYS are reliable for mass numbers $A \geq 12$. Therefore, additional photodisintegration cross sections for light nuclei have been added in the modeling. The list of isotopes for which the cross sections were calculated was generated using data from Ref. [276]. It is assumed that excited nuclei will immediately return to their ground state. Hence, only nuclei in their ground states are considered when calculating the cross sections. Note that in this way the photons created in nuclear de-excitation are neglected as well. These photons might contribute to the overall gamma-ray flux at energies $E \lesssim 0.1-1$ EeV, which thus might cause a moderate underestimation of the gamma-ray flux in this energy range for heavy cosmic ray scenarios, as discussed in e.g. Refs. [277, 278].

All cross sections were calculated for photon energies $1 \text{ keV} \leq \epsilon' \leq 250 \text{ MeV}$ in the rest frame of the nucleus and stored in 500 bins of energy. Reaction channels emitting neutrons (n), protons (p), deuterium (d), tritium (t), helium-3 (^{3}He) and helium-4 (α) nuclei and combinations thereof are considered by TALYS and implemented in CRPropa. All the available TALYS output ($A > 5$ and $N > 2$) has been generated, thus including the output for mass numbers $A \leq 12$. For light ($A \leq 12$) and stable nuclei the cross sections generated with TALYS were then replaced and complemented as follows:

- ^{9}Be, ^{4}He, ^{3}He, t and d as given in Ref. [279].
- A parametrization of the total photonuclear cross section as function of the mass number A is used for ^{8}Li, ^{9}Li, ^{7}Be, ^{10}Be, ^{11}Be, ^{8}B, ^{10}B, ^{11}B, ^{9}C, ^{10}C, ^{11}C as described in Ref. [280]. In these cases the loss of one proton (neutron) is assumed if the neutron number $N < Z$ ($N > Z$). For $N = Z$, the loss of one neutron or proton is modeled with equal probability.

- For ^{7}Li the experimental data from Ref. [281, 282] is applied and, instead of using a parametrization, linear interpolation is implemented between the measured data points.

In total 78449 exclusive channels are taken into account.

In the nucleus rest frame, for typical UHECR energies, the CMB photons are boosted to energies in the range between a few hundreds of keV to a few hundreds of MeV. The interaction process between the UHECRs and the CMB is dominated by the giant dipole resonance (GDR) at photon energies below 30-50 MeV, and to a lesser extent by the quasideuteron (QD) emission for energies between 50-150 MeV. However, as far as elements of interest in the propagation of UHECRs are concerned, the photonuclear cross sections are only known for a limited number of nuclei, namely the total photodisintegration cross section as a function of energy for 10 nuclei and the integrated total photodisintegration cross section for no more than 16 nuclei [283]. Therefore, in the cross-section calculations with TALYS, all the remaining rates are estimated on the basis of theoretical reaction models.

The cross sections are calculated with TALYS by using the default settings, in the same way as suggested in Ref. [200]. TALYS takes into account all types of direct, pre-equilibrium and compound mechanisms. All the experimental information on nuclear masses, deformation and low-lying states spectra is considered, whenever available. Otherwise, global nuclear-level formulae as well as nucleon and alpha-particle optical-model potentials are considered to estimate the particle transmission coefficients and the nuclear level. Details on the codes and the nuclear physics input (ground state properties, nuclear level densities, optical potential) can be found in Refs. [202, 284, 285]. The various nuclear inputs are known to affect the photodisintegration rates mainly around the corresponding threshold energies, but have a lower impact than the gamma-ray strength function [200].

The photodisintegration cross sections in TALYS are given by [285]

$$\sigma_{PD}(\epsilon') = \sigma_{\rm GDR}(\epsilon') + \sigma_{\rm QD}(\epsilon') \ , \tag{2.6}$$

where $\sigma_{\rm GDR}(\epsilon')$ and $\sigma_{\rm QD}(\epsilon')$ are the GDR cross sections and the QD cross sections, respectively.

The GDR component is given by

$$\sigma_{\rm GDR}(\epsilon') = \sum_i \sigma_{E1} \frac{(\epsilon' \Gamma_{E1,i})^2}{(\epsilon'^2 - \epsilon'^2_{E1,i})^2 + \epsilon'^2 \Gamma^2_{E1,i}} \ , \tag{2.7}$$

where σ_{E1}, Γ_{E1} and ϵ'_{E1} are the strength, width and energy of the GDR for $E1$ radiation, respectively, and the sum is over the number of parts i into which the GDR is split. TALYS uses the generalized Lorentzian form of Ref. [286] for $E1$ radiation,

$$f_{E1}(\epsilon', T) = K_{E1} \left[\frac{\epsilon' \tilde{\Gamma}_{E1}(\epsilon')}{(\epsilon'^2 - \epsilon'^2_{E1})^2 + \epsilon'^2 \tilde{\Gamma}_{E1}(\epsilon')^2} + \frac{0.7 \Gamma_{E1} 4\pi^2 T^2}{\epsilon'^3_{E1}} \right] \sigma_{E1} \Gamma_{E1} \ , \tag{2.8}$$

where $K_{E1} = 1/(3\pi^2 \hbar^2 c^2)$, the energy-dependent damping width $\tilde{\Gamma}_{E1}(\epsilon')$ is given by

$$\tilde{\Gamma}_{E1}(\epsilon') = \Gamma_{E1} \frac{\epsilon'^2 + 4\pi^2 T^2}{\epsilon'^2_{E1}} \ , \tag{2.9}$$

and T is the nuclear temperature (see Ref. [287]).

GDR parameters for various individual nuclei have been tabulated in TALYS, obtained from Ref. [283]. Certain nuclei have a split GDR, i.e. a second set of Lorentzian parameters. For these cases the incoherent sum of two strength functions is taken (see Eq. 2.7). For nuclei for which no tabulated data exists the following parameters are used [285]:

$$\begin{aligned} \sigma_{E1} &= 1.2 \frac{120NZ}{A\pi\Gamma_{E1}} \text{ mb}, && (2.10) \\ \Gamma_{E1} &= 0.026 \epsilon'^{1.19}_{E1} \text{ MeV}, && (2.11) \\ \epsilon'_{E1} &= 63 A^{-1/3} \text{ MeV}. && (2.12) \end{aligned}$$

The QD component σ_{QD} is given by [285]

$$\sigma_{\text{QD}}(\epsilon') = L \frac{NZ}{A} \sigma_d(\epsilon') f(\epsilon') \ . \tag{2.13}$$

Here $\sigma_d(\epsilon')$ is the experimental deuteron photodisintegration cross section, parameterized as (with ϵ' in MeV)

$$\sigma_d(\epsilon') = \begin{cases} 61.2 \frac{(\epsilon' - 2.224)^{3/2}}{\epsilon'^3} & \text{for } \epsilon' > 2.224 \text{ MeV}, \\ 0 & \text{otherwise.} \end{cases} \tag{2.14}$$

$L = 6.5$ is the so-called Levinger parameter. The Pauli-blocking function $f(\epsilon')$ is approximated by the polynomial expression (with ϵ' in MeV)

$$f(\epsilon') = \begin{cases} 8.3714 \times 10^{-2} - 9.8343 \times 10^{-3}\epsilon' + 4.1222 \times 10^{-4}\epsilon'^2 & \\ \quad -3.4762 \times 10^{-6}\epsilon'^3 + 9.3537 \times 10^{-9}\epsilon'^4 & \text{for } 20 < \epsilon' < 140 \text{ MeV}, \\ \exp(-73.3/\epsilon') & \text{for } \epsilon' < 20 \text{ MeV}, \\ \exp(-24.2348/\epsilon') & \text{for } \epsilon' > 140 \text{ MeV}. \end{cases} \tag{2.15}$$

The output of TALYS 1.0 in general agrees well with available measured data and only in rare cases differs up to a factor of two for the full all-channels cross sections [200].

2.4.2.2 Mean free path calculations and channel thinning

From the photodisintegration cross section in the nucleus rest frame $\sigma(\epsilon')$ the energy-weighted average cross section

$$\bar{\sigma}(\epsilon'_{\text{max}}) = \frac{2}{(\epsilon'_{\text{max}})^2} \int_0^{\epsilon'_{\text{max}}} \epsilon' \sigma(\epsilon') \text{d}\epsilon' \tag{2.16}$$

is obtained and tabulated as a function of $\epsilon'_{\text{max}} = 2\Gamma\epsilon$. From a given $\bar{\sigma}(\epsilon'_{max})$, the mean free path $\lambda(\Gamma)$ can be calculated for each isotope as a function of the Lorentz factor with [8],

$$\lambda(\Gamma)^{-1} = \int_{\epsilon_{\text{min}}}^{\epsilon_{\text{max}}} n(\epsilon, z) \bar{\sigma}(\epsilon'_{\text{max}} = 2\Gamma\epsilon) \text{d}\epsilon \ , \tag{2.17}$$

where $n(\epsilon, z)$ is the number density per energy interval and volume of the isotropic low-energy photons in the photon background. See Sec. 2.5 for how the dependence on the cosmological redshift z is taken into account. For performance reasons, $\lambda(\Gamma)$ is tabulated as a function of energy E. The values of the integration limits ϵ_{min}, ϵ_{max} in Eq. 2.17 are listed in Tab. 2.1.

Table 2.1: Values of the parameters used in Eq. 2.17 to create the mean free path tables for photodisintegration in CRPropa.

	CMB	IRB
$\epsilon_{\rm min}$ (GeV)	4.00×10^{-19}	10^{-12}
$\epsilon_{\rm max}$ (GeV)	10^{-11}	10^{-7}

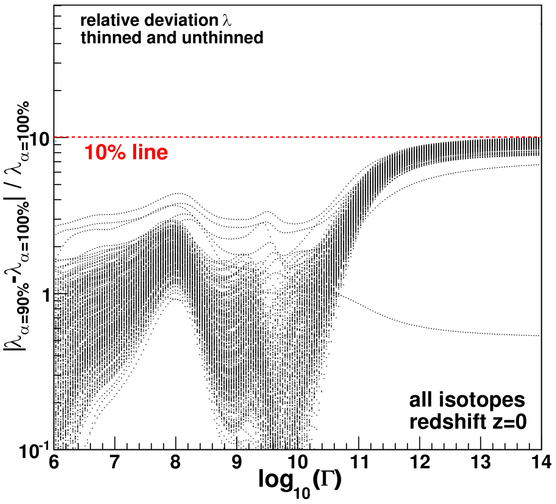

Figure 2.2: The relative deviation of the total mean free path λ in photodisintegration reactions with the CMB and IRB for the thinned ($\alpha = 90\%$) and unthinned case for all 287 isotopes (redshift $z = 0$) are shown (obtained from Ref. [1]).

As the code slows down significantly with increasing number of exclusive channels to be sampled, a thinning procedure has been implemented. For each isotope only the channels with the n largest interaction rates out of the N available exclusive channels have been included, such that the sum $\sum_i^n \lambda_i^{-1}/\lambda_{\rm tot}^{-1} > \alpha$ in at least one energy bin. Here α is the thinning factor, $\lambda_{\rm tot}^{-1} = \sum_i^N \lambda_i^{-1}$ for each isotope and the λ_i^{-1} are summed up in decreasing order. In this way a $\alpha = 90\%$ channel-thinning reduces the number of photodisintegration channels to be tracked from 78449 to 6440. The thinning procedure leads to a systematic overestimation of the mean free path in the order of 1% for Lorentz factors of the UHECR below 10^{10}. This deviation increases to 10% for Lorentz factors above 10^{12} (see Fig. 2.2).

Fig. 2.3 gives five examples of full photodisintegration mean free paths on the CMB and IRB as a function of the Lorentz factor γ. The mean free paths for the nuclei ^{56}Fe, ^{16}O, ^{14}N, ^{12}C and ^{4}He are shown.

2.4.3 Photopion production

UHE nucleons can produce secondary mesons in interactions with the CMB and IRB. The most important reaction of this type is the production of pions in reactions of UHE protons with the CMB through the delta resonance:

$$p + \gamma \to \Delta^+ \to p + \pi^0 \to p + \gamma\gamma \ , \tag{2.18}$$

$$\to n + \pi^+ \to n + \mu^+ + \nu_\mu \ . \tag{2.19}$$

This leads to the well known Greisen-Zatsepin-Kuzmin (GZK) cut-off [76, 77] at an energy of about $E_{\rm GZK} = 5 \times 10^{19}$ eV. For photopion production the energy loss per

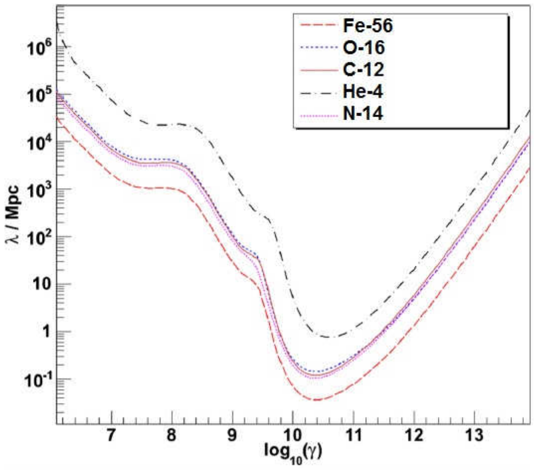

Figure 2.3: The total mean free path λ for photodisintegration with the CMB and IRB as a function of the Lorentz factor Γ for ^{56}Fe (red dashed line), ^{16}O (blue dotted line), ^{14}N (magenta close-dotted line), ^{12}C (brown straight line) and ^{4}He (black dashed-dotted line).

interaction is about $m_\pi/m_p \approx 15\%$, where m_π is the pion mass. Thus this process is treated in a stochastic way, taking into account the mean free paths of all interaction channels. The photopion production mean free paths for protons and neutrons, λ_p and λ_n, are modeled by the SOPHIA package [268]. SOPHIA has been explicitly designed to study this phenomenon and determines the mean free paths from the particle-production cross sections measured in accelerators.

Nuclei can also produce mesons, albeit with a higher threshold energy of $E_{\text{th}} \approx A \times E_{\text{GZK}}$. This is due to the fact that to good approximation the center of mass system (CMS) coincides with the rest frame of the nucleus. The threshold energy, therefore, does not depend on the total energy of the nucleus E, but on the Lorentz factor $\Gamma \propto E/A$. Pion production is thus only relevant for extremely energetic nuclei. However, it is important to be included to properly account for the production of secondary UHE photons and neutrinos, as well as for the propagation of secondary and primary protons and neutrons.

Photopion production on nuclei has been studied extensively at accelerators, see e.g. Refs. [288–290], and the cross section has been shown to scale with mass number A. Within the experimental uncertainties, all cross sections per nucleon are similar for nuclei with $A > 8$ but differ significantly from free nucleon data. For $A \leq 8$, a scaling according to $A^{2/3}$ was found to provide a good approximation of the data. In CRPropa 2.0 this effective scaling law is employed and the photopion cross section of nuclei, and thereby their mean free path, is based on that of protons and neutrons according to:

$$\lambda_{A,Z}^{-1}(E) = 0.85 \times \left[Z^\zeta \cdot \lambda_p^{-1}\left(\frac{E}{A}\right) + (A-Z)^\zeta \cdot \lambda_n^{-1}\left(\frac{E}{A}\right) \right] , \qquad (2.20)$$

with $\zeta = 2/3$ for $A \leq 8$ and $\zeta = 1$ for heavier nuclei. Downsides of this approximation are that it neglects Fermi motion in nuclei and does not account for in-medium modifications of the spectral shape of resonances. However, Eq. 2.20 is found to describe the absolute photopion-production cross sections for all nuclei to an accuracy better than a difference of about 20 %, which is adequate for our purpose where photodisintegration dominates in the propagation of cosmic-ray nuclei up to $E \approx 10^{22}$ eV.

For propagating nuclei through photon fields, the reaction is split into four parts so that the cross sections of protons and neutrons on the CMB and on the IRB are calculated separately. The mean free path for nuclei interacting with one of the photon backgrounds, $\lambda_{A,Z}$, is then obtained by Eq. 2.20. If this reaction then takes place, it is treated as an interaction of a free nucleon. The interacting nucleon will suffer energy loss and will be stripped off the nucleus. The separated nucleon will then be propagated individually. The produced meson will decay leading to secondary leptons, photons or neutrinos, which can then be propagated by the corresponding modules of CRPropa. Both the decay of the meson as well as the energy loss of the primary nucleon are again calculated by using the SOPHIA package.

2.4.4 Nuclear decay

During the propagation of UHECRs unstable nuclei can be produced due to photodisintegration and pion production of nuclei. This makes it important to take nuclear decay into account correctly. Nuclear decay can change both the nucleus type and its energy, as well as produce secondary neutrinos and photons at the same time. Furthermore it technically ensures that unstable nuclei decay back to (more) stable nuclei for which photodisintegration cross sections are known.

In CRPropa the decays are modeled as a combination of α and $\beta^{\pm}$ decays and the dripping of single nucleons (p, n). The decay length of a nucleus is given by its life time τ and the Lorentz factor Γ as

$$\lambda_{\text{decay}} = \Gamma\tau \ . \tag{2.21}$$

In case of p, n dripping and α decay, the decay products are assumed to inherit the Lorentz factor Γ from the parent nucleus. This assumption is justified since the binding energy per nucleon is small compared to the masses of the decay products. The energy of all produced nuclei is, therefore, given by

$$E_{A',Z'} = \Gamma m_{A',Z'} \ . \tag{2.22}$$

In case of $\beta^{\pm}$ decay the momenta of the $e^{\pm}$ and the neutrino are calculated from a three-body decay (see e.g. Ref. [291]) and are then boosted to the simulation frame.

In CRPRopa the decay channels of the different nuclei as well as their decay constants at rest are stored in an internal database. It is based on the NuDat2 database [276] and contains 434 different nuclides with mass number $A \leq 56$ and charge $Z \leq 26$. Note that UHECRs, unlike the isotopes in the NuDat2 database, are fully ionized. This means that electron capture (EC) is not possible for UHECRs. Thus the β^{+} decay rates are recalculated from the EC rates given in the NuDat2 database. For details about how this is done, see Ref. [1]. In Fig. 2.1, as an example, the decay length is shown together with the other energy loss processes for ^{47}Ca.

2.5 Cosmological evolution of background photon fields

In the 1D mode of CRPropa the travel distance of the cosmic ray to the observer is known beforehand so that the cosmological evolution of the background photon fields can be taken into account. This is done in the following way.

The implementation of photodisintegration and pion production in CRPropa 2.0 is based on tabulated mean-free-path data calculated with the photon density $n(\epsilon, z = 0)$ at a redshift $z = 0$. As the photon density $n(\epsilon, z)$ evolves as a function of z, $\lambda = \lambda(\Gamma, z)$ is effectively altered as well. To model this change of λ as a function of z, a scaling function $s(z)$ is used. It approximates $\lambda(\Gamma, z)$ from the available tabulated data of $\lambda(\Gamma, z=0)$. For this scaling function $s(z)$ it is assumed that the normalized spectral shape of the photon field $n(\epsilon, z)$ does not change as function of z in the comoving cosmological frame. In this approach the evolution of the photon number density $n(\epsilon, z)$ can be absorbed by a separated evolution factor $e(z)$ as

$$n(\epsilon, z) = (1+z)^2 n(\epsilon/(1+z), 0) e(z) \ . \tag{2.23}$$

In the approximation of a redshift independent spectral shape of $n(\epsilon, z)$, the evolution factor is defined by

$$e(z) = \begin{cases} 1 & \text{CMB,} \\ \frac{\int_{\epsilon_i}^{\infty} n(\epsilon,z)\mathrm{d}\epsilon}{\int_{\epsilon_i}^{\infty} n(\epsilon,0)\mathrm{d}\epsilon} & \text{IRB.} \end{cases} \tag{2.24}$$

Here ϵ_i is the intersection energy of the CMB and IRB photon number densities, $n_{\mathrm{CMB}}(\epsilon_i, z) = n_{\mathrm{IRB}}(\epsilon_i, z)$, in the comoving frame.

Substitution of Eq. 2.23 in Eq. 2.17 gives

$$\begin{aligned} \lambda^{-1}[\Gamma, z] &= (1+z)^2 e(z) \int_{\epsilon_{\mathrm{min}}}^{\epsilon_{\mathrm{max}}} n(\epsilon/(1+z), 0)\bar{\sigma}(= 2\Gamma\epsilon)\mathrm{d}\epsilon \ , \\ &= (1+z)^2 e(z) \int_{\epsilon_{\mathrm{min}}/(1+z)}^{\epsilon_{\mathrm{max}}/(1+z)} n(\epsilon/(1+z), 0)\bar{\sigma}\left(\frac{2\Gamma\epsilon(1+z)}{(1+z)}\right)(1+z)\mathrm{d}\frac{\epsilon}{(1+z)} \ , \end{aligned} \tag{2.25}$$

with a change of integration variable to $\epsilon^* = \epsilon/(1+z)$ as well as $\epsilon^*_{\mathrm{min}} = \epsilon_{\mathrm{min}}/(1+z)$ and $\epsilon^*_{\mathrm{max}} = \epsilon_{\mathrm{max}}/(1+z)$ this becomes

$$\lambda^{-1}[\Gamma, z] = (1+z)^3 e(z) \int_{\epsilon^*_{\mathrm{min}}}^{\epsilon^*_{\mathrm{max}}} n(\epsilon^*, 0)\bar{\sigma}(2\Gamma\epsilon^*(1+z))\mathrm{d}\epsilon^* \ . \tag{2.26}$$

This leads to the scaling relation for the mean free path

$$\lambda^{-1}[\Gamma, z] = (1+z)^3 e(z) \lambda^{-1}[\Gamma(1+z), z=0] \tag{2.27}$$

from which it follows that $s(z) = (1+z)^3 e(z)$. It should be noted that this result is valid under the assumption that the spectral shape of the IRB does not depend on redshift. This approximation does not hold exactly for the IRB, due to energy injection in the IGM from galaxy formation. Nevertheless, this approximation provides a reasonable model for the redshift evolution of the IRB, which is especially important for the production of secondary neutrinos [255].

In CRPropa version 1.4 the IRB model of Ref. [292] was implemented with a CMB-like scaling with redshift, $e(z) = 1$, up to a maximum redshift z_{max}, after which reactions in the IRB were switched off [42]. In CRPropa version 2.0 the switch to the 'best-fit model' of Ref. [272] with the corresponding values of $e(z)$ calculated at eight redshift values ($z = 0$, 0.2, 0.4, 0.6, 1, 2, 3, 4) and a linear interpolation between the values of $e(z)$ for these redshifts was made.

2.6 Large scale structure and extragalactic magnetic fields

The strength and distribution of the EGMF is currently poorly known and their impact on UHECRs are difficult to quantify, as demonstrated by the difference in results from e.g. Ref. [3] and Refs. [145, 293]. In Ref. [3] the differences between these results are discussed.

EGMFs and large scale structures from several different simulations (e.g Refs. [3, 142, 143, 145, 147, 148]) have so far been implemented in CRPropa, but in principle any magnetic field model can be used. The properties of gamma-ray sources associated with UHECR sources as well as the feasibility of UHECR astronomy depend strongly on the extragalactic magnetic field model [3, 145, 293].

Large-scale-structure simulations usually cover only a small fraction of today's Universe, typically of order 100 Mpc in linear scale. Since sources at much larger, cosmological distances can contribute to the flux of UHECRs below the GZK cut-off as well as to the flux of photons below ∼TeV and to the flux of neutrinos, the EGMF and source distributions can be periodically continued in the 3D version of CRPropa. Additionally, EGMFs with homogeneous statistical properties and power law spectra in Fourier space (e.g. a Kolmogorov spectrum) have been implemented in the code.

The deflection of the cosmic rays in these EGMFs is calculated from the equation of motion in the 6D phase space with $Y \equiv (\vec{r}, \vec{p})$:

$$\frac{\mathrm{d}Y}{\mathrm{d}t} = \begin{pmatrix} \frac{\mathrm{d}\vec{r}}{\mathrm{d}t} \\ \frac{\mathrm{d}\vec{p}}{\mathrm{d}t} \end{pmatrix} = \begin{pmatrix} c\frac{\vec{p}}{|\vec{p}|} \\ q\left[\frac{\mathrm{d}\vec{r}}{\mathrm{d}t} \times \vec{B}\right] \end{pmatrix} . \tag{2.28}$$

Here $\vec{r}$ and $\vec{p}$ are the position and momentum vectors of a particle of charge q, $\vec{B}$ denotes the magnetic field vector.

To solve this equation and investigate the propagation of particles in structured magnetic fields it is necessary to use an adaptive step integrator, as it is possible that the Larmor radius varies by a factor of up to $\sim 10^6$ in a few propagation steps. In CRPropa 2.0 a fifth order Runge Kutta (RK) integrator, derived from the Numerical Recipes [294], is implemented. This integrator is called repeatedly until the equations of motion are integrated over the total time step Δt. The time step of the integrator itself is limited to $h_{\mathrm{min}} \leq h_{\mathrm{Int}} \leq h_{\mathrm{max}}$, where h_{min} can be set in the input file and $h_{\mathrm{max}} = 1$ Mpc. Distances shorter than h_{min} are not propagated using the RK integrator, but by a linear correction.

Numerical dissipation in the integration of the Lorentz force can generate artificial energy losses. For example, with an integrator accuracy of $\epsilon = 10^{-4}$, a proton of energy 10 EeV in a uniform magnetic field of 1 μG looses 5% of its energy over 300 Mpc (only a small loss of energy compared with the other energy-loss processes). This effect is corrected for by imposing by hand that the energy of the particle is the same before and after the integration step.

2.7 Propagation algorithm and Monte Carlo approach

UHECRs are injected at specified sources and propagated step-by-step in either a 1D or a 3D environment. The trajectories are regularly sampled or recorded only at specific locations, namely at a given distance from a source or at an "observer" position. In the 3D case a simulation box is defined and periodic boundary conditions can be implemented.

When deflections are taken into account, cosmological redhifts cannot be computed in advance, as the propagation time from source to observer is not known beforehand. Therefore, redshift evolution is only accounted for in the 1D mode of CRPropa. In the

1D mode the concordance cosmology is used for which, assuming a flat Universe, the Hubble rate $H(z)$ at redshift z in the matter dominated regime, $z \lesssim 10^3$, is given by

$$H(z) = H_0[\Omega_m(1+z)^3 + \Omega_\Lambda]^{1/2} \ , \tag{2.29}$$

with H_0 the Hubble constant, Ω_m the matter density parameter and Ω_Λ the vacuum density parameter. The default values in CRPropa for these parameters are $\Omega_m = 0.3$, $\Omega_\Lambda = 0.7$ and $H_0 = h_0 100$ km s^{-1} Mpc^{-1} with $h_0 = 0.72$, but they can be changed in the input file.

To handle the widely ranging interaction rates of UHE nuclei, the following propagation algorithm has been implemented in CRPropa 2.0. The main assumption for this algorithm is that the mean free paths λ are approximately constant during a time step. As $\lambda = \lambda(E)$ is in general a function of the UHECR energy E, the numerical step size has to be small enough to ensure that no significant energy loss occurs.

With λ_i being the mean free path for a given interaction or decay channel of a certain nucleus, where i runs over all N possible interaction and decay channels, the algorithm works as follows:

1. The inverse total mean free path $\lambda_{\text{tot}}^{-1} = \sum_{i=1}^{N} \lambda_i^{-1}$ is calculated and the distance Δx_1 to the next interaction is obtained. This is realized by using a uniformly distributed random number $0 \leq r \leq 1$ via

$$\Delta x_1 = -\lambda_{\text{tot}} \ln(1-r) \ . \tag{2.30}$$

2. The fractional energy loss due to pair production (c.f. Sec. 2.4.1) is limited by imposing a maximum step size Δx_2 obtained from

$$\int_x^{x+\Delta x_2} \mathrm{d}x \frac{\mathrm{d}E_{A,Z}^{e^+e^-}}{\mathrm{d}x}(E) < \delta E \ , \tag{2.31}$$

   where δ is the maximal allowed fractional energy loss.

3. The distance over which the particle will be propagated is selected by

$$\Delta x = \min(\Delta x_1, \Delta x_2, \Delta x_3) \, , \tag{2.32}$$

   where Δx_3 is an upper limit on the propagation step that can be provided by the user, with typical values of $\Delta x_3 \sim 0.1 - 50$ Mpc. This increases the accuracy of the calculation of pair production energy losses and the secondary photon spectra from pair production as well as the determination of the deflections in EGMFs for 3D simulations.

4. In 3D mode when deflections in EGMFs are included, after the correct Δx is determined, the deflection of the cosmic ray due to the magnetic field is applied.

5. If $\Delta x = \Delta x_1$, the particle is propagated over the path length Δx_1, where it performs an interaction. The choice of the specific interaction undergone by the UHECR is obtained by finding the smallest index i for which

$$\sum_{a=1}^{i} \frac{\lambda_{\text{tot}}}{\lambda_a} > w \ , \tag{2.33}$$

   for a uniformly distributed random number $0 \leq w \leq 1$.

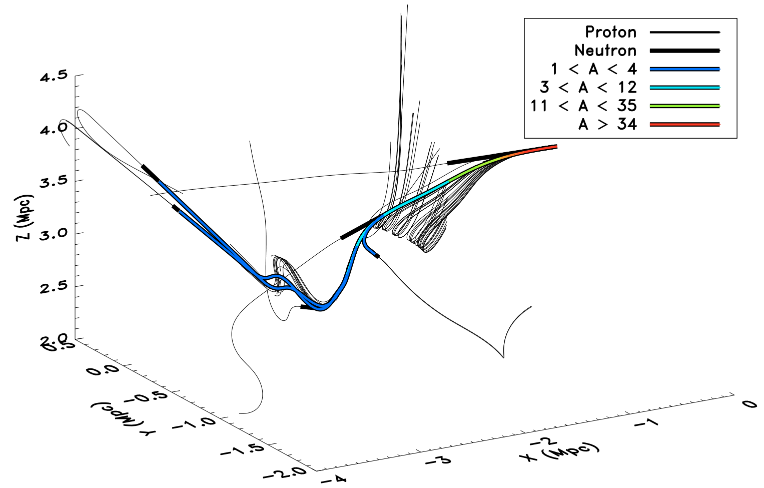

Figure 2.4: 3D trajectory of an iron nucleus with an initial energy of $E = 1.2 \times 10^{21}$ eV (around the minimun of the photodisintegration mean free path) and its hadronic secondaries (obtained from Ref. [1]). The propagation is done in a strong structured magnetic field region (10^{-9} G $< B < 10^{-7}$ G).

6. If instead $\Delta x_1 > \min(\Delta x_2, \Delta x_3)$, continuous energy losses are too large to allow for accurate propagation until the next interaction point or the user has requested that the maximum step size be smaller than the Δx_1 selected in step 1. In this case, the particle is propagated over the distance Δx but no interaction occurs.

7. The continuous energy losses are applied and the new particles produced in the interaction are added to the list of particles to be propagated.

8. If the particle ends up in an observer area after the propagation step Δx the particle is considered detected and no further actions are performed. If this does not happen this algorithm is restarted again from the new position.

From this description it is clear that if one of the interaction channels has a small mean free path λ_a, the step size of the propagation will adjust itself automatically. A comparison for ^{47}Ca of the exclusive mean free paths of the different channels λ_a, the total mean free path λ_{tot} and the pair production loss length (Eq. 2.5) is shown in Fig. 2.1.

The above approach is also applied to select an exclusive channel for example in the case of photodisintegration. If photodisintegration is chosen to be the next reaction by the propagation algorithm, the exclusive channel is found by applying Eq. 2.33. In analogy, here $\lambda_{\text{tot}}^{-1} = (\sum_i \lambda_i^{-1})$ is the inverse of the total mean free path for photodisintegration of the isotope under consideration. The λ_i are the mean free path values of the exclusive channels for the corresponding isotope.

This algorithm can lead to a cascade of secondary nuclei originating from the primary nucleus. In Fig. 2.4 (obtained from Ref. [1]) an example is given of a 3D trajectory starting with an iron nucleus with an energy of $E = 1.2 \times 10^{21}$ eV (around the minimun of the photodisintegration mean free path). Note that after photodisintegration the primary nucleus and its secondary particles have the same Lorentz factor $\Gamma \propto E/A$. Therefore, secondary protons undergo a stronger deflection than heavier nuclei due to their higher charge-to-mass ratio.

If secondary gamma-rays and/or neutrinos are included in the simulation, these neutral secondaries are propagated over a distance equal to the maximum propagation distance provided by the user minus the time of their production, such that they reach an observer after the maximum propagation time independently of the chosen 1D or 3D environment.

The accuracy of the determination of the arrival direction and traveled distance at the observer is related to the actual implementation of detection and propagation in our algorithm. Besides the numerical error intrinsic to the detection algorithm, an additional error is introduced by the choice to take continuous energy losses into account only at the end of the time step.

2.8 Secondary electromagnetic cascades and neutrinos

The secondary neutrinos from pion production and decays are propagated in a straight line assuming no energy losses except redshift effects.

The electromagnetic (EM) secondaries from any of the interactions are propagated using the EM cascade module called DINT based on Ref. [266]. The photons and e^+e^- pairs are followed until either their energy drops below 100 MeV or they reach an observer. All relevant interactions with background photons γ_b are taken into account, namely single pair production ($\gamma\gamma_b \to e^+e^-$), double pair production ($\gamma\gamma_b \to e^+e^-e^+e^-$), inverse Compton scattering ($e\gamma_b \to e\gamma$) and triplet pair production ($e\gamma_b \to ee^+e^-$), see Ref. [295] for a detailed discussion on implemented interactions. Furthermore, synchrotron losses of electrons in inhomogeneous EGMFs are taken into account and the resulting lower energy synchrotron photons are followed in the subsequent EM cascades.

The same module has been applied to EM cascades from discrete magnetized proton sources in galaxy clusters in Ref [296]. The EM cascades that are followed with CRPropa 2.0 are propagated in straight lines, also in the case of 3D simulations when UHECRs are concerned. Every time an EM cascade is initiated by an interaction of a primary nucleus, it is assumed that the secondaries propagate along straight lines and it is checked whether the line of sight crosses the observer. If this is the case, the EM cascade module is called with the corresponding propagation distance and the projected magnetic field profile. Electrons in the EM cascade can be deflected by EGMFs, it is not possible to take their trajectories into account correctly in an 1D approximation. For a discussion on the validity of this 1D approach, see Ref. [42].

2.9 Detection at the observer

The observer can be specified in several different ways in CRPropa. In the 1D mode a particle is detected when its position is closer to the origin than the maximal step size Δx_3, which can be specified in the input file.

In 3D three different options are possible for the type of observer. One possibility is that the particle is detected when its position reaches a certain distance from the source, in which case only one discrete source should be specified. Observer spheres of different radii can be implemented at the same time. Technically a particle is detected if it has crossed a sphere during the last time step. A crossing is defined as either the particle being inside the sphere at the beginning of the time step and outside of it afterwards, or vice versa. The propagation algorithm ensures that this crossing step is never larger than Δx_3, which therefore, as in the case of a 1D observer, defines the error of this detection algorithm.

Furthermore, observers can be defined as small spheres at positions and with radii of the user's choice. A particle is recorded each time it enters one of these spheres. The detection algorithm works as follows (see Fig. 2.5, obtained from Ref. [2], for the geometry):

- For a particle at position P with velocity $\overrightarrow{v}$ near an observer sphere centered at O with radius $r = OB$ the closest distance of the particle to the edge of the observer sphere CP is computed. After this propagation step, except when the particle was detected, the next step will be smaller than CP in order not to miss the detection due to a too large time step.
- If $OP \leq r(1 + \epsilon_1)$, with $\epsilon_1 = 5\%$,

  $$(OA)^2 = (OP)^2 - \overrightarrow{OP} \cdot \frac{\overrightarrow{v}}{|\overrightarrow{v}|} \tag{2.34}$$

  and

  $$\Delta \equiv r^2 - (OA)^2 \tag{2.35}$$

  are computed. The particle will be detected if $\overrightarrow{AP} \cdot \overrightarrow{v} \leq 0$ and $\Delta \geq 0$. In that case $\sqrt{\Delta} = AB$.
- The particle is then propagated in a straight line along the direction of its velocity, up to a point P' such that $PP' = PB(1 + \epsilon_2)$, where $\epsilon_2 = 0.1\%$. The particle has then entered the sphere and is recorded.
- Even if the particle is recorded, its propagation continues. It will not be detected again before it leaves the observer sphere. It can, however, exit the sphere and come back in again, or enter another observer sphere. In those cases the particle will be recorded a second time.

This algorithm functions correctly as long as the Larmor radius of the particle in the region of the observation sphere is much larger than the radius r of the sphere. In this case the accuracy of the detection algorithm does not depend on Δx_3 but is of the order of $\epsilon_1 \times \epsilon_2$.

Additionally, it is possible to follow the full trajectory of the cosmic rays. In this case the trajectory is regularly sampled and written to the output file.

2.10 Overview

Fig. 2.6 shows an overview of the different aspects of CRPropa, from the sources through the propagation and ending at the observer. For the sources the source distribution, the injection spectrum at the source and the composition at the source can be specified. The source distribution can either be set as a continuous distribution, possibly following a certain density structure, or one or more discrete sources can be specified. The injection spectrum can consist of a single energy (monochromatic) or can be specified as a power law $\frac{\mathrm{d}N}{\mathrm{d}E} \propto E^{-\alpha}$ up to a maximum energy or rigidity.

During the propagation the UHECRs can interact with photon backgrounds through pair production, pion production and photodisintegration. If unstable particles are created, they can undergo nuclear decay. In any of these processes neutral secondaries,

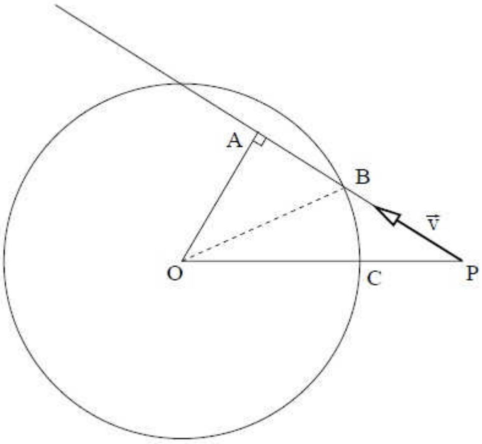

Figure 2.5: Geometry of the detection of a particle in a small observer sphere, obtained from Ref. [2].

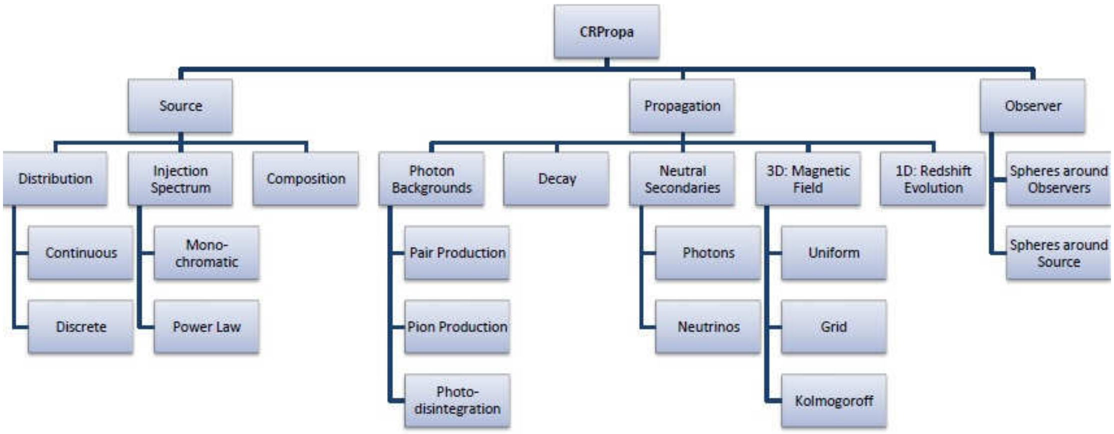

Figure 2.6: Overview of the different aspects of CRPropa.

photons as well as neutrinos, can be produced and propagated to the observer as well. Furthermore, in the 3D mode, it is possible to account for deflections in extragalactic magnetic fields. These magnetic fields can be specified in several different ways, namely as a uniformly distributed field, as magnetic field vectors on a grid or as a Kolmogoroff field. In addition, in the 1D mode, it is possible to take into account evolutions with redshift, affecting the photon backgrounds, the sources and the cosmic ray energy itself.

The observer can be specified in two different ways. When implemented as a sphere around an observer the particle is detected when it comes within a certain distance from a specified position. When the "spheres around source" case is selected, the particle state is stored when it reaches a certain distance from the source.

2.11 Applications

In this section the results of several simulations with CRPropa 2.0 are presented to demonstrate some of its features. The applications discussed here are presented as well in Refs. [1, 43]. The simulations are restricted to a pure-iron, pure-proton or a mixed composition injected at the source. The mixed composition is modeled to match the abundances of the galactic cosmic rays determined at lower energies, as described in Ref. [201], similar to the approach of Ref. [193].

The UHECRs are injected at the sources following a power law of

$$\mathrm{d}N_i/\mathrm{d}E \propto x_i A_i^{\alpha-1} E^{-\alpha} \;, \tag{2.36}$$

where x_i are the relative abundances at constant energy per nucleon, A_i are the mass numbers and α is the spectral index, arbitrarily chosen to be equal to 2.2. For the galactic composition case the abundances in Ref. [201] have been determined per element. For each element the most abundant species on Earth is selected. When available, the upper limit of the abundance was used for elements without best-fit values. The complete list of species and abundances is given in Table 2.2. To improve the comparison of the simulated spectrum with the measured spectrum, the abundances of all elements with $Z > 2$ are scaled up by a factor 10.

The IRB considered is the 'best-fit model' of Ref. [272]. For the 3D simulations, a (75 Mpc)^3 simulation box with periodic boundary conditions is implemented and filled with the EGMF and source distribution following the large-scale structure (LSS) baryon density from the cosmological simulations given in Ref. [3].

2.11.1 Composition and cosmological evolution in 1D

In 1D simulations it is possible to include the effects of the cosmological evolution on the UHECRs, on the UHECR sources and on the background photon fields, as a function of the redshift. These effects are especially important when secondary neutrinos are considered, as they can reach Earth even after being created at high redshifts.

In Fig. 2.7 (adopted from Ref. [1]) the results of two 1D simulations, including all effects of cosmological evolution, are shown which differ only in the composition injected at the source, namely the mixed galactic composition from Ref. [201] and a pure-iron injection. In this way the effects of the poorly known initial composition can be investigated.

For the cosmic-ray and neutrino-spectra simulations the UHECRs are injected at the sources with a power law of $\mathrm{d}N/\mathrm{d}E \propto E^{-1}$, to achieve sufficient statistics at high energy, which is reweighted afterwards to a power law of $\mathrm{d}N/\mathrm{d}E \propto E^{-2.2}$ (see Sec 2.3

Table 2.2: Injected UHECR species and abundances at equal energy per nucleon for the galactic composition (based on Ref. [201]). Abundances denoted by an asterisk are upper limits.

Species	Abundance x_i
^{1}H	0.95
^{4}He	0.04
^{9}Be*	3.16986×10^{-5}
^{11}B*	3.16986×10^{-5}
^{12}C	0.00315155
^{14}N	0.00024091
^{16}O	0.00370733
^{19}F*	2.11324×10^{-6}
^{20}Ne	0.00040856
^{23}Na	2.2823×10^{-5}
^{24}Mg	0.000760767
^{27}Al	5.48034×10^{-5}
^{28}Si	0.000704414
^{31}P	4.64913×10^{-6}
^{32}S	9.22782×10^{-5}
^{35}Cl	7.74855×10^{-7}
^{40}Ar	1.57084×10^{-5}
^{39}K	2.0428×10^{-6}
^{40}Ca	4.57869×10^{-5}
^{45}Sc*	6.83282×10^{-6}
^{48}Ti*	6.83282×10^{-6}
^{51}V*	6.83282×10^{-6}
^{52}Cr	1.05662×10^{-5}
^{55}Mn	7.74855×10^{-6}
^{56}Fe	0.000683281

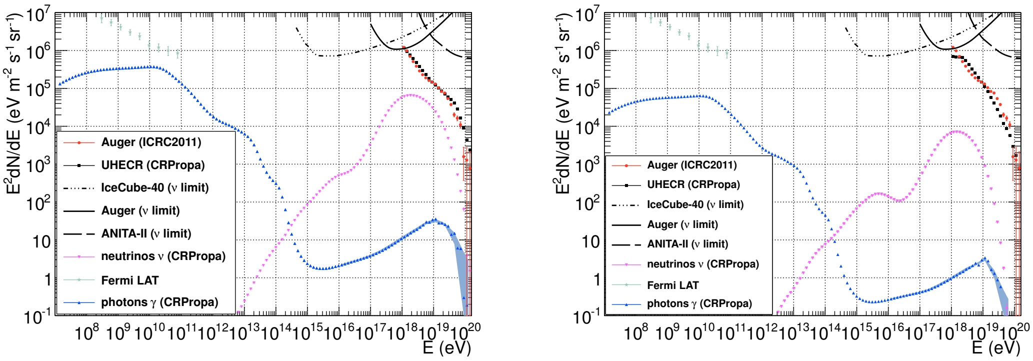

(a) Injected galactic composition

(b) Pure iron injection

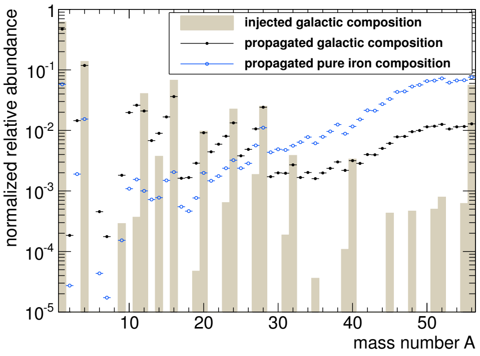

(c) Mass number abundance

Figure 2.7: Results of a 1D simulation with CRPropa 2.0 (adopted from Ref. [1]) taking into account cosmological expansion and implementing a continuous source distribution with comoving injection rate scaling as $(1+z)^4$ up to $z_{\max} = 2$. The shown results are for UHECRs injected with an $\mathrm{d}N/\mathrm{d}E \propto E^{-2.2}$ spectrum from a minimal energy of 1 EeV up to a maximum rigidity of $R_{\max} = E_{\max}/Z = 384.6$ EeV. The scaling of the IRB is done as described in Eq. 2.24.

(a,b) In the top panels the simulated UHECR spectrum (black rectangles) has been normalized to the Auger spectrum [297, 298] (red dots). The spectra of secondary gamma rays (blue triangles) and neutrinos (magenta triangles) have been normalized accordingly. The neutrino flux and neutrino limits (black lines) [299–301] are all for single-flavor neutrinos assuming a ratio of (1:1:1). Furthermore, the simulated photon spectrum can be compared with the isotropic gamma-ray flux measured by Fermi LAT (green stars) [132].

(a) In the left upper panel a mixed galactic composition has been injected at the sources.

(b) In the right upper panel a pure-iron composition has been injected.

(c) In the lower panel the abundance of UHECRs after propagation, for $E > 1$ EeV, is shown for both the galactic-composition-injection scenario (black solid circles) and the pure-iron-injection scenario (blue open circles). For comparison, the original injected galactic composition (light brown area) is given as well.

for more details on the reweighting method). This method is not possible for photons in 1D, so that an additional simulation including photons is run with an injection spectrum of $\mathrm{d}N/\mathrm{d}E \propto E^{-2.2}$ so that no reweighting is necessary. These two simulations are then combined in such a way that the UHECR spectra at 1 EeV are normalized to each other as the statistics are the highest at the lowest energies in the $\mathrm{d}N/\mathrm{d}E \propto E^{-2.2}$ injection case.

The UHECRs are injected up to a maximum rigidity of $R = E/Z = 384.6$ EeV and are followed as long as their energy remains above 1 EeV. They originate from a continuous source distribution with comoving injection rate scaling as $(1+z)^4$ up to $z_{\max} = 2$. The cosmological evolution is characterized by a concordance ΛCDM Universe with $\Omega_m = 0.3$, $\Omega_\lambda = 0.7$ and a Hubble constant of $H_0 = 72$ km s^{-1} Mpc^{-1}.

In Fig. 2.7(a) and Fig. 2.7(b), the simulated UHECR flux is normalized to the spectrum observed by the Pierre Auger Observatory [297] as presented during the ICRC 2011 [298] (which has a 22% systematic uncertainty on the energy scale, not shown in this plot) at an energy of 10 EeV and the secondary gamma-ray and neutrino fluxes are normalized accordingly. Besides the simulated cosmic ray, gamma-ray and neutrino spectra and the measured Auger cosmic ray flux, the bounds on the neutrino fluxes obtained by IceCube [299], Auger [300] and ANITA [301] as well as the diffuse gamma-ray flux level observed by Fermi LAT [132] are shown. The neutrino limits and spectra are all for single flavor neutrinos, assuming a ratio of (1:1:1).

The reduction of the flux of secondary neutrinos and gamma-rays for pure-iron injection, shown in Fig. 2.7(b), compared with the injected mixed galactic composition case of Fig. 2.7(a), is due to photodisintegration dominating with respect to pion production for the heavier composition. Note that photons from nuclear de-excitation during a photodisintegration event are not taken into account in CRPropa 2.0. This might cause a moderate increase of the flux of photons at energies below $\sim 10^{17}$ eV (see also Sec. 2.4.2.1).

The resulting simulated abundances of UHE nuclei for $E > 1$ EeV is shown in Fig. 2.7(c) for both the galactic-composition-injection scenario and the pure-iron-injection scenario. For comparison the abundances of the injected galactic composition, before propagation, are given as well. In all cases the abundances are normalized so that the sum of all individual abundances is equal to 1.

In order to maximize the neutrino flux to see if the neutrino limits can be reached, Fig. 2.8 shows the spectra for a 1D simulation with CRPropa 2.0 with a pure-proton composition and the following settings. A continuous source distribution is implemented with comoving injection rate scaling as $(1+z)^4$ up to $z_{\max} = 11$. Note that this is an unrealistically high $z_{\max}$, it was $z_{\max} = 2$ in the previous scenarios. The UHECRs were injected with an $\mathrm{d}N/\mathrm{d}E \propto E^{-2.2}$ spectrum from a minimal energy of 1 EeV up to a maximum energy of $E_{\max} = 10^4$ EeV (was $R_{\max} = E_{\max}/Z = 384.6$ EV in the previous scenarios). The scaling of the IRB is done as described in Eq. 2.24. The simulated UHECR spectrum has been normalized again to the Auger spectrum [297, 298]. The neutrino flux has again been normalized accordingly. The neutrino flux and neutrino limits [299–301] are again all for single-flavor neutrinos assuming a ratio of (1:1:1).

The change to a pure-proton composition, the increase in the maximum energy and the increased propagation distance all led to an enhanced neutrino flux. However, especially the comoving injection rate scaling as $(1+z)^4$ up to $z_{\max} = 11$ should not be considered as physically realistic, so that this should just be considered as an example of what a simulation with extreme settings could produce. For the discussion of more realistic neutrino flux scenarios, see Chapter 3.

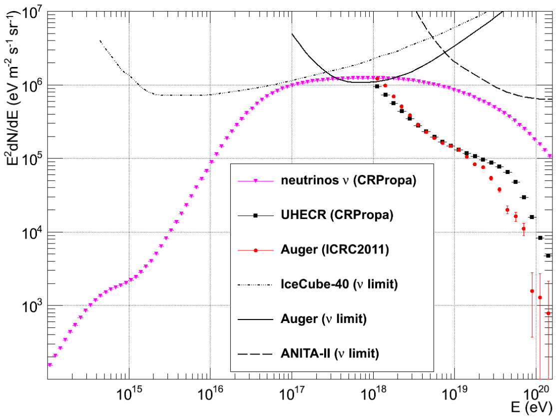

Figure 2.8: Results of a 1D simulation with CRPropa 2.0 aimed at maximizing the neutrino flux. To achieve this a pure-proton composition has been injected at the sources. Furthermore, a continuous source distribution is implemented with comoving injection rate scaling as $(1+z)^4$ up to $z_{\max} = 11$. The shown results are for UHECRs injected with an $\mathrm{d}N/\mathrm{d}E \propto E^{-2.2}$ spectrum from a minimal energy of 1 EeV up to a maximum energy of $E_{\max} = 10^4$ EeV. The scaling of the IRB is done as described in Eq. 2.24. The simulated UHECR spectrum (black rectangles) has been normalized to the Auger spectrum [297, 298] (red dots). The neutrino flux (magenta triangles) has been normalized accordingly. The neutrino flux and neutrino limits (black lines) [299–301] are all for single-flavor neutrinos assuming a ratio of (1:1:1).

2.11.2 Large scale structure and magnetic field effects in 3D

With 3D simulations of CRPropa it is possible to investigate the effects of sources following the LSS baryon density and of cosmic rays being deflected in structured EGMFs. Here it is investigated how the EGMF and source distribution following the LSS baryon density from the cosmological simulations given in Ref. [3] influence the UHECR spectrum, composition and travel distance.

For these simulations the UHECRs are injected at the sources with a power law of $\mathrm{d}N/\mathrm{d}E \propto E^{-1}$ to achieve sufficient statistics at the highest energies, which is reweighted afterwards to a power law of $\mathrm{d}N/\mathrm{d}E \propto E^{-2.2}$. The same galactic composition as in the previous example as well as a pure-iron and a pure-proton composition are injected at the sources. The sources are assumed to have a maximum acceleration rigidity of $R = 384.6$ EeV and the UHECRs are tracked as long as their energy remains above 1 EeV. The observer is defined as a sphere with a radius of 1 Mpc and is placed in a magnetic environment that is similar to what is found in the vicinity of our galaxy. The maximum distance that the UHECRs have been allowed to propagate is 3000 Mpc. The IRB considered is the 'best-fit model' of Ref. [272].

The results are shown in Fig. 2.9. Fig. 2.9(a) shows the UHECR flux after propagation for the different injection scenarios. Besides the three source-composition scenarios with source-distributions following the LSS and deflections in the EGMF, a pure-iron-injection scenario with the same source distribution, but without deflections in magnetic fields, and a pure-proton case with a continuous flat source distribution (not following the LSS), also without any deflections in magnetic fields, are shown. The flux is normalized to 1 in the first bin to allow for a better comparison of the spectral shape. These results indicate that there is a significant difference in shape of the spectrum for pure-iron injection compared with pure-proton or mixed-galactic-composition injection. Furthermore, comparing the two pure-iron injection lines with each other shows that

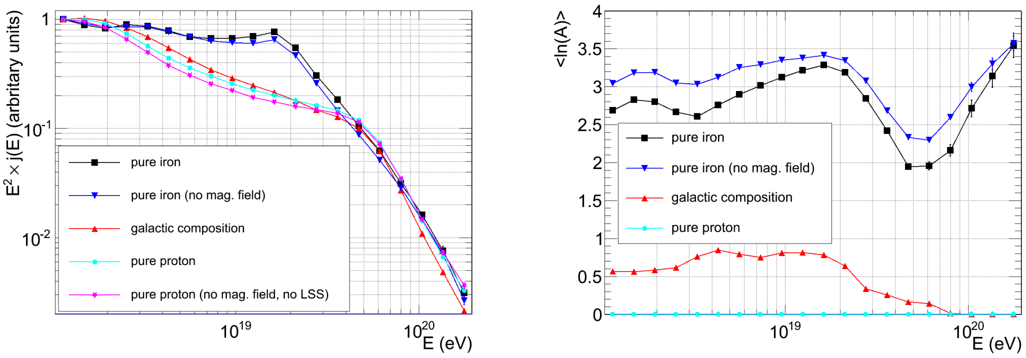

(a) Energy spectra

(b) Mass Spectra

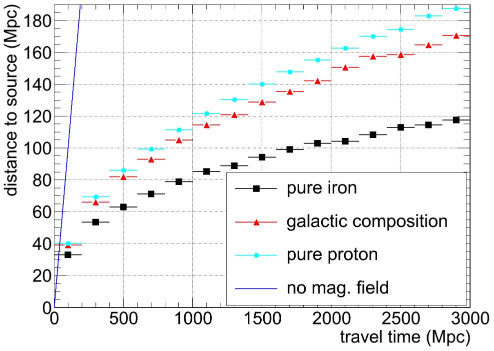

(c) Source distance versus travel time

Figure 2.9: Results of 3D CRPropa simulations (adopted from Ref. [1]) with a continuous source distribution which follows the LSS density of Ref. [3] including deflections in the corresponding extragalactic magnetic fields. A pure-iron composition (black rectangles), a mixed galactic composition (red triangles) and a pure-proton composition (light-blue dots) have been injected at the sources. The UHECRs are injected at the sources following a power law with a slope of $\alpha = 2.2$ up to a maximum rigidity of $R = 384.6$ EeV.
(a) The top left panel shows the UHECR flux after propagation for the different injection scenarios. Next to the three previously mentioned compositions at injection, a pure-iron-injection scenario with a continuous source distribution which follows the same LSS density but without deflections in magnetic fields (dark-blue triangles) and a pure-proton case with a continuous flat source distribution (not following the LSS) also without any deflections in magnetic fields (magenta stars) are shown. The flux is normalized to 1 in the first bin to allow for a better comparison of the spectral shape.
(b) The top right panel shows the averaged logarithm of the mass number $\langle \ln(A) \rangle$ of the UHECRs at detection as a function of the energy of the UHECRs. Here the same pure-iron-injection scenario without deflections in magnetic fields as in the top left panel is given as well.
(c) The bottom panel shows the distance of the UHECRs from their source as function of the propagation time for all cosmic rays above 1 EeV. The dark blue line indicates what a scenario without any deflections in magnetic fields would look like.

there is only a small effect of the EGMF on these cosmic-ray spectra. Comparing the two pure-proton injection lines with each other indicates that also the source distribution following the LSS has little effect on the spectrum.

Fig. 2.9(b) shows the averaged logarithm of the mass number $\langle \ln(A) \rangle$ of the UHECRs at detection as a function of the energy of the UHECRs. Here the same pure-iron-injection scenario without deflections in magnetic fields as in Fig. 2.9(a) is given as well. From Fig. 2.9(b) it can be seen that the detected composition of the pure-iron injection case is affected by the EGMF. As deflections increase the propagation path length of a cosmic ray from its source to the observer, more interactions can occur on the way and therefore the average mass number at detection is reduced.

Fig. 2.9(c) shows the distance of the UHECRs from their source as function of the propagation time for all cosmic rays above 1 EeV for the three different injection cases. Here it is indicated what a scenario without any deflections in magnetic fields would look like as well. This plot illustrates that the average distance to the source of the cosmic ray after a specific travel time is reduced drastically (when considering all cosmic rays above 1 EeV) if deflections in EGMFs are included. Additionally can be seen that the source horizon depends as well on the injected composition, which is due to the increase of deflections in magnetic fields for heavier, and thus more charged, compositions.

2.11.3 Observables at a given distance from the source in 3D

In CRPropa 2.0 the possibility exists to define the observer as a sphere around one specific source (see Sec. 2.9 for the different possible observer types). In this detection mode an event is registered and written to the output file when it reaches a certain distance from the source. In this way the spectrum, composition and anisotropy of the UHECRs from a given source as function of the distance to that source can be investigated.

For this simulation the same mixed galactic composition as in the previous sections is injected from the center of a (75 Mpc)^3 simulation box filled with the magnetic field configuration of Ref. [3]. The detection spheres are placed at distances of 4, 8, 16 and 32 Mpc around the source. The initial spectrum of $dN/dE \propto E^{-1.0}$ up to a rigidity of $R = 384.6$ EeV is reweighted afterwards to a source spectrum of $dN/dE \propto E^{-2.2}$. Only particles with an energy larger than 55 EeV are considered. The IRB considered is again the 'best-fit model' of Ref. [272].

The results are shown in Fig. 2.10. Fig. 2.10(a) shows the cosmic ray spectrum at different distances from the sources. The spectra have been normalized to 1 in the first bin. From this figure can be seen that the flux of UHECRs at the highest energies is suppressed by particle interactions as the distance from the source increases.

Fig. 2.10(b) shows the sky maps in Hammer-Aitoff projections of cosmic rays at the different distances from the source. From these sky maps it can be seen that the cosmic-ray distribution becomes more anisotropic with increasing distance from the source due to the increase of deflections in the LSS-EGMFs.

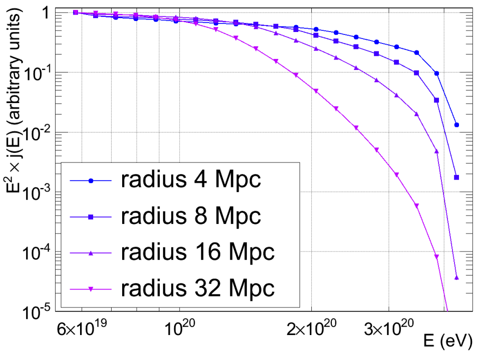

(a) Energy spectra

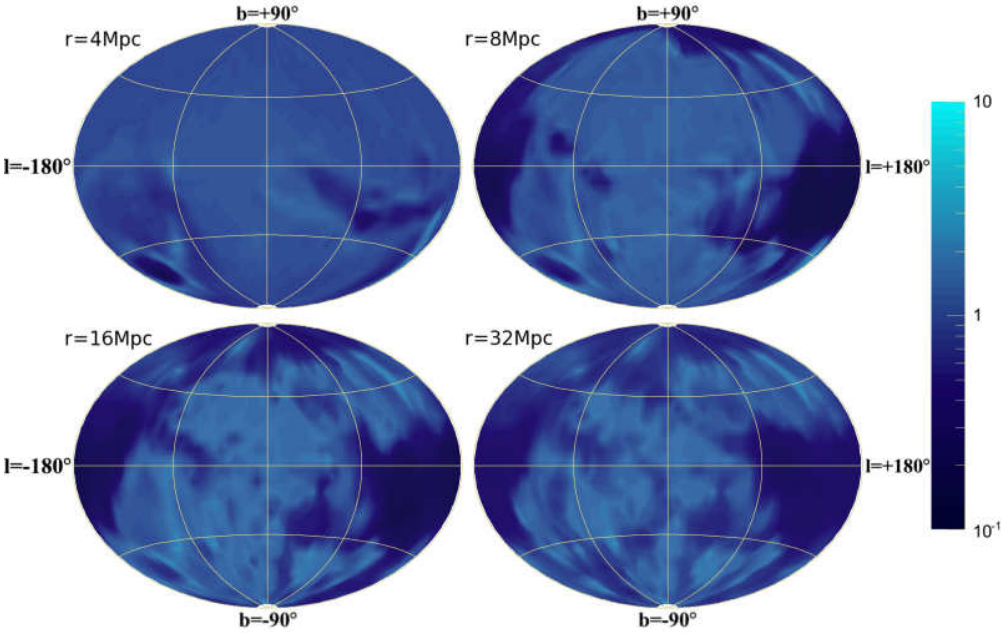

(b) Sky maps

Figure 2.10: Spectra and sky maps (adopted from Ref. [1]) of UHECRs from a single source with energies $E > 55$ EeV after propagating in a $(75\ \text{Mpc})^3$ simulation box filled with the LSS-EGMF of Ref. [3]. In this simulation detection spheres have been placed around the single source present in the simulated environment with four different radii: 4, 8, 16 and 32 Mpc. The injection spectrum has been reweighted to a $dN/dE \propto E^{-2.2}$ source spectrum up to a maximum rigidity of $R = 384.6$ EeV.
(a) UHECR spectrum as detected at the four spheres, normalized to 1 at the first bin.
(b) Hammer-Aitoff projections of the arrival directions of the simulated UHECR trajectories as registered on the different detection spheres around the source.

Chapter 3

PSB photodisintegration

In Sec. 2.4.2 is discussed how photodisintegration is handled in CRPropa 2.0. To test and compare this implementation, an additional photodisintegration set up has been developed for CRPropa 2.0 based on the widely-used method described by Puget, Stecker and Bredekamp (PSB) [8], who were the first to study the effects of the propagation of ultra-high-energy (UHE) nuclei including a detailed calculation of their photodisintegration. This PSB photodisintegration implementation can be applied instead of the TALYS cross sections extended by the different treatments of light nuclei.

In the rest frame of the nucleus, photodisintegration is particularly important for most nuclei between ∼10 and 30 MeV, where the giant dipole resonance (GDR) has its peak. The PSB scheme is based on empirically determined cross section data as a function of energy for all nuclei with $1 \leq A \leq 56$, with A the mass number of the nucleus. Due to the position of ^{56}Fe on the binding energy curve, it is considered to be a significant end product of stellar evolution (as in the standard CRPropa setup), and higher-mass nuclei are found to be much rarer in the cosmic radiation.

Furthermore, cross-section data for $1 \leq A \leq 56$ for multi-nucleon emission interactions as well as single-nucleon emission interactions is used. Multi-nucleon losses, except for double-nucleon loss, involve non-resonant processes and are particularly important at energies between the position of the GDR and the pion production threshold, i.e. for $\epsilon'_1 = 30$ MeV $< \epsilon' < \epsilon'_{\mathrm{max}} = 150$ MeV, with ϵ' the photon energy in the rest frame of the nucleus.

At higher energies than ϵ'_{max} detailed cross-section data are more scarce. See, for example, Ref. [279] for discussions on photodisintegration cross sections in this energy range. The smaller residual cross section at these energies is approximated by zero in the PSB setup. This is done as interactions with photons of energy greater than ϵ'_{max} (in the nucleus rest frame) will have a negligible contribution to the photodisintegration process for UHE nuclei with energies below 1000 EeV due to the fact that the density of the background photons seen by the UHE nuclei near the peak of the GDR cross section falls rapidly with energy, along with that the photodisintegration cross section is about two orders of magnitude lower in the energy region from ϵ'_{max} to ∼1 GeV than at the GDR peak [9, 302, 303]. In Ref. [9] was verified by numerical tests that interactions with photons of energy greater than ϵ'_{max} indeed have a negligible effect on UHE nuclei propagation.

3.1 Photodisintegration cross sections

The energy range employed in the PSB setup for photodisintegration, $\epsilon'_{\rm min} < \epsilon' < \epsilon'_{\rm max} = 150$ MeV, can be split into two parts. The lower region, extending up to $\epsilon'_1 = 30$ MeV, is the domain of the GDR. Here most of the interaction cross section will lead to the emission of only single nucleons, neutrons or protons, although two-nucleon emission does take place as well [279].

Experimental data are generally consistent with a two-step process, photoabsorption by the nucleus to form a compound state, followed by a statistical decay process involving the emission of one or more nucleons from the nucleus. For heavy nuclei, $A \geq 50$, the total photoabsorption cross section can be represented reasonably well by a single or, in the case of a deformed nuclei, by the superposition of two Lorentzian curves of the form [8]

$$\sigma(\epsilon') = \sigma_0 \frac{\epsilon'^2 \Gamma_d^2}{(\epsilon_0'^2 - \epsilon'^2)^2 + \epsilon'^2 \Gamma_d^2} \; . \tag{3.1}$$

For the lighter nuclei the photodisintegration cross section often shows considerably more structure than this. For all nuclei at these energies the basic photonuclear interaction is pictured as being with the individual uncorrelated nucleons comprising the nucleus. The collective giant-resonance state is described by a coherent superposition of individual single-particle transitions.

Between ϵ'_1 and $\epsilon'_{\rm max}$ PSB concluded from the available measurements that the total cross section is a relatively smooth function of energy. Reactions in which a number of nucleons is emitted seem to make up most of the total photodisintegration cross section. At these energies the photon's wavelength is comparable or less than the nuclear dimensions, therefore it becomes very difficult to conserve both energy and momentum in a single-particle emission interaction within the nucleus. The dominant process is then pictured as the quasideuteron effect [304], where the photon interacts with a nucleon pair while they are scattering within the nucleus.

For the calculations of the parameters of the photodisintegration cross section done in Ref. [8], each cross section was assumed to be independent of energy over a finite energy band of width Δ. For energies below ϵ'_1, this band is assumed to be centered about a mean energy ϵ'_0 for each reaction. As a further simplification it was assumed that the half-lifes of the various reaction products resulting from photodisintegration were all short compared with the rate at which the reactions take place. With this assumption, not all individual interactions need to be considered. This leads to a reduced reaction network involving one nucleus for each atomic mass number A up to ^{56}Fe.

For energies below ϵ'_1, in the PSB setup, the total photodisintegration cross section is assumed to result in reactions in which only one or two nucleons are emitted. These are given in terms of the quantities ϵ'_0, ξ and Δ. For each interaction these parameters are defined as [8]

$$\xi_1 \equiv \frac{1}{\Sigma_{\rm d}} \int_0^{\epsilon'_1} \sigma^{(1)}(\epsilon') {\rm d}\epsilon' \; , \tag{3.2}$$

where $\sigma^{(1)}(\epsilon')$ is the actual single-nucleon-emission cross section as a function of the photon energy ϵ'. Furthermore, $\Sigma_{\rm d}$ is the integral of the cross section over the energy interval obeying a Thomas-Reiche-Kuhn (TRK) sum rule [8, 9]

$$\Sigma_{\rm d} = \int \sigma(\epsilon') {\rm d}\epsilon' = \frac{2\pi^2 e^2}{Mc} \frac{NZ}{A} \approx 59.8 \frac{NZ}{A} \text{ MeV mb}, \tag{3.3}$$

where M is the nucleon mass, A the mass number, Z the charge of the nucleus, and $N = A - Z$ the number of neutrons in the nucleus. No real physical significance should be attached to this normalization, it is just a convenient scale factor that removes the principal dependence of the total photodisintegration cross section on N, Z and A.

The quantity ϵ'_0 is defined as the mean energy for the reaction corresponding to $\sigma^{(1)}(\epsilon')$. The energy bandwidth Δ_1 and the mean cross section σ_m, with [8]

$$\Delta_1 \sigma_m = \int_0^{\epsilon'_1} \sigma^{(1)}(\epsilon') \mathrm{d}\epsilon' \ , \tag{3.4}$$

were chosen in the PSB setup so as to match the actual dependence of $\sigma^{(1)}(\epsilon')$ on energy as closely as possible. The corresponding quantities for the two-nucleon interactions were chosen in a similar way.

The data for the region from ϵ'_1 to ϵ'_{max} are parameterized by two quantities, the total strength of the interaction given by ζ, and a branching ratio f_i. The total strength of the interaction is defined as [8]

$$\zeta \equiv \frac{1}{\Sigma_{\mathrm{d}}} \int_{\epsilon'_1}^{\epsilon'_{\mathrm{max}}} \sigma_t(\epsilon') \mathrm{d}\epsilon' \ , \tag{3.5}$$

where $\sigma_t(\epsilon')$ is the total photodisintegration cross section. These data should not be taken to represent anything more than a first approximation of the yields that might be expected from a $1/\epsilon'$ photon energy spectrum.

3.2 Implementation in CRPropa

As significant deviations do occur, for the lighter nuclei, from the pure Lorentzian shape (Eq. 3.1) in the energy range where the maximum cross section occurs, a Gaussian approximation for the cross section for one- and two-nucleon photodisintegration in this energy range was implemented by PSB. This functions as an adequate fit to the cross section data as well as an expedient in performing the numerical calculations. Moreover, a constant cross section above $\epsilon'_1 = 30$ MeV was implemented in the original PSB paper (Ref. [8]). Exceptions to this are the four nuclei ^{2}H, ^{3}He, ^{4}He and ^{9}Be with nonresonant channels having large values of Δ ($\Delta \gg 10$ MeV), so that the 30 MeV cut-off formalism was not employed.

In Ref. [8] a threshold energy of 2 MeV in the rest system of the nucleus was used for all reaction channels. This value is far smaller than the true thresholds. Single-nucleon emission has a typical threshold of ∼10 MeV, while the double-nucleon emission has a threshold of, typically, around ∼20 MeV. Therefore, for the implementation in CRPropa, the threshold energy is updated to the variable threshold energies ϵ'_{min} given in Ref. [9].

The cross sections implemented in the PSB setup of CRPropa are of the form [8]

$$\sigma_i(\epsilon') = W_i^{-1} \xi_i \Sigma_{\mathrm{d}} \Delta_i^{-1} \Theta_+(\epsilon'_{\mathrm{min},i}) \Theta_-(\epsilon'_1) e^{-2\left(\frac{\epsilon' - \epsilon'_{0,i}}{\Delta_i}\right)^2} + \frac{\zeta f_i \Sigma_{\mathrm{d}} \Theta_+(\epsilon'_1) \Theta_-(\epsilon'_{\mathrm{max}})}{\epsilon'_{\mathrm{max}} - \epsilon'_1} \tag{3.6}$$

for $i = 1, 2$ and

$$\sigma_i(\epsilon') = \frac{\zeta f_i \Sigma_{\mathrm{d}} \Theta_+(\epsilon'_1) \Theta_-(\epsilon'_{\mathrm{max}})}{\epsilon'_{\mathrm{max}} - \epsilon'_1} \tag{3.7}$$

for $i > 2$. Here the normalization factor is [8]

$$W_i = \sqrt{\frac{\pi}{8}} \left[\mathrm{erf}\left(\frac{\epsilon'_1 - \epsilon'_{0,i}}{\Delta_i/\sqrt{2}} \right) + \mathrm{erf}\left(\frac{\epsilon'_{0,i} - \epsilon'_{\mathrm{min},i}}{\Delta_i/\sqrt{2}} \right) \right] \tag{3.8}$$

with

$$\mathrm{erf}(x) \equiv 2\pi^{-1/2} \int_0^x \exp(-t^2)\mathrm{d}t \tag{3.9}$$

and $\Theta_+(x)$ and $\Theta_-(x)$ are the Heaviside step functions

$$\Theta_+(x) \equiv \begin{cases} 1 & \text{for } \epsilon' \geq x \\ 0 & \text{otherwise ,} \end{cases} \tag{3.10}$$

$$\Theta_-(x) \equiv \begin{cases} 0 & \text{for } \epsilon' > x \\ 1 & \text{otherwise .} \end{cases} \tag{3.11}$$

The values of Z, $\epsilon'_{0,i}$, ξ_i, Δ_i, $\epsilon'_{\mathrm{min},i}$ and ζ, with $i = 1, 2$, for each mass number A used for the PSB setup in CRPropa can be found in Table A.1 for ζ and $i = 1$ and in Table A.3 for $i = 2$. The branching ratios f_i can be found in Table A.5. Tables 1 and 2 of Ref. [8] show the parameters used in the calculations in the original PSB setup. In Ref. [9] this PSB setup was updated to include variable energy thresholds ϵ'_{min}. The values for these thresholds can be found in Table 1 of this reference. For the data developed for CRPropa, these three tables have been used.

As CRPropa does not support a photodisintegration step where the mass number A goes down while the charge Z goes up, some small adjustments had to be done. Normally, by photodisintegration alone, it is not possible to increase the charge of the nucleus. However, in the PSB scheme, this can be seen as a photodisintegration combined with a β^- decay. Due to the assumption in the PSB setup that the half-lives of the various reaction products resulting from photodisintegration are all short compared with the rate at which the reactions take place, the decay of nuclei is taken into account implicitly in the photodisintegration scheme. In CRPropa the photodisintegration and decay are considered as separate processes. Therefore some small adjustments had to be made to incorporate the PSB scheme into CRPropa.

Furthermore, in Table 1 of Ref. [9] multiple values of ϵ'_{min} for single-nucleon and double-nucleon photodisintegration are given. For the implementation in CRPropa the lowest values of ϵ'_{min} for the corresponding one- and two-nucleon photodisintegration channels have been implemented. This was done as in principle all photodisintegration channels should be taken into account, making the ϵ'_{min} for all single-nucleon photodisintegration channels the same as the lowest ϵ'_{min} of the separate single-nucleon photodisintegration channels. The same holds for double-nucleon photodisintegration. See Appendix A for the values of all parameters used for the PSB setup in CRPropa.

3.3 Comparison with original photodisintegration setup

To see the effect of the PSB setup for photodisintegration compared with the standard setup (see Sec. 2.4.2) in CRPropa, as well as to check different features of the implemented cross sections in the standard setup, several comparisons between the two different photodisintegration setups are made here.

3.3.1 Exclusive-channel cross sections

One way to compare the two different photodisintegration setups is by looking at the exclusive cross-section channels directly. In the PSB setup, due to the photodisintegration chain with one nucleus per mass number, only one end product is possible when photodisintegrating while emitting a specific number of nucleons. In the standard setup of CRPropa, however, there are, in general, many different possibilities. Therefore, a photodisintegration of a specific nucleus N with the loss of i nucleons in the PSB setup can either be compared with the combination of all i-nucleon-loss channels of the same nucleus N or with the exact same exclusive channel in the standard CRPropa case (e.g. if the 1-nucleon photodisintegration of a nucleus N in the PSB setup would be the loss of a proton, it could either be compared with the combined cross sections of 1-proton ($1p$) emission and 1-neutron ($1n$) emission or with the same 1-proton-emission cross section for the same nucleus N in the standard CRPropa setup).

To give an example for one specific nucleus, all possible exclusive photodisintegration channels of ^{14}N in the PSB setup are compared with their equivalents and the combination of all i-nucleon emission cross sections in the standard CRPropa setup in Fig. 3.1. Fig. 3.1(a) shows the cross sections for one-nucleon emission. In the PSB setup the only possible one-nucleon emission for ^{14}N is by emitting a proton. For the CRPropa setup both the $1p$ channel and the combination of the $1p$ and the $1n$ channel are shown. In both cases a clear difference is visible between the different energies at the peak values as well as between the heights of the peaks.

Fig. 3.1(b) shows the cross sections for two-nucleon emission. In this case the only possible two-nucleon emission in the PSB model is the $1p1n$ channel. Again both the $1p1n$ channel as well as the full two-nucleon photodisintegration cross section for the standard CRPropa implementation are given. In this case the energies at the peak values agree rather well, but the cross sections at the peaks still differ significantly. It is also noteworthy that the PSB cross sections are actually larger than the CRPropa cross sections at the lowest and highest energies.

Fig. 3.1(c) shows the cross sections for three-nucleon emission. In the PSB scenario emission of $i > 2$ nucleons only occurs in the energy regime $\epsilon'_1 < \epsilon' < \epsilon'_{\mathrm{max}}$ and is approximated with a flat distribution between these energies. In this figure it can be seen how this compares to the same $2p1n$ channel in the standard CRPropa setup as well as to the full three-nucleon cross section.

Fig. 3.1(d) shows the cross sections for four-nucleon emission. The only possible channel in the PSB case is the $2p2n$ emission, which is parametrized as a flat distribution between $\epsilon'_1 < \epsilon' < \epsilon'_{\mathrm{max}}$. In the CRPropa setup, however, a large peak in the full four-nucleon cross section occurs at energies below $\epsilon'_1 = 30$ MeV. This is due to, as can be seen from this figure, the cross-section channel for the emission of one ^{4}He particle. As only single nucleons can be emitted as secondaries in the PSB setup, this channel is ignored in that scenario.

For completeness, Fig. 3.1(e) and Fig. 3.1(f) show the exclusive $3p2n$ and $4p2n$ channels, respectively, for both the PSB and the standard CRPropa setup. The differences for these multi-nucleon-emission channels between these two setups are extensive.

3.3.2 Full cross sections

Four examples of comparisons between the PSB setup and the standard CRPropa setup for the full cross section are given in Fig. 3.2. Fig. 3.2(a) shows the cross sections for ^{9}Be, one of the nuclei in the PSB case with large Δ_i so that the 30 MeV cut-off formalism was not employed (see also Sec. 3.2). From this figure it is clear that the CRPropa case continuous to higher energies, while the PSB case approaches zero. As will be shown in the next section, this is one of the nuclei where the relative difference between the total summed PSB cross section and the total summed standard CRPropa implementation is

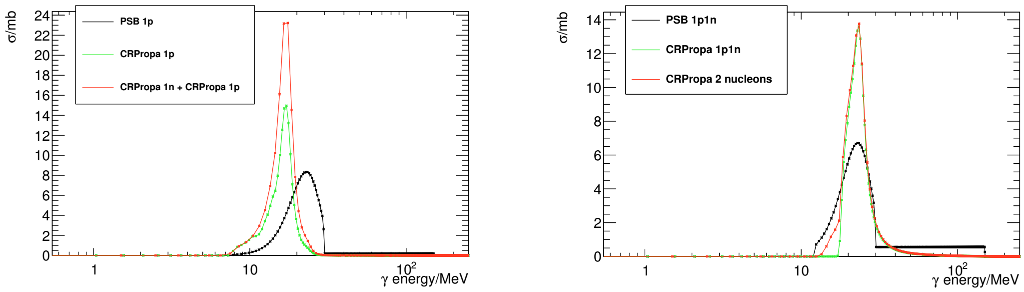

(a) ^{14}N, 1 nucleon channels

(b) ^{14}N, 2 nucleons channels

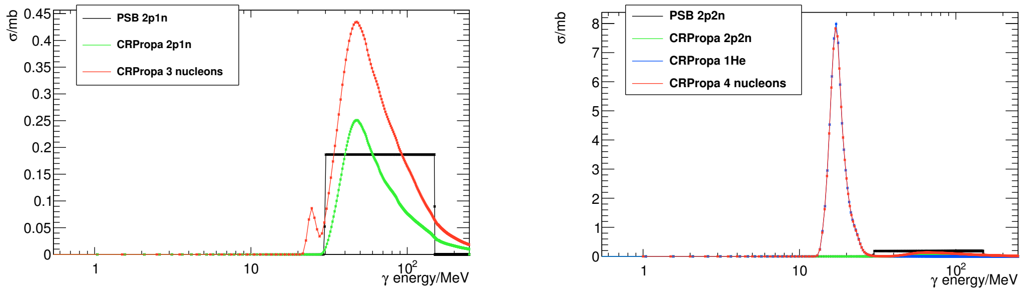

(c) ^{14}N, 3 nucleons channels

(d) ^{14}N, 4 nucleons channels

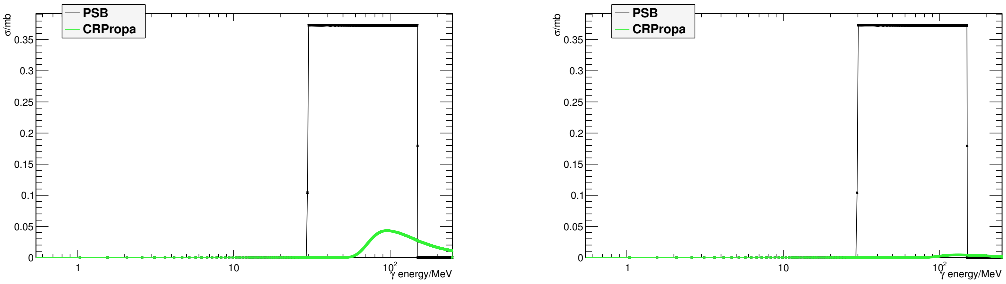

(e) ^{14}N, $3p2n$ channel

(f) ^{14}N, $4p2n$ channel

Figure 3.1: Exclusive-channel cross-section comparisons for ^{14}N between the PSB setup (in black) and the standard CRPropa setup, showing the same exclusive channel (in green) as in the PSB case.
(a) The $1p$ channel for both scenarios, including the combination of all one-nucleon channels in the standard CRPropa setup (in red).
(b) The $1p1n$ channel for both scenarios, including the combination of all two-nucleon channels in the standard CRPropa setup (in red).
(c) The $2p1n$ channel for both scenarios, including the combination of all three-nucleon channels in the standard CRPropa setup (in red).
(d) The $2p2n$ channel for both scenarios, including the combination of all four-nucleon channels (in red) and the 1^4He channel (in blue) in the standard CRPropa setup.
(e) The $3p2n$ channel for both scenarios.
(f) For completeness, the $4p2n$ channel for both scenarios. This is the channel with the most secondaries addressed in the PSB setup for ^{14}N.

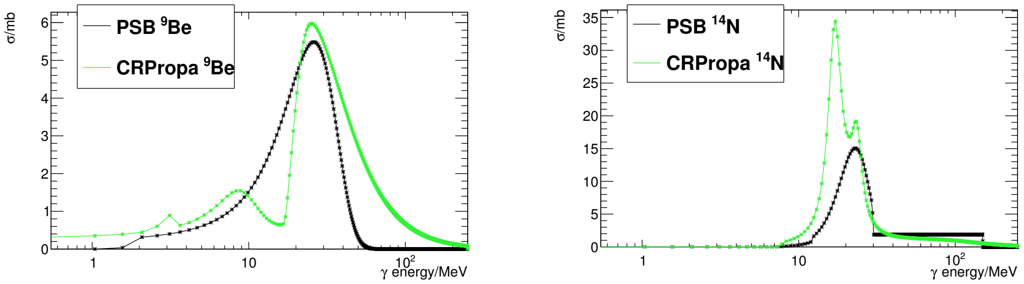

(a) ^{9}Be

(b) ^{14}N

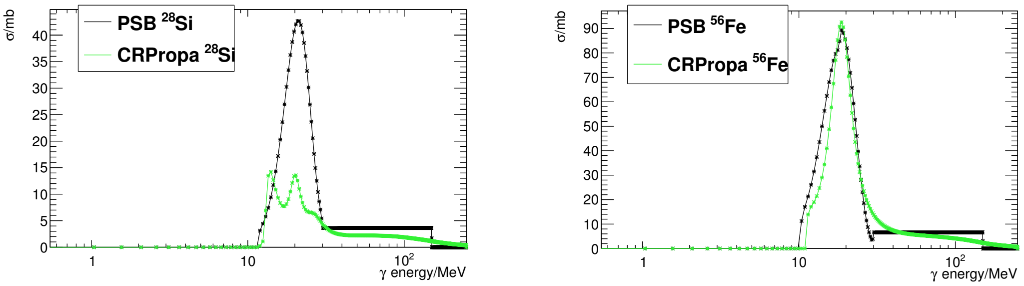

(c) ^{28}Si

(d) ^{56}Fe

Figure 3.2: All-channel cross-section comparisons between the PSB setup (in black) and the standard CRPropa setup (in green).
(a) The top-left panel shows the cross sections for ^{9}Be.
(b) The top-right panel shows the cross sections for ^{14}N.
(c) The bottom-left panel shows the cross sections for ^{28}Si.
(d) The bottom-right panel shows the cross sections for ^{56}Fe.

the largest.

In Fig. 3.2(b) it concerns again the nucleus ^{14}N, as in Fig. 3.1. In the standard CRPropa setup there is a clear two-peak structure, not present in the PSB setup. Where the one peak of the PSB case seems to resemble the second peak in the CRPropa case, the first and highest peak of the CRPropa setup does not seem to be present in the PSB setup. This is mostly due to the different position and peak height of the one-nucleon photodisintegration case, shown in Fig. 3.1(a).

Fig. 3.2(c) indicates the cross sections for ^{28}Si. Together with ^{9}Be (Fig. 3.2(a)), this nucleus shows the largest relative difference between the total summed cross sections of the standard CRPropa setup and the PSB setup (see the next section).

Finally, Fig. 3.2(d) shows the full photodisintegration cross section of both setups for ^{56}Fe. For this scenario the two cross section models seem to agree rather well.

To give a full overview of the relative differences for all mass numbers available in the PSB chain, Fig. 3.3 shows the cross sections of both setups divided by each other for all mass numbers and over the whole energy range of the PSB setup. The cases where either $\sigma_{\text{PSB}}(\epsilon'_i) = 0$ or $\sigma_{\text{CRPropa}}(\epsilon'_i) = 0$ are disregarded and not shown in the plots. Fig. 3.3(a) gives the CRPropa cross section divided by the PSB cross sections $(\sigma_{\text{CRPropa}}(\epsilon'_i)/\sigma_{\text{PSB}}(\epsilon'_i))$ while Fig. 3.3(b) shows the PSB cross sections divided by the CRPropa cross sections $(\sigma_{\text{PSB}}(\epsilon'_i)/\sigma_{\text{CRPropa}}(\epsilon'_i))$. The color scale, indicating the value of the two cross sections divided by each other, is limited to a maximum of six in both cases to be able to get a feeling for the differences over the whole energy and mass range.

An interesting feature to note in these plots, is the large relative differences at low

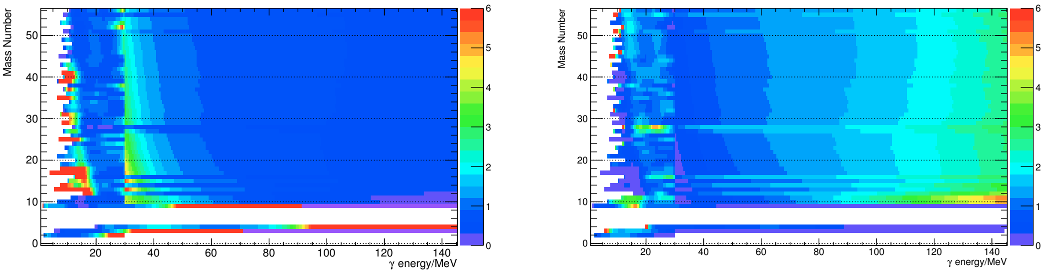

(a) $\sigma_{\mathrm{CRPropa}}(\epsilon_i')/\sigma_{\mathrm{PSB}}(\epsilon_i')$

(b) $\sigma_{\mathrm{PSB}}(\epsilon_i')/\sigma_{\mathrm{CRPropa}}(\epsilon_i')$

Figure 3.3: All-channel cross-section comparison between the PSB setup and the standard CRPropa setup for all mass numbers A. The results are only shown when both $\sigma_{\mathrm{PSB}}(\epsilon_i') > 0$ and $\sigma_{\mathrm{CRPropa}}(\epsilon_i') > 0$. The color scale, indicating the value of the two cross sections divided by each other, is limited to a maximum of six.
(a) The left panel shows the CRPropa cross section divided by the PSB cross section for each energy bin and mass number.
(b) The right panel shows the PSB cross section divided by the CRPropa cross section for each energy bin and mass number.

energies in some cases. This is, for different mass numbers, either due to different threshold energies between the two photodisintegration setups or due to a difference in energy of the first peak of the cross sections (see e.g. Fig. 3.2(b)) or due to both.

In addition, a clear abrupt transition occurs at 30 MeV. This is due to the transition in the PSB setup from the low-energy to the high-energy regime. These two regions are parametrized in different ways, and the transition between them can be rather abrupt, while there is no division in energy regimes in the standard CRPropa setup.

Furthermore, for $A \leq 9$, significant differences occur at relatively high energies. This is due to the CRPropa results continuing to higher energies for these mass numbers, while the PSB cross sections approach $\sigma_{\mathrm{PSB}}(\epsilon_i') = 0$. The nuclei for which this occurs are the four nuclei ^{2}H, ^{3}He, ^{4}He and ^{9}Be with nonresonant channels having large values of Δ so that the 30 MeV cut-off formalism was not employed (see also Sec. 3.2). See, for example, Fig. 3.2(a) for the cross sections of ^{9}Be.

Moreover, there seem to be some outliers, nuclei for which the differences are bigger than, or in the other direction as, the nuclei with mass numbers close to them. ^{28}Si is one such example, see Fig. 3.2(c) for the cross sections of this nucleus. TALYS 1.0 gives a significantly lower cross section for this nucleus than for the nuclei with mass numbers close to it.

To look at the differences in energy threshold, Fig. 3.4 compares them directly. Here they are compared by dividing ϵ'_{min} for the standard CRPropa setup by ϵ'_{min} for the PSB setup for all mass numbers. This indicates that for $A = 9$, 10 and 11 the energy threshold in the CRPropa case is significantly lower than in the PSB case. After close investigation this led to the increase of ϵ'_{min} for these mass numbers in the standard CRPropa case, before the release of CRPropa 2.0. The threshold energies of all other mass numbers agree to within a factor of ∼2.

3.3.3 Summed full cross section

However, even when there are significant differences at specific photon energies, the total cross section summed over all photon energies could still be comparable. Therefore, in Fig. 3.5, the summed cross sections, starting at the lowest energies, for both pho-

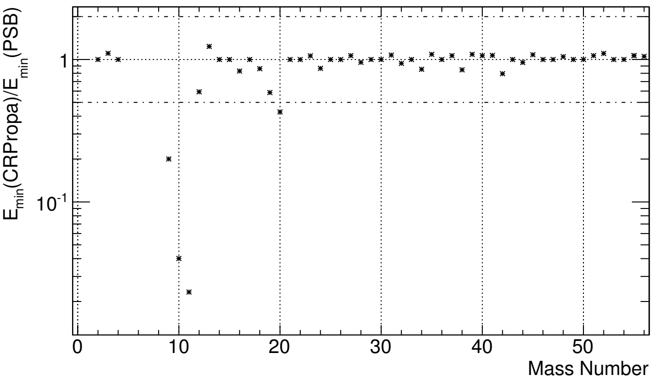

Figure 3.4: Energy threshold comparison by dividing ϵ'_{min} for the standard CRPropa setup by ϵ'_{min} for the PSB setup for all mass numbers.

todisintegration setups divided by each other ($\Sigma_i\sigma_{\text{CRPropa}}(\epsilon'_i)/\Sigma_i\sigma_{\text{PSB}}(\epsilon'_i)$ and the other way around) are shown. The color scale, indicating the value of the two summed cross sections divided by each other, is limited to a maximum of 2.4 in both cases to be able to get a feeling for the differences over the whole range.

Fig. 3.5(a) shows the summed CRPropa cross section divided by the summed PSB cross section ($\Sigma_i\sigma_{\text{CRPropa}}(\epsilon'_i)/\Sigma_i\sigma_{\text{PSB}}(\epsilon'_i)$) whereas Fig. 3.5(a) shows the summed PSB cross section divided by the summed CRPropa cross section ($\Sigma_i\sigma_{\text{PSB}}(\epsilon'_i)/\Sigma_i\sigma_{\text{CRPropa}}(\epsilon'_i)$) for each energy bin and mass number where, in all cases, the sums are from the first energy bin until the shown energy bin. The results are only shown when both $\Sigma_i\sigma_{\text{PSB}}(\epsilon'_i) > 0$ and $\Sigma_i\sigma_{\text{CRPropa}}(\epsilon'_i) > 0$.

From these figures it can again be seen that there are large differences at the lower energies, but that these differences are reduced, in most cases, when the sum over a significant number of energy bins is taken. Exceptions to this are, however, the nuclei with $A \leq 9$, where the ratio increases for larger energies. This is due to the CRPropa given significant cross section values up to higher energies, while the PSB cross sections approach $\sigma_{\text{PSB}}(\epsilon'_i) \to 0$, as discussed in the previous section (see e.g. Fig. 3.2(a)).

There are still a few outliers, however, which show larger differences than the other cross sections. One of these is again ^{28}Si, as was noted in the previous section. See Fig. 3.2(c) for the cross sections of this nucleus.

In Fig. 3.5(c), for a clearer comparison, the ratios between the total sums over the whole energy range are shown for all mass numbers. From this plot it can be seen that the difference in total summed cross section is never larger than a factor of two.

3.3.4 Mean free paths

Not the cross sections directly, but the mean free paths are looked at in the code to determine which interaction takes place (see Sec. 2.4.2.2 and Eq. 2.17). So here it is investigated what effects the differences in cross section have on the mean free paths of the different nuclei. In Fig. 3.6 the mean free paths are given for both photodisintegration setups and for the same nuclei as for which the cross sections were given in Fig. 3.2. The mean free paths were calculated with Eq. 2.17 for interactions with both the cosmic microwave background (CMB) and the default UV/optical/IR background (IRB) in CRPropa (the 'best-fit model' of Ref. [272]).

Fig. 3.6(a) shows the mean free paths for ^{9}Be (the cross sections for this nucleus are

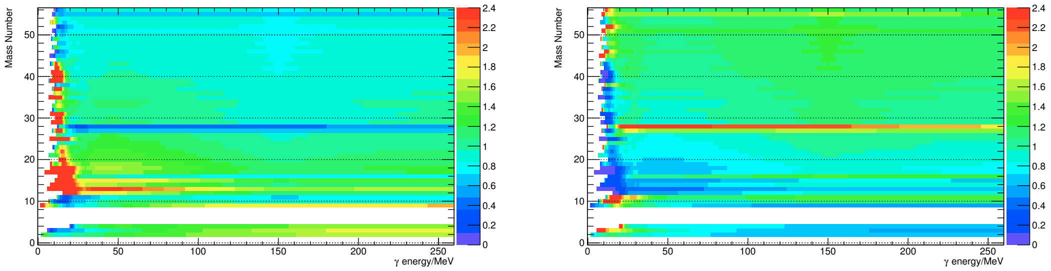

(a) $\Sigma_i \sigma_{\mathrm{CRPropa}}(\epsilon_i')/\Sigma_i \sigma_{\mathrm{PSB}}(\epsilon_i')$ (b) $\Sigma_i \sigma_{\mathrm{PSB}}(\epsilon_i')/\Sigma_i \sigma_{\mathrm{CRPropa}}(\epsilon_i')$

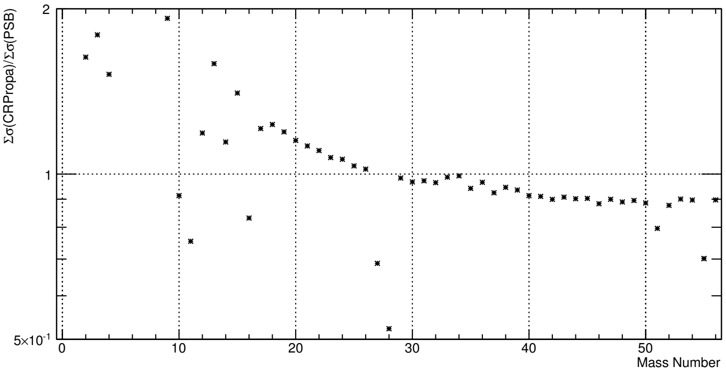

(c) Total sum

Figure 3.5: Summed all-channel cross-section comparison between the PSB setup and the standard CRPropa setup for all mass numbers A. The results are only shown when both $\Sigma_i \sigma_{\mathrm{PSB}}(\epsilon_i') > 0$ and $\Sigma_i \sigma_{\mathrm{CRPropa}}(\epsilon_i') > 0$. The color scale, indicating the value of the two summed cross sections divided by each other, is limited to a maximum of 2.4.

(a) The top left panel shows the summed CRPropa cross section divided by the summed PSB cross section for each energy bin and mass number.

(b) The top right panel shows the summed PSB cross section divided by the summed CRPropa cross section for each energy bin and mass number.

(c) The bottom panel gives, for easier comparison, the values for the total summed cross sections divided by each other.

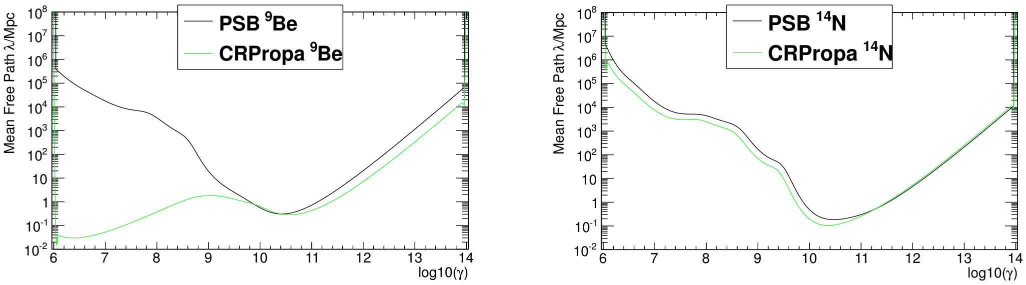

(a) ^{9}Be (b) ^{14}N

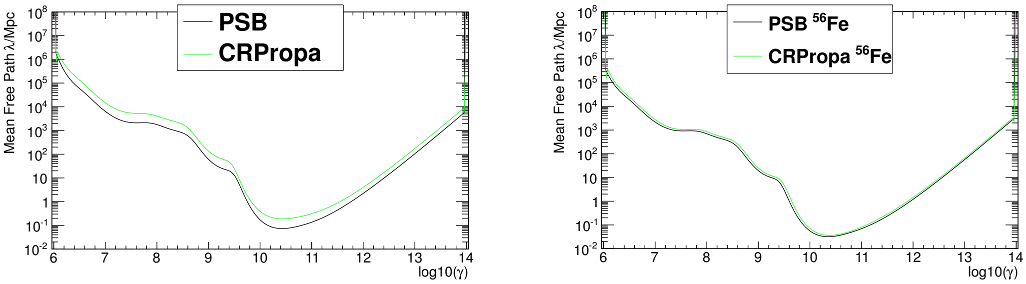

(c) ^{28}Si (d) ^{56}Fe

Figure 3.6: Mean free path comparison between the PSB setup (in black) and the standard CRPropa setup (in green).
(a) The top-left panel shows the mean free paths for ^{9}Be.
(b) The top-right panel shows the mean free paths for ^{14}N.
(c) The bottom-left panel shows the mean free paths for ^{28}Si.
(d) The bottom-right panel shows the mean free paths for ^{56}Fe.

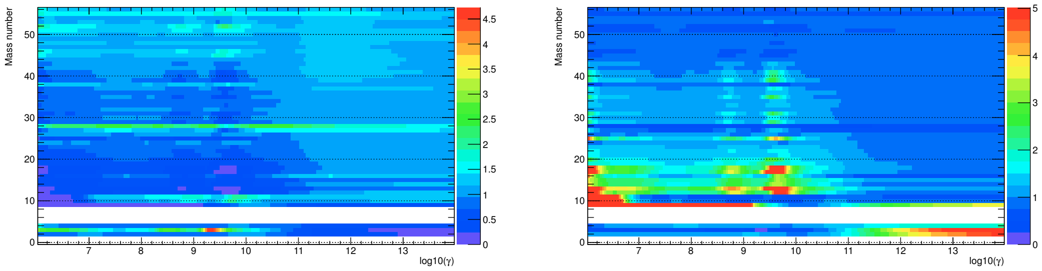

(a) $\lambda_{\text{CRPropa}}/\lambda_{\text{PSB}}$

(b) $\lambda_{\text{PSB}}/\lambda_{\text{CRPropa}}$

Figure 3.7: Mean free path comparisons between the PSB setup and the standard CRPropa setup for all mass numbers A.
(a) The left panel shows the CRPropa mean free path divided by the PSB mean free path for each mass number. The color scale, indicating the value of $\lambda_{\text{CRPropa}}/\lambda_{\text{PSB}}$, is limited to a maximum of 4.6.
(b) The right panel shows the PSB mean free path divided by the CRPropa mean free path for each mass number. The color scale, indicating the value of $\lambda_{\text{PSB}}/\lambda_{\text{CRPropa}}$, is limited to a maximum of 5.

given in Fig. 3.2(a)), one of the nuclei in the PSB case with large Δ so that the 30 MeV cut-off formalism was not employed (see also Sec. 3.2) and which has a significant difference in energy threshold ϵ'_{min} between the two different cross section implementations (see Fig. 3.4). The fact that the CRPropa case continuous to higher energies, while the PSB cross section approaches zero, can be seen in the differences at $\log_{10}(\Gamma) \gtrsim 10.6$. The difference in energy threshold causes the differences at $\log_{10}(\Gamma) \lesssim 9.6$. This investigation led, before the release of CRPropa 2.0, to the increase of ϵ'_{min} in the standard CRPropa setup for, amongst others, this nucleus.

In Fig. 3.6(b) it concerns again the nucleus ^{14}N, as in Fig. 3.1 and Fig. 3.2(b). The different position and peak value of the one-nucleon photodisintegration case, shown in Fig. 3.1(a), is the main reason behind the lower mean free path for the CRPropa case at $\log_{10}(\Gamma) \lesssim 11$.

Fig. 3.6(c) shows the mean free paths for ^{28}Si (the cross sections for the same nucleus are shown in Fig. 3.2(c)). Together with ^{9}Be (Fig. 3.6(a)), this nucleus shows the largest relative difference between the total summed cross sections of the standard CRPropa setup and the PSB setup (as can be seen from Fig. 3.5(c)). The mean free path of ^{28}Si shows a clear difference between the PSB case and the CRPropa case over the whole energy range.

Finally, Fig. 3.6(d) shows the mean free paths of both setups for ^{56}Fe. For this scenario the two cross section models agree rather well, as can be seen from Fig. 3.2(d), and this figure shows that the mean free paths agree nicely as well.

To again give a full overview of the relative differences for all mass numbers available in the PSB chain, Fig. 3.7 shows the mean free paths of both setups divided by each other for all mass numbers. Fig. 3.7(a) gives the CRPropa mean free path divided by the PSB mean free path ($\lambda_{\text{CRPropa}}/\lambda_{\text{PSB}}$) while Fig. 3.7(b) shows the PSB mean free paths divided by the CRPropa mean free paths ($\lambda_{\text{PSB}}/\lambda_{\text{CRPropa}}$). The color scale, indicating the value of the two mean free paths divided by each other, is limited to a maximum of 4.6 for $\lambda_{\text{CRPropa}}/\lambda_{\text{PSB}}$ and 5 for $\lambda_{\text{PSB}}/\lambda_{\text{CRPropa}}$ to be able to get a feeling for the differences over the whole range.

The differences at the lower energies, noted in the previous sections, are again clearly visible, as well as the differences at the higher energies for $A \leq 9$ and the outliers as, for example, ^{28}Si.

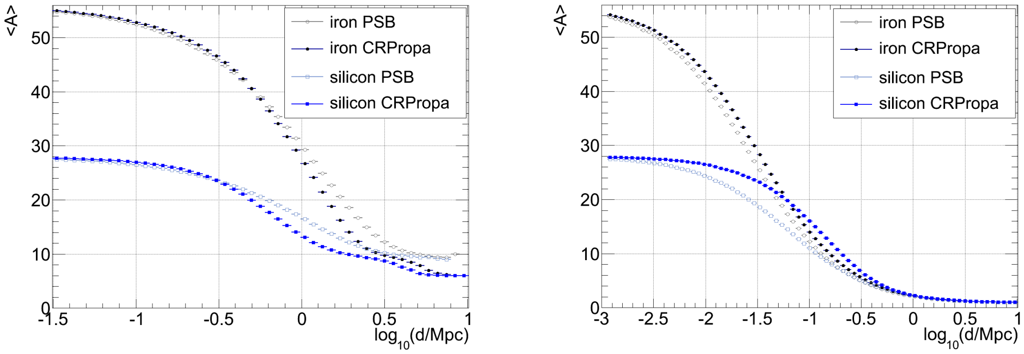

(a) Primary cosmic rays (b) Cosmic rays including secondaries

Figure 3.8: Average nuclear mass number $\langle A \rangle$ as a function of the distance from the source, resulting from the CRPropa photodisintegration cross-section tables (see Sec. 2.4.2) (solid markers) and the PSB cross section tables [8, 9] (open markers). These figures are adopted from Ref. [1]). These 1D simulations assume pure-iron (black circles) and pure-silicon (blue rectangles) injection at the source with an injection rigidity of $R = 38.4$ EeV. Pair production, pion production and redshift evolution have been disabled, photodisintegration is considered on the CMB only and the cosmic rays are tracked as long as their energy is above 0.1 EeV. In the PSB case, decay has been disabled in order to strictly follow the reduced reaction network of Ref. [8].
(a) Average mass number of the primary cosmic rays, disregarding all nuclei with $A < 5$.
(b) Average mass number of all cosmic rays, including hadronic secondaries.

3.3.5 Average mass number after propagation

To investigate the effect of these two different photodisintegration setups on actual observables, the results of CRPropa simulations using each of these photodisintegration setups can be compared with each other. As photodisintegration has the most direct effect on the nuclear mass number of the cosmic rays, the average mass number $\langle A \rangle$ as a function of the distance from the source for both cross section scenarios are here compared with each other. Here the updated cross-section tables as distributed with the release of CRPropa 2.0 with increased ϵ'_{min} for several nuclei are used.

Fig. 3.8 (adopted from Ref. [1]) shows the results of example 1D simulations comparing the standard CRPropa photodisintegration setup (Sec. 2.4.2) and the PSB photodisintegration setup [8, 9]. Here the average mass number $\langle A \rangle$ of UHECRs as a function of the distance from the source is indicated for the two cross-section models under consideration. Two different composition scenarios at the source, namely pure-iron and pure-silicon injection, with the same rigidity ($R = 38.4$ EeV, corresponding to injection energies of $E =$1000 EeV and 538 EeV, respectively) at the source, are considered. In these simulations pair production, pion production and redshift evolution have been disabled, photodisintegration is considered on the CMB only and the cosmic rays are tracked as long as their energy is above 0.1 EeV. In the PSB case, decay has been disabled in order to strictly follow the reduced reaction network of Ref. [8].

Fig. 3.8(a) shows the results considering only the primary cosmic ray. To do this, all nuclei (also the primary nuclei) with $A < 5$ have been ignored. As the heaviest secondary particle that can possibly be produced in either the PSB or the standard CRPropa photodisintegration setup is ^{4}He, this disregards all secondaries that can possibly be produced. These results can be compared with, for instance, Fig. 5 of Ref. [200].

As noted in Ref. [200], the PSB agreement with experimental data is not as good as the one obtained with the Lorentzian parameterization of TALYS. Moreover, the PSB case employs a reduced reaction network involving only one nucleus for each atomic mass number A up to ^{56}Fe, whereas 287 different nuclides with their photodisintegration cross sections have been implemented in CRPropa. Fig. 3.8(a) shows the effect of these differences on the average mass of the primary particle. In particular it can be seen that the standard photodisintegration setup of CRPRopa results, on average, in a faster photodisintegration rate for $A \lesssim 40$ than the PSB photodisintegration setup does.

Note furthermore that the PSB photodisintegration setup converges to $\langle A \rangle = 9$, whereas in the standard CRPropa cases the results converge to $\langle A \rangle = 6$. This is due to the fact that there is no photodisintegration data available in the PSB case for $A = [5...8]$. If a particle ends up in this regime, it is assumed to photodisintegrate or decay immediately to $A = 4$ plus secondaries (which are ignored in this scenario). If ^{9}Be photodisintegrates it is assumed to go through the following process: $^9\text{Be}+\gamma \rightarrow n+2{\cdot}^4\text{He}$, leaving only particles with $A \leq 4$. The standard CRPropa cases converge to $\langle A \rangle = 6$ as there are no stable particle with $A = 5$.

Fig. 3.8(b) gives the full results including all secondary cosmic rays produced during photodisintegration reactions. Due to the light secondary particles that are produced with each photodisintegration of the primary particle the average mass number decreases faster in this scenario than in Fig. 3.8(a). This shows the importance of taking secondary particles into account when predicting the average mass number.

A noticeable feature in Fig. 3.8(b) is that, for the standard CRPropa case, after a certain propagation length the average mass number of silicon injection exceeds the average mass number of iron injection. This is due to the larger number of light secondaries disintegrated off the iron nucleus. This, in combination with the cross section dependence on the mass number, can cause a lower total *average* mass at a certain distance, even though the primary cosmic ray still has, on average, a higher mass.

Furthermore, in this scenario both iron and silicon injection show, at all distances, an average mass for the CRPropa tables larger or equal to the average mass for the PSB tables. This can be traced back to a difference in the type of secondaries that are created. In the standard CRPropa setup, photodisintegration can yield secondaries with mass number up to four (n, p, d, t, ^{3}He and ^{4}He). In the PSB case all secondaries, with the exception of the reaction $^9\text{Be}+\gamma \rightarrow n + 2{\cdot}^4\text{He}$, where one of the helium nuclei can be considered as a secondary, have a mass number of one, therefore decreasing the average mass number with respect to the CRPropa case.

Chapter 4

IceCube neutrinos

As discussed in Sec. 1.2.4, the IceCube Collaboration recently reported the observation of multiple neutrino events with energies between 30 TeV and 2 PeV [41]. The best-fit E^{-2} astrophysical spectrum with a per-flavor normalization $(1 : 1 : 1)$ to these events suggests a flux level of $E_\nu^2 \mathrm{d}\Phi_\nu/\mathrm{d}E = 10^{-8}$ GeV $\mathrm{cm}^{-2}\mathrm{s}^{-1}\mathrm{sr}^{-1}$ in the 100 TeV - PeV range.

Possible sources for the origin of these neutrinos include astrophysical neutrinos produced by photopion or proton-proton interactions of accelerated protons with ambient radiation or matter in sources such as gamma-ray bursts (GRBs), active galactic nuclei (AGNs) or starburst galaxies. These astrophysical source scenarios may produce the required flux. However, another possible source scenario is that these neutrinos are produced during the propagation of ultra-high-energy cosmic rays (UHECRs) through the extragalactic radiation backgrounds, so-called cosmogenic neutrinos. Here we investigate whether the neutrinos recently observed by IceCube with energies between 30 TeV and 2 PeV [41] could have originated as cosmogenic neutrinos.

Neutrinos can be produced during the propagation of UHECRs through the intergalactic medium (IGM) in several different ways. When UHECRs traverse the universe they interact with extragalactic background light like the cosmic microwave background (CMB) and the UV/optical/IR background (IRB). One possible interaction with the CMB or IRB is photopion production. In this case the process

$$p + \gamma \rightarrow n + \pi^+ \tag{4.1}$$

will produce neutrinos [239] from the decay of the neutron as well as from pion decay. When the UHECRs are nuclei instead of protons, these nuclei can be photodisintegrated by photons from the CMB or IRB. In this way single neutrons can be separated from the nuclei, which will again decay and produce neutrinos. The nuclei themselves could also become unstable in this way and emit neutrinos in their decay.

To simulate these interactions during the propagation of UHECRs and the production of the secondary neutrinos and gamma rays, we used CRPropa 2.0 (see Chapter 2 and Refs. [1, 43]). CRPropa includes all relevant interactions (pair production, pion production, photodisintegration and decay) as well as cosmological and source evolution and redshift scaling of the background light intensity in one dimensional (1D) simulations. This chapter is based on Ref. [45], done in collaboration with Günter Sigl, Silvia Mollerach and Esteban Roulet, and Ref. [46] done in collaboration with Günter Sigl.

4.1 Neutrino fluxes from UHECR protons on the CMB

Extragalactic UHECR protons with energies above 6×10^{19} eV get attenuated predominantly by pion production processes when propagating through the CMB, which leads to the well-known expected GZK suppression [76, 77]. These losses reach a maximum strength at the $\Delta(1232)$ resonance, i.e. when $m_\Delta^2 \simeq m_p^2 + 2E_pE_\gamma(1-\cos\theta)$, with m_Δ the delta-resonance mass, m_p the proton mass, E_p the proton energy, E_γ the photon energy and θ the angle between the proton (p) and photon (γ) momenta in the lab frame. For $\theta = \pi$ this corresponds to a proton energy of $E_p(\Delta) \simeq 1.6 \times 10^{20}$ eV$/(E_\gamma/10^{-3}$eV), with the average CMB photon energy being $\approx 0.7 \times 10^{-3}$ eV at present (see Ref. [305] for a comprehensive review).

The pion production process (Eq. 4.1) will produce cosmogenic neutrinos through the decay of the neutron $n \to p + e^- + \overline{\nu}_e$ as well as through pion decay $\pi^+ \to \mu^+ + \nu_\mu \to e^+ + \nu_e + \overline{\nu}_\mu + \nu_\mu$ [243]. Since the pions typically carry about 1/5th of the proton energy, each neutrino from the pion decay has on average an energy of about $E_\nu^\pi \simeq E_p/20$. On the other hand, the $\overline{\nu}_e$ from the neutron decay has a typical energy of $E_\nu^n \simeq 4 \times 10^{-4} E_n \simeq 3 \times 10^{-4} E_p$.

As the CMB temperature scales as $(1+z)$, with z being the redshift, the proton energies for which the photopion production starts to be efficient are $E_p \simeq E_{\rm GZK}/(1+z)$ with $E_{\rm GZK} = 10^{20}$ eV the typical proton energy for pion production at present ($z = 0$). Note also that the CMB photon density increases as $(1+z)^3$, making the opacity of the universe to ultra-high-energy (UHE) protons correspondingly higher. The energy of a neutrino produced at high redshift gets further reduced by adiabatic losses as it propagates towards us, leading to $E_\nu^\pi \simeq E_{\rm GZK}/(20(1+z)^2)$ for a neutrino originating from pion decays, and $E_\nu^n \simeq 3 \times 10^{-4} E_{\rm GZK}/(1+z)^2$ for a neutrino from neutron decay.

The neutrino production is sizeable up to redshifts of 3-5 [243], depending on the actual source redshift evolution. Considering a typical neutrino production redshift of $z \simeq 1.2$ one gets peaks in the neutrino spectrum resulting from interactions with the CMB at an energy of $\approx 10^{18}$ eV from pion decay and at $\approx 6 \times 10^{15}$ eV from neutron decay. Wide peaks around these energies are expected as the Δ resonance is wide, other pion production channels contribute as well, the CMB photons have a wide thermal spectrum and different redshifts contribute to the neutrino production.

A useful relation can be obtained between the two neutrino fluxes just considered, since from the interaction $p + \gamma \to n + \pi^+$ the same number of $\overline{\nu}_e$ at $E_\nu^n \simeq 3 \times 10^{-4} E_{\rm GZK}/(1+z)^2$ and ν_e, $\overline{\nu}_\mu$ or ν_μ at $E_\nu^\pi \simeq E_{\rm GZK}/(20(1+z)^2)$ are produced. As $E_\nu^n \simeq 6 \times 10^{-3} E_\nu^\pi$ one has, for the fluxes produced in interactions with the CMB alone, that

$$\left[\frac{{\rm d}\Phi_{\overline{\nu}_e}}{{\rm d}\log E}\right]^{n,{\rm CMB}}_{(E^n_{\overline{\nu}_e}=6\times10^{15}{\rm eV})} \simeq \left[\frac{{\rm d}\Phi_{\nu_\mu}}{{\rm d}\log E}\right]^{\pi,{\rm CMB}}_{(E^\pi_{\nu_\mu}=10^{18}{\rm eV})}, \tag{4.2}$$

with Φ_ν the resulting neutrino diffuse fluxes.

Rewriting this so that it is easier to compare with the measured flux level gives

$$\left[E_\nu^2\frac{{\rm d}\Phi_{\overline{\nu}_e}}{{\rm d}E}\right]^{n,{\rm CMB}}_{(E^n_{\overline{\nu}_e}=6\times10^{15}{\rm eV})} \simeq 6\times10^{-3}\left[E_\nu^2\frac{{\rm d}\Phi_{\nu_\mu}}{{\rm d}E}\right]^{\pi,{\rm CMB}}_{(E^\pi_{\nu_\mu}=10^{18}{\rm eV})}. \tag{4.3}$$

Furthermore, as not only a ν_μ is produced in the pion decay, but also a ν_e and a $\overline{\nu}_\mu$, ignoring the effects of the neutrino oscillations on the $\overline{\nu}_e$ for the time being,

$$\left[E_\nu^2\frac{{\rm d}\Phi_{\overline{\nu}_e}}{{\rm d}E}\right]^{n,{\rm CMB}}_{(E^n_{\overline{\nu}_e}=6\times10^{15}{\rm eV})} \simeq 2\times10^{-3}\left[E_\nu^2\frac{{\rm d}\Phi_{{\rm all}\,\nu}}{{\rm d}E}\right]^{\pi,{\rm CMB}}_{(E^\pi_{\nu}=10^{18}{\rm eV})}. \tag{4.4}$$

As the EeV neutrinos are dominated by those produced in interactions with the CMB (see below), the following equation holds as well:

$$\left[E_\nu^2 \frac{\mathrm{d}\Phi_{\overline{\nu}_e}}{\mathrm{d}E}\right]^{n,\mathrm{CMB}}_{(E^n_{\overline{\nu}_e}=6\times 10^{15}\mathrm{eV})} \simeq 2\times 10^{-3}\left[E_\nu^2 \frac{\mathrm{d}\Phi_{\mathrm{all}\ \nu}}{\mathrm{d}E}\right]_{(E^\pi_\nu=10^{18}\mathrm{eV})} . \tag{4.5}$$

The all-flavor diffuse neutrino flux has been constrained at EeV energies by the unsuccessful searches by IceCube [306] and Auger [34], which implies the approximate bound of $E_\nu^2 \mathrm{d}\Phi_\nu/\mathrm{d}E < 2\times 10^{-7}$ GeV $\mathrm{cm}^{-2}\mathrm{s}^{-1}\mathrm{sr}^{-1}$ at EeV energies. Furthermore, for pure-proton scenarios a stronger bound has been obtained indirectly from the so-called cascade decays [264]. This bound is derived from the requirement that the photons from the π^0 decay (the π^0 is produced in the pion-production process $p+\gamma \to p+\pi^0$) and the e^+e^- pairs do not produce too large amounts of GeV-TeV photons when they cascade down to low energies as they interact with the CMB and IRB. The allowed amount of low-energy photons is bounded by the diffuse photon background measured by the Fermi LAT experiment [132]. The cascade limit which results for the all-flavor cosmogenic neutrino flux at EeV energies is at the level of $E_\nu^2 \mathrm{d}\Phi_\nu/\mathrm{d}E < 5\times 10^{-8}$ GeV $\mathrm{cm}^{-2}\mathrm{s}^{-1}\mathrm{sr}^{-1}$ [256, 257]. This, together with Eq. 4.5, implies that the $\overline{\nu}_e$ flux at PeV energies produced from interactions with the CMB photons should satisfy $E_\nu^2 \mathrm{d}\Phi_{\overline{\nu}_e}/\mathrm{d}E < 10^{-10}$ GeV $\mathrm{cm}^{-2}\mathrm{s}^{-1}\mathrm{sr}^{-1}$. This upper bound is about two orders of magnitude below the flux level suggested by the observed events reported by the IceCube collaboration, and hence can hardly be responsible for those events (this is at variance with the interpretation suggested in Ref. [240]).

4.2 Total neutrino fluxes from UHECR protons

Cosmic ray protons with energies below 6×10^{19} eV at $z=0$ loose energy mainly by e^+e^- pair production interactions with the CMB, without producing neutrinos. However, below $\approx 10^{18}$ eV the dominant attenuation process becomes photopion production in interactions with the IRB. As the IRB photons are more energetic than the CMB photons, this leads to a reduced proton energy to produce the Δ resonance of $E_p(\Delta) \simeq 1.6\times 10^{17}$ eV$/(E_\gamma/\mathrm{eV})$. In this case, as $E^\pi_\nu \simeq E_p/20$ and as the energies of neutrinos produced at high redshift get reduced by adiabatic losses as they propagate, neutrinos produced by pion decays have energies of $E^\pi_\nu \approx 8\times 10^{15}$ eV$/[(1+z)(E_\gamma/\mathrm{eV})]$, and hence can contribute in the PeV range. On the other hand, the neutrinos from the corresponding neutron decays will be at energies of around $E^n_\nu \approx 4.8\times 10^{13}$ eV$/[(1+z)(E_\gamma/\mathrm{eV})]$ and are hence currently undetectable below the atmospheric neutrino background.

The PeV neutrino fluxes from UHE proton scenarios are indeed dominated by those from pion decays produced in interaction with IRB photons. Numerical simulations show that all-flavor neutrino flux levels of $E_\nu^2 \mathrm{d}\Phi_\nu/\mathrm{d}E \simeq$ few $\times 10^{-9}$ GeV $\mathrm{cm}^{-2}\mathrm{s}^{-1}\mathrm{sr}^{-1}$ can be achieved for $E_\nu \simeq$ PeV, see e.g. Refs. [194, 250, 253, 255]. The precise value of the flux level depends on the assumed source evolution, the adopted IRB and the shape of the extragalactic proton spectrum at the source.

To illustrate this, Fig. 4.1 shows the UHECR and neutrino fluxes obtained by simulating the propagation of UHECR protons from their sources to the observer with CRPropa 2.0. As for all figures we use 1D simulations including pair production, pion production and all relevant decay channels. Furthermore, cosmological and source evolution as well as redshift scaling of the background light intensity are included. The IRB considered, including its redshift evolution, is the 'best-fit model' of Ref. [272]. For this scenario a source power spectrum of $\mathrm{d}N/\mathrm{d}E_0 \propto E_0^{-\alpha}$ with $\alpha = 2.4$ up to a maximum energy of 200 EeV and down to a minimum energy of 2×10^{16} eV was adopted. A continuous source density following a redshift evolution (for the density times CR emissivity) according to the gamma-ray burst evolution has been adopted. This source evolution corresponds to the SFR6 model derived in Ref. [307] and is here referred to as GRB2.

In this so-called 'dip' scenario the ankle results from the pair production interactions off the CMB. For the UHECR spectrum to resemble the measured spectrum in this scenario, the spectral slope at the sources should be close to $\alpha = 2.4$ for the GRB2 source evolution considered here, and could even be harder ($\alpha \simeq 2.2$) for a stronger source evolution such as that following the evolution of the Faranoff Riley AGNs (see the AGN evolution model from Ref. [308], named FRII). Note that, for a given source evolution, steepening the spectral slope at the sources could lead to an enhanced PeV neutrino flux, but would affect the resulting UHECR flux causing it to no longer match the match the observed one. Regarding the maximum energy at the sources, increasing it would have the effect of slightly modifying the details of the CR GZK suppression and extending the EeV neutrino peak to slightly higher energies, but will have little impact on the PeV neutrino fluxes.

The PeV neutrino flavors produced in these scenarios arising from pion decays, are in the ratios $(\nu_e : \nu_\mu : \nu_\tau) = (1 : 1 : 0)$ and $(\overline{\nu}_e : \overline{\nu}_\mu : \overline{\nu}_\tau) = (0 : 1 : 0)$. These ratios will then be affected by the incoherent flavor oscillations that take place from their production until their detection on Earth. For instance, if one adopts the tri-bi maximal (TBM) neutrino mixing pattern, these fluxes get transformed into $(0.78 : 0.61 : 0.61)$ and $(0.22 : 0.39 : 0.39)$ upon detection [309]. Departures from the TBM mixing predictions, as required by the recent measurement of a non-vanishing θ_{13} [310], will induce small shifts on the above mentioned flavor ratios.

Fig. 4.1(a) is adopted from Ref. [45] and for this scenario CRPropa 2.0.2 was used. In this figure, besides the total fluxes, the contributions resulting from the interactions with CMB photons and the part of the flux that comes from antineutrinos of n-decays alone are shown separately. The resulting UHECR spectrum is normalized at 10 EeV to that measured by the Pierre Auger Collaboration [297] as presented during the International Cosmic Ray Conference (ICRC) 2011 [298] (which has a 22% systematic uncertainty on the energy scale, not shown in this plot). The all-flavor neutrino spectra have been normalized accordingly. The overall shape of the UHECR spectrum is found to be in reasonable agreement with the measured one. The spectrum measured by the HiRes Collaboration [10], the bounds on the all-flavor neutrino fluxes obtained by IceCube [299], Auger [300] and ANITA [301] and the approximate flux level indicated the first two events measured by IceCube [39] are displayed as well.

Fig. 4.1(b) is adopted from Ref. [46] and shows a similar simulation to the one of Fig. 4.1(a). Compared with Fig. 4.1(b) the Pierre Auger UHECR spectrum [34] (which in this case has a 14% systematic uncertainty on the energy scale, not shown in the figures), Pierre Auger neutrino limit [34], IceCube neutrino flux level [41] and IceCube neutrino limit [306] have been updated. Furthermore, for these simulations an updated version of CRPropa 2.0 (CRPropa v2.0.4) was used, which includes an improved energy interpolation for the pion production as well as some bug fixes. All other simulation parameters are the same as in Fig. 4.1(a).

It is clear that, in these scenarios, the simulated neutrino fluxes remain far below the neutrino bounds as well as from the IceCube flux levels. The relation obtained in Eq. 4.5 can be seen to hold from Fig. 4.1(a) by comparing the height of the EeV all-

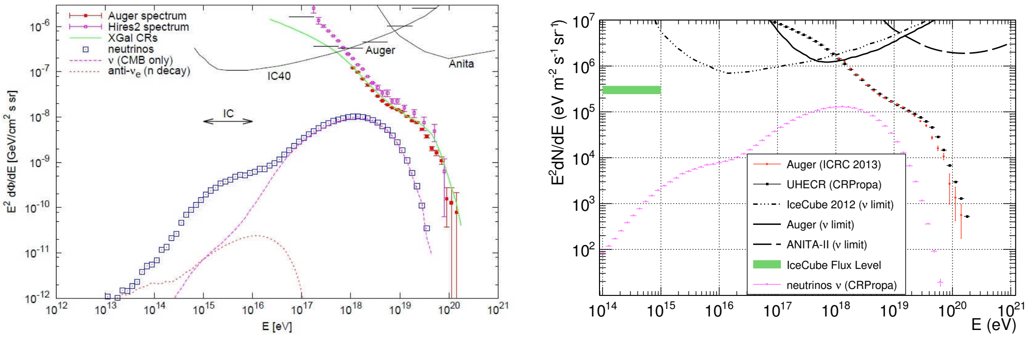

(a) CRPropa 2.0.2 (b) CRPropa 2.0.4

Figure 4.1: Pure-proton 'dip' scenario with a spectral index at injection of $\alpha = 2.4$ and a maximum energy of $E_{\max} = 200$ EeV. The GRB2 source evolution model has been implemented.
(a) In the left panel (adopted from Ref. [45]) in red points the measured Auger UHECR spectrum [297, 298] and in magenta points the HiRes UHECR spectrum [10] are shown, while the propagated proton spectrum (using CRPropa 2.0.2) is indicated as green straight line. The blue squares show the simulated all-flavor neutrino flux. The neutrino backgrounds due to interactions with the CMB alone (magenta dashed line) and the one resulting from n decay (red dotted line) are shown separately as well. The black lines show the bounds on the all-flavor neutrino flux by IceCube [299], Auger [300] and ANITA [301]. The approximate IceCube flux level indicated by the first two events detected by IceCube [39] is given as a two-sided arrow.
(b) In the right panel (adopted from Ref. [46]) in red points the updated Auger UHECR spectrum [34] is shown, while in black points the simulated UHECR spectrum (using CRPropa 2.0.4) is given. The magenta points show the simulated neutrino flux. The lines show the updated bounds on the all-flavor neutrino flux by IceCube (dashed dotted) [306] and Auger (straight) [34] as well as the same bounds as in the left panel from ANITA (dashed) [301]. The green area indicates the updated flux level of the IceCube events [41].

flavor peak with the height of the PeV peak from n-decays. No significant differences in either the UHECR or neutrino spectrum between Fig. 4.1(a) and Fig. 4.1(b) are visible. Note that the PeV neutrino flux is sensitive to the amount of UV photons, so scenarios with an enhanced UV background, as considered is Refs. [194, 255], can lead to some enhancement in PeV neutrino fluxes.

4.3 Cascade photon fluxes from UHECR protons

In addition to neutrinos, photons will be produced in the different interactions of UHECRs with the CMB and IRB as well. In Fig. 4.2 these cascade photons, originating from UHECR interactions, are shown together with the neutrino and proton spectra. Furthermore, for comparison, the diffuse gamma-ray flux level observed by Fermi LAT [132] is given.

In Fig. 4.2(a) (adopted from Ref. [45] and using CRPropa 2.0.2) the predicted proton spectra, the all-flavor neutrino fluxes as well as the cascade photons for three different source evolution models are shown. These models follow the star formation rate (SFR1 from Ref. [307]), the GRB2 model considered in Fig. 4.1, and the FRII evolution model. In the case with the FRII source evolution, instead of $\alpha = 2.4$ for the SFR1 and the GRB2 models, a spectral index of $\alpha = 2.2$ at the sources was set, as this, for this scenario, produces a closer resemblance to the measured UHECR spectrum. All other parameters have remained the same.

In Fig. 4.2(b) (adopted from Ref. [46] and using CRPropa 2.0.4) the same spectra, bounds and neutrino flux level are shown as in Fig. 4.1(b). However, in this case the cascade photons and Fermi LAT diffuse gamma-ray flux measurement are included as well. In Fig. 4.2(c) (using CRPropa 2.0.4 as well) the same spectra and bounds are shown again, however now for the FRII source evolution model with $\alpha = 2.2$ (to provide a closer resemblance of the simulated UHECR spectrum to the Auger UHECR spectrum). Furthermore, the approximate neutrino flux level is replaced by the measured neutrino flux from Ref. [41].

The neutrino flux is expected to increase when, instead of the GRB2 source evolution, a stronger source evolution, as for instance the FRII evolution model, is implemented. This is confirmed by the simulation results in Fig. 4.2(a) and Fig. 4.2(c). However, as visible from both these figures, not only the neutrino flux but the photon flux increases with a stronger source evolution as well. Whereas the simulated neutrino flux is still far below the IceCube flux level, the gamma-ray flux is on the verge of conflicting with the diffuse gamma-ray flux level observed by Fermi. Comparing Fig. 4.2(b) and Fig. 4.2(c) with Fig. 4.2(a) shows that no significant changes are visible due to the change from CRPropa 2.0.2 to CRPropa 2.0.4.

One further issue is that the height of the PeV neutrino peak (resulting mostly from interactions of $\approx 10^{17}$ eV protons with IRB photons) and that of the EeV peak (resulting from interactions of $\approx 10^{20}$ eV protons with the CMB photons) are in principle related, depending on the underlying proton spectral shape. Hence, the bounds on the EeV diffuse neutrino fluxes (direct or from cascade decays) may also constrain the allowed maximum height of the PeV neutrino peak. Note, however, that if the proton spectrum above a few tens of EeV is suppressed, for instance due to the existence of a low maximum rigidity in the acceleration process at the sources, the EeV neutrino peak would be suppressed as well, but the PeV peak would not. In this case there would not be any constraint from the associated photon cascades.

Of interest in this respect is the so-called disappointing model [22], which actually

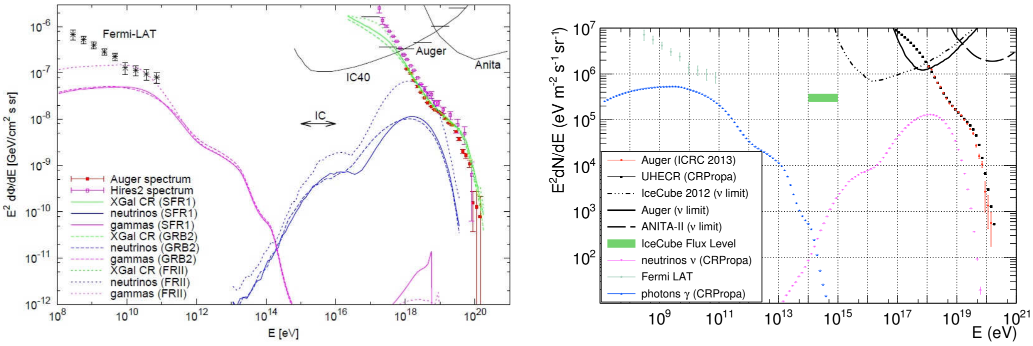

(a) CRPropa 2.0.2

(b) CRPropa 2.0.4, GRB2

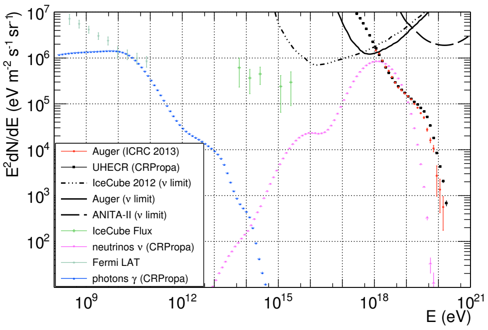

(c) CRPropa 2.0.4, FRII

Figure 4.2: Pure proton 'dip' scenario including secondary photon fluxes with a maximum energy at the sources of $E_{\max} = 200$ EeV.
(a) In the top left panel (adopted from Ref. [45] and using CRPropa 2.0.2) the same Auger spectrum, HiRes spectrum, simulated proton spectrum, simulated neutrino flux, neutrino bounds and approximate neutrino flux level are shown as in Fig. 4.1(a). In addition, the simulated gamma-ray flux originating from UHECR interactions is shown in magenta and the diffuse gamma-ray flux observed by Fermi LAT [132] is given in black crosses. The UHECR spextrum, neutrino flux and gamma-ray flux are provided for three different scenarios, the GRB2 (dashed lines) and SFR1 (straight lines) source evolution models with a source spectral index of $\alpha = 2.4$ and the FRII model with $\alpha = 2.2$.
(b) In the top right panel (adopted from Ref. [46] and using CRPropa 2.0.4) the same simulated proton spectrum and simulated neutrino flux implementing the GRB2 source evolution model and a source spectral index of $\alpha = 2.4$ as well as the same neutrino bounds and approximate neutrino flux level are shown as in Fig. 4.1(b). Furthermore, the resulting gamma-ray flux from UHECR interactions (blue points) as well as the diffuse gamma-ray flux measured by Fermi LAT (green stars) [132] are given.
(c) In the bottom panel the same spectra, bounds and flux level are displayed as in the top right panel. However, in this case the simulated proton spectrum, neutrino flux and gamma-ray flux are for the FRII source evolution model with a source spectral index of $\alpha = 2.2$ (to provide a closer resemblance to the Auger UHECR spectrum). Furthermore, the approximate neutrino flux level is replaced by the measured neutrino flux from Ref. [41] (light-green crosses).

has an enhanced proton flux at EeV energies, with a cut-off at a few EeV, and in this scenario the cosmic rays above the ankle at ≈ 4 EeV are nuclei with increasingly heavier masses. This model would predict an enhanced neutrino flux at PeV energies with no sizeable neutrino peak at EeV energies (see the next two sections).

4.4 Neutrino fluxes from iron nuclei

Scenarios in which heavier nuclei make a significant contribution to the UHECR flux are qualitatively different (see e.g. Refs. [248, 249]) from pure-proton scenarios. In the case of heavier nuclei the photopion production off CMB photons only occurs for energies above $\approx AE_{\rm GZK}$, where A is the mass number of the nucleus. On the other hand, photodisintegration processes play an important role at lower energies. Photodisintegration is dominated by the giant dipole resonance (GDR) which, in the nucleus rest frame, has a threshold for photon energies in the rest frame of the nucleus between a few MeV and 10 MeV (depending on the nucleus), and peaking at about 20 MeV.

The photon energy in the CR rest frame can be expressed as

$$\epsilon' = \frac{E}{Am_p}(1-\beta\cos\theta)\epsilon \simeq 3.8\text{MeV}\left(\frac{56}{A}\right)\left(\frac{E}{10^{20}\text{eV}}\right)\left(\frac{1-\beta\cos\theta}{2}\right)\frac{\epsilon}{10^{-3}\text{eV}}\ , \tag{4.6}$$

where $\beta \equiv \sqrt{1-(m_pA/E)^2}$ is the boost factor and θ is the angle between the CR and photon momenta in the lab frame. When nuclei photodisintegrate, they emit nucleons or small nuclei without changing their Lorentz factor, hence just losing energy because the mass of the leading fragment gets reduced. In this process secondary nucleons and small nuclei are emitted with an energy per emitted nucleon of E/A for energies $E > E_{\rm GDR} \simeq 10^{20}\text{eV} \times A/56$. If the photodisintegration takes place at non-zero redshift instead, the secondary nucleon's final energy will be $E/A(1+z)$, where the contributions arise from $E > E_{\rm GDR}/(1+z)$. About half of these nucleons will be emitted as neutrons, which then decay to produce $\overline{\nu}_e$ with energies $E_\nu \geq (4\times10^{-4})(10^{20}\text{eV}/56)/(1+z)^2 \simeq \text{few}10^{14}$ eV, assuming interactions with the CMB alone). Note that for interactions with the CMB only those neutrinos produced by energetic nuclei at or above the GDR will end up with energies above one PeV. The nuclei of smaller energies may also photodisintegrate by interacting with the IRB, leading to a flux of $\overline{\nu}_e$ of energy below 10^{14} eV, and hence are not relevant here.

A conservative bound on the flux of $\overline{\nu}_e$ produced at PeV energies can be obtained by noting that the secondary nucleons produced by photodisintegration with CMB photons end up, regardless of the primary nucleus mass (as long as its energy was high enough), piled up around a few EeV, and only about half of these were produced as neutrons. Thus, by requiring that the flux of secondary nucleons at the relevant energy lies below the actually measured CR flux, one ends up with

$$\left[E_\nu^2\frac{\mathrm{d}\Phi_{\overline{\nu}_e}}{\mathrm{d}E}\right]^{n\text{-decay}}_{(E_{\overline{\nu}_e}\simeq10^{15}\text{eV})} \simeq 2\times10^{-4}\left[E^2\frac{\mathrm{d}\Phi_{\rm CR}}{\mathrm{d}E}\right]_{(E=2.5\times10^{18}\text{eV})} < 10^{-11}\ \text{GeV cm}^{-2}\text{s}^{-1}\text{sr}^{-1}\ , \tag{4.7}$$

where it was used that the measured CR flux at 2.5 EeV is about $\mathrm{d}\Phi_{\rm CR}/\mathrm{d}E \simeq 7\times10^{-18}/(\text{EeV cm}^2\text{s sr})$ [34]. These bounds may be slightly modified if one considers that the energy of the secondary nucleons could be degraded by pair production processes. At energies of a few EeV, however, this process does not have a large impact. Hence, the $\overline{\nu}_e$ flux produced by decays of neutrons resulting from the photodisintegration of UHECR nuclei is quite suppressed at PeV energies.

On the other hand, neutrinos with PeV energies may be produced by the interactions of extragalactic nuclei with IRB photons by photopion production. This would require that the energy per nucleon is about $\approx 20E_\nu$ so that the nucleus should have an energy of about $20AE_\nu$. Due to that the UHECR source spectrum is expected to be steeper than E^{-2}, the photopion contribution from scenarios dominated by nuclei will not be larger than that arising from the proton dominated scenarios discussed in the previous sections. To clarify with an example, if all CRs had a given mass number A, the number of nucleons per logarithmic energy interval at energy E is related to the corresponding number in a pure-proton scenario with the same spectral slope α by the factor $A^{2-\alpha}$. Furthermore, the direct production of pions from the nucleons bound inside the nuclei is suppressed with respect to that from free nucleons [194]. Thus, nuclei scenarios give rise to PeV neutrinos by photopion production of IRB photons but at a level which is not expected to succeed that achievable in pure-proton scenarios.

Fig. 4.3 shows a scenario with pure-iron injection at the sources to illustrate the predictions from a heavy-composition scenario. The spectral index at the sources is $\alpha = 2.0$ and the maximum energy of iron nuclei is $E_{\max} = 5200$ EeV. This corresponds to a maximum rigidity of $R_{\max} \equiv E_{\max}/Z = 100$ EeV, with Z the charge of the nucleus, equal to $R_{\max}$ in the previous pure-proton scenarios. The implemented source redshift evolution is the GRB2 model.

In Fig. 4.3(a) (adopted from Ref. [45] and using CRPropa 2.0.2) the same spectra, bounds and neutrino-flux level as in Fig. 4.1(a) are shown, but now the simulated spectra represent the pure-iron-injection scenario. In this case the neutrino flux arising from neutron decays alone is shown separately again as well. The bound from Eq. 4.7 can be seen to hold from this figure. The main contribution to the PeV neutrino flux arises from interactions with the IRB photons.

In Fig. 4.3(b) (adopted from Ref. [46] and using CRPropa 2.0.4) the same spectra, bounds and neutrino flux level are shown as in Fig. 4.1(b), but now again the simulated spectra represent the pure-iron-injection scenario. No significant deviation in the simulated spectra is visible between Fig. 4.3(a) and Fig. 4.3(b). In both cases the UHECR spectrum resembles the measured spectrum reasonably well above the ankle ($E > 4$ EeV).

Note that the EeV neutrino peak strongly depends on the assumed maximum iron energy at the sources. Applying lower maximum energies can drastically reduce this peak, which even essentially disappears for $E_{\max} < 1000$ EeV, corresponding to $R <$ 40 EeV. This would not, however, affect the expectations for the PeV neutrinos in a significant way for this iron-injection scenario.

4.5 Neutrino flux based on the "disappointing" model

A lower maximum energy can drastically reduce the neutrino peak at around 10^{18} eV, but is not expected to significantly reduce the PeV neutrino flux. In Fig. 4.4 two mixed-composition scenarios, inspired by the "disappointing" model [22], are shown with proton and iron injected and a relatively low maximum rigidity ($R_{\max} = E_{\max}/Z = 5$ EeV) at the sources. The source spectral index is $\alpha = 2.0$ and the GRB2 source evolution model has been implemented.

In Fig. 4.4(a) (adopted from Ref. [45] and using CRPropa 2.0.2) a relative source abundance of $n_p/n_{\mathrm{Fe}} = 10$ at a given energy below the proton cut-off was implemented. From this figure it is clearly visible that the EeV neutrino peak has been reduced drastically, compared with the pure-proton and pure-iron scenarios, due to the low maximum

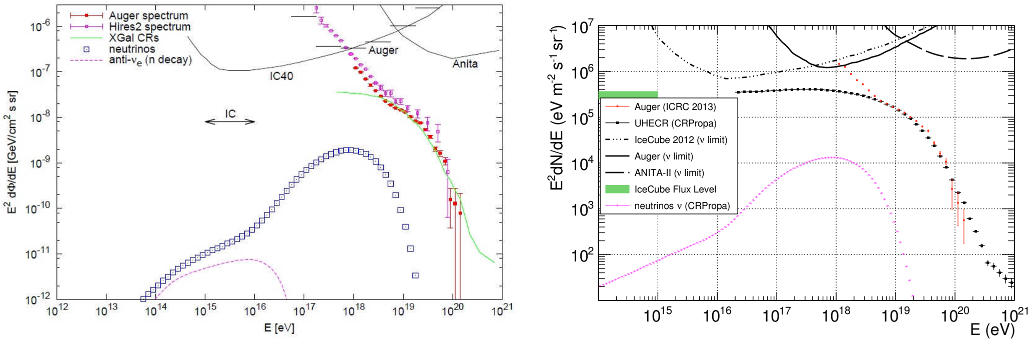

(a) CRPropa 2.0.2 (b) CRPropa 2.0.4

Figure 4.3: Pure-iron-injection scenario with a spectral index at the sources of $\alpha = 2.0$ and a maximum energy of $E_{\max} = 5200$ EeV. The GRB2 source evolution model has been implemented.
(a) In the left panel (adopted from Ref. [45] and using CRPropa 2.0.2) the same spectra, bounds and neutrino flux level are shown as in Fig. 4.1(a), but now for this pure-iron injection scenario.
(b) In the right panel (adopted from Ref. [46] and using CRPropa 2.0.4) the same spectra, bounds and neutrino flux level are given as in Fig. 4.1(b), but now again for this pure-iron injection scenario.

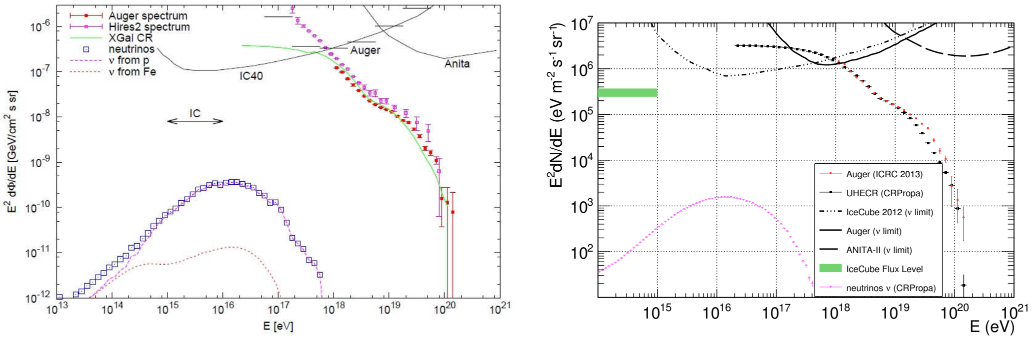

(a) CRPropa 2.0.2 (b) CRPropa 2.0.4

Figure 4.4: Mixed-composition scenario based on the "disappointing" model with proton and iron injected at the sources and a relatively low maximum rigidity ($R_{\max} = E_{\max}/Z = 5$ EeV) at injection. The source spectral index is $\alpha = 2.0$ and the GRB2 source-evolution model has been implemented.
(a) In the left panel (adopted from Ref. [45] and using CRPropa 2.0.2) the same spectra, bounds and neutrino flux level are shown as in Fig. 4.1(a), but now for this mixed-composition scenario. The relative source abundances considered are $n_p/n_{\mathrm{Fe}} = 10$ at a given energy below the proton cut-off. The separate contribution to the neutrino flux from proton primaries (magenta dashed line) and iron primaries (red dotted line) are shown as well.
(b) In the right panel (adopted from Ref. [46] and using CRPropa 2.0.4) the same spectra, bounds and neutrino-flux level are given as in Fig. 4.1(b), but now again for this mixed-composition-injection scenario. Proton and iron were injected at the sources, with a ratio of $n_p/n_{Fe} = 250$ at any given E/A.

energy. Furthermore it can be seen that the enhanced proton contribution below the ankle helps to reach a larger flux of PeV neutrinos with respect to the pure-iron case. In this mixed-composition scenario the UHECR spectrum in the ankle region is similar to the measured one, but it does not fit the highest energies very well. This may however depend on the precise distribution of nearby sources and on the adopted shape of the source cut-off.

In Fig. 4.4(b) (adopted from Ref. [46] and using CRPropa 2.0.4) the ratio between injected proton and iron nuclei is $n_p/n_{Fe} = 250$ at any given energy per nucleon E/A. Comparable spectra to the one of Fig. 4.4(a) are obtained. In this case the shape of the simulated spectrum is in reasonable agreement with the full measured spectrum, while in the pure-iron case it only resembled the spectrum above the ankle.

Note that in scenarios with more than two components, e.g. those in which the average CR mass gradually increases above the ankle, harder injection spectra for each source component are required to fit the observed overall spectrum, and hence will tend to reduce the flux of PeV neutrinos with respect to those found for the proton and iron only mixture.

Chapter 5

CRPropa 3.0

In order to interpret the available experimental data of ultra-high-energy cosmic rays (UHECRs) above 10^{17} eV in the context of realistic concrete astrophysical scenarios, a comprehensive numerical tool that can simulate the deflections and interactions of UHECRs over several orders of magnitude in energy and length scales, ranging from thousands of megaparsecs down to galactic scales of the order of kiloparsecs, is required. Such a tool should be highly modular, as constraining the origin of UHECRs requires simulations predicting energy spectra, compositions and anisotropies, and comparing these with experimental data, for a large number of astrophysical scenarios.

To improve on the possibilities to do this, CRPropa version 3.0 is currently under development. This will be the next major release of the publicly available numerical UHECR-propagation tool CRPropa, see Chapter 2 for details about CRPropa version 2.0. With CRPropa the measured UHECR data, as well as secondary neutrino and photon spectra, can be tested against concrete astrophysical scenarios for the distribution of sources, their injection characteristics such as energy spectrum, maximal energy and mass composition, as well as for the distribution and strength of large-scale cosmic magnetic fields. It includes all relevant interactions such as photodisintegration, photopion production, pair production and nuclear decay as well as deflections using different magnetic-field models and cosmological-evolution effects.

CRPropa 3.0 incorporates a complete redesign of the code structure to facilitate high performance computing. Additionally, it includes new physical features such as an interface for galactic propagation using lensing techniques, and the possibility to do four-dimensional (4D) simulations, which makes it possible to include cosmological effects as well as deflections in magnetic fields in the same simulation. All the features included in CRPropa 2.0, discussed in detail in Chapter 2, are available as well in CRPropa 3.0. This chapter is partially based on Ref. [44], where CRPropa 3.0 was introduced for the first time, and Ref. [4], a recent conference proceeding on CRPropa 3.0. A paper accompanying the release of CRPropa 3.0 is currently being written. CRPropa 3.0 can be obtained from `https://crpropa.desy.de`.

5.1 Code structure

To allow for new use cases and easier testing, maintenance and physics extensions, the propagation of cosmic rays in CRPropa 3.0 is now composed of independent modules which access and modify a cosmic-ray candidate. Due to this modular structure, it has become easier to add new features as well as to use and test all parts of the software individually. The modules correspond to, for example, individual photo-nuclear interactions, boundary conditions, observers, etc. Since there are no direct dependences between modules, any combination of modules can in principle be selected, allowing for multiple use cases and to study in detail individual propagation aspects.

The single interface between the modules is the cosmic-ray candidate class. The simulation modules provide a method to update the cosmic-ray particle according to the module's purpose. These cosmic-ray candidates contain information about all aspects of their propagation: the particle states at different times, a list of created secondary particles and their properties, a list of states for stochastic interactions, a list of arbitrary properties and some module-specific information. All information about the propagation state, including the states of the modules, is stored in the cosmic-ray candidates themselves. In this way modules can process multiple cosmic rays at the same time, which is required for high-performance parallel computing. Cosmic-ray candidates can be created manually or by a modular source-model class, in which source properties such as position, energy spectrum and composition are included. The simulation itself is a user-defined sequence of simulation modules, that are called in turn to update the cosmic-ray candidate until the propagation is completed.

Efficient Monte Carlo (MC) propagation depends on dynamically adjusting the step size to accommodate for varying conditions, e.g. making smaller steps when the mean free path of a specific interaction is small or in regions of strong magnetic deflections. A bidding system allows all modules of a simulation to bid for the next step. The lowest bid is then selected as step size for the next iteration of the module sequence. Therefore the propagation proceeds with the largest possible step that still ensures the numerical accuracy as defined by the user.

Cosmic ray propagation is a perfectly parallel task as interactions between cosmic rays are negligible. Current multicore processors can therefore be adequately utilized by just running multiple simulation instances in parallel. However, for better memory utilization, in CRPropa 3.0 shared-memory multiprocessing using OpenMP [311] is implemented. This allows the use of higher-resolution magnetic fields and matter distributions in the simulation. The parallelization occurs on the level of the module sequence with a dynamic distribution of cosmic rays among the available threads. As the modules do not carry any information about the cosmic rays themselves, only a single instance of each module is needed. The speedup is limited by the number of critical sections that are not thread safe and can only be executed by one thread at a time. The critical section with the largest impact is the external library SOPHIA [268], used to simulate photopion interactions. Thus, the speedup depends on the frequency of these interactions. For a typical extragalactic propagation setup the speedup is limited to a factor of about 6-8, see Fig. 5.1 obtained from Ref. [4].

Fig. 5.2 (obtained from Ref. [5]) shows a graphical illustration of the propagation process. To start, cosmic-ray candidates are created by the source class. These cosmic rays are then processed one-by-one by the modules in the module list. In general the first module is the propagation module which deflects the particle in magnetic fields and updates the position, direction and trajectory length. The next modules make the cosmic ray undergo interactions and can change its energy and nature. In these interactions secondary particles can be produced as well. Stochastic interaction modules decide independently if an interaction occurs during each propagation step. After these interactions boundary and observer modules check if the cosmic ray is still to be considered for further propagation or can be deactivated. If the particle reached an observer, or other specifiable conditions are met, the output modules store the state of the cosmic ray.

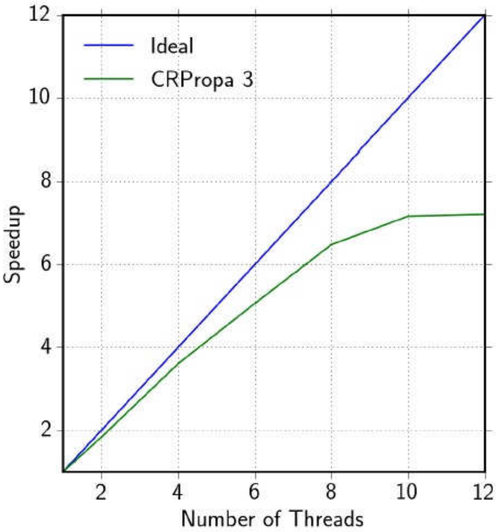

Figure 5.1: Speedup of CRPropa 3.0 in a typical simulation of extragalactic propagation due to shared-memory multiprocessing (obtained from Ref. [4]). The presence of non-parallelized sections limits the speedup to a factor of about 7-8 in this simulation.

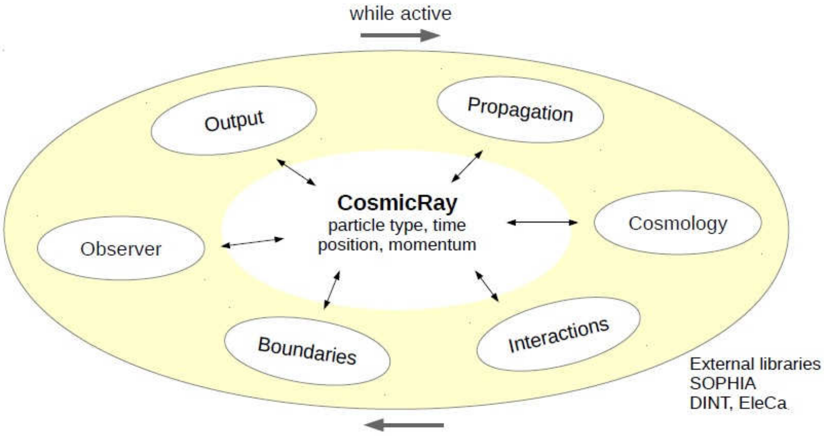

Figure 5.2: Illustration of the CRPropa 3.0 modular structure (obtained from Ref. [5]). Each module contained in the module list acts on the cosmic-ray candidate class as long as the cosmic ray remains active.

5.2 Steering

The steering of the code was in CRPropa 2.0 only possible with XML steering cards. In CRPropa 3.0 XML steering is still a convenient way to use the code that is compatible with CRPropa 2.0. The CRPropa 3.0 executable instantiates a list of modules which mimic the behavior of CRPropa 2.0.

However, a more flexible way of steering CRPropa 3.0 is to use its Python bindings to configure and run simulations. CRPropa 3.0 is written in C++ and interfaced to Python using SWIG [312]. All classes and modules are available in Python, allowing steering and set up of magnetic fields, sources and modules in a high level scripting language as well as an interactive way of running the simulations, while all computations are performed with the underlying C++ code. Furthermore, the SWIG interface enables cross-language polymorphism, which can be used to extend a CRPropa simulation directly from the Python script that runs it. The user can, for example, write a custom simulation module in Python to be used in combination with the existing C++ modules.

5.3 New features

Next to the improvements on the code structure and steering, CRPropa 3.0 also includes several new physical features. These features include a 4D mode which makes it possible to take into account cosmological effects as well as deflections in magnetic fields in the same simulation, the possibility to propagate cosmic rays through the galactic magnetic field (GMF), new techniques to handle large extragalactic magnetic fields (EGMFs) and matter distributions as well as updated photodisintegration cross sections, which will all be described in the next sections. Furthermore, several different UV/optical/IR background (IRB) models will be added, an additional way to handle the propagation of photons and electron-positron pairs (e^-e^+) (with the code called EleCa [313]) will be implemented and improvements on the interpolations for redshift evolution suggested by Kalashev and Kido (see Ref. [314]) will be added.

5.3.1 4D mode

Cosmological effects such as the redshift evolution of the photon backgrounds and the adiabatic expansion of the universe can affect UHECR observables in a significant way. These effects can easily be taken into account in one-dimensional (1D) simulations. However, in three-dimensional (3D) simulations, when deflections due to the EGMF are considered, the effective propagation length, and therefore the redshift, of the simulated cosmic ray are, in general, not known beforehand. To solve this, in CRPropa 3.0 the possibility to do 4D simulations has been introduced. In this 4D mode the observer is not only specified at a certain position in space, but also during a specific period in time, indicated by for instance a redshift window of $\delta z = 0.1$. In this case only cosmic rays arriving at the observer within a redshift of 0.1 from $z = 0$ will be accepted. Therefore δz is a measure for the error on these cosmological effects. When lowering δz the error will be smaller, but less events will be accepted so that it will take longer to get enough statistics.

5.3.2 Propagation through the galactic magnetic field

The GMF is expected to significantly contribute to the total deflections of charges UHECRs, but without propagating diffusively. Due to the short galactic propagation distances as compared to extragalactic distances, energy loss processes can usually be neglected and it is sufficient to only take into account magnetic deflections. To provide for galactic propagation, the possibility of both forward- and backtracking of UHECRs through different models of the GMF implemented in the code have been added to CRPropa 3.0. Generic combinations of axisymmetric or bisymmetric spiral-disc and halo fields can be implemented as GMF models, as well as the Jansson-Farrar 2012 model including the regular, random large-scale and turbulent small-scale components [150, 151]. Furthermore, arbitrary GMF models can be defined using one of the grid techniques described in the next section.

Forward tracking is computationally expensive, however, as the Earth is a very small target compared with galactic distances, resulting in a very small hit probability. Besides, when propagating the cosmic rays backwards from Earth to the galactic border, it is not straightforward to connect them with extragalactic forward tracking. Therefore, a different, highly efficient, way to model deflections in GMFs after extragalactic propagation, the lensing technique described in Ref. [315] for the PARSEC software, is implemented in CRPropa 3.0. This lensing technique uses a set of transformation matrices for different rigidities to map the directions of UHECRs at the border of the galaxy to directions observed at Earth.

A set of lenses for a GMF model consists of one matrix per log-linear spaced energy bin. To construct a matrix a large number of anti-protons are backtracked from Earth to the galactic border. The initial and final directions are then discretized using HEALPix [316] in ~ 50000 pixels for angular resolutions $< 1^\circ$ and used to fill the corresponding matrix elements. Therefore, these kind of matrices have $\sim 50000^2$ entries, corresponding to ~ 9 GB in single precision. These memory requirements are lowered to typically less than 10 MB per matrix by using sparse matrices. Finally, the matrices are normalized to correctly include flux suppression and enhancement.

When applying this lensing technique, the arrival directions of cosmic rays at the galactic border are randomly mapped to an observer pixel at Earth according to the probability distribution contained in the matrix of the corresponding energy bin. The lenses can be used to transform entire arrival distributions through matrix-vector multiplications, or, in the context of individual cosmic rays, as a lookup table of precomputed trajectories. For comparisons with specific experimental results the probability distribution can be weighted with the detector acceptance. This method allows for the simulation of the propagation of UHECRs through both the EGMF and the GMF, which would be computationally unfeasible with pure forward tracking.

5.3.3 Environment-handling technique

Models of the structured extragalactic magnetic field and matter distribution are provided by magnetohydrodynamical simulations of structure formation. These models cover a large range in scales between the simulation volume of $\sim (0.1 - 1\ \text{Gpc})^3$ and the required resolution to resolve the structures down to the level of galaxies at $\sim 1 - 10$ kpc. Several new ways to handle this kind of simulations have been incorporated in CRPropa 3.0. One way is that they can now be stored as so-called smooth particles, for which an interface is provided to the smooth-particle code Gadget [317]. Another technique that can be used in this context is adaptive mesh refinement. An interface to the adaptive-mesh-refinement code RAMSES [318] is provided in CRPropa 3.0. Both smooth particles and adaptive mesh refinement have the advantage of a dynamic resolution and a relatively small memory demand. However, they lack the performance

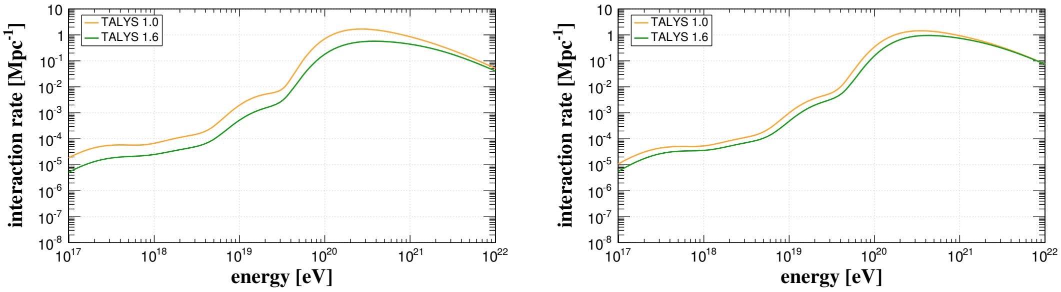

(a) ^{12}C (b) ^{14}N

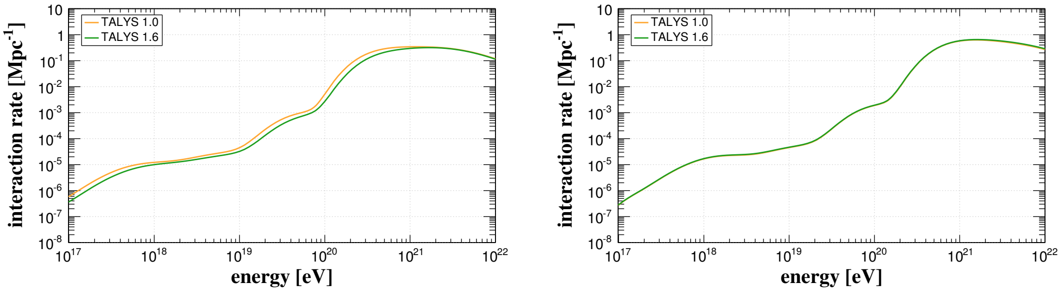

(c) ^{28}Si (d) ^{56}Fe

Figure 5.3: All-channel interaction rate comparisons for photodisintegration between TALYS 1.0 (in yellow) and TALYS 1.6 (in green) (obtained from Ref. [6]).
(a) Interaction rates for ^{12}C.
(b) Interaction rates for ^{14}N.
(c) Interaction rates for ^{28}Si.
(d) Interaction rates for ^{56}Fe.

for a fast lookup of magnetic field or mass density values, which can easily become the bottleneck for tracking cosmic rays. In contrast, regular grids provide fast lookup times but could require a memory of more than a terabyte. As a compromise CRPropa 3.0 provides the possibility to use modulated grids, which are a combination of a small-scale high-resolution vector grid that is repeated periodically to cover a larger volume, and a large-scale low-resolution modulation grid that carries information about the large-scale structure (LSS).

5.3.4 Updated photodisintegration cross sections

CRPropa 2.0 uses photodisintegration cross sections obtained from TALYS 1.0 [202], including extensions for mass numbers $A < 12$ (see Sec. 2.4.2.1). By now, however, a newer version of TALYS, TALYS 1.6, is available. Therefore, the cross sections that were obtained with TALYS 1.0 will be updated to the ones TALYS 1.6 provides. In some cases there are significant differences between TALYS 1.0 and TALYS 1.6, see Fig. 5.3 (obtained from Ref. [6]) for comparisons between TALYS 1.0 and TALYS 1.6 for four different nuclei. While nothing changed in the case of ^{56}Fe (see Fig. 5.3(d)), the changes become more and more significant for lighter nuclei (see Figs. 5.3(a), 5.3(b) and 5.3(c)). A full description of the changes from TALYS 1.0 to TALYS 1.6 can be found in Ref. [285].

5.4 Performance tests

Two typical use cases are discussed here to demonstrate the code performance. The runtime of these cases is compared to that of CRPropa 2.0. The test are performed on an i5-3317U CPU at 1.7GHz. Note that the runtime is highly dependent on the simulation settings. Therefore, the following values should be considered as examples only.

The first test case is a 1D simulation with a uniform source distribution emitting a mixed composition of protons, helium, nitrogen and iron with an energy spectrum of $\mathrm{d}N/\mathrm{d}E \propto E^{-1}$ between 1-1000 EeV. With CRPropa 3.0 the simulations took, on average, 4.5 ms per injected particle, compared to 8.7 ms with CRPropa 2.0.

The second scenario is a 3D simulation with pure-proton injection and an energy spectrum at injection of $\mathrm{d}N/\mathrm{d}E \propto E^{-1}$ between 1-1000 EeV. It includes deflections in a turbulent magnetic field with a root-mean-square strength of $B_{\mathrm{rms}} = 1$ nG. The particles are propagated over a distance of 1 Gpc while neglecting energy-loss processes. Here, when XML-steering cards are used in both cases, the CRPropa 3.0 run takes on average 7.5 ms per trajectory, while CRPropa 2.0 runs in, on average, 3.3 ms per trajectory. The slower performance of CRPropa 3.0 is due to the unoptimized compatibility mode for XML-steering cards. Running the same simulation with Python-steering gives an average run time of 1.0 ms per trajectory.

Furthermore, it is possible to make use of parallelization in CRPropa 3.0, which can also lead to run-time improvements. The resulting run-time speedup scales well up to 8 threads. Thus, on a computing cluster with 2 GB RAM per core, a CRPropa 3.0 simulation can efficiently run on 8 cores in parallel, providing 16 GB RAM for simulation data.

5.5 Code comparisons

In the development of CRPropa 3.0 a complete redesign of the code structure compared with CRPropa 2.0 has been employed. Therefore, to make sure every aspect of the code still functions correctly, extensive tests have been done between the two codes. These tests have been performed for all interactions, for both Python and XML steering as well as for both ROOT and ASCII output types. They led to several bug fixes and improvements in CRPropa 3.0.

An example of comparison plots is given in Fig. 5.4. Here CRPropa 3.0 is indicated as "MPC", the working title during some stages of the development. The results for the composition (Fig. 5.4(a)) and the spectrum (Fig. 5.4(b)) after propagation for three different versions during the development of CRPropa 3.0 are shown, for either ASCII or ROOT output. They can be compared with the indicated CRPropa 2.0 simulation. The simulations with the third development version of CRPropa 3.0 indicated here all show a good comparison (within the statistics) with the CRPropa 2.0 results.

This specific comparison is for XML steering of CRPropa 3.0 with one discrete source located at (3,3,3) Mpc, with the observer at (0,0,0) Mpc with a radius of 2 Mpc, in a 3D environment. Three different nuclei were injected, protons, ^{24}Mg and ^{56}Fe with abundances at constant energy per nucleon of 2, 1 and 1 respectively. The energy spectrum at the source $\mathrm{d}N/\mathrm{d}E \propto E^{-\alpha}$ has a slope of $\alpha = 2.2$, a minimal energy of $E_{\mathrm{min}} = 40$ EeV and a sharp cutoff at $E_{\mathrm{max}} = 300$ EeV. All interactions were included on the CMB only. No magnetic field was specified and the maximum propagation time was set to 10 Mpc.

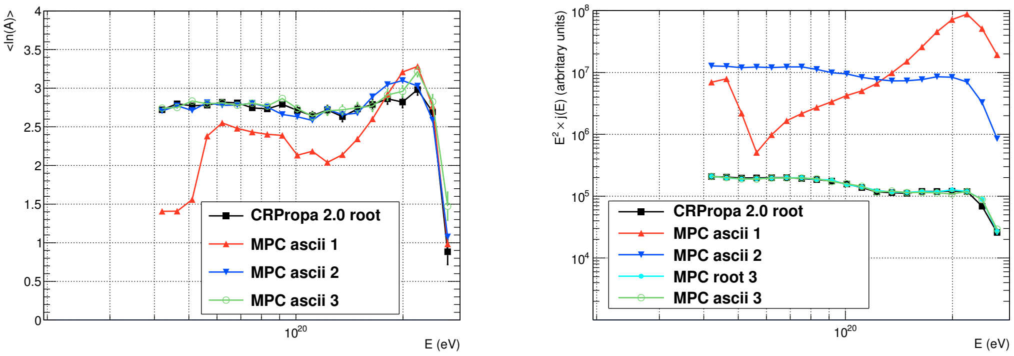

(a) Composition comparison (b) Spectrum comparison

Figure 5.4: Example of comparison plots between CRPropa 2.0 and CRPropa 3.0. Here CRPropa 3.0 is indicated as "MPC", the working title during some stages of the development. The results for the composition (left panel) and the spectrum (right panel) after propagation for three different versions during the development of CRPropa 3.0 (first version in red triangles, second version in blue up-side-down triangles, third version in green open circles) are shown for ASCII output. They can be compared with the indicated CRPropa 2.0 simulation (black squares). In the right panel an additional simulation with the third development version of CRPropa 3.0 is shown for ROOT output (light-blue solid circles).

Next to these kind of full-simulation comparisons, all interactions have been compared separately. This was done by running simulations with one specific source, with injected particles at one specific energy and all interactions switch off except for the interaction that was tested for both CRPropa 2.0 and CRPropa 3.0. The latest results agree very well with each other [5].

5.6 Example application: Benchmark scenario

In Ref. [7] a benchmark scenario, using CRPropa 3.0, for UHECR propagation is introduced. This benchmark scenario provides a comprehensive simulation of cosmic rays propagating from their sources to Earth through background photon fields as well as extragalactic and galactic magnetic fields calibrated by observations. The propagation of cosmic rays in the benchmark scenario can be divided into two regimes, namely extragalactic and galactic propagation.

5.6.1 Extragalactic propagation

In the extragalactic propagation all relevant interactions of cosmic rays with background photons are taken into account as well as deflections in EGMFs. The 3D mode of CRPropa 3.0 is used for this benchmark scenario, thus neglecting cosmological evolution as including cosmological evolution in the 4D mode of CRPropa 3.0 would decrease the simulation efficiency significantly.

The EGMF as well as the distribution of cosmic-ray sources are expected to follow the large-scale matter distribution in the universe. Therefore, structure-formation simulations which result in LSS densities and EGMFs that are consistent with observations (see e.g. Refs. [3, 145, 293, 319]) can be used for simulations of source distributions and deflections in magnetic fields. This allows for a combined model for the UHECR sources and the EGMF.

5.6.1.1 Sources

For the LSS the simulation of Ref. [145] (the Dolag simulation), which was constrained with a smoothed density map generated using the PSCz catalogue [320], is used. This simulation roughly reproduces the local LSS. Therefore, the observer position is fixed in this method. The simulated structure of the Dolag simulation makes up a sphere of ~230 Mpc diameter. The largest box that fits completely inside this sphere is a cube with edges of 132 Mpc. Since the universe is isotropic on scales of ~100 Mpc the simulation volume can be increased up to the maximum trajectory length by repeating the cube, using reflective boundary conditions to prevent discontinuities.

The cosmic ray sources are randomly distributed according to the matter density of the LSS. A minimum distance of 3 Mpc is implemented, which roughly corresponds to the distance to Cen-A. The contribution of all sources up to the maximum propagation distance of 2 Gpc are taken into account automatically due to the reflective boundary conditions. The sources are assumed to emit cosmic rays isotropically.

The cosmic ray composition at the sources matches the abundances of the galactic cosmic rays determined at lower energies as described in Ref. [201] (see Chapter 2.11 for a detailed description). To improve the match between the simulated spectrum and the measured spectrum, the abundances of all elements with charge number $Z > 2$ are scaled up by a factor $k = 10$. The spectrum $\mathrm{d}N/\mathrm{d}E \propto E^{-\alpha}$ for each species extends up to a maximum rigidity of $R_{\max} = E_{\max,i}/Z_i$ where Z_i is the species charge number and $E_{\max,i}$ its maximum energy. Above this maximum rigidity the flux drops to zero.

Further parameters of the source model used for this specific application are a source density of $\rho = 10^{-4}$ Mpc^{-3}, a spectral index of $\alpha = 2$ and a maximum rigidity of $R_{\max} = 150$ EeV.

5.6.1.2 Extragalactic magnetic field

As the EGMF is constrained very poorly, the overall strength of simulated magnetic fields vary greatly. For this benchmark scenario a generic model was developed that reproduces the structure of the EGMF of Refs. [3, 145, 293, 319] (the Dolag and Miniati simulations). This model consists of a random turbulent field, modulated with the LSS using the correlation between matter density and magnetic field strength. This is done by translating the matter density $\rho(\overrightarrow{x})$ in the Dolag structure into a field strength $|\overrightarrow{B}(\overrightarrow{x})|$ using the logarithmic mean of the $\log_{10}(\rho(\overrightarrow{x})) - \log_{10}(\overrightarrow{B}(\overrightarrow{x}))$ distribution in the Miniati structure simulation. The mean field strength is extrapolated for densities smaller than 10^{-32} g/cm^3 or larger than 10^{-28} g/cm^3. The obtained field strength is then used to create a random turbulent magnetic field with a Kolmogorov power spectrum.

The total magnetic field is then calculated from a combination of two regular grids. The turbulent-field grid has a size of (13.2 Mpc)^3 sampled on a 256^3 grid resulting in a grid spacing of ~50 kpc. This field is periodically repeated to cover the complete simulation box. The modulation grid, on the other hand, covers the whole simulation box. This grid carries the magnetic-field strength correlated with the LSS. It has a size of (132 Mpc)^3 sampled on a 256^3 grid resulting in a grid spacing of ~500 kpc. The field vector at any point is calculated from the vector grid and multiplied with the field strength from the scalar grid.

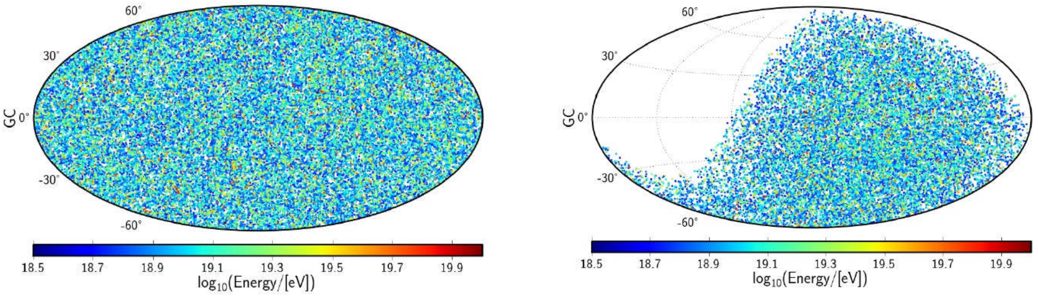

(a) Edge of the galaxy (b) Auger acceptance

Figure 5.5: Distribution of events in galactic coordinates for the benchmark scenario (obtained from Ref. [7]).
(a) In the left panel 40000 events at the edge of the galaxy are shown.
(b) In the right panel 20000 events after deflection in the GMF and after application of the detector acceptance of Auger are given.

5.6.2 Galactic propagation

As galactic propagation involves (kilo)parsec length scales, compared with megaparsec (Mpc) scales for the extragalactic case, interactions with photon fields can be neglected. As GMFs can be of order micro gauss (μG) [321] and thus much larger than typical large-scale EGMF stengths [141], UHECRs can still be deflected considerably within the galaxy. To efficiently simulate the galactic propagation, the lensing technique described in Sec. 5.3.2 has been used. This lensing technique, besides being efficient, has as advantage that it is independent of the extragalactic propagation. Therefore, for a given set of extragalactic events, observed directions at Earth can be generated using different GMF models.

The GMF model implemented here is the Jansson-Farrar 2012 model [150]. The large-scale regular field of the model consists of three components, a spiral disk, a toroidal halo and a poloidal out-of-plane field. Additionally a striated-random field is considered. In Ref. [151] the model is extended with a galactic small-scale random field, which can now also be incorporated as part of the lens in CRPropa 3.0.

The event distribution in galactic coordinates of this benchmark scenario is shown in Fig. 5.5 (obtained from Ref. [7]). These distributions can be used to test and evaluate observables or to constrain the parameter space of specific scenarios. Fig. 5.5(a) is an example of a distribution of 40000 events at the galactic border, while Fig. 5.5(b) shows a distribution of 20000 events after application of the GMF lens and the geometrical detector acceptance of the Pierre Auger Observatory.

Chapter 6

Dipole analysis

As discussed in Sec. 1.2.3, one of the observables measured by the Pierre Auger Observatory is the incoming direction of the ultra-high-energy cosmic rays (UHECRs). Anisotropies can be looked for in the distribution of these arrival directions in several different ways. One way is by their correlation with nearby extragalactic objects. This was for instance done by the Pierre Auger Collaboration in Refs. [13, 27, 28, 32], where the observation of a correlation between the arrival directions of their highest-energy cosmic rays and the positions of nearby active galactic nuclei (AGNs) from the 12^{th} edition of the catalog of quasars and active nuclei by Véron-Cetty and Véron [153] (VCV catalog) was reported. In the most recent update of this correlation a correlation signal at 2σ above the expected fraction for an isotropic sky is indicated [13, 32]. The start of the correlation signal is visible at about 55 EeV.

Whereas the correlation with the VCV catalog disappears for energies below 55 EeV, the spherical harmonic moments in the distribution of arrival directions can show interesting features in this energy range. In Refs. [35, 36] for example, an investigation into large-scale anisotropies of cosmic rays above 1 EeV detected at the Pierre Auger Observatory is undertaken. Both the declination and right ascension have been taken into account in this search. The dipolar and quadrupolar coefficients are presented for several energy ranges above 1 EeV. No significant deviation from isotropy, within the systematic uncertainties, is revealed.

Here we investigate what dipolar amplitudes can be expected if UHECRs above 1 EeV have a predominant extragalactic origin. The simulated results can then be compared with the measurements of the dipole coefficients by the Pierre Auger Collaboration [36].

Naively one would expect an isotropic distribution to a high level for UHECRs of an extragalactic origin. However, there are several effects that might cause a deviation from isotropy in the data. When the sources of UHECRs, for instance, follow the large-scale structure (LSS) in the local universe, this structure could be visible in the arrival directions of the cosmic rays. This is the case especially at the highest energies, where cosmic rays have a limited propagation distance due to the GZK effect for protons and photodisintegration for heavier nuclei.

Furthermore, the density of the sources might play a role in the level of isotropy. A low source density might cause an increase in anisotropy due to close-by sources becoming more prominent. Lower bounds on the density of sources have, for instance, already been obtained by the Pierre Auger Collaboration from the lack of significant clustering in the arrival directions of the highest energy events [322]. A high source density following the LSS, however, might increase the correlation with the LSS and increase the anisotropy in that way.

In addition, both the extragalactic magnetic field (EGMF) and the galactic magnetic field (GMF) might play a role in the determination of the level of isotropy. Deflections in the EGMF could wash out existing anisotropies or focus the cosmic rays along the LSS, increasing the correlation with the local LSS and thus increase the level of anisotropy. The GMF could as well wash out the existing anisotropies, or deflect the cosmic rays in such a way that the anisotropy is increased, depending on the structure of the GMF.

6.1 Simulation setup

To investigate which of these effects are dominant we use CRPropa 3.0 (see Chapter 5 and Ref. [44]) in three-dimensional (3D) mode to run simulations of UHECRs from their sources to the observer, including all relevant interactions (pair production, pion production, photodisintegration and decay) with both the cosmic microwave background (CMB) and the UV/optical/IR background (IRB) as well as deflections in the EGMF and GMF. The implemented IRB is the best-fit model of Ref. [272].

In these simulations cosmic rays were injected with an initial spectrum $E_0^{-\alpha_{\rm init}}$, where E_0 is the energy of the cosmic ray at injection, with spectral index $\alpha_{\rm init} = -1.0$ (to obtain reasonable statistics over the whole energy range) up to an initial maximum rigidity of $R_{\rm max}^{\rm init} = E_{\rm max}^{\rm init}/Z_0 = 1000$ EeV, where $E_{\rm max}^{\rm init}$ is the maximum initial energy and Z_0 the initial charge of the injected particle. This will be reweighted afterwards to a spectrum with an exponential cut-off

$$\frac{{\rm d}N}{{\rm d}E} \propto E_0^{-\alpha} e^{-E_0/(Z_0 R_{\rm max})} \tag{6.1}$$

and the desired maximum rigidity $R_{\rm max} < R_{\rm max}^{\rm init}$ and spectral index α. The particles are followed down to an energy of $E_{\rm min} = 1$ EeV. The maximum trajectory length up to which the cosmic rays are followed is $L_{\rm max} = 4000$ Mpc.

Four different nuclei are injected at the sources, protons (p), helium nuclei (He), nitrogen nuclei (N) and iron nuclei (Fe). Their relative abundances for a constant energy of the nucleus before the cut-off are 8 for p, 4 for He, 2 for N and 1 for Fe. The abundances were chosen in this way to compensate for that nuclei with $A > 1$ can split up in maximally A different particles.

The implemented GMF is the full Jansson-Farrar 2012 (JF12) field [150, 151], applied with the PARSEC code by the lensing technique explained in Section 5.3.2. The normalization of the lenses was done with the PARSEC function ”normalizeLens()”. The minimal rigidity of these lenses is $R_{\rm min}^{\rm lens} = 0.1$ EeV. As the dipole amplitude will be calculated between an energy of 1 and 16 EeV, this does not pose a problem for the pure-proton injection case. For the mixed-composition and pure-iron injection cases, however, a too small estimation of the deflection might occur for $E < 0.1Z$ EeV. On the other hand, the spectrum of the iron and mixed-composition cases only fits the Pierre Auger spectrum above ≈ 5 EeV, so that only above this energy the dipole amplitude calculations are relevant anyway. In this energy range the lenses are correctly defined even for iron nuclei at the observer.

Two different models for the EGMF are used. The first results are for the so-called Miniati field for which a $(50/h\ {\rm Mpc})^3$ simulation box, where the normalized Hubble constant $h \equiv H_0/(100\ {\rm km\ s^{-1}\ Mpc^{-1}}) = 0.673$, with periodic boundary conditions is filled with the LSS-EGMF from the cosmological simulations given in Ref. [3].

The second case is based on the constrained EGMF and LSS setup developed for the benchmark scenario for UHECR propagation described in Sec. 5.6.1, called benchmark field from here on. This benchmark field is updated compared with the one described in Sec. 5.6.1. The turbulent field grid now has a size of (13.2 Mpc)^3 sampled on a 440^3 grid, resulting in a grid spacing of 30 kpc. This field is again periodically repeated to cover the complete simulation box. The modulation grid, covering the whole simulation box, carries the LSS field strength. It now has a size of (132 Mpc)^3 sampled on a 440^3 grid, resulting in a grid spacing of 300 kpc. The field vector at any point is calculated from the vector grid and multiplied with the field strength from the scalar grid. Furthermore, the matter density $\rho(\overrightarrow{x})$ in the Dolag LSS (Ref. [145]) is translated into a field strength $|\overrightarrow{B}(\overrightarrow{x})|$ using the logarithmic root mean square of the $\log_{10}(\rho(\overrightarrow{x})) - \log_{10}(\overrightarrow{B}(\overrightarrow{x}))$ distribution in the Miniati structure simulation (Ref. [3]).

The source positions have been generated randomly, following, for the Miniati field, the corresponding LSS baryon density [3], and, for the benchmark field, following the LSS baryon density from the simulations given in Ref. [145]. The initial source density is, in both cases, 10^{-3} Mpc^{-3}. To create a data-set for lower source densities, events from specific sources can be selected.

The observer position in the Miniati field has been set to (4, 41.7, 45.5) Mpc, the observer position in the benchmark field, being a constrained simulation, is fixed at (118.34, 117.69, 119.2) Mpc. In both cases the radius of the observer has been set to 1 Mpc.

6.2 Effects of reweighting and statistics

As mentioned in the previous section, the simulations are started with an initial spectral index of $\alpha_{\mathrm{init}} = 1.0$ up to a sharp cut-off at $R_{\max}^{\mathrm{init}} = 1000$ EeV. To obtain the desired spectral index α, the maximum rigidity $R_{\max}$ and the exponential cut-off of Eq. 6.1, the output events have to be reweighted afterwards. Here we discuss two different ways of doing the reweighting and show their effects on the dipole amplitude.

The first way to do the reweighting is by multiplying every event with a specific weight factor. To reweight to Eq. 6.1, the weight factor for each event is

$$w(E_0, Z_0) = E_0^{\alpha_{\mathrm{init}} - \alpha} \cdot e^{-E_0/(Z_0 R_{\max})} \; . \tag{6.2}$$

This has as advantage that every event is used such that no statistics are lost. The disadvantage is, however, that in this way events with a high weight are seen as many hits in exactly the same position. In the limit of infinite statistics this should not matter for the calculation of the dipole amplitude. For finite statistics, however, this might cause a significant shift in the dipole amplitude.

The second way to do the reweighting is by accepting or rejecting the event based on whether a random number r is smaller or larger than the weight w of the particle. If r is linearly distributed between 0 and 1, the weight should also lie between 0 and 1. For the calculation of the dipole amplitude, only the weight differences within one energy bin are important. So, to optimize the number of statistics, the weight w of Eq. 6.2 can be divided by the maximal possible weight within each energy bin $w_{\max}$ to get the optimized weight for each event:

$$w_{\mathrm{opt}}(E_0, Z_0) = \frac{w(E_0, Z_0)}{w_{\max}} = w(E_0, Z_0)/({E_{\min}^{*}}^{\alpha_{\mathrm{init}} - \alpha} \cdot e^{-E_{\min}^{*}/(Z_{0\max}^{*} R_{\max})}) \; , \tag{6.3}$$

where $E^*_{\rm min}$ is the lowest energy within the specific energy bin and $Z^*_{0\rm max}$ is the highest charge an injected particle could have. The advantage of this method, with respect to the previous method, is that in this case you do not get many events at exactly the same position due to a high weight. The disadvantage is the loss of statistics due to the rejected events. In the limit of infinite statistics this method should give the same results as the first one and as a simulation for which no reweighting is necessary. With finite statistics, however, this method decreases the statistics even further due to the rejected events.

To test the effects of these different types of reweighting and the effect of a low number of statistics, a 3D simulation with CRPropa 2.0 (see Chapter 2 and Refs. [1, 43]), including all relevant interactions, has been run with only iron injected at the sources. The initial spectral index of this simulation is $\alpha_{\rm init} = -1.0$ and the initial maximum rigidity is $R^{\rm init}_{\rm max} = 1000$ EeV. This will then be reweighted to a sharp cut-off at a maximum rigidity of $R_{\rm max} = 200$ EeV and a spectral index of $\alpha = -2.4$. No GMF or EGMF is implemented and a continuous isotropic source distribution is simulated, so that no significant dipole amplitude is expected. To be complete, the particles are followed down to an energy of $E_{\rm min} = 1$ EeV and the maximum trajectory length up to which they are followed is $L_{\rm max} = 4000$ Mpc. To compare the reweighted results an additional simulation was run with the same settings except for an initial spectral index of $\alpha_{\rm init} = -2.4$ and an initial maximum rigidity of $R^{\rm init}_{\rm max} = 200$ EeV so that no reweighting is necessary.

6.2.1 Effects of reweighting and statistics on the energy spectrum

In Fig. 6.1 the spectra for the different ways of reweighting are compared with each other and with the simulation for which no reweighting was necessary. The dashed lines are this reference simulation with $\alpha_{\rm init} = -2.4$ and $R^{\rm init}_{\rm max} = 200$ EeV without any reweighting. They are the same in Fig. 6.1(a) and Fig. 6.1(b). For the other cases Fig. 6.1(a) shows the situation for relatively low statistics and, to show the effect of higher statistics, Fig. 6.1(b) shows what changes when more events are simulated.

In each specific plot the dash-dotted, dotted, and straight lines are created from the same data set of a CRPropa 2.0 simulation. In both figures the dashed-dotted lines show the original data, so for $\alpha_{\rm init} = -1.0$ and $R^{\rm init}_{\rm max} = 1000$ EeV without any reweighting. It is clear that the differences between these scenarios and the reference simulation are extensive.

The dotted lines show, in both cases, the "multiply each event by its weight" method of reweighting, where the original data has been reweighted to $\alpha = -2.4$ and $R_{\rm max} = 200$ EeV. In this case the weight was calculated by

$$w(E_0, Z_0) = \begin{cases} E_0^{\alpha_{\rm init}-\alpha} & \text{for } E_0/Z_0 \leq R_{\rm max}, \\ 0 & \text{otherwise.} \end{cases} \tag{6.4}$$

In this way a sharp cut-off is created instead of the exponential cut-off of Eq. 6.1. This was done to better compare with the reference simulation, as by default CRPropa 2.0 simulates a sharp cut-off at $R_{\rm max}$.

As can be seen in Fig. 6.1, the "multiply each event by its weight" method shows a good comparison to the reference simulation for both the lower- and higher-statistics case. It even shows an improvement at the highest energies over the reference simulation, as the reference simulation has relatively low statistics at the highest energies due to the $\alpha_{\rm init} = -2.4$ initial spectral index.

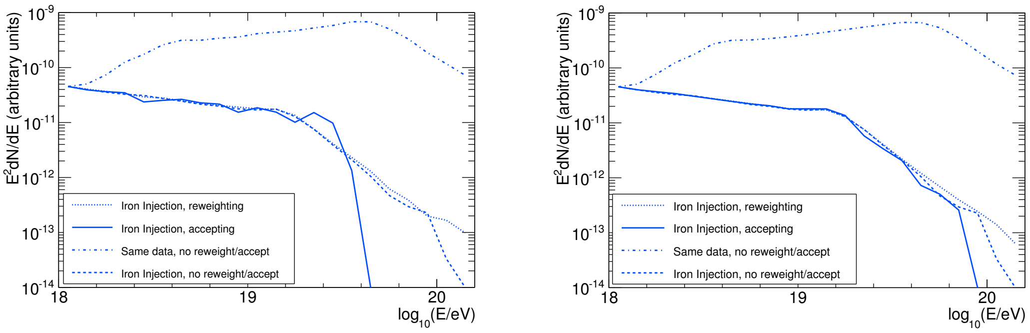

(a) Lower Statistics

(b) Higher Statistics

Figure 6.1: UHECR energy spectra for pure-iron injection including all relevant interactions without GMF or EGMF. A continuous isotropic source distribution is simulated. The dashed lines are the same for the left and right panel and are the reference simulation with $\alpha_{\rm init} = -2.4$ and $R_{\rm max}^{\rm init} = 200$ EeV without any reweighting. In each specific panel the dash-dotted, dotted, and straight lines are created from the same data set, a smaller data set for the left panel compared with the right panel. The dashed-dotted lines show the original data for $\alpha_{\rm init} = -1.0$ and $R_{\rm max}^{\rm init} = 1000$ EeV without any reweighting. The dotted lines show the "multiply each event by its weight" method of reweighting. The straight line shows the "accepting or rejecting" reweighting method.

The straight lines show the "accepting or rejecting" reweighting method, where the original data has again been reweighted to $\alpha = -2.4$ and $R_{\rm max} = 200$ EeV. Here the weight has been calculated using Eq. 6.4 with E_0 in EeV so that $w(E_0, Z_0) = 1$ for $E_0 = 1$ EeV. In this way the values of $w(E_0, Z_0)$ are distributed between 0 and 1 and can be compared with a random number distributed in this same range. As can be seen from Fig. 6.1, this way of reweighting suffers from too low statistics above $E \approx 20$ EeV for the lower-statistics case and above $E \approx 70$ EeV for the higher-statistics case.

Thus increasing the statistics extends the reliability of the "accepting or rejecting" method towards higher energies. The "multiply each event by its weight" method, however, already produced correct results even for the lower-statistics case. Therefore the "multiply each event by its weight" method is preferred in the case of the energy spectrum. This will now be tested as well for the dipole amplitude.

6.2.2 Effects of reweighting and statistics on the dipole amplitude

The dipole amplitudes of the simulations described in the previous section are calculated by filling a separate sky map for each scenario and each energy bin with the output of the CRPropa 2.0 simulation. When multiple events of the same originally injected particle arrive at the observer in the simulations, only the first of these events is processed. This is done as in nature it is very unlikely that two or more particles originating from the same UHECR nucleus are measured by our detector at Earth.

In the scenarios where reweighting is applied the weight is calculated by $w_{\rm opt}(E_0, Z_0) = w(E_0, Z_0)/w_{\rm max}$ with $w_{\rm max} = E_{\rm min}^{*\ \alpha_{\rm init}-\alpha}$ and $E^*_{\rm min}$ the lowest energy within the specific energy bin. Therefore this weight factor is optimized in the range [0,1] so that it can be compared efficiently with a random number within this same range.

From the resulting sky map the spherical harmonic coefficients are calculated by fitting a dipole to the sky map with the "fit_dipole" function of healpy [323]. The function returns the monopole value a_{00} and the dipole vector $(a_{10}, a_{11}, a_{1-1})$. The

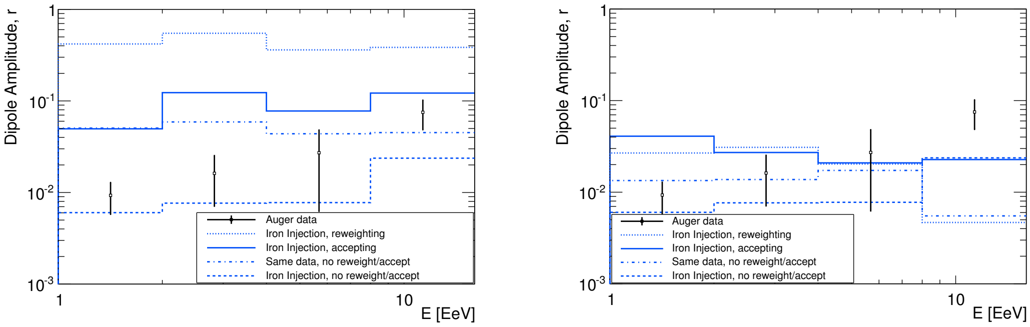

(a) Lower Statistics

(b) Higher Statistics

Figure 6.2: Dipole amplitudes for the same scenarios as the UHECR spectra of Fig. 6.1. The black data points are the Auger measurements from the left panel of Fig. 5 of Ref. [36].

Table 6.1: Number of events before reweighting between 1 EeV and 16 EeV for the reweighted data set N_{rew} and the reference simulation N_{ref}.

	Lower Statistics	Higher Statistics
Reweighted data set N_{rew}	4×10^4	8×10^5
Reference simulation N_{ref}	8×10^5	8×10^5

dipole amplitude r can then be calculated from these spherical harmonic coefficients by:

$$r = \sqrt{3(a_{10}^2 + a_{11}^2 + a_{1-1}^2)/a_{00}} \ . \tag{6.5}$$

Fig. 6.2 shows the dipole amplitude for the same scenarios as in Fig. 6.1. The black data points are, for comparison, the Auger measurements from the left panel of Fig. 5 of Ref. [36]. As the source distribution was completely continuous and isotropic and no deflections by GMF or EGMF were implemented, a dipole amplitude going to zero for infinite statistics is expected. In both the lower- and higher-statistics case the dashed line is again the reference simulation with $\alpha_{\mathrm{init}} = -2.4$ and $R_{\mathrm{max}}^{\mathrm{init}} = 200$ EeV without any reweighting and has the same statistics in both cases. The dashed-dotted lines are again the same data sets as the straight and dotted lines in the same plots, but without any reweighting. The dotted line is again the "multiply each event by its weight" method and the straight line the "accepting or rejecting" method of reweighting.

From Fig. 6.2(a) it can be seen that the "accepting or rejecting" method gives a far lower dipole amplitude than the "multiply each event by its weight" method, and can thus be considered as the better method for calculating the dipole amplitude (and will be used in dipole amplitude calculations later on in this Chapter). It is also clear that both the "accepting or rejecting" method and the "multiply each event by its weight" method as well as the same data set without reweighting give a relatively large dipole amplitude compared with the reference simulation for which reweighting was not necessary. When comparing with Fig. 6.2(b) it can be seen that this is due to the low statistics in Fig. 6.2(a). In Tab. 6.1 the number of registered events between 1 EeV and 16 EeV for the different scenarios is given.

In Fig. 6.2(b) the difference between the "accepting or rejecting" method and the "multiply each event by its weight" method are negligible, showing that it does not matter which way of reweighting is used when the statistics are large enough. An important thing to note here, however, is that even for the higher-statistics case the reweighted lines have not converged yet with the reference simulations, meaning that even for this scenario the statistics might not have been large enough yet for a reliable calculation of the dipole amplitude. Thus the effect of statistics should be investigated closely before drawing any conclusions on the dipole amplitudes of different scenarios. Similar results were found for pure-proton and mixed-composition scenarios.

6.3 Results for the Miniati field

The way of calculating the dipole amplitude and the method of reweighting that have been established will now be applied to the simulation setup specified in Sec. 6.1. The reweighting is done with the "accepting or rejecting" method with the weight calculated by Eq. 6.3. For the EGMF the Miniati field [3] and its corresponding sources are set as simulation environment.

6.3.1 Pure-proton scenario

First we consider here a pure-proton-injection scenario which fits the Pierre Auger spectrum down to 1 EeV. This pure-proton scenario obviously does not fit the composition measurements of Pierre Auger. The original simulation is reweighted to $\alpha = -2.6$ and $R_{\max} = 398.1$ EeV.

These parameters were obtained from Ref. [324]. They were obtained by fitting a pure-proton simulation to the Pierre Auger ICRC2013 energy spectrum [34] above 1 EeV. In this fit the same initial spectrum and exponential cut-off at the sources (Eq. 6.1) were implemented as are used here.

There are a few differences, however, between the simulations of Ref. [324] and the simulations done here for the calculation of the dipole amplitude. In Ref. [324] one-dimensional (1D) simulations including cosmology were done, whereas here 3D simulations without cosmology have been done. Furthermore, in Ref. [324] a uniform source distribution from 4 Mpc to 2600 Mpc from the observer was simulated, whereas here a source density of 10^{-3} Mpc^{-3} with sources following the Miniati LSS is implemented. Furthermore, in Ref. [324] the spectrum was adjusted to include the magnetic suppression described in Ref. [234] with $X_s = 2$ and $E_c = 1$ EeV (for definitions of these parameters, see Ref. [234]). In this work this magnetic suppression is not included as the simulations run here are 3D simulations including the deflections in the Miniati EGMF, instead of 1D simulations, so that the effects of diffusion in EGMF are automatically taken into account.

These differences in the simulations can explain small deviations between the simulated spectrum of this work and the simulated spectrum in Ref. [324]. As can be seen from Fig. 6.3, the simulated spectrum of this work still fits the Pierre Auger ICRC 2013 spectrum reasonably well down to 1 EeV. The reweighting for the spectrum was done by the "multiply each event by its weight" method.

The sky maps obtained from this simulation are shown in Fig. 6.4. Here in the left panel the sky map before GMF deflections and in the right panel after GMF deflections is shown. The EGMF is included in both cases. Both sky maps are for all events between 1 and 16 EeV after reweighting with the "accepting or rejecting" method and in both cases the bin with the most hits is normalized to one. From these sky maps it can already be seen that before the GMF a clear structure is visible with a large spot

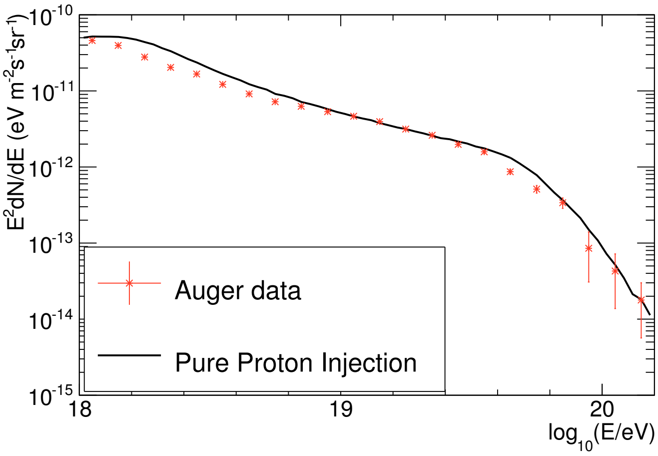

Figure 6.3: In red crosses, the Pierre Auger ICRC 2013 spectrum is shown. The CRPropa simulation (black line) with pure-proton injection at the sources, reweighted to a spectral index at injection of $\alpha = -2.6$ and a maximum energy of $E_{\max} = 398.1$ EeV is given as well. The source density is 10^{-3} Mpc^{-3} with sources following the Miniati LSS. Deflections in the Miniati EGMF are included. For further simulation parameters see Sec. 6.1.

with relatively few events, whereas these structures are washed out after the deflections in the GMF and the sky looks more isotropic.

The results for the dipole amplitude for this scenario are shown in Fig. 6.5. Fig. 6.5(a) shows the cases without deflections in the GMF. The straight line shows the dipole amplitude for a source density of 10^{-3} Mpc^{-3} for one specific source realization. The dashed line represents the dipole amplitude for a source density of 10^{-4} Mpc^{-3}, as well for one specific source realization. Comparing these two lines shows that there is barely any effect of the source density on the dipole amplitude, at least for the chosen source realizations. The dotted line indicates the dipole amplitude of a simulation with the same parameters as the other two lines (with a source density of 10^{-3} Mpc^{-3}) but with deflections in the EGMF being switched off. This shows a dramatic decrease of the dipole amplitude, indicating that the EGMF can introduce a strong dipole in the UHECR sky. This is probably due to deflection by the EGMF along the large-scale structure, shielding parts of the sky where relatively strong EGMFs deflect the UHECRs away from the observer.

Fig. 6.5(b) shows the same scenarios as Fig. 6.5(a), but now including deflections in the GMF. The value for the dipole amplitude for a source density of 10^{-3} Mpc^{-3} including EGMF (straight line), has dropped significantly due to the GMF. However, the dipole amplitude for the same scenario, but excluding deflections in the EGMF (dotted line), increased significantly. This could point to the washing-out of large structures by the GMF, but if initially no large structures are visible, the structure of the GMF itself appears in the sky. It is, however, too early to draw any strong conclusions as first the effects of statistics in these cases should be investigated rigorously.

The case with a source density of 10^{-4} Mpc^{-3} including EGMF (dashed line) shows a slightly larger dipole than the same scenario with a source density of 10^{-3} Mpc^{-3}. It is highly doubtful, however, that this is actually due to the lower source density. If there is an effect of the source density, it should already show up before the deflections in the GMF are applied, not only afterwards. A more likely explanation is that this is due to low statistics. The scenarios with a source density of 10^{-4} Mpc^{-3} have about ten times lower statistics than the same scenarios with a source density of 10^{-3} Mpc^{-3}.

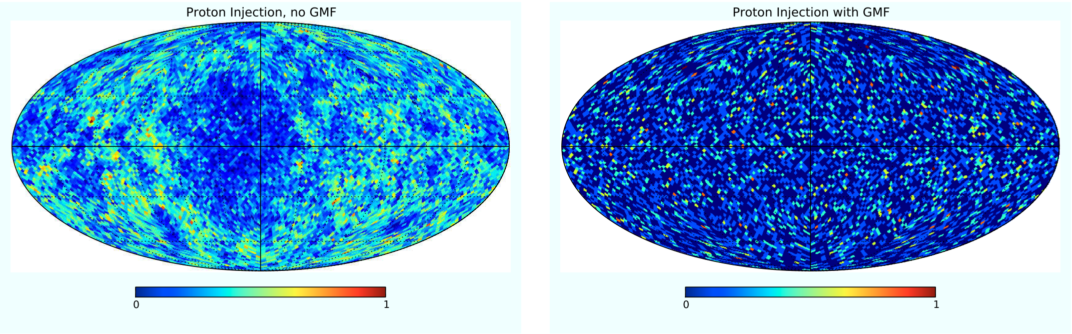

(a) Without GMF

(b) With GMF

Figure 6.4: Sky maps of a CRPropa simulation with pure-proton injection at the sources, reweighted to a spectral index at injection of $\alpha = -2.6$ and a maximum energy of $E_{\max} = 398.1$ EeV. The source density is 10^{-3} Mpc^{-3} with sources following the Miniati LSS. Deflections in the Miniati EGMF are included. Both sky maps are for all events with energy between 1 and 16 EeV and in both cases the bin with the most hits is normalized to one. In the left panel (a) the case before GMF deflections, in the right panel (b) the case after GMF deflections. For further simulation parameters see Sec 6.1.

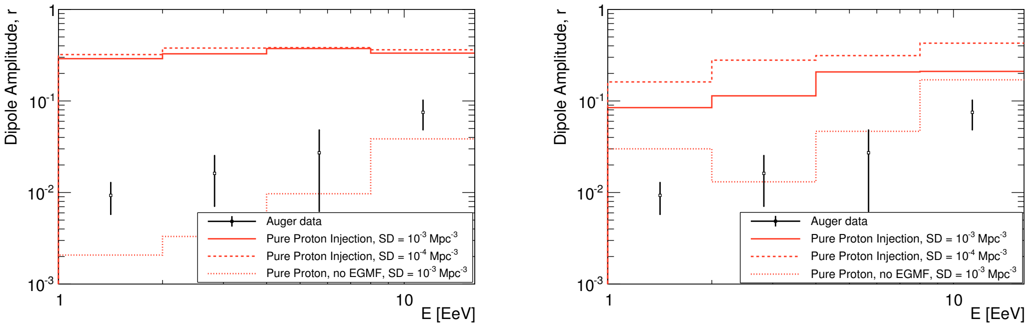

(a) Without GMF

(b) With GMF

Figure 6.5: Dipole amplitude for pure-proton injection. The black data points are the Auger measurements from the left panel of Fig. 5 of Ref. [36]. The straight lines show the dipole amplitude for a source density of 10^{-3} Mpc^{-3}. The dashed lines give the dipole amplitude for a source density of 10^{-4} Mpc^{-3}. The dotted lines represent the dipole amplitude of a simulation with the same parameters as the other two lines (with a source density of 10^{-3} Mpc^{-3}) but without deflections in the EGMF. The left panel (a) shows the cases without deflections in the GMF, wheres the right panel (b) shows the cases with deflections in the GMF.

Table 6.2: Number of events before reweighting between 1 EeV and 16 EeV for the different pure-proton-injection scenarios.

	Without GMF	With GMF
Source Density 10^{-3} Mpc^{-3}	2×10^6	1×10^5
Source Density 10^{-4} Mpc^{-3}	2×10^5	1×10^4
Source Density 10^{-3} Mpc^{-3}, no EGMF	5×10^6	3×10^5

Furthermore, including the GMF decreases the statistics as well by about an order of magnitude due to many "blind spots" in the sky from which no event will reach Earth. The number of events for each scenario is shown in Tab. 6.2.

6.3.2 Mixed-composition scenario

The second composition scenario considered here is a mixed-composition case which should fit the Pierre Auger spectrum and composition measurements above $E = 5$ EeV. The applied spectral index and maximum rigidity at the sources are $\alpha = -1.8$ and $R_{\max} = 20.0$ EeV. The composition at the sources is $p_p = 12.7\%$ proton, $p_{\mathrm{He}} = 0.0\%$ helium, $p_{\mathrm{N}} = 71.1\%$ nitrogen and $p_{\mathrm{Fe}} = 16.2\%$ iron. These percentages are given for a fixed energy of the nucleus before the cut-off.

These parameters were again obtained from Ref. [324]. They were determined by fitting simulations of proton, helium, nitrogen and iron injection to the Pierre Auger ICRC2013 energy spectrum, $\langle X_{\max} \rangle$ and $\sigma(X_{\max})$ [34] measurements above 5 EeV. In his fit he again implemented the same initial spectrum and exponential cut-off at the sources (Eq. 6.1) as is used here.

As the original simulation had p, He, N and Fe injected at the sources with relative abundances for a constant E_0 of $a_p = 8$ for p, $a_{\mathrm{He}} = 4$ for He, $a_{\mathrm{N}} = 2$ for N and $a_{\mathrm{Fe}} = 1$ for Fe, not only the energy spectrum at the sources, but also the composition has to be reweighted afterwards. The weight factor for the composition for each specific element (el) is given by:

$$w_{\mathrm{comp}}^{\mathrm{el}} = \frac{p_{\mathrm{el}}}{p_{\mathrm{N}}} \frac{a_{\mathrm{N}}}{a_{\mathrm{el}}} \ , \tag{6.6}$$

so that $w_{\mathrm{comp}}^{\mathrm{N}} = 1$ and the weight of all other elements lies between 0 and 1. The total weight for each event then becomes:

$$w_{\mathrm{tot}}(E_0, Z_0) = w_{\mathrm{opt}}(E_0, Z_0) \cdot w_{\mathrm{comp}}^{\mathrm{el}} \ , \tag{6.7}$$

with $w_{\mathrm{opt}}(E_0, Z_0)$ equal to Eq. 6.3 for the calculation of the sky map and the dipole amplitude and equal to Eq. 6.2 for the calculation of the spectrum.

The same differences as mentioned in the previous section between the simulations in Ref. [324] and the simulations done here hold for this scenario as well. These differences in the simulations could explain differences between the simulated spectrum and composition at the observer of this work and of Ref. [324]. As can be seen from Fig. 6.6, the simulated spectrum of this work (black straight line) fits the Pierre Auger ICRC 2013 spectrum reasonably well.

To test if the composition reweighting was done correctly and see the effect of cosmology and deflections in the EGMF on the spectrum, two more spectra are shown in Fig. 6.6. The blue dashed line shows a 1D simulation with the same initial spectrum

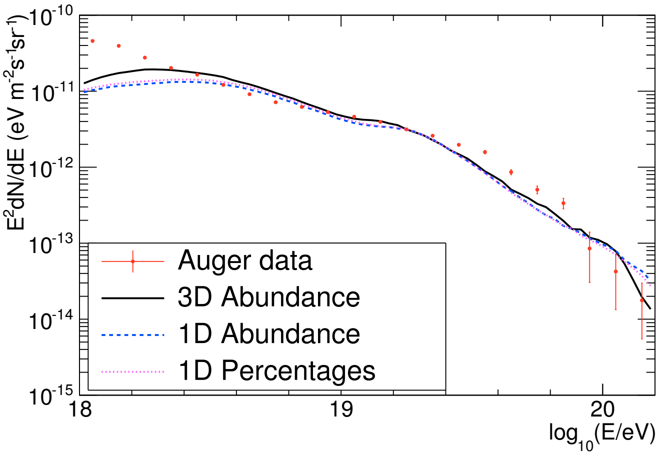

Figure 6.6: In red crosses, the Pierre Auger ICRC 2013 spectrum is shown. The black straight line shows the CRPropa simulation with composition at the sources of 12.7% proton, 71.1% nitrogen and 16.2% iron as well as a spectral index and maximum rigidity of $\alpha = -1.8$ and $R_{\max} = 20.0$ EeV, respectively. The source density is again 10^{-3} Mpc^{-3} with sources following the Miniati LSS. Deflections in the Miniati EGMF are included. For further simulation parameters, see Sec 6.1. To test if the composition reweighting was done correctly, the blue dashed line shows a reweighted 1D simulation with the same initial spectrum and composition as the 3D simulation, whereas the dotted magenta line shows a combination of separate 1D pure-proton, pure-nitrogen and pure-iron simulations added with the percentages specified above.

and composition as the 3D simulation. It has been reweighted in the same way as the 3D simulation. The differences between the 1D and 3D simulation are due to the inclusion of cosmology effects (cosmological and source evolution and redshift scaling of the background light intensity) in the 1D case as well as a continuous source distribution from 4 to 2600 Mpc without deflection in the EGMF in the 1D case with respect to the source density of 10^{-3} Mpc^{-3} and deflections in the Miniati EGMF in the 3D case.

The dotted magenta line shows a combination of separate 1D pure- proton, pure-nitrogen and pure-iron simulations with all other parameters the same as the other 1D case, added with the percentages p_{el}. This gives a close resemblance to the other 1D scenario, showing that the reweighting of the composition was done correctly. The reweighting for the spectrum in all cases was again done by the "multiply each event by its weight" method.

The sky maps from the 3D simulation are shown in Fig. 6.7. In Fig. 6.7(a) the sky map is shown before GMF deflections and in Fig. 6.7(b) after GMF deflections. The EGMF is included in both cases. Both sky maps are again for all events between 1 and 16 EeV after reweighting with the "accepting or rejecting" method and in both cases the bin with the most hits is normalized to one. These sky maps look very similar to the pure-proton cases (Fig. 6.4) and show again that before deflections in the GMF a clear structure is visible, whereas these structures are washed out after the deflections in the GMF. Compared with Fig. 6.4, no large differences between the dipole amplitudes of pure-proton or mixed-composition injection are expected.

The results for the dipole amplitude for this scenario are shown in Fig. 6.8. Fig. 6.8(a) shows the cases without deflections in the GMF. The straight line shows the dipole amplitude for a source density of 10^{-3} Mpc^{-3} for the same source realization as in the pure-proton case. The dashed line represents the dipole amplitude for a source density of 10^{-4} Mpc^{-3} for the same source realization as in the pure-proton case. Comparing these

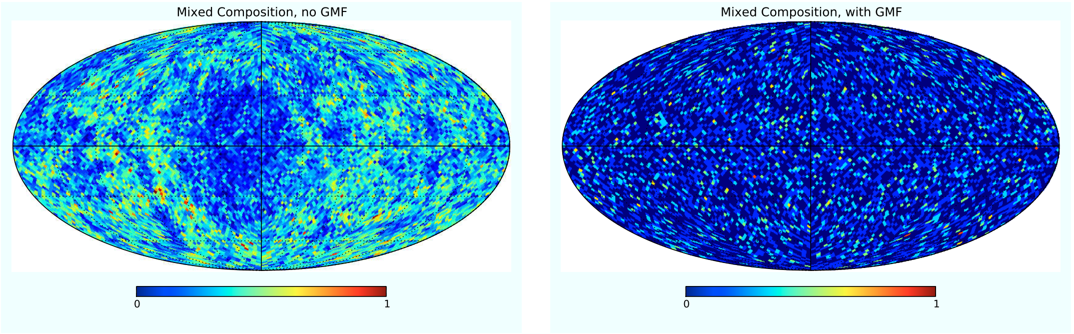

(a) Without GMF (b) With GMF

Figure 6.7: Sky maps of a CRPropa simulation with a mixed composition injected at the sources ($p_\mathrm{p} = 12.7\%$, $p_\mathrm{He} = 0.0\%$, $p_\mathrm{N} = 71.1\%$ and $p_\mathrm{Fe} = 16.2\%$). The spectral index and maximum rigidity at the sources are $\alpha = -1.8$ and $R_\mathrm{max} = 20.0$ EeV. The source density is again 10^{-3} Mpc^{-3} with sources following the Miniati LSS. Deflections in the Miniati EGMF are included. Both sky maps are again for all events with energy between 1 and 16 EeV and in both cases the bin with the most hits is again normalized to one. In the left panel (a) the case before GMF deflections, in the right panel (b) the case after GMF deflections.

two lines shows that in this mixed-composition case the lower-source-density scenario has a slightly lower dipole amplitude than the higher-source-density scenario. The difference is so small, however, that this is probably not significant, although this is the scenario with the most statistics of all dipole-amplitude calculations presented for the Miniati EGMF.

The dotted line indicates again the dipole amplitude of a simulation with a source density of 10^{-3} Mpc^{-3} and with deflections in the EGMF being switched off. This shows, similar to the pure-proton scenario, a dramatic decrease of the dipole amplitude, indicating that the EGMF can introduce a strong dipole in the UHECR sky.

Fig. 6.8(b) shows the same scenarios as Fig. 6.8(a), but now including deflections in the GMF. One should note here that the GMF lens only goes down in energy to 0.1 EeV, so that for heavy elements at low energies the deflections in the GMF might not have been produced correctly. This could cause small errors for the first two energy bins, but does not pose a problem for the two bins with the highest energy.

The same changes are visible as in the pure-proton case. The value for the dipole amplitude for a source density of 10^{-3} Mpc^{-3} including EGMF (straight line) has dropped significantly due to the GMF. However, the dipole amplitude for the same scenario but excluding deflections in the EGMF (dotted line), increased significantly again. This could again point to the washing-out of large structures by the GMF, but if initially no large structures are visible, the structure of the GMF itself appears in the sky. Even though this scenario has slightly better statistics than the pure-proton case, it is still too early to draw any strong conclusions.

The case with a source density of 10^{-4} Mpc^{-3} including EGMF (dashed line) shows again a slightly larger dipole than the same scenario with a source density of 10^{-3} Mpc^{-3}. This is again most likely due to low statistics of the scenario with a source density of 10^{-4} Mpc^{-3}. This scenario has, as in the pure-proton case, around ten times less statistics than the same scenarios with a source density of 10^{-3} Mpc^{-3}. The number of events for each scenario is shown in Tab. 6.3.

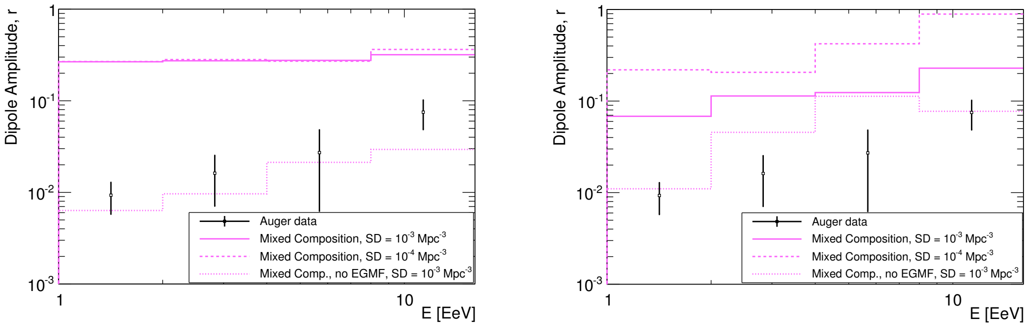

(a) Without GMF

(b) With GMF

Figure 6.8: Dipole amplitude for mixed-composition injection at the sources ($p_{\mathrm{p}} = 12.7\%$, $p_{\mathrm{He}} = 0.0\%$, $p_{\mathrm{N}} = 71.1\%$ and $p_{\mathrm{Fe}} = 16.2\%$). The spectral index and maximum rigidity at injection are $\alpha = -1.8$ and $R_{\mathrm{max}} = 20.0$ EeV. The straight lines show the dipole amplitude for a source density of 10^{-3} Mpc^{-3}. The dashed lines give the dipole amplitude for a source density of 10^{-4} Mpc^{-3}. The dotted lines represent the dipole amplitude of a simulation with a source density of 10^{-3} Mpc^{-3} but without deflections in the EGMF. The left panel (a) shows the cases without deflections in the GMF, whereas the right panel (b) shows the same scenarios with deflections in the GMF. The black data points are, for comparison, the Auger measurements from the left panel of Fig. 5 of Ref. [36].

Table 6.3: Number of events before reweighting between 1 EeV and 16 EeV for the different mixed-composition-injection scenarios.

	Without GMF	With GMF
Source Density 10^{-3} Mpc^{-3}	1×10^7	1×10^6
Source Density 10^{-4} Mpc^{-3}	1×10^6	1×10^5
Source Density 10^{-3} Mpc^{-3}, no EGMF	9×10^6	6×10^5

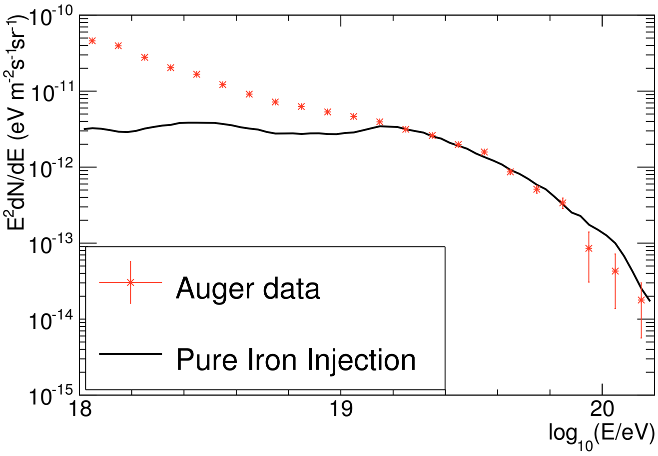

Figure 6.9: In red crosses, the Pierre Auger ICRC 2013 spectrum. The black line shows the CRPropa simulation with pure-iron injection and spectral index and maximum rigidity of $\alpha = -2.0$ and $R_{\max} = 200.0$ EeV. The source density is again 10^{-3} Mpc^{-3} with sources following the Miniati LSS. Deflections in the Miniati EGMF are included. For further simulation parameters, see Sec 6.1.

6.3.3 Iron-injection scenario

The third composition scenario considered here is a pure-iron injection case which should roughly fit the Pierre Auger spectrum above $E = 8$ EeV. The applied spectral index and maximum rigidity at the sources are $\alpha = -2.0$ and $R_{\max} = 200.0$ EeV. These parameters were obtained from Fig. 3 of Ref. [45]. They were determined by comparing a pure-iron injection simulation by eye to the Auger ICRC 2011 UHECR spectrum [298].

There are again a few differences, however, between the simulations done for Ref. [45] and the simulations done here. For instance, in Ref. [45] a sharp cut-off at $R_{\max}$ was implemented, whereas here an exponential cut-off (Eq. 6.1) is used.

In addition, for Ref. [45] 1D simulations including cosmology were done, whereas here 3D simulations have been performed without cosmology but including deflections in EGMFs. Furthermore, for Ref. [45] a continuous source density following a source redshift evolution for the density times CR emissivity of gamma ray burst was implemented (corresponding to the SFR6 model derived in Ref. [307]), whereas here a source density of 10^{-3} Mpc^{-3} with sources following the Miniati LSS is implemented. Besides, for the simulations done here CRPropa 3.0 was used, while for Ref. [307] an older version of CRPropa 2.0 had been deployed.

These differences in the simulations can explain differences between the simulated spectrum of this work and the simulated spectrum of Fig. 3 in Ref. [45]. As can be seen from Fig. 6.9, the simulated spectrum of this work still fits the Pierre Auger ICRC 2013 spectrum reasonably well down to 8 EeV. The reweighting for the spectrum was again done by the "multiply each event by its weight" method.

The sky maps from this simulation are shown in Fig. 6.10. In Fig. 6.10(a) the sky map is shown before GMF deflections and in Fig. 6.10(b) after GMF deflections. The EGMF is included in both cases. Both sky maps are again for all events between 1 and 16 EeV after reweighting with the "accepting or rejecting" method and in both cases the bin with the most hits is normalized to one. These sky maps look again similar to the pure-proton (Fig. 6.4) and mixed-composition (Fig. 6.7) scenarios, except that the number of events is lower. They show again that before deflections in the GMF some structure is visible, whereas these structures are washed out after the deflections

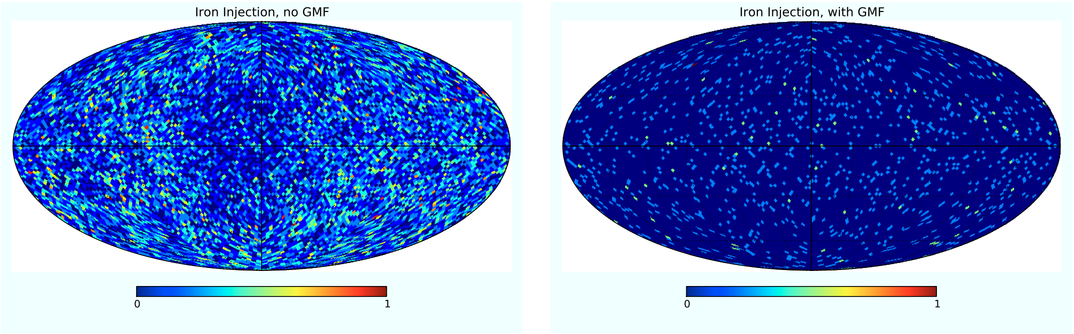

(a) Without GMF

(b) With GMF

Figure 6.10: Sky maps of a CRPropa simulation with a pure-iron injection. The spectral index and maximum rigidity at the sources are $\alpha = -2.0$ and $R_{\max} = 200.0$ EeV. The source density is again 10^{-3} Mpc^{-3} with sources following the Miniati LSS. Deflections in the Miniati EGMF are included. Both sky maps are again for all events with energy between 1 and 16 EeV and in both cases the bin with the most hits is again normalized to one. In the left panel (a) the case before GMF deflections, in the right panel (b) the case after GMF deflections is shown.

in the GMF. Compared with Fig. 6.4 and Fig. 6.7 no large differences between the dipole amplitudes of pure-proton, mixed-composition or pure-iron injection are expected.

The results for the dipole amplitude for this scenario are shown in Fig. 6.11. Note that the spectrum in this case only fits the Auger spectrum above $E > 8$ EeV, so that only the highest energy bin is relevant for comparing with Auger data. Fig. 6.11(a) shows the cases without deflections in the GMF. The straight line shows the dipole amplitude for a source density of 10^{-3} Mpc^{-3} for the same source realization as in the pure-proton and mixed-composition scenarios. The dashed line represents the dipole amplitude for a source density of 10^{-4} Mpc^{-3}, as well for the same source realization as in the pure-proton and mixed-composition case. Comparing these two lines shows that in this case the lower-source-density scenario has again a slightly lower dipole amplitude than the higher-source-density scenario. The difference is small, however, and this scenario has the lowest statistics of the three scenarios presented here, so that this is probably not significant.

The dotted line indicates again the dipole amplitude of a simulation with a source density of 10^{-3} Mpc^{-3} and with deflections in the EGMF switched off. This shows, similar to the pure-proton and mixed-composition scenarios, a dramatic decrease of the dipole amplitude, indicating again that the EGMF can introduce a strong dipole in the UHECR sky.

Fig. 6.11(b) shows the same scenarios as Fig. 6.11(a), but now including deflections in the GMF. One should note here again that the GMF lens only goes down in energy to 0.1 EeV, so that for heavy elements at low energies the deflections in the GMF might not have been calculated correctly. This could cause small errors for the first two energy bins, but does not pose a problem for the bins with the highest energy. As the spectrum in this scenario only fits the Auger spectrum above $E > 8$ EeV, the highest energy bin is anyway the only relevant bin for comparing with Auger data.

Similar changes are again visible, however less pronounced due to the lower statistics, as in the pure-proton and mixed-composition cases. The value for the dipole amplitude for a source density of 10^{-3} Mpc^{-3} including EGMF (straight line), has dropped due to the GMF. However, the dipole amplitude for the same scenario but excluding deflections in the EGMF (dotted line), increased significantly again. This could again point to the

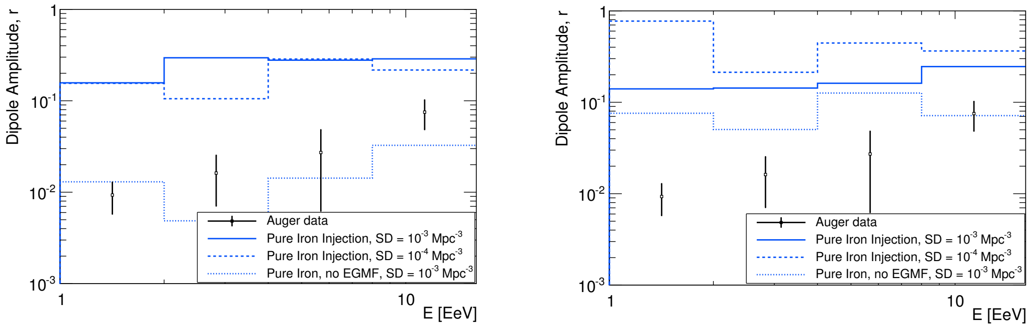

(a) Without GMF

(b) With GMF

Figure 6.11: Dipole amplitude for the pure-iron-injection scenario. The spectral index and maximum rigidity at injection are $\alpha = -2.0$ and $R_{\max} = 200.0$ EeV. The straight lines show the dipole amplitude for a source density of 10^{-3} Mpc^{-3}. The dashed lines give the dipole amplitude for a source density of 10^{-4} Mpc^{-3}. The dotted lines represent the dipole amplitude of a simulation with a source density of 10^{-3} Mpc^{-3} but without deflections in the EGMF. The left panel (a) shows the cases without deflections in the GMF, whereas the right panel (b) shows the same scenarios with deflections in the GMF. The black data points are, for comparison, the Auger measurements from the left panel of Fig. 5 of Ref. [36].

Table 6.4: Number of events before reweighting between 1 EeV and 16 EeV for the different pure-iron-injection scenarios.

	Without GMF	With GMF
Source Density 10^{-3} Mpc^{-3}	6×10^{6}	4×10^{5}
Source Density 10^{-4} Mpc^{-3}	6×10^{5}	4×10^{4}
Source Density 10^{-3} Mpc^{-3}, no EGMF	8×10^{5}	6×10^{4}

washing-out of large structures by the GMF, but if no large structures are visible to begin with, the structure of the GMF itself appears in the sky. This scenario has, however, the lowest statistics of the three scenarios presented here for the Miniati EGMF, so no firm conclusions should be drawn from these results.

The case with a source density of 10^{-4} Mpc^{-3} including EGMF (dashed line) shows again a slightly larger dipole than the same scenario with a source density of 10^{-3} Mpc^{-3}. This is again most likely due to low statistics of the scenario with a source density of 10^{-4} Mpc^{-3}. This scenario has, as in the pure-proton and mixed-composition cases, one order of magnitude less statistics than the same scenarios with a source density of 10^{-3} Mpc^{-3}. The number of events for each scenario are shown in Tab. 6.4.

6.4 Results for the benchmark scenario

Here the same analysis has been started, but for sources following the Dolag LSS [145, 293] and deflections in the benchmark EGMF (see Sec. 5.6.1 for details on this magnetic-field setup). This was done in order to investigate if the previously obtained results change for a different EGMF setup, as well as to switch to a constrained LSS and EGMF scenario which more-closely resembles the local universe. In this case the observer position is fixed, which also eliminates the possible dependence on that parameter.

While this work is still in progress, some first preliminary results of simulated sky

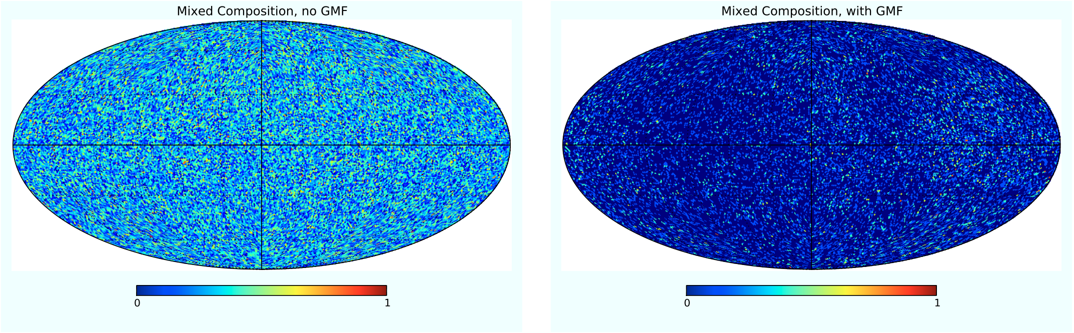

(a) Without GMF (b) With GMF

Figure 6.12: Sky maps of a CRPropa simulation with a mixed composition injected at the sources ($p_{\mathrm{p}} = 12.7\%$, $p_{\mathrm{He}} = 0.0\%$, $p_{\mathrm{N}} = 71.1\%$ and $p_{\mathrm{Fe}} = 16.2\%$). The spectral index and maximum rigidity at the sources are $\alpha = -1.8$ and $R_{\mathrm{max}} = 20.0$ EeV, respectively. The source density is 10^{-3} Mpc^{-3} with sources following the Dolag LSS. Deflections in the benchmark EGMF are included. The sky maps are again presented for all events with energy between 1 and 16 EeV and the bin with the most hits is again normalized to one. In the left panel (a) the case before GMF deflections, in the right panel (b) the case after GMF deflections is given.

maps are shown here. Fig. 6.12 shows the sky map of a CRPropa simulation with a mixed-composition injected at the sources ($p_{\mathrm{p}} = 12.7\%$, $p_{\mathrm{He}} = 0.0\%$, $p_{\mathrm{N}} = 71.1\%$ and $p_{\mathrm{Fe}} = 16.2\%$). The spectral index and maximum rigidity at the sources are $\alpha = -1.8$ and $R_{\mathrm{max}} = 20.0$ EeV, respectively. The source density is 10^{-3} Mpc^{-3}. All these parameters are the same as for the mixed-composition scenario with the Miniati field. The sky maps are again for all events with energy between 1 and 16 EeV and the bin with the most hits is again normalized to one. Fig. 6.12(a) shows the incoming directions at the edge of the galaxy, it does not include deflections in the GMF. The case including deflections in the GMF is shown in Fig. 6.12(b). While before deflections in the GMF the sky looks, at least by eye, relatively isotropic, after deflections in the GMF a deviation from isotropy seems to be visible.

6.4.1 Effects due to double counting

During the simulated propagation of the UHECRs it can happen that the same particle is detected more than once. For instance, when an UHECRs enters the observer sphere, and is thus registered as detected, it can then continue its propagation to leave the observer sphere, get turned around by deflections in the EGMF, and enter the observer sphere again, therefore being detected a second time. Even though the same particle would, in reality, never be detected twice, it is still correct to include this effect is the simulations. This is due to that the simulated observer sphere is much larger than the actual realistic observer.

For example, consider the scenario in which there is a strong nearby source in a specific position in the sky emitting particles in all directions and the observer is located in a region with a relatively strong magnetic field. In that case, in reality, only a very small fraction of the particles emitted by the source will hit the observer right away. The particles would be very likely to miss the observer in their first pass, get turned around by the magnetic fields in the vicinity of the observer, and hit the observer from the other side. However, if we now, instead of a realistic small observer, have a large observer sphere (as in the simulations) the particles coming from that specific source are very likely to be detected right away in their first pass towards the observer position. If

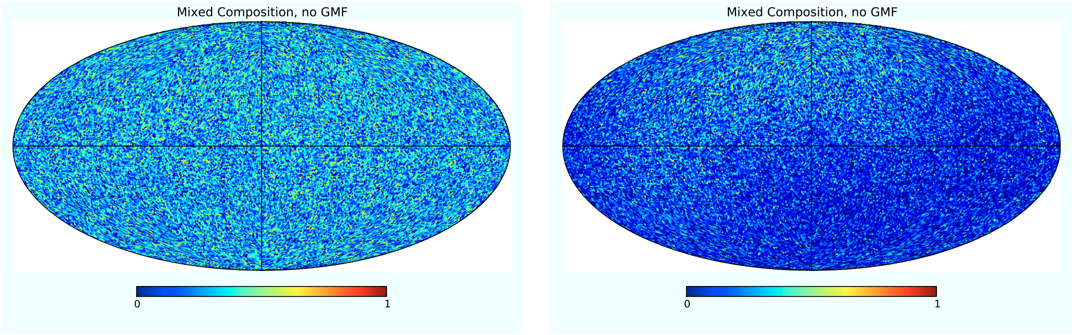

(a) With double counting (b) Without double counting

Figure 6.13: Sky maps with and without allowing for the double-counting of cosmic-ray trajectories. In the left panel (a), for comparison, the same sky map as Fig. 6.12(a) is shown. In the right panel (b) the skymap for the same simulation is shown, but without allowing for the double counting of cosmic-ray trajectories.

these particles would not be allowed to continue on, the fact that they could be turned around hit the observer from the other side is neglected.

For the benchmark scenario a significant change in the distribution of events in the sky was found when not allowing for this double counting. For example, Fig. 6.13(b) shows the sky map (before deflections in the GMF) of the same mixed-composition scenario as shown in Fig. 6.12(a) (shown again, for comparison, in Fig. 6.13(a)) but only including the first observation of every cosmic-ray trajectory. About 25% of all events were ignored due to this limitation. For the simulations with the Miniati EGMF no significant differences were found when including or excluding this double counting.

Chapter 7

Conclusions and outlook

There are still many open questions concerning the interpretation of the measurements on ultra-high-energy cosmic rays (UHECRs). In order to be able to interpret these measurements in terms of the different possible astrophysical scenarios, and thus to investigate what the sources of UHECRs and their characteristics are, dedicated simulations of the propagation of UHECRs from their sources to Earth are needed. CRPropa is a publicly available software package which is designed to simulate this propagation for UHE protons and nuclei as well as for their secondary photons and neutrinos. From simulations with CRPropa realistic energy spectra, mass compositions and arrival directions can be obtained.

Version 2.0 of CRPropa has been publicly released and is discussed in Chapter 2. Several example applications are shown there as well. With these examples the possibility to include cosmological evolution effects as well as the propagation of secondary neutrinos and photons is shown. Furthermore, the effects of different initial source compositions on the UHECR spectrum, the cosmogenic-neutrino and -photon spectra and the mass-number abundance at observation are indicated. Both the discussed source-composition scenarios, a mixed-composition injection scenario and a pure-iron injection scenario, can provide an UHECR spectrum that resembles the measured spectrum reasonably well, at least above the ankle for the pure-iron injection case and for the whole energy range of 1-100 EeV in the mixed-composition scenario. In the case of pure-iron injection at the sources the cosmogenic neutrino and photon fluxes are reduced significantly compared with the mixed-composition injection. This is due to photodisintegration dominating with respect to pion production for the heavier composition.

Furthermore, the possibility to do three-dimensional (3D) simulations with sources following the large-scale-structure (LSS) baryon density and including deflections in structured extragalactic magnetic fields (EGMFs) is shown. Here a significant difference in the shape of the spectrum for pure-iron injection compared with pure-proton injection, leaving all other simulation parameters the same, is found. The effects of deflections in the EGMF and a source distribution following the LSS on the spectrum are, however, very small. The detected composition, for initial pure-iron injection, is affected by the deflections in the EGMF. As these deflections increase the propagation path length from specific sources to the observer, more interactions will occur during the propagation, lowering the average mass at detection. The fact that the distance from their source as a function of the propagation time decreases drastically due to deflections in the EGMF is shown as well.

Moreover, an example which shows the possibility to have observer spheres at different distances from one single source, in order to be able to investigate the UHECR characteristics as a function of the distance to the source, is discussed. The cosmic-ray spectra at different distances from the source indicate that the flux at the highest energies is increasingly reduced, due to the increase in path length and thus in number of energy-loss interactions, as the distance from the source increases. The sky maps become more anisotropic with increasing distance from the source as well. This is due to the increase of deflections with larger travel distances in the structured EGMFs.

These examples show some of the many possible applications of CRPropa. With all the different aspects of CRPropa, discussed in Chapter 2, it is the most complete publicly-available UHECR propagation code at the moment. With the upcoming release of CRPropa 3.0, reviewed in Chapter 5, this will even be improved upon.

An integral part of CRPropa is its photodisintegration setup. In Chapter 3 this is compared extensively with the photodisintegration scheme developed by Puget, Stecker and Bredekamp (PSB). Significant differences between the two photodisintegration setups were found. This was, however, also expected as the PSB scheme uses a relatively simple parametrization of the cross sections including only a limited number of exclusive channels and a reduced reaction network involving only one nucleus for each atomic mass number A. On the other hand, the photodisintegration cross sections for all possible isotopes and exclusive channels given by the advanced code called TALYS are implemented in CRPropa. Especially the photodisintegration channels where a helium nucleus is emitted, which are neglected in the PSB case, give rise to significant differences between the two setups. Additionally, noticeable differences in the energy thresholds for photodisintegration were found for mass numbers $9 \leq A \leq 11$. As TALYS is not reliable for $A < 12$, in the CRPropa setup additional photodisintegration-cross-section parameterizations were added in this mass range. This led to additional investigations and improvements on the energy thresholds for these mass numbers in the CRPropa setup.

An additional application of CRPropa 2.0 is discussed in Chapter 4. There the cosmogenic-neutrino and -photon fluxes are shown for several different scenarios, with the UHECR spectrum normalized to the measured spectrum by the Pierre Auger Observatory (Auger). The simulated cosmogenic neutrino fluxes are compared with the neutrino-flux measurements of the IceCube Neutrino Observatory (IceCube) at PeV energies. The largest neutrino fluxes occur for the pure-proton scenarios. The impact of the different production mechanisms of cosmogenic neutrinos on the fluxes at PeV energies is shown. We found that the neutrinos resulting from the decay of neutrons produced in photopion interactions with the cosmic microwave background (CMB) or in photodisintegration reactions of heavy nuclei make a negligible contribution at these energies. The neutrinos resulting from pion decays created during photopion production with the UV/optical/infrared background (IRB) provide the dominant contribution at PeV energies.

The neutrino flux is increased when considering stronger source evolutions with redshift. However, in those cases the predicted photon flux also increases, and for strong source-evolution models like the ones of Fanaroff Riley active galactic nuclei the cosmogenic photon flux is on the verge of conflicting with the diffuse gamma-ray flux observed by Fermi LAT. Therefore, even stronger source-evolution models are disfavored.

Even in the most positive scenario presented in this work, the neutrino flux still remains about one order of magnitude below the flux level measured by IceCube at PeV energies. Therefore, we concluded that it is unlikely that the dominant contribution to the observed neutrinos by IceCube are of cosmogenic origin.

In the near future more data of IceCube will become available. If they will also find neutrino events at even higher energies (in the PeV to EeV range), or if they will set stringent limits on the neutrino flux in this energy range, follow-up investigations can show whether a cosmogenic origin of the measured flux is completely ruled out, or set strong bound on specific UHECR models. Furthermore, upcoming improvements on the measurements of the composition of UHECRs will impact the range of possible cosmogenic-neutrino and -photon flux scenarios strongly. At the moment a paper is in progress for the whole Pierre Auger Collaboration on combined fits with CRPropa to the UHECR spectrum and composition measurements. It will be interesting to also calculate the expected cosmogenic-neutrino and -photon flux for the best-fit scenarios found in that paper.

At the moment version 3.0 of CRPropa is under development. In Chapter 5 the changes in this version of CRPropa are discussed. For instance, CRPropa 3.0 incorporates a complete redesign of the code structure. It is now composed of independent modules which access and modify a cosmic-ray candidate. This modular structure allows for new use cases, easier testing, maintenance and physics extensions and it facilitates high-performance computing.

While the steering of CRPropa 2.0 was only possible with XML steering cards, CRPropa 3.0 can now as well be run through Python bindings. This allows for a more flexible way of steering the code in a high-level scripting language as well as for an interactive way of running the simulations. Moreover, it is possible to write custom simulation modules in Python to be used in combination with the existing C++ modules as well.

New physical features of CRPropa 3.0 include a four-dimensional mode, which allows to take into account cosmological effects as well as deflections in magnetic fields in a single simulation. Furthermore, the possibility to propagate cosmic rays through the galactic magnetic field (GMF) through an efficient lensing technique is developed. Additionally, new techniques to handle large extragalactic magnetic fields (EGMFs) and matter distributions, additional IRB models, an additional way to propagate electromagnetic cascades, updated photodisintegration cross sections and improvements on the interpolations for redshift evolution will be added.

At the moment work is in progress on finalizing the last improvements on CRPropa 3.0 and it will be officially released with an accompanying paper soon. Even after this release the development of CRPropa will continue. In the mean time progress is being made towards a paper on comparisons between CRPropa 3.0 and another UHECR propagation code called SimProp.

Taking into account deflections in the GMF, one of the new features in CRPropa 3.0, is especially important for anisotropy studies. In that light, an application of CRPropa 3.0 is discussed in Chapter 6. Here the dipole amplitudes are calculated for three-dimensional simulations in a structured EGMF, including deflections in the GMF. These dipole-amplitude calculations are compared with dipole-amplitude measurements of Auger. The effects of deflections in the EGMF and in the GMF, as well as the dependence on the source density, are investigated separately.

This study shows that, in the case without deflections in the GMF, a significant dipole amplitude can occur just due to deflections in the EGMF. While, with the same source distribution and without deflections in the EGMF, negligible dipole amplitudes were found, including the deflections in the EGMF gave dipole amplitudes significantly larger than the measured dipole amplitudes by Auger. This could be due to the fact that, in the case with deflections in the EGMF, the cosmic rays are directed along the large-scale structures in the EGMF and they will not be able to reach distances as far away from their sources as when traveling in straight lines. Therefore, the local structures in the EGMF could be visible in the UHECR sky.

When including the deflections in the GMF, the dipole amplitude for the case with deflections in the EGMF is significantly reduced, but still exceeds the dipole amplitude measurements by Auger. The GMF washes out the structures that were visible before the deflections in the GMF. The dipole amplitude actually increases after the deflections in the GMF in the case without deflections in the EGMF. This might be due to structures in the GMF becoming visible when starting with small deviations from isotropy, but it is too early to tell if this is a real effect or if this is due to limited statistics after deflections in the GMF.

The dipole-amplitude calculations (for the case including deflections in the EGMF) have been done for two different source densities, the higher source density being one order of magnitude higher than the lower source density. In the case before deflections in the GMF no significant difference is visible between the lower and higher source density cases. However, when looking at the scenario including deflections in the GMF, an increase in dipole amplitude is observed for the lower source density with respect to the higher source density. But, when no difference due to the source density is visible before deflections in the GMF, there should also not be any difference after deflections in the GMF. Therefore, this is probably due to too low statistics, as especially the case with the lower source density after deflections in the GMF suffers from low statistics.

The dipole amplitudes have been calculated for three different composition scenarios, pure-proton injection, pure-iron injection and a mixed-composition injection scenario. For all these cases the above conclusions hold.

This investigation was done for an unconstrained EGMF model, meaning that the results could depend on the observer position. As a follow up on this research the same analysis will be done for simulations in a constrained EGMF model, where the observer position is fixed and which better represents the local EGMF and large-scale structure. Some first preliminary results of sky maps for this EGMF setup are already shown in this thesis. The analysis of this investigation will be done with a larger number of simulated events as well as for a different method of calculating the deflections in the GMF, which should suffer less from decreasing statistics. Furthermore, more values for the source density will be tested. It is planned to include calculations of higher multiple moments as well.

Appendix A

PSB tables as implemented in CRPropa

Here the tables with the different parameters of the Puget, Stecker and Bredekamp (PSB) [8] cross-section set up, as has been implemented in CRPropa, are given. Values given in Tables 1 and 2 of Ref. [8] and Table 1 of Ref. [9] have been used for the data developed for CRPropa.

Note that in Table A.3, compared with Table A.1, the parameters for mass number $A = 12$, 9 and 2 are not shown. This is due to PSB considering the two-nucleon emission being negligible for $A = 12$ and 9 and two-nucleon emission not being possible for $A = 2$. Furthermore, the parameters for $A = [5...8]$ are not included for either case. In the PSB setup implemented in CRPropa, if a particle ends up in this regime, it is assumed to photodisintegrate or decay immediately to $A = 4$ plus secondaries. If ^{9}Be photodisintegrates it is assumed to go through the following process: $^9\text{Be}+\gamma \rightarrow n+2{\cdot}^4\text{He}$, leaving only particles with $A \leq 4$.

Table A.1: Cross section parameters for the PSB photodisintegration setup (based on Table 1 of Ref. [8] and Table 1 of Ref. [9]) as used in CRPropa for one-nucleon photodisintegration. Furthermore, the parameter ζ for the total strength of the interaction between ϵ'_1 and ϵ'_{max} is shown as well.

A	Z	$\epsilon'_{\text{min},1}$ (MeV)	$\epsilon'_{0,1}$ (MeV)	ξ_1	Δ_1 (MeV)	ζ
56	26	10.2	18	0.98	8	0.95
55	25	8.1	18	0.93	7	0.95
54	24	9.7	18	0.93	7	0.95
53	24	7.9	18	1.03	7	0.95
52	24	10.5	18	1.08	7	0.95
51	23	8.1	19	1.02	7	0.95
50	22	10.9	19	1.03	8	0.95
49	22	8.1	19	1.03	8	0.95

Table A.2: Table A.1 continued.

A	Z	$\epsilon'_{\mathrm{min},1}$ (MeV)	$\epsilon'_{0,1}$ (MeV)	ξ_1	Δ_1 (MeV)	ζ
48	22	11.4	19	1.03	8	0.95
47	22	8.9	19	1.03	8	0.95
46	22	10.3	19	1.03	8	0.95
45	21	6.9	19	0.97	9	0.95
44	20	11.1	20	0.92	9	0.96
43	20	7.9	20	0.97	8	0.96
42	20	10.3	20	1.02	7	0.96
41	20	7.8	20	0.92	6	0.96
40	20	8.3	20	0.84	6	0.96
39	19	6.4	20	0.73	7	0.98
38	18	10.2	18	0.86	8	0.98
37	17	8.4	20	0.81	7	1.00
36	16	9.9	22	0.82	12	1.00
35	16	6.4	20	0.87	7	1.00
34	16	10.9	22	0.87	12	1.00
33	16	8.6	22	0.82	12	1.00
32	16	8.9	22	0.97	12	1.00
31	15	7.3	21	0.85	8	1.02
30	14	10.6	20	0.83	7	1.04
29	14	8.5	20	0.83	7	1.04
28	14	11.6	21	1.01	8	1.04
27	13	8.3	21	0.80	8	1.05
26	12	11.1	18	0.77	8	1.08
25	12	7.3	23	0.77	9	1.08
24	12	11.7	19	0.94	11	1.08
23	11	8.8	22	0.83	12	1.09
22	10	10.4	22	0.81	12	1.09
21	10	6.8	22	0.84	12	1.09
20	10	12.8	22	0.87	12	1.09
19	9	8.0	23	0.76	14	1.10
18	8	8.0	24	0.67	9	1.10
17	8	4.1	24	0.77	9	1.10
16	8	12.1	24	0.83	9	1.10
15	7	10.2	23	0.73	10	1.07
14	7	7.6	23	0.46	10	1.07
13	6	4.9	23	0.71	8	1.06
12	6	16.0	23	0.76	6	1.06
11	5	11.2	26	0.85	11	1.03
10	5	6.6	25	0.54	11	1.03
9	4	1.7	26	0.67	20	1.00
4	2	19.8	27	0.47	12	1.11
3	2	5.5	13	0.33	18	1.11
2	1	2.2	5	0.97	3	1.

Table A.3: Cross section parameters for the PSB photodisintegration setup (based on Table 1 of Ref. [8] and Table 1 of Ref. [9]) as used in CRPropa for two-nucleon photodisintegration.

A	Z	$\epsilon'_{\mathrm{min},2}$ (MeV)	$\epsilon'_{0,2}$ (MeV)	ξ_2	Δ_2 (MeV)
56	26	18.3	22	0.15	7
55	25	17.8	23.5	0.20	8
54	24	17.7	24	0.20	8
53	24	18.4	24	0.10	8
52	24	18.6	24	0.05	8
51	23	19.0	25	0.11	6
50	22	19.1	25	0.10	6
49	22	19.6	25	0.10	6
48	22	19.9	25	0.10	6
47	22	18.7	25	0.10	6
46	22	17.2	25	0.10	6
45	21	18.0	26	0.15	8
44	20	19.1	26	0.20	8
43	20	18.2	26	0.15	8
42	20	18.1	26	0.15	8
41	20	17.7	26	0.20	8
40	20	14.7	26	0.28	10
39	19	16.6	25	0.38	12
38	18	18.6	22	0.24	8
37	17	18.3	24	0.28	7
36	16	16.9	22	0.25	12
35	16	17.3	26	0.22	10
34	16	20.1	22	0.20	12
33	16	17.5	22	0.25	12
32	16	16.2	30	0.10	12
31	15	17.9	29	0.20	12
30	14	19.1	26	0.20	8
29	14	20.1	26	0.20	8
28	14	19.9	30	0.02	8
27	13	19.4	29	0.20	12
26	12	18.4	26	0.20	8
25	12	19.0	28	0.20	7
24	12	20.5	29	0.03	6
23	11	19.2	25	0.12	10
22	10	17.1	21	0.11	4
21	10	19.6	25	0.08	6
20	10	20.8	26	0.05	8
19	9	16.0	29	0.14	14
18	8	12.2	29	0.20	10
17	8	16.3	29	0.20	10
16	8	22.3	30	0.04	10
15	7	18.4	23	0.10	10

Table A.4: Table A.3 continued.

A	Z	$\epsilon'_{\mathrm{min},2}$ (MeV)	$\epsilon'_{0,2}$ (MeV)	ξ_2	Δ_2 (MeV)
14	7	12.5	23	0.37	10
13	6	20.9	27	0.05	8
11	5	18.0	26	0.15	11
10	5	8.3	25	0.15	11
4	2	26.1	45	0.11	40
3	2	5.5	15	0.33	13

Table A.5: Branching ratios f_i (based on Table 2 of Ref. [8]) for i-nucleon emission in the ϵ'_1 - ϵ'_{max} energy range used in the PSB setup for CRPropa.

A	i	f_i	Channel
4	1	0.8	
	2	0.2	
9	1	1	$^9\mathrm{Be}+\gamma \rightarrow n + 2\cdot{}^4\mathrm{He}$
10-22	1	0.1	
	2	0.3	
	3	0.1	
	4	0.1	
	5	0.2	
	6	0.2	
23-56	1	0.10	
	2	0.35	
	3	0.10	
	4	0.05	
	5	0.15	
	6	0.045	
	7	0.04	
	8	0.035	
	9	0.03	
	10	0.025	
	11	0.02	
	12	0.018	
	13	0.015	
	14	0.012	
	15	0.01	

Bibliography

[1] K.-H. Kampert, J. Kulbartz, L. Maccione, N. Nierstenhoefer, P. Schiffer *et al.*, *CRPropa 2.0 – a public framework for propagating high energy nuclei, secondary gamma rays and neutrinos*, Astropart. Phys. **42** (2013) 41–51. doi:10.1016/j.astropartphys.2012.12.001 [`arXiv:1206.3132[astro-ph.IM]`].

[2] K.-H. Kampert, J. Kulbartz, L. Maccione, N. Nierstenhoefer, P. Schiffer *et al.*, "CRPropa 2.0 user guide." crpropa.desy.de.

[3] G. Sigl, F. Miniati and T. A. Ensslin, *Ultrahigh energy cosmic ray probes of large scale structure and magnetic fields*, Phys. Rev. **D70** (2004) 043007. doi:10.1103/PhysRevD.70.043007 [`arXiv:astro-ph/0401084`].

[4] R. Alves Batista, M. Erdmann, C. Evoli, K.-H. Kampert, D. Kuempel *et al.*, *Cosmic ray propagation with CRPropa 3*, `arXiv:1410.5323[astro-ph.IM]`.

[5] D. Walz, "Private communication."

[6] R. Alves Batista, "Private communication."

[7] M. Erdmann, D. Kuempel, G. Mueller, G. Sigl, D. Walz and T. Winchen, *A benchmark scenario for UHECR propagation*, Auger internal note GAP-2012-138.

[8] J. L. Puget, F. W. Stecker and J. H. Bredekamp, *Photonuclear interactions of ultrahigh-energy cosmic rays and their astrophysical consequences*, Astrophys. J. **205** (1976) 638–654. doi:10.1086/154321.

[9] F. W. Stecker and M. H. Salamon, *Photodisintegration of ultrahigh-energy cosmic rays: A new determination*, Astrophys. J. **512** (1999) 521–526. doi:10.1086/306816 [`arXiv:astro-ph/9808110`].

[10] **HiRes Collaboration**, R. U. Abbasi *et al.*, *First observation of the Greisen-Zatsepin-Kuzmin suppression*, Phys. Rev. Lett. **100** (2008) 101101. doi:10.1103/PhysRevLett.100.101101 [`arXiv:astro-ph/0703099`].

[11] **Telescope Array Collaboration**, T. Abu-Zayyad *et al.*, *The cosmic ray energy spectrum observed with the surface detector of the Telescope Array experiment*, Astrophys. J. **768** (2013) L1. doi:10.1088/2041-8205/768/1/L1 [`arXiv:1205.5067[astro-ph.HE]`].

[12] **Telescope Array Collaboration, Pierre Auger Collaboration**, T. Abu-Zayyad *et al.*, *Pierre Auger Observatory and Telescope Array: Joint Contributions to the 33rd International Cosmic Ray Conference (ICRC 2013)*, `arXiv:1310.0647[astro-ph.HE]`.

[13] **Pierre Auger Collaboration**, A. Aab *et al.*, *Highlights from the Pierre Auger Observatory*, Braz. J. Phys. **44** (2014) 560–570. doi:10.1007/s13538-014-0218-6 [`arXiv:1310.4620[astro-ph.HE]`].

[14] C. T. Hill and D. N. Schramm, *The ultrahigh-energy cosmic ray spectrum*, Phys. Rev. **D31** (1985) 564. doi:10.1103/PhysRevD.31.564.

[15] V. Berezinsky, A. Z. Gazizov and S. I. Grigorieva, *On astrophysical solution to ultrahigh-energy cosmic rays*, Phys. Rev. **D74** (2006) 043005. doi:10.1103/PhysRevD.74.043005 [`arXiv:hep-ph/0204357`].

[16] R. Aloisio, V. Berezinsky, P. Blasi, A. Gazizov, S. Grigorieva *et al.*, *A dip in the UHECR spectrum and the transition from galactic to extragalactic cosmic rays*, Astropart. Phys. **27** (2007) 76–91. doi:10.1016/j.astropartphys.2006.09.004 [`arXiv:astro-ph/0608219`].

[17] S. D. Wick, C. D. Dermer and A. Atoyan, *High-energy cosmic rays from gamma-ray bursts*, Astropart. Phys. **21** (2004) 125–148. doi:10.1016/j.astropartphys.2003.12.008 [`arXiv:astro-ph/0310667`].

[18] D. Allard, E. Parizot and A. V. Olinto, *On the transition from galactic to extragalactic cosmic-rays: spectral and composition features from two opposite scenarios*, Astropart. Phys. **27** (2007) 61–75. doi:10.1016/j.astropartphys.2006.09.006 [`arXiv:astro-ph/0512345`].

[19] D. Hooper and A. M. Taylor, *On the heavy chemical composition of the ultra-high energy cosmic rays*, Astropart. Phys. **33** (2010) 151–159. doi:10.1016/j.astropartphys.2010.01.003 [`arXiv:0910.1842[astro-ph.HE]`].

[20] A. M. Taylor, *UHECR composition models*, Astropart. Phys. **54** (2014) 48–53. doi:10.1016/j.astropartphys.2013.11.006 [`arXiv:1401.0199[astro-ph.HE]`].

[21] R. Aloisio, V. Berezinsky and P. Blasi, *Ultra high energy cosmic rays: implications of Auger data for source spectra and chemical composition*, JCAP **1410** (2014), no. 10 020. doi:10.1088/1475-7516/2014/10/020 [`arXiv:1312.7459[astro-ph.HE]`].

[22] R. Aloisio, V. Berezinsky and A. Gazizov, *Ultra high energy cosmic rays: The disappointing model*, Astropart. Phys. **34** (2011) 620–626. doi:10.1016/j.astropartphys.2010.12.008 [`arXiv:0907.5194[astro-ph.HE]`].

[23] A. Calvez, A. Kusenko and S. Nagataki, *The role of Galactic sources and magnetic fields in forming the observed energy-dependent composition of ultrahigh-energy cosmic rays*, Phys. Rev. Lett. **105** (2010) 091101. doi:10.1103/PhysRevLett.105.091101 [`arXiv:1004.2535[astro-ph.HE]`].

[24] **Pierre Auger Collaboration**, J. Abraham *et al.*, *Measurement of the depth of maximum of extensive air showers above* 10^{18} *eV*, Phys. Rev. Lett. **104** (2010) 091101. doi:10.1103/PhysRevLett.104.091101 [`arXiv:1002.0699[astro-ph.HE]`].

[25] **Pierre Auger Collaboration**, A. Aab *et al.*, *Depth of maximum of air-shower profiles at the Pierre Auger Observatory: Measurements at energies above* $10^{17.8}$ *eV*, Phys. Rev. D (2014) [`arXiv:1409.4809[astro-ph.HE]`].

[26] **Pierre Auger Collaboration**, A. Aab *et al.*, *Depth of maximum of air-shower profiles at the Pierre Auger Observatory: Composition implications*, Phys. Rev. D (2014) [`arXiv:1409.5083[astro-ph.HE]`].

[27] **Pierre Auger Collaboration**, J. Abraham *et al.*, *Correlation of the highest energy cosmic rays with nearby extragalactic objects*, Science **318** (2007) 938–943. doi:10.1126/science.1151124 [`arXiv:0711.2256[astro-ph]`].

[28] **Pierre Auger Collaboration**, P. Abreu *et al.*, *Update on the correlation of the highest energy cosmic rays with nearby extragalactic matter*, Astropart. Phys. **34** (2010) 314–326. doi:10.1016/j.astropartphys.2010.08.010 [`arXiv:1009.1855[astro-ph.HE]`].

[29] **Pierre Auger Collaboration**, P. Abreu *et al.*, *Anisotropy and chemical composition of ultra-high energy cosmic rays using arrival directions measured by the Pierre Auger Observatory*, JCAP **1106** (2011) 022. doi:10.1088/1475-7516/2011/06/022 [`arXiv:1106.3048[astro-ph.HE]`].

[30] **Pierre Auger Collaboration**, P. Abreu *et al.*, *A search for anisotropy in the arrival directions of ultra high energy cosmic rays recorded at the Pierre Auger Observatory*, JCAP **1204** (2012) 040. doi:10.1088/1475-7516/2012/04/040 [`arXiv:1210.3602[astro-ph.HE]`].

[31] **Telescope Array Collaboration**, T. Abu-Zayyad *et al.*, *Search for anisotropy of ultra-high energy cosmic rays with the Telescope Array Experiment*, Astrophys. J. **757** (2012) 26. doi:10.1088/0004-637X/757/1/26 [`arXiv:1205.5984[astro-ph.HE]`].

[32] **Pierre Auger Collaboration**, K.-H. Kampert, *Highlights from the Pierre Auger Observatory*, `arXiv:1207.4823[astro-ph.HE]`.

[33] **Telescope Array** in *Proc. of the 33rd Int. Cosmic Ray Conf.*, 2013. Brazil.

[34] **Pierre Auger Collaboration**, A. Aab *et al.*, *The Pierre Auger Observatory: Contributions to the 33rd International Cosmic Ray Conference (ICRC 2013)*, `arXiv:1307.5059[astro-ph.HE]`.

[35] **Pierre Auger Collaboration**, P. Abreu *et al.*, *Constraints on the origin of cosmic rays above* 10^{18} *eV from large scale anisotropy searches in data of the Pierre Auger Observatory*, Astrophys. J. **762** (2012) L13. doi:10.1088/2041-8205/762/1/L13 [`arXiv:1212.3083[astro-ph.HE]`].

[36] **Pierre Auger Collaboration**, P. Abreu *et al.*, *Large scale distribution of arrival directions of cosmic rays detected above* 10^{18} *eV at the Pierre Auger Observatory*, Astrophys. J. Suppl. **203** (2012) 34. doi:10.1088/0067-0049/203/2/34 [`arXiv:1210.3736[astro-ph.HE]`].

[37] **Telescope Array Collaboration, Pierre Auger Collaboration**, A. Aab *et al.*, *Searches for large-scale anisotropy in the arrival directions of cosmic rays detected above energy of* 10^{19} *eV at the Pierre Auger Observatory and the Telescope Array*, Astrophys. J. (2014) [`arXiv:1409.3128[astro-ph.HE]`].

[38] **Telescope Array Collaboration**, R. U. Abbasi *et al.*, *Indications of intermediate-scale anisotropy of cosmic rays with energy greater than 57 EeV in the northern sky measured with the surface detector of the Telescope Array experiment*, Astrophys. J. **790** (2014) L21. doi:10.1088/2041-8205/790/2/L21 [`arXiv:1404.5890[astro-ph.HE]`].

[39] **IceCube Collaboration**, M. G. Aartsen *et al.*, *First observation of PeV-energy neutrinos with IceCube*, Phys. Rev. Lett. **111** (2013), no. 2 021103. doi:10.1103/PhysRevLett.111.021103 [`arXiv:1304.5356[astro-ph.HE]`].

[40] **IceCube Collaboration**, M. G. Aartsen *et al.*, *Evidence for high-energy extraterrestrial neutrinos at the IceCube detector*, Science **342** (2013), no. 6161 1242856. doi:10.1126/science.1242856 [`arXiv:1311.5238[astro-ph.HE]`].

[41] **IceCube Collaboration**, M. G. Aartsen *et al.*, *Observation of high-energy astrophysical neutrinos in three years of IceCube data*, Phys. Rev. Lett. **113** (2014) 101101. doi:10.1103/PhysRevLett.113.101101 [`arXiv:1405.5303[astro-ph.HE]`].

[42] E. Armengaud, G. Sigl, T. Beau and F. Miniati, *CRPropa: a numerical tool for the propagation of uhe cosmic rays, gamma-rays and neutrinos*, Astropart. Phys. **28** (2007) 463–471. doi:10.1016/j.astropartphys.2007.09.004 [`arXiv:astro-ph/0603675`].

[43] A. van Vliet, K.-H. Kampert, J. Kulbartz, L. Maccione, N. Nierstenhoefer *et al.*, *CRPropa 2.0*, EPJ Web Conf. **52** (2013) 06006. doi:10.1051/epjconf/20125206006.

[44] R. Alves Batista, M. Erdmann, C. Evoli, K.-H. Kampert, D. Kuempel *et al.*, *CRPropa 3.0 - a public framework for propagating UHE cosmic rays through galactic and extragalactic space*, `arXiv:1307.2643[astro-ph.IM]`.

[45] E. Roulet, G. Sigl, A. van Vliet and S. Mollerach, *PeV neutrinos from the propagation of ultra-high energy cosmic rays*, JCAP **1301** (2013) 028. doi:10.1088/1475-7516/2013/01/028 [`arXiv:1209.4033[astro-ph.HE]`].

[46] G. Sigl and A. van Vliet, *PeV neutrinos from ultra-high-energy cosmic rays*, `arXiv:1407.6577[astro-ph.HE]`.

[47] A. Letessier-Selvon and T. Stanev, *Ultrahigh energy cosmic rays*, Rev. Mod. Phys. **83** (2011) 907–942. doi:10.1103/RevModPhys.83.907 [`arXiv:1103.0031[astro-ph.HE]`].

[48] D. Allard, *Extragalactic propagation of ultrahigh energy cosmic-rays*, Astropart. Phys. **39-40** (2012) 33–43. doi:10.1016/j.astropartphys.2011.10.011 [`arXiv:1111.3290[astro-ph.HE]`].

[49] K.-H. Kampert and P. Tinyakov, *Cosmic rays from the ankle to the cut-off*, `arXiv:1405.0575[astro-ph.HE]`.

[50] C. T. R. Wilson, *On the Ionization of Atmospheric Air*, Proc. R. Soc. Lond. **68** (1901) 151–161. doi:10.1098/rspl.1901.0032.

[51] F. Linke, *Luftelektrische Messungen bei zwölf Ballonfahrten*, Abh. Konigl. Ges. Wiss. G. **3** (1904) 1–90.

[52] V. F. Hess, *Über Beobachtungen der durchdringenden Strahlung bei sieben Freiballonfahrten*, Physik. Z. **13** (1912) 1084–1091.

[53] W. Pauli, *Dear radioactive ladies and gentlemen*, Phys. Today **31N9** (1978) 27. doi:10.1063/1.2995181.

[54] P. A. M. Dirac, *Quantized singularities in the electromagnetic field*, Proc. Roy. Soc. Lond. **A133** (1931) 60–72. doi:10.1098/rspa.1931.0130.

[55] C. D. Anderson, *The apparent existence of easily deflectable positives*, Science **76** (1932) 238–239. doi:10.1126/science.76.1967.238.

[56] C. D. Anderson, *The positive electron*, Phys. Rev. **43** (1933) 491–494. doi:10.1103/PhysRev.43.491.

[57] W. Baade and F. Zwicky, *On super-novae*, Proceedings of the National Academy of Sciences **20** (1934), no. 5 254–259. doi:10.1073/pnas.20.5.254.

[58] H. Yukawa, *On the interaction of elementary particles*, Proc. Phys. Math. Soc. Jap. **17** 48–57. doi:10.1143/PTPS.1.1.

[59] C. D. Anderson and S. H. Neddermeyer, *Cloud chamber observations of cosmic rays at 4300 meters elevation and near sea-level*, Phys. Rev. **50** (1936) 263–271. doi:10.1103/PhysRev.50.263.

[60] S. H. Neddermeyer and C. D. Anderson, *Note on the nature of cosmic ray particles*, Phys. Rev. **51** (1937) 884–886. doi:10.1103/PhysRev.51.884.

[61] D. H. Perkins, *Nuclear disintegration by meson capture*, Nature **159** (1947) 126–127. doi:10.1038/159126a0.

[62] C. M. G. Lattes, G. P. S. Occhialini and C. F. Powell, *Observations on the tracks of slow mesons in photographic emulsions. 1*, Nature **160** (1947) 453–456. doi:10.1038/160453a0.

[63] C. M. G. Lattes, G. P. S. Occhialini and C. F. Powell, *Observations on the tracks of slow mesons in photographic emulsions. 2*, Nature **160** (1947) 486–492. doi:10.1038/160486a0.

[64] P. Auger, P. Ehrenfest, R. Maze, J. Daudin and A. F. Robley, *Extensive cosmic ray showers*, Rev. Mod. Phys. **11** (1939) 288–291. doi:10.1103/RevModPhys.11.288.

[65] E. Fermi, *On the origin of the cosmic radiation*, Phys. Rev. **75** (1949) 1169–1174. doi:10.1103/PhysRev.75.1169.

[66] S. N. Vernov, I. Y. Logachev, N. L. Grigorov and A. E. Chudakov, *Study of cosmic radiation on board 2 AES*, D.A.N. **120** (1958) 1231–1233.

[67] N. A. Porter, T. E. Cranshaw, J. F. De Beer, A. G. Parham and A. C. Sherwood, *Observations on extensive air showers vii. the lateral distribution of energy in the electron-photon component*, Philos. Mag. **3** (1958), no. 32 826–830. doi:10.1080/14786435808237020.

[68] G. V. Kulikov and G. B. Kristiansen JETP **35** (1958) 635.

[69] M. A. Markov, *On high-energy neutrino physics*, in *Proceedings of the 1960 Annual International Conference on High-Energy Physcs*, p. 578, University of Rochester, 1960.

[70] J. Linsley, *Evidence for a primary cosmic-ray particle with energy* 10^{20} eV, Phys. Rev. Lett. **10** (1963) 146–148. doi:10.1103/PhysRevLett.10.146.

[71] A. A. Penzias and R. W. Wilson, *A measurement of excess antenna temperature at 4080-Mc/s*, Astrophys. J. **142** (1965) 419–421. doi:10.1086/148307.

[72] R. H. Dicke, P. J. E. Peebles, P. G. Roll and D. T. Wilkinson, *Cosmic black-body radiation*, Astrophys. J. **142** (1965) 414–419. doi:10.1086/148306.

[73] C. V. Achar, M. G. K. Menon, V. S. Narasimham, P. V. R. Murthy, B. V. Sreekantan *et al.*, *Detection of muons produced by cosmic ray neutrinos deep underground*, Phys. Lett. **18** (1965), no. 2 196 – 199. doi:10.1016/0031-9163(65)90712-2.

[74] C. V. Achar, M. G. K. Menon, V. S. Narasimham, P. V. R. Murthy, B. V. Sreekantan *et al.*, *Observation of a non-elastic cosmic ray neutrino interaction*, Phys. Lett. **19** (1965), no. 1 78 – 80. doi:10.1016/0031-9163(65)90969-8.

[75] F. Reines, M. F. Crouch, T. L. Jenkins, W. R. Kropp, H. S. Gurr *et al.*, *Evidence for high-energy cosmic ray neutrino interactions*, Phys. Rev. Lett. **15** (1965) 429–433. doi:10.1103/PhysRevLett.15.429.

[76] K. Greisen, *End to the cosmic ray spectrum?*, Phys. Rev. Lett. **16** (1966) 748–750. doi:10.1103/PhysRevLett.16.748.

[77] G. T. Zatsepin and V. A. Kuzmin, *Upper limit of the spectrum of cosmic rays*, JETP Lett. **4** (1966) 78–80.

[78] The Yakutsk Collaboration, “Yakutsk array website.” See http://eas.ysn.ru/.

[79] R. M. Baltrusaitis, R. Cady, G. L. Cassiday, R. Cooper, J. W. Elbert *et al.*, *The Utah Fly's Eye Detector*, Nucl. Instrum. Meth. **A240** (1985) 410–428. doi:10.1016/0168-9002(85)90658-8.

[80] D. J. Bird, S. C. Corbato, H. Y. Dai, J. W. Elbert, K. D. Green *et al.*, *Detection of a cosmic ray with measured energy well beyond the expected spectral cutoff due to cosmic microwave radiation*, Astrophys. J. **441** (1995) 144–150. doi:10.1086/175344.

[81] W. D. Arnett, J. N. Bahcall, R. P. Kirshner and S. E. Woosley, *Supernova SN1987A*, Ann. Rev. Astron. Astrophys. **27** (1989) 629–700. doi:10.1146/annurev.aa.27.090189.003213.

[82] M. Takeda, N. Hayashida, K. Honda, N. Inoue, K. Kadota *et al.*, *Extension of the cosmic ray energy spectrum beyond the predicted Greisen-Zatsepin-Kuz'min cutoff*, Phys. Rev. Lett. **81** (1998) 1163–1166. doi:10.1103/PhysRevLett.81.1163 [`arXiv:astro-ph/9807193`].

[83] **AMANDA Collaboration**, J. Ahrens *et al.*, *Search for extraterrestrial point sources of neutrinos with AMANDA-II*, Phys. Rev. Lett. **92** (2004) 071102. doi:10.1103/PhysRevLett.92.071102 [`arXiv:astro-ph/0309585`].

[84] **IceCube Collaboration**, R. Abbasi *et al.*, *Search for point sources of high energy neutrinos with final data from AMANDA-II*, Phys. Rev. **D79** (2009) 062001. doi:10.1103/PhysRevD.79.062001 [`arXiv:0809.1646[astro-ph]`].

[85] **KASCADE Collaboration**, T. Antoni *et al.*, *The cosmic ray experiment KASCADE*, Nucl. Instrum. Meth. **A513** (2003) 490–510. doi:10.1016/S0168-9002(03)02076-X.

[86] **KASCADE Collaboration**, T. Antoni *et al.*, *Electron, muon, and hadron lateral distributions measured in air-showers by the KASCADE experiment*, Astropart. Phys. **14** (2001) 245–260. doi:10.1016/S0927-6505(00)00125-0 [`arXiv:astro-ph/0004233[astro-ph]`].

[87] G. Navarra, T. Antoni, W. D. Apel, F. Badea, K. Bekk *et al.*, *KASCADE-Grande: A large acceptance, high-resolution cosmic-ray detector up to* 10^{18} eV, Nucl. Instrum. Meth. **A518** (2004) 207–209. doi:10.1016/j.nima.2003.10.061.

[88] **KASCADE Collaboration**, T. Antoni *et al.*, *KASCADE measurements of energy spectra for elemental groups of cosmic rays: Results and open problems*, Astropart. Phys. **24** (2005) 1–25. doi:10.1016/j.astropartphys.2005.04.001 [`arXiv:astro-ph/0505413`].

[89] **KASCADE Collaboration**, W. D. Apel *et al.*, *Energy spectra of elemental groups of cosmic rays: Update on the KASCADE unfolding analysis*, Astropart. Phys. **31** (2009) 86–91. doi:10.1016/j.astropartphys.2008.11.008 [`arXiv:0812.0322[astro-ph]`].

[90] **KASCADE-Grande Collaboration**, W. D. Apel *et al.*, *Kneelike structure in the spectrum of the heavy component of cosmic rays observed with KASCADE-Grande*, Phys. Rev. Lett. **107** (2011) 171104. doi:10.1103/PhysRevLett.107.171104 [`arXiv:1107.5885[astro-ph.HE]`].

[91] D. Heck *et al.*, "CORSIKA web page." See https://web.ikp.kit.edu/corsika/.

[92] T. Abu-Zayyad, M. Al-Seady, K. Belov, G. Chen, H. Y. Dai *et al.*, *The prototype high-resolution Fly's Eye cosmic ray detector*, Nucl. Instrum. Meth. **A450** (2000) 253–269. doi:10.1016/S0168-9002(00)00307-7.

[93] **HiRes Collaboration**, R. Abbasi *et al.*, *Measurement of the flux of ultra high energy cosmic rays by the stereo technique*, Astropart. Phys. **32** (2009) 53–60. doi:10.1016/j.astropartphys.2009.06.001 [`arXiv:0904.4500[astro-ph.HE]`].

[94] **HiRes**, P. Sokolsky, *Final results from the High Resolution Fly's Eye (HiRes) experiment*, PoS **ICHEP2010** (2010) 444 [`arXiv:1010.2690[astro-ph.HE]`].

[95] **HiRes Collaboration**, R. U. Abbasi *et al.*, *Indications of proton-dominated cosmic ray composition above 1.6 EeV*, Phys. Rev. Lett. **104** (2010) 161101. doi:10.1103/PhysRevLett.104.161101 [`arXiv:0910.4184[astro-ph.HE]`].

[96] **HiRes Collaboration**, R. Abbasi, *A search for three and four point correlation in HiRes stereo data*, `arXiv:0901.3740[astro-ph.HE]`.

[97] **HiRes Collaboration**, R. U. Abbasi *et al.*, *Analysis of large-scale anisotropy of ultra-high energy cosmic rays in HiRes stereo data*, Astrophys. J. **713** (2010), no. 1 L64–L68. doi:10.1088/2041-8205/713/1/L64.

[98] **IceCube Collaboration**, J. Ahrens *et al.*, *Icecube - the next generation neutrino telescope at the south pole*, Nucl. Phys. Proc. Suppl. **118** (2003) 388–395. doi:10.1016/S0920-5632(03)01337-9 [`arXiv:astro-ph/0209556`].

[99] **IceCube Collaboration**, R. Abbasi *et al.*, *The design and performance of IceCube DeepCore*, Astropart. Phys. **35** (2012) 615–624. doi:10.1016/j.astropartphys.2012.01.004 [`arXiv:1109.6096[astro-ph.IM]`].

[100] **IceCube Collaboration**, R. Abbasi *et al.*, *IceTop: The surface component of IceCube*, Nucl. Instrum. Meth. **A700** (2013) 188–220. doi:10.1016/j.nima.2012.10.067 [`arXiv:1207.6326[astro-ph.IM]`].

[101] **IceCube Collaboration**, R. Abbasi *et al.*, *An absence of neutrinos associated with cosmic-ray acceleration in γ-ray bursts*, Nature **484** (2012) 351–353. doi:10.1038/nature11068 [`arXiv:1204.4219[astro-ph.HE]`].

[102] **Pierre Auger Collaboration**, J. Abraham *et al.*, *Properties and performance of the prototype instrument for the Pierre Auger Observatory*, Nucl. Instrum. Meth. **A523** (2004) 50–95. doi:10.1016/j.nima.2003.12.012.

[103] **Pierre Auger Collaboration**, J. Abraham *et al.*, *Trigger and aperture of the surface detector array of the Pierre Auger Observatory*, Nucl. Instrum. Meth. **A613** (2010) 29–39. doi:10.1016/j.nima.2009.11.018 [`arXiv:1111.6764[astro-ph.IM]`].

[104] **Pierre Auger Collaboration**, J. Abraham *et al.*, *The fluorescence detector of the Pierre Auger Observatory*, Nucl. Instrum. Meth. **A620** (2010) 227–251. doi:10.1016/j.nima.2010.04.023 [`arXiv:0907.4282[astro-ph.IM]`].

[105] **Pierre Auger Collaboration**, P. Abreu *et al.*, *The Pierre Auger Observatory V: Enhancements*, J. Phys. Conf. Ser. **375** (2012) 052006. doi:10.1088/1742-6596/375/1/052006 [`arXiv:1107.4807[astro-ph.IM]`].

[106] J. Alvarez-Muniz, E. Amaral Soares, A. Berlin, M. Bogdan, M. Bohacova *et al.*, *The MIDAS telescope for microwave detection of ultra-high energy cosmic rays*, Nucl. Instrum. Meth. **A719** (2013) 70–80. doi:10.1016/j.nima.2013.03.030 [`arXiv:1208.2734[astro-ph.IM]`].

[107] **Pierre Auger Collaboration**, J. Abraham *et al.*, *Observation of the suppression of the flux of cosmic rays above $4 \times 10^{19} eV$*, Phys. Rev. Lett. **101** (2008) 061101. doi:10.1103/PhysRevLett.101.061101 [`arXiv:0806.4302[astro-ph]`].

[108] **Pierre Auger Collaboration**, J. Abraham *et al.*, *Correlation of the highest-energy cosmic rays with the positions of nearby active galactic nuclei*, Astropart. Phys. **29** (2008) 188–204. doi:10.1016/j.astropartphys.2008.06.004, 10.1016/j.astropartphys.2008.01.002 [`arXiv:0712.2843[astro-ph]`].

[109] **Telescope Array Collaboration**, H. Kawai *et al.*, *Telescope array experiment*, Nucl. Phys. Proc. Suppl. **175-176** (2008) 221–226. doi:10.1016/j.nuclphysbps.2007.11.002.

[110] H. Tokuno, Y. Tameda, M. Takeda, K. Kadota, D. Ikeda *et al.*, *New air fluorescence detectors employed in the Telescope Array experiment*, Nucl. Instrum. Meth. **A676** (2012) 54–65. doi:10.1016/j.nima.2012.02.044 [`arXiv:1201.0002[astro-ph.IM]`].

[111] **Telescope Array Collaboration**, T. Abu-Zayyad *et al.*, *The surface detector array of the Telescope Array experiment*, Nucl. Instrum. Meth. **A689** (2012) 87–97. doi:10.1016/j.nima.2012.05.079 [`arXiv:1201.4964[astro-ph.IM]`].

[112] **Telescope Array Collaboration**, K. Martens, *The Telescope Array and its low energy extension*, Nucl. Phys. Proc. Suppl. **165** (2007) 33–36. doi:10.1016/j.nuclphysbps.2006.11.006.

[113] **Telescope Array Collaboration**, Y. Tsunesada, *Highlights from Telescope Array*, `arXiv:1111.2507[astro-ph.HE]`.

[114] **Telescope Array Collaboration**, T. Abu-Zayyad *et al.*, *The energy spectrum of ultra-high-energy cosmic rays measured by the Telescope Array FADC fluorescence detectors in monocular mode*, Astropart. Phys. **48** (2013) 16–24. doi:10.1016/j.astropartphys.2013.06.007 [`arXiv:1305.6079[astro-ph.HE]`].

[115] **Telescope Array Collaboration**, T. Abu-Zayyad *et al.*, *Energy spectrum of ultra-high energy cosmic rays observed with the Telescope Array using a hybrid technique*, `arXiv:1305.7273[astro-ph.HE]`.

[116] **PAMELA Collaboration**, M. Circella, *The space mission PAMELA*, Nucl. Instrum. Meth. **A518** (2004) 153–157. doi:10.1016/j.nima.2003.10.048.

[117] **PAMELA Collaboration**, O. Adriani *et al.*, *An anomalous positron abundance in cosmic rays with energies 1.5-100 GeV*, Nature **458** (2009) 607–609. doi:10.1038/nature07942 [`arXiv:0810.4995[astro-ph]`].

[118] **PAMELA Collaboration**, O. Adriani *et al.*, *Cosmic-Ray positron energy spectrum measured by PAMELA*, Phys. Rev. Lett. **111** (2013), no. 8 081102. doi:10.1103/PhysRevLett.111.081102 [`arXiv:1308.0133[astro-ph.HE]`].

[119] O. Adriani, G. C. Barbarino, G. A. Bazilevskaya, R. Bellotti, M. Boezio *et al.*, *A new measurement of the antiproton-to-proton flux ratio up to 100 GeV in the cosmic radiation*, Phys. Rev. Lett. **102** (2009) 051101. doi:10.1103/PhysRevLett.102.051101 [`arXiv:0810.4994[astro-ph]`].

[120] **PAMELA Collaboration**, O. Adriani *et al.*, *PAMELA results on the cosmic-ray antiproton flux from 60 MeV to 180 GeV in kinetic energy*, Phys. Rev. Lett. **105** (2010) 121101. doi:10.1103/PhysRevLett.105.121101 [`arXiv:1007.0821[astro-ph.HE]`].

[121] N. Gehrels and P. Michelson, *GLAST: The next generation high-energy gamma-ray astronomy mission*, Astropart. Phys. **11** (1999) 277–282. doi:10.1016/S0927-6505(99)00066-3.

[122] **LAT Collaboration**, W. B. Atwood *et al.*, *The Large Area Telescope on the Fermi Gamma-ray Space Telescope Mission*, Astrophys. J. **697** (2009) 1071–1102. doi:10.1088/0004-637X/697/2/1071 [`arXiv:0902.1089[astro-ph.IM]`].

[123] G. G. Lichti, M. S. Briggs, R. Diehl, G. Fishman, R. Georgii *et al.*, *The GLAST burst monitor (GBM)*, AIP Conf. Proc. **662** (2003) 469–472. doi:10.1063/1.1579404 [`arXiv:astro-ph/0109144`].

[124] **Fermi LAT Collaboration**, A. A. Abdo *et al.*, *Fermi Large Area Telescope bright gamma-ray source list*, Astrophys. J. Suppl. **183** (2009) 46–66. doi:10.1088/0067-0049/183/1/46 [`arXiv:0902.1340[astro-ph.HE]`].

[125] **Fermi LAT collaboration**, A. A. Abdo *et al.*, *The first Fermi Large Area Telescope catalog of gamma-ray pulsars*, Astrophys. J. Suppl. **187** (2010) 460–494. doi:10.1088/0067-0049/193/1/22, 10.1088/0067-0049/187/2/460 [`arXiv:0910.1608[astro-ph.HE]`].

[126] **Fermi-LAT Collaboration**, A. A. Abdo *et al.*, *Fermi Large Area Telescope first source catalog*, Astrophys. J. Suppl. **188** (2010) 405–436. doi:10.1088/0067-0049/188/2/405 [`arXiv:1002.2280[astro-ph.HE]`].

[127] **Fermi-LAT Collaboration**, *Fermi Large Area Telescope second source catalog*, Astrophys. J. Suppl. **199** (2012) 31. doi:10.1088/0067-0049/199/2/31 [`arXiv:1108.1435[astro-ph.HE]`].

[128] **Fermi LAT Collaboration**, A. A. Abdo *et al.*, *Measurement of the Cosmic Ray e^+ plus e^- spectrum from 20 GeV to 1 TeV with the Fermi Large Area Telescope*, Phys. Rev. Lett. **102** (2009) 181101. doi:10.1103/PhysRevLett.102.181101 [`arXiv:0905.0025[astro-ph.HE]`].

[129] **Fermi LAT Collaboration**, M. Ackermann *et al.*, *Fermi LAT observations of cosmic-ray electrons from 7 GeV to 1 TeV*, Phys. Rev. **D82** (2010) 092004. doi:10.1103/PhysRevD.82.092004 [`arXiv:1008.3999[astro-ph.HE]`].

[130] **Fermi LAT Collaboration**, M. Ackermann *et al.*, *Measurement of separate cosmic-ray electron and positron spectra with the Fermi Large Area Telescope*, Phys. Rev. Lett. **108** (2012) 011103. doi:10.1103/PhysRevLett.108.011103 [`arXiv:1109.0521[astro-ph.HE]`].

[131] **Fermi-LAT Collaboration**, M. Ackermann *et al.*, *Detection of the characteristic pion-decay signature in supernova remnants*, Science **339** (2013) 807. doi:10.1126/science.1231160 [`arXiv:1302.3307[astro-ph.HE]`].

[132] **Fermi-LAT Collaboration**, A. A. Abdo *et al.*, *The spectrum of the isotropic diffuse gamma-ray emission derived from first-year Fermi Large Area Telescope data*, Phys. Rev. Lett. **104** (2010) 101101. doi:10.1103/PhysRevLett.104.101101 [`arXiv:1002.3603[astro-ph.HE]`].

[133] **AMS-02 Collaboration**, F. Barao, *AMS: Alpha Magnetic Spectrometer on the International Space Station*, Nucl. Instrum. Meth. **A535** (2004) 134–138. doi:10.1016/j.nima.2004.07.196.

[134] **AMS Collaboration**, M. Aguilar *et al.*, *First result from the Alpha Magnetic Spectrometer on the International Space Station: Precision measurement of the positron fraction in primary cosmic rays of 0.5-350 GeV*, Phys. Rev. Lett. **110** (2013) 141102. doi:10.1103/PhysRevLett.110.141102.

[135] **AMS Collaboration**, L. Accardo *et al.*, *High statistics measurement of the positron fraction in primary cosmic rays of 0.5-500 GeV with the Alpha Magnetic Spectrometer on the International Space Station*, Phys. Rev. Lett. **113** (2014) 121101. doi:10.1103/PhysRevLett.113.121101.

[136] **AMS Collaboration**, M. Aguilar *et al.*, *Electron and positron fluxes in primary cosmic rays measured with the Alpha Magnetic Spectrometer on the International Space Station*, Phys. Rev. Lett. **113** (2014) 121102. doi:10.1103/PhysRevLett.113.121102.

[137] **Euso Collaboration**, M. Pallavicini, *The Extreme Universe Space Observatory*, Nucl. Instrum. Meth. **A502** (2003) 155–157. doi:10.1016/S0168-9002(03)00266-3.

[138] **JEM-EUSO Collaboration**, Y. Takahashi, *The JEM-EUSO mission*, New J. Phys. **11** (2009) 065009. doi:10.1088/1367-2630/11/6/065009.

[139] B. A. Khrenov, V. V. Aleksandrov, D. I. Bugrov, G. K. Garipov, N. N. Kalmykov *et al.*, *KLYPVE/TUS space experiments for study of ultrahigh-energy cosmic rays*, Phys. Atom. Nucl. **67** (2004) 2058–2061. doi:10.1134/1.1825529.

[140] **Pierre Auger Collaboration**, C. Bonifazi, *The angular resolution of the Pierre Auger Observatory*, Nucl. Phys. Proc. Suppl. **190** (2009) 20–25. doi:10.1016/j.nuclphysbps.2009.03.063 [`arXiv:0901.3138[astro-ph.HE]`].

[141] P. P. Kronberg, *Extragalactic magnetic fields*, Rept. Prog. Phys. **57** (1994) 325–382. doi:10.1088/0034-4885/57/4/001.

[142] D. Ryu, H. Kang and P. L. Biermann, *Cosmic magnetic fields in large scale filaments and sheets*, Astron. Astrophys. **335** (1998) 19–25 [`arXiv:astro-ph/9803275`].

[143] F. Miniati, *Inter-galactic shock acceleration and the cosmic gamma-ray background*, Mon. Not. Roy. Astron. Soc. **337** (2002) 199. doi:10.1046/j.1365-8711.2002.05903.x [`arXiv:astro-ph/0203014`].

[144] K. Dolag, M. Bartelmann and H. Lesch, *Evolution and structure of magnetic fields in simulated galaxy clusters*, Astron. Astrophys. **387** (1999) 386 [`arXiv:astro-ph/0202272`].

[145] K. Dolag, D. Grasso, V. Springel and I. Tkachev, *Constrained simulations of the magnetic field in the local Universe and the propagation of UHECRs*, JCAP **0501** (2005) 009. doi:10.1088/1475-7516/2005/01/009 [`arXiv:astro-ph/0410419`].

[146] J. Donnert, K. Dolag, H. Lesch and E. Muller, *Cluster magnetic fields from galactic outflows*, Mon. Not. Roy. Astron. Soc. **392** (2009) 1008–1021. doi:10.1111/j.1365-2966.2008.14132.x [`arXiv:0808.0919[astro-ph]`].

[147] D. Ryu, H. Kang, J. Cho and S. Das, *Turbulence and magnetic fields in the large scale structure of the universe*, Science **320** (2008) 909 [`arXiv:0805.2466[astro-ph]`].

[148] D. Ryu, S. Das and H. Kang, *Intergalactic magnetic field and arrival direction of ultra-high-energy protons*, Astrophys. J. **710** (2010) 1422–1431. doi:10.1088/0004-637X/710/2/1422 [`arXiv:0910.3361[astro-ph.HE]`].

[149] M. S. Pshirkov, P. G. Tinyakov, P. P. Kronberg and K. J. Newton-McGee, *Deriving global structure of the galactic magnetic field from Faraday rotation measures of extragalactic sources*, Astrophys. J. **738** (2011) 192. doi:10.1088/0004-637X/738/2/192 [`arXiv:1103.0814[astro-ph.GA]`].

[150] R. Jansson and G. R. Farrar, *A new model of the galactic magnetic field*, Astrophys. J. **757** (2012) 14. doi:10.1088/0004-637X/757/1/14 [`arXiv:1204.3662[astro-ph.GA]`].

[151] R. Jansson and G. R. Farrar, *The galactic magnetic field*, Astrophys. J. **761** (2012) L11. doi:10.1088/2041-8205/761/1/L11 [`arXiv:1210.7820[astro-ph.GA]`].

[152] P. G. Tinyakov and I. I. Tkachev, *Correlation function of ultrahigh energy cosmic rays favors point sources*, JETP Lett. **74** (2001) 1–5. doi:10.1134/1.1402195 [`arXiv:astro-ph/0102101`].

[153] M.-P. Veron-Cetty and P. Veron, *A catalogue of quasars and active nuclei: 12th edition*, Astron. Astrophys. **455** (2006) 773–777. doi:10.1051/0004-6361:20065177.

[154] H. B. J. Koers and P. Tinyakov, *Testing large-scale (an)isotropy of ultra-high energy cosmic rays*, JCAP **0904** (2009) 003. doi:10.1088/1475-7516/2009/04/003 [`arXiv:0812.0860[astro-ph]`].

[155] **Telescope Array**, H. Sagawa, *Highlights from the Telescope Array Experiment*, Braz. J. Phys. **44** (2014) 589–599. doi:10.1007/s13538-014-0253-3.

[156] F. Oikonomou, A. Connolly, F. B. Abdalla, O. Lahav, S. A. Thomas *et al.*, *A search for correlation of ultra-high energy cosmic rays with IRAS-PSCz and 2MASS-6dF galaxies*, JCAP **1305** (2013) 015. doi:10.1088/1475-7516/2013/05/015 [`arXiv:1207.4043[astro-ph.HE]`].

[157] **Pierre Auger Collaboration**, P. Abreu *et al.*, *Search for signatures of magnetically-induced alignment in the arrival directions measured by the Pierre Auger Observatory*, Astropart. Phys. **35** (2012) 354–361. doi:10.1016/j.astropartphys.2011.10.004 [`arXiv:1111.2472[astro-ph.HE]`].

[158] **Pierre Auger Collaboration**, A. Aab *et al.*, *Search for patterns by combining cosmic-ray energy and arrival directions at the Pierre Auger Observatory*, Eur. Phys. J. C (2014) [`arXiv:1410.0515[astro-ph.HE]`].

[159] C. Lunardini, S. Razzaque, K. T. Theodoseau and L. Yang, *Neutrino events at IceCube and the Fermi bubbles*, Phys. Rev. **D90** (2014) 023016. doi:10.1103/PhysRevD.90.023016 [`arXiv:1311.7188[astro-ph.HE]`].

[160] Y. Bai, R. Lu and J. Salvado, *Geometric compatibility of IceCube TeV-PeV neutrino excess and its galactic dark matter origin*, `arXiv:1311.5864[hep-ph]`.

[161] A. M. Taylor, S. Gabici and F. Aharonian, *A galactic halo origin of the neutrinos detected by IceCube*, Phys. Rev. **D89** (2014) 103003. doi:10.1103/PhysRevD.89.103003 [`arXiv:1403.3206[astro-ph.HE]`].

[162] **The IceCube Collaboration**, M. G. Aartsen *et al.*, *The IceCube Neutrino Observatory part I: Point source searches*, `arXiv:1309.6979[astro-ph.HE]`.

[163] E. Waxman, *Cosmological gamma-ray bursts and the highest energy cosmic rays*, Phys. Rev. Lett. **75** (1995) 386–389. doi:10.1103/PhysRevLett.75.386 [`arXiv:astro-ph/9505082`].

[164] M. Vietri, *On the acceleration of ultrahigh-energy cosmic rays in gamma-ray bursts*, Astrophys. J. **453** (1995) 883–889. doi:10.1086/176448 [`arXiv:astro-ph/9506081`].

[165] M. Milgrom and V. Usov, *Possible association of ultrahigh-energy cosmic ray events with strong gamma-ray bursts*, Astrophys. J. **449** (1995) L37. doi:10.1086/309633 [`arXiv:astro-ph/9505009`].

[166] E. Waxman and J. N. Bahcall, *High-energy neutrinos from cosmological gamma-ray burst fireballs*, Phys. Rev. Lett. **78** (1997) 2292–2295. doi:10.1103/PhysRevLett.78.2292 [`arXiv:astro-ph/9701231`].

[167] J. P. Rachen and P. Meszaros, *Cosmic rays and neutrinos from gamma-ray bursts*, AIP Conf. Proc. **428** (1997) 776 [`arXiv:astro-ph/9811266`].

[168] D. Guetta, D. Hooper, J. Alvarez-Muniz, F. Halzen and E. Reuveni, *Neutrinos from individual gamma-ray bursts in the BATSE catalog*, Astropart. Phys. **20** (2004) 429–455. doi:10.1016/S0927-6505(03)00211-1 [`arXiv:astro-ph/0302524`].

[169] M. Ahlers, M. C. Gonzalez-Garcia and F. Halzen, *GRBs on probation: testing the UHE CR paradigm with IceCube*, Astropart. Phys. **35** (2011) 87–94. doi:10.1016/j.astropartphys.2011.05.008 [`arXiv:1103.3421[astro-ph.HE]`].

[170] C. D. Dermer, *Statistics of cosmological black hole jet sources: Blazar predictions for GLAST*, Astrophys. J. **659** (2007) 958–975. doi:10.1086/512533 [`arXiv:astro-ph/0605402`].

[171] C. D. Dermer, *High-energy cosmology: Gamma rays and neutrinos from beyond the Galaxy*, Astrophys. Space Sci. **309** (2007) 127–137. doi:10.1007/s10509-007-9417-8 [`arXiv:astro-ph/0610195`].

[172] V. Pavlidou and B. D. Fields, *The guaranteed gamma-ray background*, Astrophys. J. **575** (2002) L5–L8. doi:10.1086/342670 [`arXiv:astro-ph/0207253`].

[173] B. D. Fields, V. Pavlidou and T. Prodanovic, *Cosmic gamma-ray background from star-forming galaxies*, Astrophys. J. **722** (2010) L199. doi:10.1088/2041-8205/722/2/L199 [`arXiv:1003.3647[astro-ph.CO]`].

[174] B. C. Lacki, S. Horiuchi and J. F. Beacom, *The star-forming galaxy contribution to the cosmic MeV and GeV gamma-ray background*, Astrophys. J. **786** (2014) 40. doi:10.1088/0004-637X/786/1/40 [`arXiv:1206.0772[astro-ph.HE]`].

[175] T. A. Thompson, E. Quataert and E. Waxman, *The starburst contribution to the extra-galactic gamma-ray background*, Astrophys. J. **654** (2006) 219–225. doi:10.1086/509068 [`arXiv:astro-ph/0606665`].

[176] F. W. Stecker and M. H. Salamon, *The gamma-ray background from blazars: A new look*, Astrophys. J. **464** (1996) 600–605. doi:10.1086/177348 [`arXiv:astro-ph/9601120`].

[177] Y. Inoue and T. Totani, *The blazar sequence and the cosmic gamma-ray background radiation in the Fermi era*, Astrophys. J. **702** (2009) 523–536. doi:10.1088/0004-637X/728/1/73, 10.1088/0004-637X/702/1/523 [`arXiv:0810.3580[astro-ph]`].

[178] A. Loeb and E. Waxman, *Gamma-ray background from structure formation in the intergalactic medium*, Nature **405** (2000) 156. doi:10.1038/35012018 [`arXiv:astro-ph/0003447`].

[179] U. Keshet, E. Waxman, A. Loeb, V. Springel and L. Hernquist, *Gamma-rays from intergalactic shocks*, Astrophys. J. **585** (2003) 128–150. doi:10.1086/345946 [`arXiv:astro-ph/0202318`].

[180] L. Bergstrom, J. Edsjo and P. Ullio, *Spectral gamma-ray signatures of cosmological dark matter annihilation*, Phys. Rev. Lett. **87** (2001) 251301. doi:10.1103/PhysRevLett.87.251301 [`arXiv:astro-ph/0105048`].

[181] **Fermi-LAT Collaboration**, A. A. Abdo *et al.*, *Constraints on cosmological dark matter annihilation from the Fermi-LAT isotropic diffuse gamma-ray measurement*, JCAP **1004** (2010) 014. doi:10.1088/1475-7516/2010/04/014 [`arXiv:1002.4415[astro-ph.CO]`].

[182] O. E. Kalashev, D. V. Semikoz and G. Sigl, *Ultra-high energy cosmic rays and the GeV-TeV diffuse gamma-ray flux*, Phys. Rev. **D79** (2009) 063005. doi:10.1103/PhysRevD.79.063005 [`arXiv:0704.2463[astro-ph]`].

[183] K. Murase, J. F. Beacom and H. Takami, *Gamma-ray and neutrino backgrounds as probes of the high-energy universe: Hints of cascades, general constraints, and implications for TeV searches*, JCAP **1208** (2012) 030. doi:10.1088/1475-7516/2012/08/030 [`arXiv:1205.5755[astro-ph.HE]`].

[184] C. D. Dermer, *The extragalactic gamma ray background*, AIP Conf. Proc. **921** (2007) 122–126. doi:10.1063/1.2757282 [`arXiv:0704.2888[astro-ph]`].

[185] U. Keshet, E. Waxman and A. Loeb, *The case for a low extragalactic gamma-ray background*, JCAP **0404** (2004) 006. doi:10.1088/1475-7516/2004/04/006 [`arXiv:astro-ph/0306442`].

[186] I. V. Moskalenko and T. A. Porter, *Isotropic gamma-ray background: Cosmic-ray induced albedo from debris in the solar system?*, Astrophys. J. **692** (2009) 54–57. doi:10.1088/0004-637X/692/1/L54 [`arXiv:0901.0304[astro-ph.HE]`].

[187] I. V. Moskalenko, T. A. Porter and S. W. Digel, *Inverse Compton scattering on solar photons, heliospheric modulation, and neutrino astrophysics*, Astrophys. J. **652** (2006) L65–L68. doi:10.1086/520882 [`arXiv:astro-ph/0607521`].

[188] E. Orlando and A. W. Strong, *Gamma-ray emission from the solar halo and disk: a study with EGRET data*, Astron. Astrophys. **480** (2008) 847. doi:10.1051/0004-6361:20078817 [`arXiv:0801.2178[astro-ph]`].

[189] C. E. Fichtel, G. A. Simpson and D. J. Thompson, *Diffuse gamma radiation*, Astrophys. J. **222** (1978) 833–849. doi:10.1086/156202.

[190] **EGRET Collaboration**, P. Sreekumar *et al.*, *EGRET observations of the extragalactic gamma-ray emission*, Astrophys. J. **494** (1998) 523–534. doi:10.1086/305222 [`arXiv:astro-ph/9709257`].

[191] R. Aloisio, D. Boncioli, A. F. Grillo, S. Petrera and F. Salamida, *SimProp: a simulation code for ultra high energy cosmic ray propagation*, JCAP **1210** (2012) 007. doi:10.1088/1475-7516/2012/10/007 [`arXiv:1204.2970[astro-ph.HE]`].

[192] M. De Domenico, *HERMES: Simulating the propagation of ultra-high energy cosmic rays*, `arXiv:1305.4364[astro-ph.IM]`.

[193] D. Allard, E. Parizot, E. Khan, S. Goriely and A. V. Olinto, *UHE nuclei propagation and the interpretation of the ankle in the cosmic-ray spectrum*, Astron. Astrophys. **443** (2005) L29–L32. doi:10.1051/0004-6361:200500199 [`arXiv:astro-ph/0505566`].

[194] D. Allard, M. Ave, N. Busca, M. A. Malkan, A. V. Olinto *et al.*, *Cosmogenic neutrinos from the propagation of ultrahigh energy nuclei*, JCAP **0609** (2006) 005. doi:10.1088/1475-7516/2006/09/005 [`arXiv:astro-ph/0605327`].

[195] D. Hooper, S. Sarkar and A. M. Taylor, *The intergalactic propagation of ultrahigh energy cosmic ray nuclei*, Astropart. Phys. **27** (2007) 199–212. doi:10.1016/j.astropartphys.2006.10.008 [`arXiv:astro-ph/0608085`].

[196] R. Aloisio and V. Berezinsky, *Diffusive propagation of UHECR and the propagation theorem*, Astrophys. J. **612** (2004) 900–913. doi:10.1086/421869 [`arXiv:astro-ph/0403095`].

[197] A. M. Hillas, *The origin of ultrahigh-energy cosmic rays*, Ann. Rev. Astron. Astrophys. **22** (1984) 425–444. doi:10.1146/annurev.aa.22.090184.002233.

[198] R. Aloisio, V. Berezinsky and S. Grigorieva, *Analytic calculations of the spectra of ultra-high energy cosmic ray nuclei. I. The case of CMB radiation*, Astropart. Phys. **41** (2013) 73–93. doi:10.1016/j.astropartphys.2012.07.010 [`arXiv:0802.4452[astro-ph]`].

[199] R. Aloisio, V. Berezinsky and S. Grigorieva, *Analytic calculations of the spectra of ultra high energy cosmic ray nuclei. II. The general case of background radiation*, Astropart. Phys. **41** (2013) 94–107. doi:10.1016/j.astropartphys.2012.06.003 [`arXiv:1006.2484[astro-ph.CO]`].

[200] E. Khan, S. Goriely, D. Allard, E. Parizot, T. Suomijarvi *et al.*, *Photodisintegration of ultra-high-energy cosmic rays revisited*, Astropart. Phys. **23** (2005) 191–201. doi:10.1016/j.astropartphys.2004.12.007 [`arXiv:astro-ph/0412109`].

[201] M. A. Duvernois and M. R. Thayer, *The elemental composition of the galactic cosmic-ray source: ULYSSES high-energy telescope results*, Astrophys. J. **465** (July, 1996) 982. doi:10.1086/177483.

[202] S. Goriely, S. Hilaire and A. J. Koning, *Improved predictions of nuclear reaction rates with the TALYS reaction code for astrophysical applications*, Astron. Astrophys. **487** (2008) 767. doi:10.1051/0004-6361:20078825 [`arXiv:0806.2239[astro-ph]`].

[203] E. G. Berezhko and H. J. Voelk, *Spectrum of cosmic rays, produced in supernova remnants*, `arXiv:0704.1715[astro-ph]`.

[204] J. Blumer, R. Engel and J. R. Horandel, *Cosmic rays from the knee to the highest energies*, Prog. Part. Nucl. Phys. **63** (2009) 293–338. doi:10.1016/j.ppnp.2009.05.002 [`arXiv:0904.0725[astro-ph.HE]`].

[205] M. G. Baring, *Using gamma-ray burst prompt emission to probe relativistic shock acceleration*, Adv. Space Res. **47** (2011) 1427–1433. doi:10.1016/j.asr.2010.02.016 [`arXiv:1002.3848[astro-ph.HE]`].

[206] P. Blasi, R. I. Epstein and A. V. Olinto, *Ultrahigh-energy cosmic rays from young neutron star winds*, Astrophys. J. **533** (2000) L123. doi:10.1086/312626 [`arXiv:astro-ph/9912240`].

[207] J. Arons, *Magnetars in the metagalaxy: an origin for ultrahigh-energy cosmic rays in the nearby universe*, Astrophys. J. **589** (2003) 871–892. doi:10.1086/374776 [`arXiv:astro-ph/0208444`].

[208] K. Fang, K. Kotera and A. V. Olinto, *Newly-born pulsars as sources of ultrahigh energy cosmic rays*, Astrophys. J. **750** (2012) 118. doi:10.1088/0004-637X/750/2/118 [`arXiv:1201.5197[astro-ph.HE]`].

[209] K. Fang, K. Kotera and A. V. Olinto, *Ultrahigh energy cosmic ray nuclei from extragalactic pulsars and the effect of their galactic counterparts*, JCAP **1303** (2013) 010. doi:10.1088/1475-7516/2013/03/010 [`arXiv:1302.4482[astro-ph.HE]`].

[210] T. Stanev, *Ultrahigh-energy cosmic rays and the large scale structure of the galactic magnetic field*, Astrophys. J. **479** (1997) 290. doi:10.1086/303866 [`arXiv:astro-ph/9607086`].

[211] D. Harari, S. Mollerach and E. Roulet, *The toes of the ultrahigh-energy cosmic ray spectrum*, JHEP **9908** (1999) 022. doi:10.1088/1126-6708/1999/08/022 [`arXiv:astro-ph/9906309`].

[212] M. Prouza and R. Smida, *The galactic magnetic field and propagation of ultrahigh energy cosmic rays*, Astron. Astrophys. **410** (2003) 1–10. doi:10.1051/0004-6361:20031281 [`arXiv:astro-ph/0307165`].

[213] H. Yoshiguchi, S. Nagataki and K. Sato, *A new method for calculating arrival distribution of ultra-high energy cosmic rays above 10**19-eV with modifications by the galactic magnetic field*, Astrophys. J. **596** (2003) 1044–1052. doi:10.1086/378201 [`arXiv:astro-ph/0307038`].

[214] M. Kachelriess, P. D. Serpico and M. Teshima, *The galactic magnetic field as spectrograph for ultrahigh energy cosmic rays*, Astropart. Phys. **26** (2006) 378–386. doi:10.1016/j.astropartphys.2006.08.004 [`arXiv:astro-ph/0510444`].

[215] H. Takami and K. Sato, *Distortion of ultrahigh-energy sky by galactic magnetic field*, Astrophys. J. **681** (2008) 1279–1287. doi:10.1086/588513 [`arXiv:0711.2386[astro-ph]`].

[216] D. Harari, S. Mollerach and E. Roulet, *Effects of the galactic magnetic field upon large scale anisotropies of extragalactic cosmic rays*, JCAP **1011** (2010) 033. doi:10.1088/1475-7516/2010/11/033 [`arXiv:1009.5891[astro-ph.HE]`].

[217] G. Giacinti, M. Kachelriess, D. V. Semikoz and G. Sigl, *Propagation of ultrahigh energy nuclei in the magnetic field of our galaxy*, `arXiv:1108.0362[astro-ph.HE]`.

[218] D. Harari, S. Mollerach and E. Roulet, *Astrophysical magnetic field reconstruction and spectroscopy with ultra high-energy cosmic rays*, JHEP **0207** (2002) 006. doi:10.1088/1126-6708/2002/07/006 [`arXiv:astro-ph/0205484`].

[219] H. Yoshiguchi, S. Nagataki, S. Tsubaki and K. Sato, *Small scale clustering in isotropic arrival distribution of ultra-high energy cosmic rays and implications for their source candidate*, Astrophys. J. **586** (2003) 1211–1231. doi:10.1086/367931 [`arXiv:astro-ph/0210132`].

[220] T. Yamamoto, K. Mase, M. Takeda, N. Sakaki and M. Teshima, *Signatures of ultrahigh-energy cosmic ray composition from propagation of nuclei in intergalactic photon fields*, Astropart. Phys. **20** (2004) 405–412. doi:10.1016/j.astropartphys.2003.08.001 [`arXiv:astro-ph/0312275`].

[221] E. Armengaud, G. Sigl and F. Miniati, *Ultrahigh energy nuclei propagation in a structured, magnetized Universe*, Phys. Rev. **D72** (2005) 043009. doi:10.1103/PhysRevD.72.043009 [`arXiv:astro-ph/0412525`].

[222] K. Kotera and M. Lemoine, *The optical depth of the Universe for ultra-high energy cosmic ray scattering in the magnetized large scale structure*, Phys. Rev. **D77** (2008) 123003. doi:10.1103/PhysRevD.77.123003 [`arXiv:0801.1450[astro-ph]`].

[223] T. Kashti and E. Waxman, *Searching for a correlation between cosmic-ray sources above* 10^{19} *eV and large-scale structure*, JCAP **0805** (2008) 006. doi:10.1088/1475-7516/2008/05/006 [`arXiv:0801.4516[astro-ph]`].

[224] H. Takami and K. Sato, *Implications to sources of ultra-high-energy cosmic rays from their arrival distribution*, Astropart. Phys. **30** (2009) 306–311. doi:10.1016/j.astropartphys.2008.10.004 [`arXiv:0807.3442[astro-ph]`].

[225] F. A. Aharonian, S. R. Kelner and A. Y. Prosekin, *Angular, spectral, and time distributions of highest energy protons and associated secondary gamma-rays and neutrinos propagating through extragalactic magnetic and radiation fields*, Phys. Rev. **D82** (2010) 043002. doi:10.1103/PhysRevD.82.043002 [`arXiv:1006.1045[astro-ph.HE]`].

[226] S. Kalli, M. Lemoine and K. Kotera, *Distortion of the ultrahigh energy cosmic ray flux from rare transient sources in inhomogeneous extragalactic magnetic fields*, `arXiv:1101.3801[astro-ph.HE]`.

[227] D. Harari, S. Mollerach and E. Roulet, *Anisotropies of ultra-high energy cosmic rays diffusing from extragalactic sources*, Phys. Rev. **D89** (2014) 123001. doi:10.1103/PhysRevD.89.123001 [`arXiv:1312.1366[astro-ph.HE]`].

[228] D. De Marco, P. Blasi and A. V. Olinto, *Small scale anisotropy predictions for the Auger Observatory*, JCAP **0607** (2006) 015. doi:10.1088/1475-7516/2006/07/015 [`arXiv:astro-ph/0603615`].

[229] T. Stanev, R. Engel, A. Mucke, R. J. Protheroe and J. P. Rachen, *Propagation of ultrahigh-energy protons in the nearby universe*, Phys. Rev. **D62** (2000) 093005. doi:10.1103/PhysRevD.62.093005 [`arXiv:astro-ph/0003484`].

[230] M. Lemoine, *Extra-galactic magnetic fields and the second knee in the cosmic-ray spectrum*, Phys. Rev. **D71** (2005) 083007. doi:10.1103/PhysRevD.71.083007 [`arXiv:astro-ph/0411173`].

[231] V. Berezinsky and A. Z. Gazizov, *Diffusion of cosmic rays in expanding universe*, Astrophys. J. **643** (2006) 8–13. doi:10.1086/502626 [`arXiv:astro-ph/0512090`].

[232] V. Berezinsky and A. Z. Gazizov, *Diffusion of cosmic rays in the expanding universe. 2. Energy spectra of ultra-high energy cosmic rays*, Astrophys.J. **669** (2007) 684–691. doi:10.1086/520498 [`arXiv:astro-ph/0702102`].

[233] N. Globus, D. Allard and E. Parizot, *Propagation of high-energy cosmic rays in extragalactic turbulent magnetic fields: resulting energy spectrum and composition*, `arXiv:0709.1541[astro-ph]`.

[234] S. Mollerach and E. Roulet, *Magnetic diffusion effects on the ultra-high energy cosmic ray spectrum and composition*, JCAP **1310** (2013) 013. doi:10.1088/1475-7516/2013/10/013 [`arXiv:1305.6519[astro-ph.HE]`].

[235] K. Kotera and M. Lemoine, *Inhomogeneous extragalactic magnetic fields and the second knee in the cosmic ray spectrum*, Phys. Rev. **D77** (2008) 023005. doi:10.1103/PhysRevD.77.023005 [`arXiv:0706.1891[astro-ph]`].

[236] R. Alves Batista and G. Sigl, *Diffusion of cosmic rays at EeV energies in inhomogeneous extragalactic magnetic fields*, `arXiv:1407.6150[astro-ph.HE]`.

[237] G. Sigl and E. Armengaud, *Magnetized sources of ultrahigh energy nuclei and extragalactic origin of the ankle*, JCAP **0510** (2005) 016. doi:10.1088/1475-7516/2005/10/016 [`arXiv:astro-ph/0507656`].

[238] G. Sigl, *Non-universal spectra of ultrahigh energy cosmic ray primaries and secondaries in a structured universe*, Phys. Rev. **D75** (2007) 103001. doi:10.1103/PhysRevD.75.103001 [`arXiv:astro-ph/0703403`].

[239] V. S. Berezinsky and G. T. Zatsepin, *Cosmic rays at ultrahigh-energies (neutrino?)*, Phys. Lett. **B28** (1969) 423–424. doi:10.1016/0370-2693(69)90341-4.

[240] V. Barger, J. Learned and S. Pakvasa, *IceCube PeV cascade events initiated by electron-antineutrinos at Glashow resonance*, `arXiv:1207.4571[astro-ph.HE]`.

[241] O. E. Kalashev, A. Kusenko and W. Essey, *PeV neutrinos from intergalactic interactions of cosmic rays emitted by active galactic nuclei*, Phys. Rev. Lett. **111** (2013), no. 4 041103. doi:10.1103/PhysRevLett.111.041103 [`arXiv:1303.0300[astro-ph.HE]`].

[242] F. W. Stecker, *Diffuse fluxes of cosmic high-energy neutrinos*, Astrophys. J. **228** (1979) 919–927. doi:10.1086/156919.

[243] R. Engel, D. Seckel and T. Stanev, *Neutrinos from propagation of ultrahigh-energy protons*, Phys. Rev. **D64** (2001) 093010. doi:10.1103/PhysRevD.64.093010 [`arXiv:astro-ph/0101216`].

[244] O. E. Kalashev, V. A. Kuzmin, D. V. Semikoz and G. Sigl, *Ultrahigh-energy neutrino fluxes and their constraints*, Phys. Rev. **D66** (2002) 063004. doi:10.1103/PhysRevD.66.063004 [`arXiv:hep-ph/0205050`].

[245] D. V. Semikoz and G. Sigl, *Ultrahigh-energy neutrino fluxes: New constraints and implications*, JCAP **0404** (2004) 003. doi:10.1088/1475-7516/2004/04/003 [`arXiv:hep-ph/0309328`].

[246] Z. Fodor, S. Katz, A. Ringwald and H. Tu, *Bounds on the cosmogenic neutrino flux*, JCAP **0311** (2003) 015. doi:10.1088/1475-7516/2003/11/015 [`arXiv:hep-ph/0309171`].

[247] D. Seckel and T. Stanev, *Neutrinos: The key to UHE cosmic rays*, Phys. Rev. Lett. **95** (2005) 141101. doi:10.1103/PhysRevLett.95.141101 [`arXiv:astro-ph/0502244`].

[248] D. Hooper, A. Taylor and S. Sarkar, *The impact of heavy nuclei on the cosmogenic neutrino flux*, Astropart. Phys. **23** (2005) 11–17. doi:10.1016/j.astropartphys.2004.11.002 [`arXiv:astro-ph/0407618`].

[249] M. Ave, N. Busca, A. V. Olinto, A. A. Watson and T. Yamamoto, *Cosmogenic neutrinos from ultra-high energy nuclei*, Astropart. Phys. **23** (2005) 19–29. doi:10.1016/j.astropartphys.2004.11.001 [`arXiv:astro-ph/0409316`].

[250] D. De Marco, T. Stanev and F. W. Stecker, *Cosmogenic neutrinos from cosmic ray interactions with extragalactic infrared photons*, Phys. Rev. **D73** (2006) 043003. doi:10.1103/PhysRevD.73.043003 [`arXiv:astro-ph/0512479`].

[251] H. Yuksel and M. D. Kistler, *Enhanced cosmological GRB rates and implications for cosmogenic neutrinos*, Phys. Rev. **D75** (2007) 083004. doi:10.1103/PhysRevD.75.083004 [`arXiv:astro-ph/0610481`].

[252] L. A. Anchordoqui, H. Goldberg, D. Hooper, S. Sarkar and A. M. Taylor, *Predictions for the cosmogenic neutrino flux in light of new data from the Pierre Auger Observatory*, Phys. Rev. **D76** (2007) 123008. doi:10.1103/PhysRevD.76.123008 [`arXiv:0709.0734[astro-ph]`].

[253] H. Takami, K. Murase, S. Nagataki and K. Sato, *Cosmogenic neutrinos as a probe of the transition from Galactic to extragalactic cosmic rays*, Astropart. Phys. **31** (2009) 201–211. doi:10.1016/j.astropartphys.2009.01.006 [`arXiv:0704.0979[astro-ph]`].

[254] M. Ahlers, L. A. Anchordoqui and S. Sarkar, *Neutrino diagnostics of ultra-high energy cosmic ray protons*, Phys. Rev. **D79** (2009) 083009. doi:10.1103/PhysRevD.79.083009 [`arXiv:0902.3993[astro-ph.HE]`].

[255] K. Kotera, D. Allard and A. V. Olinto, *Cosmogenic neutrinos: parameter space and detectabilty from PeV to ZeV*, JCAP **1010** (2010) 013. doi:10.1088/1475-7516/2010/10/013 [`arXiv:1009.1382[astro-ph.HE]`].

[256] M. Ahlers, L. A. Anchordoqui, M. C. Gonzalez-Garcia, F. Halzen and S. Sarkar, *GZK neutrinos after the Fermi-LAT diffuse photon flux measurement*, Astropart. Phys. **34** (2010) 106–115. doi:10.1016/j.astropartphys.2010.06.003 [`arXiv:1005.2620[astro-ph.HE]`].

[257] V. Berezinsky, A. Gazizov, M. Kachelriess and S. Ostapchenko, *Restricting UHECRs and cosmogenic neutrinos with Fermi-LAT*, Phys. Lett. **B695** (2011) 13–18. doi:10.1016/j.physletb.2010.11.019 [`arXiv:1003.1496[astro-ph.HE]`].

[258] M. Ahlers and J. Salvado, *Cosmogenic gamma-rays and the composition of cosmic rays*, Phys. Rev. **D84** (2011) 085019. doi:10.1103/PhysRevD.84.085019 [`arXiv:1105.5113[astro-ph.HE]`].

[259] X.-Y. Wang, R.-Y. Liu and F. Aharnonian, *Constraining the emissivity of ultrahigh energy cosmic rays in the distant universe with the diffuse gamma-ray emission*, Astrophys. J. **736** (2011) 112. doi:10.1088/0004-637X/736/2/112 [`arXiv:1103.3574[astro-ph.HE]`].

[260] G. B. Gelmini, O. Kalashev and D. V. Semikoz, *Gamma-ray constraints on maximum cosmogenic neutrino fluxes and UHECR source evolution models*, JCAP **1201** (2012) 044. doi:10.1088/1475-7516/2012/01/044 [`arXiv:1107.1672[astro-ph.CO]`].

[261] G. Decerprit and D. Allard, *Constraints on the origin of ultrahigh energy cosmic rays from cosmogenic neutrinos and photons*, Astron. Astrophys. **535** (2011) A66. doi:10.1051/0004-6361/201117673 [`arXiv:1107.3722[astro-ph.HE]`].

[262] M. Ahlers and F. Halzen, *Minimal cosmogenic neutrinos*, Phys. Rev. **D86** (2012) 083010. doi:10.1103/PhysRevD.86.083010 [`arXiv:1208.4181[astro-ph.HE]`].

[263] A. W. Strong, A. W. Wolfendale and J. Wdowczyk, *Consequences of a universal cosmic-ray theory for γ-ray astronomy*, Nature **241** (1973) 109–110. doi:10.1038/241109b0.

[264] V. S. Berezinsky and A. Y. Smirnov, *Cosmic neutrinos of ultra-high energies and detection possibility*, Astrophys. Space Sci. **32** (1975) 461–482. doi:10.1007/BF00643157.

[265] A. W. Strong, I. V. Moskalenko and O. Reimer, *A new estimate of the extragalactic gamma-ray background from EGRET data*, `arXiv:astro-ph/0306345[astro-ph]`.

[266] S. Lee, *On the propagation of extragalactic high-energy cosmic and gamma-rays*, Phys. Rev. **D58** (1998) 043004. doi:10.1103/PhysRevD.58.043004 [`arXiv:astro-ph/9604098`].

[267] "CLHEP - A Class Library for High Energy Physics." See http://proj-clhep.web.cern.ch/.

[268] A. Mucke, R. Engel, J. P. Rachen, R. J. Protheroe and T. Stanev, *SOPHIA: Monte Carlo simulations of photohadronic processes in astrophysics*, Comput. Phys. Commun. **124** (2000) 290–314. doi:10.1016/S0010-4655(99)00446-4 [`arXiv:astro-ph/9903478`].

[269] "ROOT Data Analysis Framework." See http://root.cern.ch/.

[270] "FFTW." See http://www.fftw.org/.

[271] "CFITSIO - A FITS File Subroutine Library." See http://heasarc.gsfc.nasa.gov/fitsio/.

[272] T. M. Kneiske, T. Bretz, K. Mannheim and D. H. Hartmann, *Implications of cosmological gamma-ray absorption. 2. Modification of gamma-ray spectra*, Astron. Astrophys. **413** (2004) 807–815. doi:10.1051/0004-6361:20031542 [`arXiv:astro-ph/0309141`].

[273] H. Bethe and W. Heitler, *On the stopping of fast particles and on the creation of positive electrons*, Proc. Roy. Soc. Lond. **A146** (1934) 83–112. doi:10.1098/rspa.1934.0140.

[274] G. R. Blumenthal, *Energy loss of high-energy cosmic rays in pair-producing collisions with ambient photons*, Phys. Rev. **D1** (1970) 1596–1602. doi:10.1103/PhysRevD.1.1596.

[275] S. R. Kelner and F. A. Aharonian, *Energy spectra of gamma-rays, electrons and neutrinos produced at interactions of relativistic protons with low energy radiation*, Phys. Rev. **D78** (2008) 034013. doi:10.1103/PhysRevD.82.099901, 10.1103/PhysRevD.78.034013 [`arXiv:0803.0688[astro-ph]`].

[276] National Nuclear Data Center, "NuDat 2 database." See http://www.nndc.bnl.gov/nudat2/, 2011.

[277] K. Murase and J. F. Beacom, *Very-high-energy gamma-ray signal from nuclear photodisintegration as a probe of extragalactic sources of ultrahigh-energy nuclei*, Phys. Rev. **D82** (2010) 043008. doi:10.1103/PhysRevD.82.043008 [`arXiv:1002.3980[astro-ph.HE]`].

[278] L. A. Anchordoqui, J. F. Beacom, H. Goldberg, S. Palomares-Ruiz and T. J. Weiler, *TeV gamma-rays from photo-disintegration/de-excitation of cosmic-ray nuclei*, Phys. Rev. Lett. **98** (2007) 121101. doi:10.1103/PhysRevLett.98.121101 [`arXiv:astro-ph/0611580`].

[279] J. Rachen, *Interaction processes and statistical properties of the propagation of cosmic rays in photon backgrounds*. PhD thesis, Universität Bonn, 1996.

[280] M. V. Kossov, *Approximation of photonuclear interaction cross-sections*, Eur. Phys. J. A **14** (2002) 377–392. doi:10.1140/epja/i2002-10008-x.

[281] V. V. Varlamov, V. V. Surgutanov, A. P. Chernyaev and N. G. Efimkin, *Photonuclear Data. Photodisintegration of Lithium. Evaluated Cross Sections of Channels and Reactions. Informational Review.* Izdatel'stvo Moskovskogo Universiteta, Moscow, 1986.

[282] L. A. Kulchitskii, Y. M. Volkov, V. P. Denisov and V. I. Ogurtsov, *Energy levels of* Li^7 *observed in its photoemission*, Izv. Rossiiskoi Akademii Nauk, Ser.Fiz. **27** (1963) 1412.

[283] "Photonuclear data for applications; cross sections and spectra." IAEA-Tecdoc-1178, 2000.

[284] A. J. Koning and J. P. Delaroche, *Local and global nucleon optical models from 1 keV to 200 MeV*, Nucl. Phys. **A713** (2003) 231–310. doi:10.1016/S0375-9474(02)01321-0.

[285] A. Koning, S. Hilaire and M. Duijvestijn, "TALYS-1.6 user manual." www.talys.eu.

[286] J. Kopecky and M. Uhl, *Test of gamma-ray strength functions in nuclear reaction model calculations*, Phys. Rev. **C41** (1990) 1941–1955. doi:10.1103/PhysRevC.41.1941.

[287] J. Kopecky, M. Uhl and R. E. Chrien, *Radiative strength in the compound nucleus Gd-157*, Phys. Rev. **C47** (1993) 312–322. doi:10.1103/PhysRevC.47.312.

[288] J. Ahrens, *The total absorption of photons by nuclei*, Nucl. Phys. **A446** (1985) 229C–239C. doi:10.1016/0375-9474(85)90591-3.

[289] N. Bianchi, V. Muccifora, E. De Sanctis, A. Fantoni, P. Levi Sandri *et al.*, *Absolute total photoabsorption cross-sections on nuclei in the nucleon resonance region*, Phys. Lett. **B325** (1994) 333–336. doi:10.1016/0370-2693(94)90021-3.

[290] B. Krusche, *Photoproduction of mesons off nuclei*, Eur. Phys. J. ST **198** (2011) 199. doi:10.1140/epjst/e2011-01491-2 [`arXiv:1110.0192[nucl-ex]`].

[291] J. L. Basdevant, J. Rich and M. Spiro, *Fundamentals in nuclear physics: From nuclear structure to cosmology.* 2005.

[292] J. R. Primack, J. S. Bullock and R. S. Somerville, *Observational gamma-ray cosmology*, AIP Conf. Proc. **745** (2005) 23–33. doi:10.1063/1.1878394 [`arXiv:astro-ph/0502177`].

[293] K. Dolag, D. Grasso, V. Springel and I. Tkachev, *Mapping deflections of ultrahigh energy cosmic rays in constrained simulations of extragalactic magnetic fields*, JETP Lett. **79** (2004) 583–587. doi:10.1134/1.1790011 [`arXiv:astro-ph/0310902`].

[294] W. H. Press, S. A. Teukolsky, W. T. Vetterling and B. P. Flannery, *Numerical recipes 3rd edition: The art of scientific computing.* Cambridge University Press, New York, NY, USA, 3 ed., 2007.

[295] P. Bhattacharjee and G. Sigl, *Origin and propagation of extremely high-energy cosmic rays*, Phys. Rept. **327** (2000) 109–247. doi:10.1016/S0370-1573(99)00101-5 [`arXiv:astro-ph/9811011`].

[296] E. Armengaud, G. Sigl and F. Miniati, *Gamma ray astronomy with magnetized zevatrons*, `arXiv:astro-ph/0511277`.

[297] **Pierre Auger Collaboration**, J. Abraham *et al.*, *Measurement of the energy spectrum of cosmic rays above 10^{18} eV using the Pierre Auger Observatory*, Phys. Lett. **B685** (2010) 239–246. doi:10.1016/j.physletb.2010.02.013 [`arXiv:1002.1975[astro-ph.HE]`].

[298] **Pierre Auger Collaboration**, P. Abreu *et al.*, *The Pierre Auger Observatory I: The cosmic ray energy spectrum and related measurements*, `arXiv:1107.4809[astro-ph.HE]`.

[299] **IceCube Collaboration**, R. Abbasi *et al.*, *Constraints on the extremely-high energy cosmic neutrino flux with the IceCube 2008-2009 data*, Phys. Rev. **D83** (2011) 092003. doi:10.1103/PhysRevD.84.079902, 10.1103/PhysRevD.83.092003 [`arXiv:1103.4250[astro-ph.CO]`].

[300] **Pierre Auger Collaboration**, P. Abreu *et al.*, *Search for point-like sources of ultra-high energy neutrinos at the Pierre Auger Observatory and improved limit on the diffuse flux of tau neutrinos*, Astrophys. J. **755** (2012) L4. doi:10.1088/2041-8205/755/1/L4 [`arXiv:1210.3143[astro-ph.HE]`].

[301] **ANITA Collaboration**, P. W. Gorham *et al.*, *Erratum: Observational constraints on the ultra-high energy cosmic neutrino flux from the second flight of the ANITA experiment*, Phys. Rev. **D85** (2012) 049901. doi:10.1103/PhysRevD.82.022004, 10.1103/PhysRevD.85.049901 [`arXiv:1011.5004[astro-ph.HE]`].

[302] G. G. Jonsson and K. Lindgren, *Compilation and analysis of intermediate- and high-energy photon and electron induced spallation yields*, Phys. Scripta **7** (1973) 49–54. doi:10.1088/0031-8949/7/1-2/004.

[303] G. G. Jonsson and K. Lindgren, *A complementary study of photospallation systematics*, Phys. Scripta **15** (1977) 308–310. doi:10.1088/0031-8949/15/5-6/004.

[304] J. S. Levinger, *The high-energy nuclear photoeffect*, Phys. Rev. **84** (1951) 43–51. doi:10.1103/PhysRev.84.43.

[305] V. L. Ginzburg, V. A. Dogiel, V. S. Berezinsky, S. V. Bulanov and V. S. Ptuskin, *Astrophysics of cosmic rays.* 1990.

[306] **IceCube Collaboration**, M. G. Aartsen *et al.*, *Probing the origin of cosmic-rays with extremely high energy neutrinos using the IceCube Observatory*, Phys. Rev. **D88** (2013) 112008 [`arXiv:1310.5477[astro-ph.HE]`].

[307] T. Le and C. D. Dermer, *On the redshift distribution of gamma ray bursts in the Swift era*, Astrophys. J. **661** (2007) 394–415. doi:10.1086/513460 [`arXiv:astro-ph/0610043`].

[308] J. V. Wall, C. A. Jackson, P. A. Shaver, I. M. Hook and K. I. Kellermann, *The Parkes quarter-Jansky flat-spectrum sample. 3. Space density and evolution of QSOs*, Astron. Astrophys. (2004) [`arXiv:astro-ph/0408122[astro-ph]`].

[309] S. Pakvasa, W. Rodejohann and T. J. Weiler, *Flavor ratios of astrophysical neutrinos: Implications for precision measurements*, JHEP **0802** (2008) 005. doi:10.1088/1126-6708/2008/02/005 [`arXiv:0711.4517[hep-ph]`].

[310] **DAYA-BAY Collaboration**, F. P. An *et al.*, *Observation of electron-antineutrino disappearance at Daya Bay*, Phys. Rev. Lett. **108** (2012) 171803. doi:10.1103/PhysRevLett.108.171803 [`arXiv:1203.1669[hep-ex]`].

[311] The OpenMP development team, "Openmp website." See www.openmp.org.

[312] The SWIG development team, "Swig website." See www.swig.org.

[313] M. Settimo and M. De Domenico, *Propagation of extragalactic photons at ultra-high energy with the EleCa code*, `arXiv:1311.6140[astro-ph.HE]`.

[314] O. E. Kalashev and E. Kido, *Simulations of ultra high energy cosmic rays propagation*, `arXiv:1406.0735[astro-ph.HE]`.

[315] H.-P. Bretz, M. Erdmann, P. Schiffer, D. Walz and T. Winchen, *PARSEC: A parametrized simulation engine for ultra-high energy cosmic ray protons*, Astropart. Phys. **54** (2014) 110–117. doi:10.1016/j.astropartphys.2013.12.002 [`arXiv:1302.3761[astro-ph.HE]`].

[316] K. M. Gorski, E. Hivon, A. J. Banday, B. D. Wandelt, F. K. Hansen *et al.*, *HEALPix - A framework for high resolution discretization, and fast analysis of data distributed on the sphere*, Astrophys. J. **622** (2005) 759–771. doi:10.1086/427976 [`arXiv:astro-ph/0409513`].

[317] K. Dolag and F. A. Stasyszyn, *An MHD gadget for cosmological simulations*, `arXiv:0807.3553[astro-ph]`.

[318] R. Teyssier, *Cosmological hydrodynamics with adaptive mesh refinement: a new high resolution code called ramses*, Astron. Astrophys. **385** (2002) 337–364. doi:10.1051/0004-6361:20011817 [`arXiv:astro-ph/0111367`].

[319] G. Sigl, F. Miniati and T. A. Ensslin, *Ultrahigh-energy cosmic rays in a structured and magnetized universe*, Phys. Rev. **D68** (2003) 043002. doi:10.1103/PhysRevD.68.043002 [`arXiv:astro-ph/0302388`].

[320] W. Saunders, W. J. Sutherland, S. J. Maddox, O. Keeble, S. J. Oliver *et al.*, *The PSCz catalogue*, Mon. Not. Roy. Astron. Soc. **317** (2000) 55. doi:10.1046/j.1365-8711.2000.03528.x [`arXiv:astro-ph/0001117`].

[321] R. Beck, *Galactic and extragalactic magnetic fields - a concise review*, ASTRA **5** (2009), no. 1 43–47. doi:10.5194/astra-5-43-2009.

[322] **Pierre Auger Collaboration**, P. Abreu *et al.*, *Bounds on the density of sources of ultra-high energy cosmic rays from the Pierre Auger Observatory*, JCAP **1305** (2013) 009. doi:10.1088/1475-7516/2013/05/009 [`arXiv:1305.1576[astro-ph.HE]`].

[323] "Healpy." See http://healpy.readthedocs.org/.

[324] B. Sarkar, "Private communication."

Acknowledgments

First of all, let me thank my supervisor, Günter Sigl, for giving me the opportunity to do my PhD in his group and become part of the Pierre Auger Collaboration. I have learned a lot from him as well as from the other people in the group. I feel it has been a privilege to do my PhD here in Hamburg with this group. I am also thankful for being part of the Pierre Auger Collaboration. I have learned a lot and gained valuable experiences during the many meetings with the Collaboration. Presenting my work to the collaboration, but also presenting the work of the collaboration at, for instance, a big conference like PASCOS 2013 in Taipei, were all experiences I will carry with me in my future career.

I would also like to thank the other (former and present) members of the group for always making me feel welcome here, for the help they provided over and over again, and for the fun times we had together. Thank you Alessandro Mirizzi, Torsten Bringmann, Luca Maccione, Peter Schiffer, Nils Nierstenhöfer, Carmelo Evoli, Michael Grefe, Enrico Borriello, Sovan Chakraborty, Masaki Asano. And of course my warmest thanks as well to the (former) PhD students of this group, Laura van den Aarschen, Rafael Alves Batista, Francesca Calore, Jörg Kulbartz, Natacha Leite, Ninetta Saviano, Andrey Saveliev, Martin Vollmann, many of which I consider to be close friends. Their companionship and support have been invaluable to me. Let me thank Andrey in particular, not just for being a good friend, but also for his help in translating the abstract of this thesis to German, for proofreading this thesis, and his help with so many more computer-related, German-related, bureaucracy-related things.

Here I would like to thank my close friends from the Netherlands as well. Even though I moved away our friendship has lasted and even became stronger. Thank you for coming to visit me here so often, and thank you for all the support and fun times. Thank you Ivo, Jeroen, Joost, Laura, Marcel, Marieke, Paul, Richard, Rosalie, Sebastiaan, Simon, Tim and Wieke, your friendship is very important to me.

Special thanks go to my parents Rob and Loes, and to my brother Marijn. I am blessed with such a nice family whom I love, and who I know love me. Thanks you for always being there for me and for giving me the feeling that, no matter what happens, I always have a save place to return to.

Finally, last but not least, I would like to express my deepest gratitudes to my girlfriend, Michelle. She has always been there for me during the whole period of my PhD, supporting me when needed and getting me through the difficult times. Without her this PhD thesis would not have been possible. Michelle, I love you.

Selbstständigkeitserklärung

Ich erkläre, dass ich die vorliegende Arbeit selbstständig und nur unter Verwendung der angegebenen Literatur und Hilfsmittel angefertigt habe.

Hamburg, den 14. April 2015

Arjen René van Vliet